Oil Recovery From Naturally Fractured Reservoirs
by Steam Injection Methods
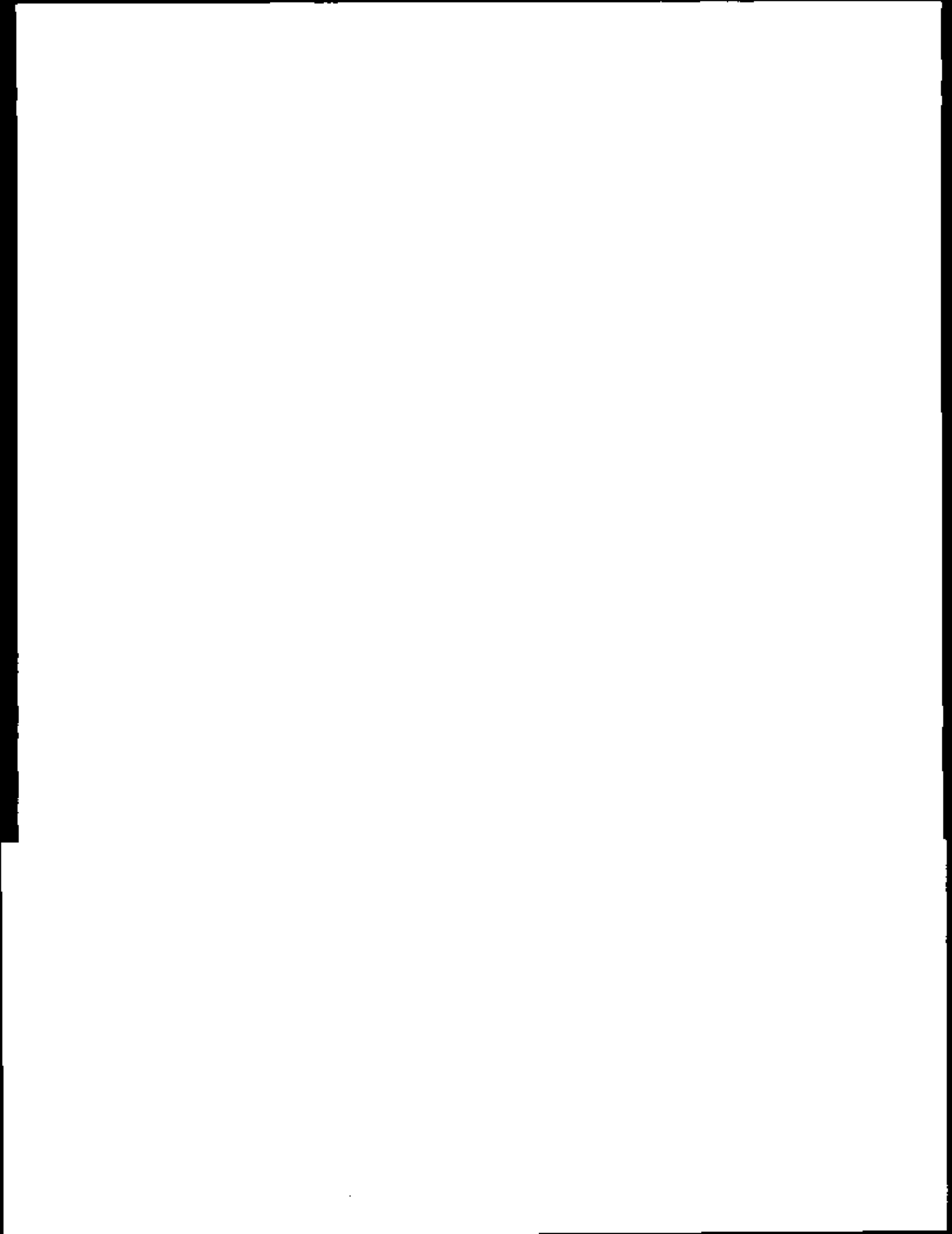
Final Report

By
John C. Reis
Mark A. Miller

May 1995

Work Performed Under Contract No. DE-AC22-90BC14661

Prepared for
U.S. Department of Energy
Assistant Secretary for Fossil Energy

DISCLAIMER

This report was prepared as an account of work sponsored

DISCLAIMER

DISCLAIMER

Portions of this document may be illegible in electronic image products. Images are produced from the best available original document.

ACKNOWLEDGMENTS

ABSTRACT

The United States of America has naturally fractured reservoirs containing many tens of billions of barrels of oil. When secondary and enhanced recovery methods are applied, fractures tend to channel injected fluids through the reservoir to production wells, resulting in much of the oil in the matrix blocks being bypassed and not recovered. This results in a low recovery efficiency from fractured reservoirs. Because of the large size of this resource, any new technology that improves recovery efficiency from naturally fractured reservoirs by as little as a few percent could result in a significant increase in overall oil production from existing petroleum formations.

Oil recovery by steam injection is a proven, successful technology for non-fractured reservoirs, but has received only limited study for fractured reservoirs. Preliminary studies suggest recovery efficiencies in fractured reservoirs may be increased by as much as 50% with the application of steam relative to that of low temperature processes. The key mechanisms enhancing oil production at high temperature are the differential thermal expansion between oil and the pore volume, and the generation of gases within matrix blocks. Other mechanisms may also contribute to increased production. These mechanisms are relatively independent of oil gravity, making steam injection into naturally fractured reservoirs equally attractive to light and heavy oil deposits.

The objectives of this research program are to quantify the amount of oil expelled by these recovery mechanisms and to develop a numerical model for predicting oil recovery in naturally fractured reservoirs during steam injection. The experimental study consists of constructing and operating several apparatuses to isolate each of these mechanisms. The first measures thermal expansion and capillary imbibition rates at relatively low temperature, but for various lithologies and matrix block shapes. The second apparatus measures the same parameters, but at high temperatures and for only one shape. A third experimental apparatus measures the maximum gas saturations that could build up within a matrix block. A fourth apparatus measures thermal conductivity and diffusivity of porous media The numerical study consists of developing transfer functions for oil expulsion from matrix blocks to fractures at high temperatures and incorporating them, along with the energy equation, into a dual porosity thermal reservoir simulator. This simulator can be utilized to make predictions for steam injection processes in naturally-fractured reservoirs. Analytical models for capillary imbibition have also been developed.

EXECUTIVE SUMMARY

This report presents the results of a number of experimental, analytical, and numerical studies addressed at the development of methods of modeling oil recovery from naturally fractured reservoirs by steam injection methods.

The first part of the report presents analytical models for oil recovery by capillary imbibition into rectilinear and cylindrical matrix blocks having arbitrary aspect ratios. The model for rectilinear geometry can be applied to reservoirs having orthogonal fracture sets, each set having a different fracture spacing. The model for cylindrical geometry can be used for laboratory measurements on cylindrical cores. These general analytical models employ Darcy's law and a material balance to determine the oil expulsion rate. They predict the oil expulsion rate based on the petrophysical properties of the matrix block and need no empirical constants. All previously reported models have required an empirical constant to be measured in the laboratory, in addition to the petrophysical properties. That need for an empirical constant has prevented the generalization of the previous models.

An analytical model for the gas saturation distribution in a matrix block has also been developed for gases generated during steam injection by high temperature chemical reactions. The model assumes a uniform gas generation rate from temperature-dependent chemical reactions everywhere in the matrix block and a fixed saturation at the edge of the matrix block. Gas then diffuses to the edge of the matrix block. The model can be used to estimate the spacing, and hence distribution, of gas bubbles following gas generation during thermal operations.

A variety of experimental studies have also been completed. These studies include measurements of capillary imbibition, gas generation, and thermal properties. Capillary pressure measurements have measured imbibition rates with matrix blocks of different sizes and shape. These studies were used to test and validate the general analytical models that have been developed in this study. An experimental apparatus to measure the change in critical gas saturation during gas generation at high temperature and pressure was also completed. In addition, a steady-state experimental apparatus to measure thermal conductivity was designed, tested, and implemented. The apparatus is capable of measuring thermal conductivity at various fluid saturation conditions. The apparatus has also been modified for transient measurements to obtain thermal diffusivity.

A new dual porosity simulation approach was developed for modeling fluid flow in naturally fractured reservoirs. The approach accurately and efficiently models transfer flow using discretized matrix blocks to enhance pressure and saturation resolution. Finite-difference equations for matrix blocks are treated by an IMPES approach while fracture equations are solved implicitly. These equations are formulated in such a way that they are mathematically decoupled. The new approach has been successfully validated against a single porosity simulator with discrete matrix blocks and fractures and against analytical transient solutions of dual porosity systems. Excellent agreement has been achieved for a variety of reservoir properties. The formulation presented in these studies should be able to be easily extended to other oil recovery processes in addition to thermal processes.

To support the dual porosity thermal code development, a fully implicit, three-dimensional, two-phase simulator was developed to model hot waterflooding in a single

matrix block with surrounding fractures. The simulator can handle one, two, or three fractures surrounding the single matrix block, and can also handle heat losses to the overburden. A study was carried out on a 2 m x 0.1 m x 0.1 m matrix with an open fracture at the end of longest axis, a 2 m x 2 m x 0.1 m matrix with two open fractures at the ends of long axes, and a 2 m x 2 m x 2 m matrix with two fractures. Cases both with and without heat loss were simulated.

A numerical model for gas generation in matrix blocks was also developed. Preliminary calculations show that significant volumes of gas can be generated during typical oil recovery times for fractured reservoirs, a result consistent with laboratory and field experience. The time for the gas phase to be generated decreases as temperature increases and increases as CO_2 partial pressure decreases. The effect of gas generation on enhanced oil recovery is determined by the reduction of residual oil saturation due to gas generation.

A new set of continuous correlation functions of saturated steam properties (density, enthalpy and viscosity) has been developed. The new correlations cover the saturation envelope from 20°C to 360°C and are highly accurate and continuous over a wide temperature range. In terms of simplicity, accuracy, and continuity, these functions offer advantages in certain applications over those previously published.

TABLE OF CONTENTS

LIST OF TABLES

LIST OF FIGURES

1.0 INTRODUCTION

Most of the large, domestic petroleum reservoirs were discovered decades ago and are approaching their economic limits with existing technology. With the most promising locations for new field discoveries being located in high-cost, remote, and environmentally sensitive areas, e.g., deep offshore or Alaska, it is vital to develop cost effective ways to improve recovery from existing fields. Many tens of billions of barrels of oil are contained in naturally fractured reservoirs located in over 30 geologic formations and scattered over a dozen states (Nelson, 1985). Because of the number of naturally fractured reservoirs and the large volume of oil they contain, any new technology that improves oil recovery by as little as a few percent could have a significant impact on overall domestic oil production.

Naturally fractured reservoirs differ from non-fractured reservoirs in that fractures provide flow paths with permeabilities that can be orders of magnitude higher than the remainder of the formation. For most reservoirs, the porosity of the fracture network is significantly lower than that of the matrix blocks defined by the fractures, which results in the oil content of the fractures being very low.

Steamflooding is a proven enhanced oil recovery method for non-fractured reservoirs. Recent studies have suggested that the steamflooding can also be effective for oil recovery from naturally fractured reservoirs. The two most important mechanisms that can potentially expel incremental oil at steam temperatures are thermal expansion of oil, and gas generation from temperature-dependent chemical reactions. Capillary imbibition into water-wet matrix blocks is believed to be important at all temperatures, although its incremental benefits at high temperatures are not clear.

Steamflooding of fractured carbonates has been attempted with some success (Warren and Root, 1963; Chen et al., 1989). Oil recovery from heated matrix blocks can be significantly higher than from unheated blocks (Sinnokrot et al., 1971; Kyte et al., 1961), with over 60% of the oil expelled at steam temperatures (Sahuquet and Ferrier, 1982; Dreher et al., 1986), even though steam flows primarily through fractures. A simulation study has indicated that thermal conduction can heat matrix blocks and recover oil within one year at distances up to 20 ft from a fracture (Nolan et al., 1980). Preliminary studies have confirmed that oil recovery at steam temperature can be 50% higher than that at reservoir temperatures (Reis, 1990).

In this study, the mechanisms of thermal expansion, gas generation, and capillary imbibition are investigated, both analytically and experimentally. These mechanisms are incorporated into a dual porosity, thermal reservoir simulator to enable accurate studies of oil recoveries from naturally fractured reservoirs by steam injection.

1

2.0 ANALYTICAL MODELS

In this section, analytical models for water imbibing into gas-saturated matrix blocks are developed. The purpose of these models is to develop simple approaches for investigating the primary mechanisms for expelling oil from matrix blocks. These models would be applicable for water imbibition into highly gas-saturated rocks, such as in petroleum reservoirs. This section also presents a model for estimating the distribution of gas within a matrix block following temperature-dependent gas generation during steam injection.

2.1 CAPILLARY IMBIBITION INTO GAS-SATURATED RECTILINEAR MATRIX BLOCKS

In this section, a closed-form analytical model for counter-current capillary imbibition of water into a gas-saturated rectilinear matrix block of arbitrary aspect ratio is derived. Capillary pressure between the water and gas is assumed to be the only driving force. Gravity is not considered.

Figures 2.1 and 2.2 depict a representative matrix block for this geometry. In this analysis, "a" is taken to be the smallest dimension of the matrix block. The imbibition front, i.e., leading edge of the imbibing water, is shown with dotted lines in these figures. Water is assumed to simultaneously contact all faces of the block and imbibe uniformly into all faces.

The flow rate of the gas from the two faces normal to direction x_1 is given by

$$q_{gasx_1} = 2 \frac{k \, k_{rgas}}{\mu_{gas}} A_{x_1} \frac{dP_{gas}}{dx_1}, \qquad (2.1)$$

where

$$A_{x_1} = (a-2x)(b-2x) \qquad (2.2)$$

with similar equations for the x_2 and x_3 directions.

Similarly, the flow rate of the water is

$$q_{waterx_1} = 2 \frac{k \, k_{rwater}}{\mu_{water}} A_{x_1} \frac{dP_{water}}{dx_1}, \qquad (2.3)$$

with similar equations for the other directions.

The total gas flow rate from the matrix block is found by summing the flow rate for all three directions:

$$q_{gas} = q_{gasx_1} + q_{gasx_2} + q_{gasx_3} = 2 \frac{k \, k_{rgas}}{\mu_{gas}} \left(A_{x_1} \frac{dP_{gas}}{dx_1} + A_{x_2} \frac{dP_{gas}}{dx_2} + A_{x_3} \frac{dP_{gas}}{dx_3} \right) \qquad (2.4)$$

and the total water flow rate into the matrix block is

2

$$q_{water} = 2 \frac{k\, k_{rwater}}{\mu_{water}} \left(A_{x_1} \frac{dP_{water}}{dx_1} + A_{x_2} \frac{dP_{water}}{dx_2} + A_{x_3} \frac{dP_{water}}{dx_3} \right) \qquad (2.5)$$

The pressure gradients in the fluids between the imbibition front and the faces of the matrix block are assumed to be independent of location, i.e.,

$$\frac{dP_{gas}}{dx} = \frac{dP_{gas}}{dx_1} = \frac{dP_{gas}}{dx_2} = \frac{dP_{gas}}{dx_3} \qquad (2.6)$$

and

$$\frac{dP_{water}}{dx} = \frac{dP_{water}}{dx_1} = \frac{dP_{water}}{dx_2} = \frac{dP_{water}}{dx_3} \qquad (2.7)$$

Total surface area of all imbibition fronts at a distance x from the matrix block face can be written as

$$A_x = 2[(a-2x)(b-2x) + (b-2x)(c-2x) + (a-2x)(c-2x)], \qquad (2.8)$$

Substituting Eqs. 2.6, 2.7, and 2.8 into Eqs. 2.4 and 2.5 yields

$$q_{gas} = \frac{k\, k_{rgas}}{\mu_{gas}} A_x \frac{dP_{gas}}{dx} \qquad (2.9)$$

and

$$q_{water} = \frac{k\, k_{rwater}}{\mu_{water}} A_x \frac{dP_{water}}{dx} \qquad (2.10)$$

For counter-current imbibition, the water and gas flow rates at any location are related through the following expression:

$$q_{water} = -q_{gas} \qquad (2.11)$$

Combining Eqs. 2.9 through 2.11 yields

$$\frac{k_{rwater}}{\mu_w} \frac{dP_{water}}{dx} = -\frac{k_{rgas}}{\mu_{gas}} \frac{dP_{gas}}{dx} \qquad (2.12)$$

The water and gas pressures are related through the capillary pressure in the porous medium. This relationship is given by

$$P_{gas} = P_{water} + P_c \qquad (2.13)$$

Using this expression to eliminate the gas pressure from Eq. 2.12 yields:

$$\frac{dP_{water}}{dx} = \frac{1}{(1 + \frac{k_{rgas}}{k_{rwater}} \frac{\mu_{water}}{\mu_{gas}})} \frac{dP_c}{dx} \qquad (2.14)$$

Substituting Eq. 2.14 into Eq. 2.10 yields the following expression for the water imbibition rate:

$$q_{water} = k\, A_x \frac{1}{(\frac{\mu_{gas}}{k_{rgas}} + \frac{\mu_{water}}{k_{rwater}})} \frac{dP_c}{dx} \qquad (2.15)$$

If the pressure gradient behind the imbibition front is assumed to vary linearly with the position, then

$$\frac{dP_c}{dx} = \frac{P_{c,swi}}{L'} \qquad (2.16)$$

where $P_{c,swi}$ is the capillary pressure at the leading edge of the imbibition front. With these assumptions, Eq. 2.15 can be rewritten as

$$q_{water} = \frac{k\, A_{L'}}{(\frac{\mu_{gas}}{k_{rgas}} + \frac{\mu_{water}}{k_{rwater}})} \frac{P_{c,swi}}{L'} \qquad (2.17)$$

The water imbibition rate can also be found from a material balance. The cumulative water imbibing into the matrix block before the imbibition front reaches the center of the block is

$$Q_{water} = \int_0^{L'} A_x\, \phi\, (S_{wi} - S_w(x))dx \qquad (2.18)$$

If the saturation is assumed to be constant with position behind the imbibition front (piston-like displacement), then the water saturation behind the advancing imbibition front can be written as

$$S_w(x) = S_{wp} \qquad (2.19)$$

The validity of this assumption will be discussed below.

The total surface area of the shrinking imbibition front in Eq. 2.18 can be rewritten in terms of x as

$$A_x = 2\left(ab + bc + ac - 4(a + b + c)x + 12x^2 \right) \qquad (2.20)$$

or

$$A_x = A_o - 8\left(a + b + c\right)x + 24x^2 \tag{2.21}$$

where the surface area of the matrix block is

$$A_o = 2\left(ab + bc + ac\right) \tag{2.22}$$

Substituting Eqs. 2.19 and Eq. 2.21 into Eq. 2.18 and integrating yields

$$Q_{water} = \phi\,\Delta S_{water}\left[A_o\,L' - 4\left(a + b + c\right)L'^2 + 8\,L'^3\right] \tag{2.23}$$

where

$$\Delta S_{water} = S_{wi} - S_{wp} \tag{2.24}$$

and ΔS_{water} is the change in water saturation during the infinite acting period.

The water imbibition rate is found by differentiating Eq. 2.23 with respect to time. This rate is given by

$$q_{water} = \frac{dQ_{water}}{dt} = \phi\,\Delta S_{water}\left[A_o - 8\left(a + b + c\right)L' + 24L'^2\right]\frac{dL'}{dt} \tag{2.25}$$

Equating Eqs. 2.17 and 2.25, and rearranging yields

$$\frac{k}{L'\,\phi\,\Delta S_{water}\left(\dfrac{\mu_{gas}}{k_{rgas}} + \dfrac{\mu_{water}}{k_{rwater}}\right)}\frac{P_{c,swi}}{} = \frac{dL'}{dt} \tag{2.26}$$

Eq. 2.26 can be solved to yield:

$$L' = \left[\frac{2\,k\,P_{c,swi}\,t}{\left(\dfrac{\mu_{gas}}{k_{rgas}} + \dfrac{\mu_{water}}{k_{rwater}}\right)\phi\,\Delta S_{water}}\right]^{1/2} \tag{2.27}$$

If the surface area of the matrix block, Eq. 2.22, is rewritten as

$$A_o = 2\,a^2\left(\frac{b}{a} + \frac{bc}{a^2} + \frac{c}{a}\right) \tag{2.28}$$

and a dimensionless imbibition front distance is defined as

$$L_D = \frac{L'}{L} \tag{2.29}$$

and L is the matrix block half thickness, a/2, the time that the imbibition front reaches the centerline of the rectangular block is found from Eq. 2.27 when $L' = a/2$:

$$t^* = \frac{L^2 \, \phi \, \Delta S_w \, (\frac{\mu_{water}}{k_{rwater}} + \frac{\mu_{gas}}{k_{rgas}})}{2k \, P_{c,swi}} \quad (2.30)$$

The cumulative gas recovery after an infinite time, Q_∞, is expressed as

$$Q_\infty = a \, b \, c \, \phi \, \Delta S_{water} \quad (2.31)$$

The normalized cumulative recovery before the imbibition front reaches the centerline can be obtained by dividing Eq. 2.17 by Eq. 2.31:

$$\frac{Q_{water}}{Q_\infty} = L_D \left[\frac{(ab+bc+ac)}{bc} \cdot \frac{a(a+b+c)}{bc} L_D + \frac{a^2}{bc} L_D^2 \right] \quad (2.32)$$

where

$$L_D = \left[\frac{2 \, k \, P_{c,swi} \, t}{(\frac{\mu_{gas}}{k_{rgas}} + \frac{\mu_{water}}{k_{rwater}}) \, \phi \, \Delta S_{water} L^2} \right]^{1/2} \quad (2.33)$$

2.2 CAPILLARY IMBIBITION INTO GAS-SATURATED CYLINDRICAL MATRIX BLOCKS

In this section, a closed form, analytical model for counter-current capillary imbibition into a gas-saturated cylindrical matrix block of arbitrary aspect ratio is derived. Capillary pressure between the water and gas is assumed to be the only driving force. Gravity is not considered.

Figure 2.3 depicts a representative matrix block with a cylindrical shape. The imbibition front, i.e., leading edge of the imbibing water, is shown with dotted lines in the figure. Water is assumed to simultaneously contact all faces of the block and imbibe uniformly into all faces.

The flow rate of the gas from the cylindrical face is given by

$$q_{gasC} = \frac{k \, k_{rgas}}{\mu_{gas}} \, A_C \, \frac{dP_{gas}}{dr} \quad (2.34)$$

where

$$A_C = 2 \, \pi \, (R - x)(h - 2x) \quad (2.35)$$

while the flow rate from the two end faces is

6

$$q_{gasL} = \frac{k \, k_{rgas}}{\mu_{gas}} \, A_L \, \frac{dP_{gas}}{dx} \qquad (2.36)$$

where

$$A_L = 2 \left[\pi \, (R - x)^2 \right] \qquad (2.37)$$

Similarly, the flow rate of the water into cylindrical face is

$$q_{waterC} = \frac{k \, k_{rwater}}{\mu_{water}} \, A_C \, \frac{dP_{water}}{dr} \qquad (2.38)$$

and flow of water into the two end faces is

$$q_{waterL} = \frac{k \, k_{rwater}}{\mu_{water}} \, A_L \, \frac{dP_{water}}{dx} \qquad (2.39)$$

The total gas flow rate from the matrix block is found by summing the flow rate for all directions;

$$q_{gas} = q_{gasC} + q_{gasL} = \frac{k \, k_{rgas}}{\mu_{gas}} \left(A_C \frac{dP_{gas}}{dr} + A_L \frac{dP_{gas}}{dx} \right) \qquad (2.40)$$

and the total water flow rate into the matrix block is

$$q_{water} = q_{waterC} + q_{waterL} = \frac{k \, k_{rwater}}{\mu_{water}} \left(A_C \frac{dP_{water}}{dr} + A_L \frac{dP_{water}}{dx} \right) \qquad (2.41)$$

The pressure gradients in the fluids between the imbibition front and the faces of the matrix block are assumed to be independent of location, i.e.,

$$\frac{dP_{gas}}{dx} = \frac{dP_{gas}}{dr} = \frac{dP_{gas}}{dx} \qquad (2.42)$$

and

$$\frac{dP_{water}}{dx} = \frac{dP_{water}}{dr} = \frac{dP_{water}}{dx} \qquad (2.43)$$

Total surface area of all imbibition fronts at a distance x from the matrix block face can be written as

$$A_x = A_C + A_L \qquad (2.44)$$

Substituting Eqs. 2.42, 2.43, and 2.44 into Eqs. 2.40 and 2.41 yields

$$q_{gas} = \frac{k\, k_{rgas}}{\mu_{gas}} A_x \frac{dP_{gas}}{dx}$$

(2.45)

and

$$q_{water} = \frac{k\, k_{rwater}}{\mu_{water}} A_x \frac{dP_{water}}{dx}$$

(2.46)

For counter-current imbibition, the water and gas flow rates at any location are related through the following expression:

$$q_{water} = -q_{gas}$$

(2.47)

Combining Eqs. 2.45 through 2.47 yields

$$\frac{k_{rwater}}{\mu_w} \frac{dP_{water}}{dx} = -\frac{k_{rgas}}{\mu_{gas}} \frac{dP_{gas}}{dx}$$

(2.48)

The water and gas pressures are related through the capillary pressure in the porous medium. This relationship is given by

$$P_{gas} = P_{water} + P_c.$$

(2.49)

Using this expression to eliminate the gas pressure from Eq. 2.48 yields:

$$\frac{dP_{water}}{dx} = \frac{1}{(1 + \dfrac{k_{rgas}}{k_{rwater}} \dfrac{\mu_{water}}{\mu_{gas}})} \frac{dP_c}{dx}$$

(2.50)

Substituting Eq. 2.50 into Eq. 2.46 yields the following expression for the water imbibition rate:

$$q_{water} = k\, A_x \frac{1}{(\dfrac{\mu_{gas}}{k_{rgas}} + \dfrac{\mu_{water}}{k_{rwater}})} \frac{dP_c}{dx}$$

(2.51)

If the pressure gradients behind the imbibition front is assumed to vary linearly with the position, then

$$\frac{dP_c}{dx} = \frac{P_{c,swi}}{L'}$$

(2.52)

where $P_{c,swi}$ is the capillary pressure at the leading edge of the imbibition front. With these assumptions, Eq. 2.51 can be rewritten as

8

$$q_{water} = \frac{k \, A_L}{(\frac{\mu_{gas}}{k_{rgas}} + \frac{\mu_{water}}{k_{rwater}})} \frac{P_{c,swi}}{L'} \qquad (2.53)$$

The water imbibition rate can also be found from a material balance. The cumulative water imbibing into the matrix block before the imbibition front reaches the center of the block is

$$Q_{water} = \int_0^{L'} A_x \, \phi \, (S_{wi} - S_w(x)) dx \qquad (2.54)$$

If the saturation is also assumed to be constant with position behind the imbibition front (piston-like displacement), then the water saturation behind the advancing imbibition front can be written as

$$S_w(x) = S_{wp} \qquad (2.55)$$

The validity of this assumption will be discussed below.

Substituting Eqs. 2.55 and Eq. 2.44 into Eq. 2.54 and integrating yields

$$Q_{water} = 2 \, \pi \, \phi \, \Delta S_{water} \left[R(h+R) \, L' - (\frac{h}{2} + 2R) \, L'^2 + L'^3 \right]. \qquad (2.56)$$

where

$$\Delta S_{water} = S_{wi} - S_{wp} \qquad (2.57)$$

The water imbibition rate is found by differentiating Eq. 2.56 with respect to time. This rate is given by

$$q_{water} = \frac{dQ_{water}}{dt} = 2 \, \pi \, \phi \, \Delta S_{water} \left[R(h+R) - 2(\frac{h}{2} + 2R) \, L' + 3L'^2 \right] \frac{dL'}{dt} \qquad (2.58)$$

Equating Eqs 2.53 and 2.58, and rearranging yields

$$\frac{k}{L' \, \phi \, \Delta S_{water}} \frac{P_{c,swi}}{(\frac{\mu_{gas}}{k_{rgas}} + \frac{\mu_{water}}{k_{rwater}})} = \frac{dL'}{dt} \qquad (2.59)$$

Equation 2.59 can be solved to yield:

$$L' = \left[\frac{2 \, k \, P_{c,swi} \, t}{(\frac{\mu_{gas}}{k_{rgas}} + \frac{\mu_{water}}{k_{rwater}}) \, \phi \, \Delta S_{water}} \right]^{1/2} \qquad (2.60)$$

9

and a dimensionless imbibition front distance is defined as

$$L_D = \frac{L'}{L} \tag{2.61}$$

Cumulative gas recovery after an infinite time, Q_∞, is expressed as

$$Q_\infty = R^2 \pi h \phi \Delta S_{water} \tag{2.62}$$

The normalized cumulative recovery before the imbibition front reaches the centerline can be obtained by dividing Eq. 2.56 by Eq. 2.62:

$$\frac{Q_{water}}{Q_\infty} = \frac{2}{R^2 h}\left[R(h+R) L' - (\frac{h}{2} + 2R) L'^2 + L'^3 \right] \tag{2.63}$$

For tall, thin cylinders,

$$\frac{h}{2R} \geq 1 \tag{2.64}$$

and the shortest distance to the center of the cylinder is the radius,

$$L=R \tag{2.65}$$

The dimensionless imbibition front distance can be defined as

$$L_D = \frac{L'}{R} \tag{2.66}$$

Equation 2.63 can be rearranged to yield the dimensionless form as

$$\frac{Q_{water}}{Q_\infty} = L_D\left[2(1+\frac{R}{h}) - (1+4\frac{R}{h}) L_D + \frac{2R}{h}L_D^2 \right] \tag{2.67}$$

For short, thick cylinders,

$$\frac{h}{2R} \leq 1 \tag{2.68}$$

and the shortest distance to the center of the cylinder is half of the cylinder height,

$$L = \frac{h}{2} \tag{2.69}$$

The dimensionless imbibition front can be defined as

10

$$L_D = \frac{L'}{\left(\frac{h}{2}\right)} \tag{2.70}$$

Equation 2.63 can be rearranged to yield the dimensionless form as

$$\frac{Q_{water}}{Q_\infty} = L_D \left[\left(1 + \frac{h}{R}\right) - \frac{h}{2R^2} \left(\frac{h}{2} + 2R\right) L_D + \frac{h^2}{4R^2} L_D^2 \right] \tag{2.71}$$

2.3 GAS GENERATION

At temperatures encountered during steam injection, temperature-dependent chemical reactions occur that can generate a significant amount of gas in matrix blocks. This gas, primarily carbon dioxide, will expel oil from the matrix blocks into the fractures where it can be recovered.

The distribution of gas within a matrix block will depend on the gas generation and gas diffusion rates. If the generation rate is low, the bubbles will initially be disperse and the gas molecules will diffuse through the fluids and join existing bubbles. In this case, the existing bubbles will grow larger and few new bubbles will form. If the generation rate is high, however, a supersaturation of gas will form locally before the gas can diffuse to an existing bubble. In this case, many small bubbles will form. If the first case, there would be a few large bubbles in the matrix block, while in the second case, there would be a large number of smaller bubbles.

If the gas is concentrated in a few large bubbles, then the gas will have a greater probability of channeling out of the matrix block at a lower overall gas saturation and ultimate oil expulsion. The gas may even diffuse directly to the fracture without ever forming gas bubbles and expelling any oil. If the gas is dispersed in a large number of small bubbles, then a higher gas saturation will be reached in the matrix block and the largest volume of oil will be expelled. The question addressed here is which case applies to oil reservoirs during steam injection.

What is desired is to determine the characteristic length over which diffusive transport acts on CO_2 in the presence of generation. This length indicates the spacing between nucleation sites, which then gives an estimate of the bubble population density.

To better predict the expulsion of oil from reservoirs by gas generation, a model is developed to determine when the gas saturation distribution is controlled by the generation rate and when it is controlled by the diffusion rate. For simplicity, the model assumes that gas molecules are generated uniformly in the medium and it diffuses in one-dimension along the x-axis to a point of zero concentration. A mass balance on the gas in solution yields the following equation:

$$-\frac{\partial M}{\partial x} + \dot{C}_{gen} = \frac{\partial C}{\partial t} \tag{2.72}$$

The mass flux can be expressed in terms of the local concentration by Fick's equation:

11

$$M = -D_m \frac{dC}{dx} \tag{2.73}$$

Substituting Eq. 2.73 into Eq. 2.72 yields

$$D_m \frac{\partial^2 C}{\partial x^2} + \dot{C}_{gen} = \frac{\partial C}{\partial t} \tag{2.74}$$

Diffusion coefficients of gas (CO_2) in various hydrocarbons may be found in the literature. An apparent diffusion coefficient of a gas through a liquid in a porous medium can be estimated from the average cross-sectional area open for diffusion and the overall length (Perkins and Johnson, 1963). For porous media, the effective diffusion coefficient can be expressed as

$$D = \frac{D_m}{\phi F} \tag{2.75}$$

The generation rate of gas is a function of temperature and can be described through chemical kinetic theory. One kinetic model that has been proposed for the generation rate of CO_2 is (Cathles *et al.*, 1987):

$$\frac{\partial C}{\partial t} = \left(f\,k_0 \middle/ \phi\right) e^{-E/RT} \left[C_{eq}(T) - C\right] \tag{2.76}$$

If the following definitions are made:

$$B = (fk_0/\phi)EXP(-E/RT) \tag{2.77}$$

$$E = C_{eq}(T) \tag{2.78}$$

then Eq. 2.76 may be written as:

$$\frac{\partial C}{\partial t} = B(E - C) \tag{2.79}$$

This is the change in dissolved CO_2 concentration due to generation and may be substituted into Eq. 2.74 to yield:

$$D \frac{\partial^2 C}{\partial x^2} + B(E - C) = dC / dt \tag{2.80}$$

Using the conditions:

$$C(x,0) = 0 \tag{2.81}$$

$$C(L,t) = 0 \tag{2.82}$$

and

$$\frac{\partial C(0,t)}{\partial x} = 0 \qquad (2.83)$$

Eq. 2.80 was solved using Laplace transforms. The solution is:

$$C(x_b, t) = (E)\left\{ \sum_{n=0}^{\infty}(-1)^n e^{-Bt} ERFC\left(\frac{b_1}{2\sqrt{t}}\right)\right.$$

$$-\sum_{n=0}^{\infty}(-1)^n(\tfrac{1}{2})\left[e^{-b_1\sqrt{B}}ERFC\left(\frac{b_1}{2\sqrt{t}}-\sqrt{Bt}\right)+e^{-b_1\sqrt{B}}ERFC\left(\frac{b_1}{2\sqrt{t}}+\sqrt{Bt}\right)\right]$$

$$+\sum_{n=0}^{\infty}(-1)^n e^{-Bt} ERFC\left(\frac{b_2}{2\sqrt{t}}\right)$$

$$-\sum_{n=0}^{\infty}(-1)^n(\tfrac{1}{2})\left[e^{-b_2\sqrt{B}}ERFC\left(\frac{b_2}{2\sqrt{t}}-\sqrt{Bt}\right)+e^{b_2\sqrt{B}}ERFC\left(\frac{b_2}{2\sqrt{t}}+\sqrt{Bt}\right)\right]$$

$$\left.+(\tfrac{1}{D})(e^{-Bt}-1)\right\} \qquad (2.84)$$

where:

H	=	inverse diffusion coefficient (D)
F	=	BE/D (see equations 15 and 16)
b_1	=	$\{(L - x) + 2Ln\}(D)^{-0.5}$
b_2	=	$[(L + x) + 2Ln](D)^{-0.5}$

Four cases were studied using this equation for two sets of kinetic data. In Cases 1, 2 and 3, the data of Cathles et al. (1987) were used. These data were determined by comparing their kinetic model to the measured CO_2 production rate from a steamflood pilot project. For those three cases, steam injection temperatures of 450, 500 and 550°F were used. In Case 4, published kinetic data from related laboratory studies were used (Tissot et al., 1987; Fassihi et al., 1990; Hayashitani et al., 1978). In this case, a temperature of 550 °F was used. A single diffusion coefficient for CO_2 was used in all four of the cases. Table 2.1 provides a summary of these data.

The first step in the evaluation was to determine the time necessary for the dimensionless concentration to reach one at the various temperatures, i.e., the time required for the CO_2 concentration to increase to its saturation concentration in water under steam injection conditions.

A plot of the dimensionless concentration profile near the fracture as it varies with time for Case 1 is provided in Fig. 2.4. For this case, the effective diffusion length was

found to be on the order of one meter. Similar plots were obtained for the other three cases. For Cases 2 and 3, the effective difference in length was also on the order of one meter. For Case 4, however, the effective diffusion length was found to be on the order of 0.1 mm.

From these data, plots were obtained for the diffusion length as a function of time and are shown in Figs. 2.5, 2.6, 2.7, and 2.8 for the four cases respectively. These plots were extrapolated to show the time when CO_2 becomes saturated in the matrix block and the effective diffusion length over which CO_2 will diffuse over that time interval.

The results for Cases 1, 2 and 3 indicate that the time required to reach CO_2 saturation in water is on the order of one year and the characteristic diffusion length is on the order of one meter. Thus, there would be no CO_2 bubbles within about one meter of the fracture because it will all diffuse to the fracture instead of forming bubbles. Laboratory studies, however, have shown that CO_2 can reach saturation in a day or two, not years (Sahuquet and Ferrier, 1982; Reis, 1992). Thus, the kinetic model proposed by Cathles *et al.* may not be accurate.

The gas generation rate for Case 4, however, allows for a CO_2 saturation to be reached in about a day and is, therefore, considered to have superior kinetic data. The effective diffusion length for this case is on the order of 0.1 mm. For this length scale, the distribution of CO_2 bubbles would result in many small bubbles, not a few large bubbles.

It is concluded that the process of gas generation could result in a high gas saturation in matrix blocks and will yield good oil recovery.

Table 2.1. Summary of input values to gas generation model.

	D [sq cm/s]	E [kcal/mol]	f	k_0 [sec^{-1}]	T [F]	ϕ	ρ_s [g/cc]
Case 1	1.0E-9	10	0.5	.05	450	0.2	1
Case 2	1.0E-9	10	0.5	.05	500	0.2	1
Case 3	1.0E-9	10	0.5	.05	550	0.2	1
Case 4	1.0E-9	49	1	8.44E15	550	0.2	1
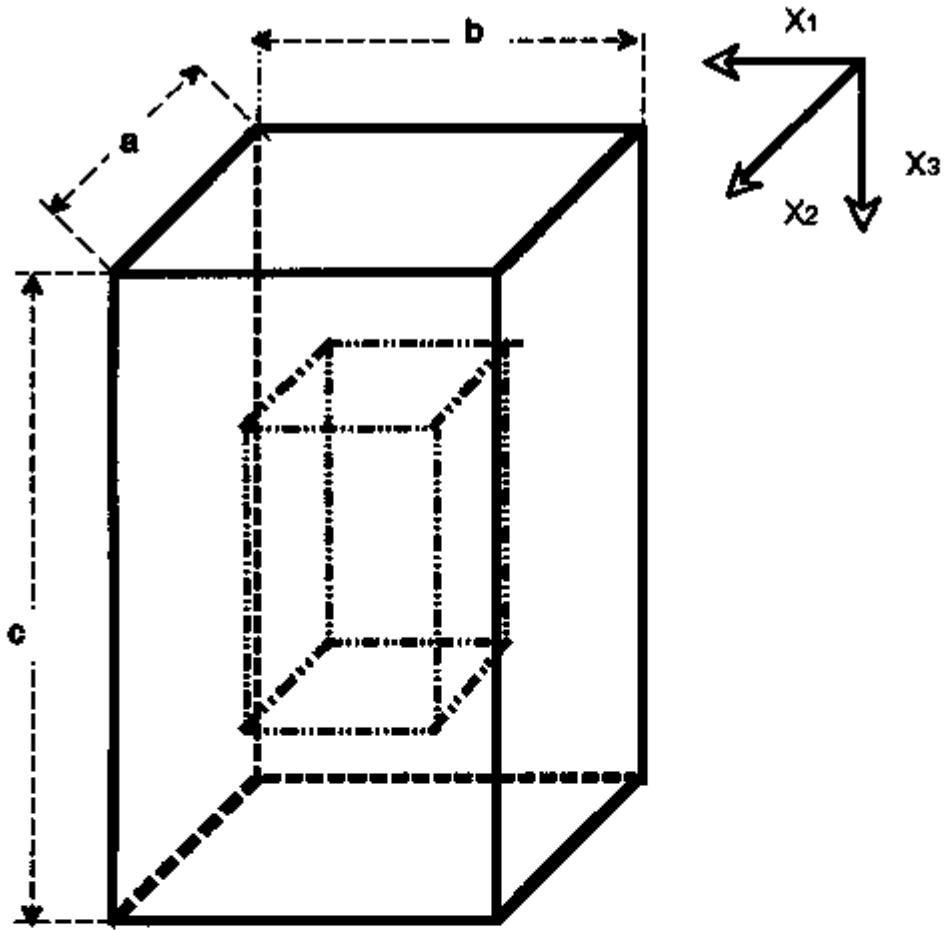
$$a \leq b \leq c$$

Fig. 2.1. Rectilinear matrix block with imbibition front.

Side view

Top view
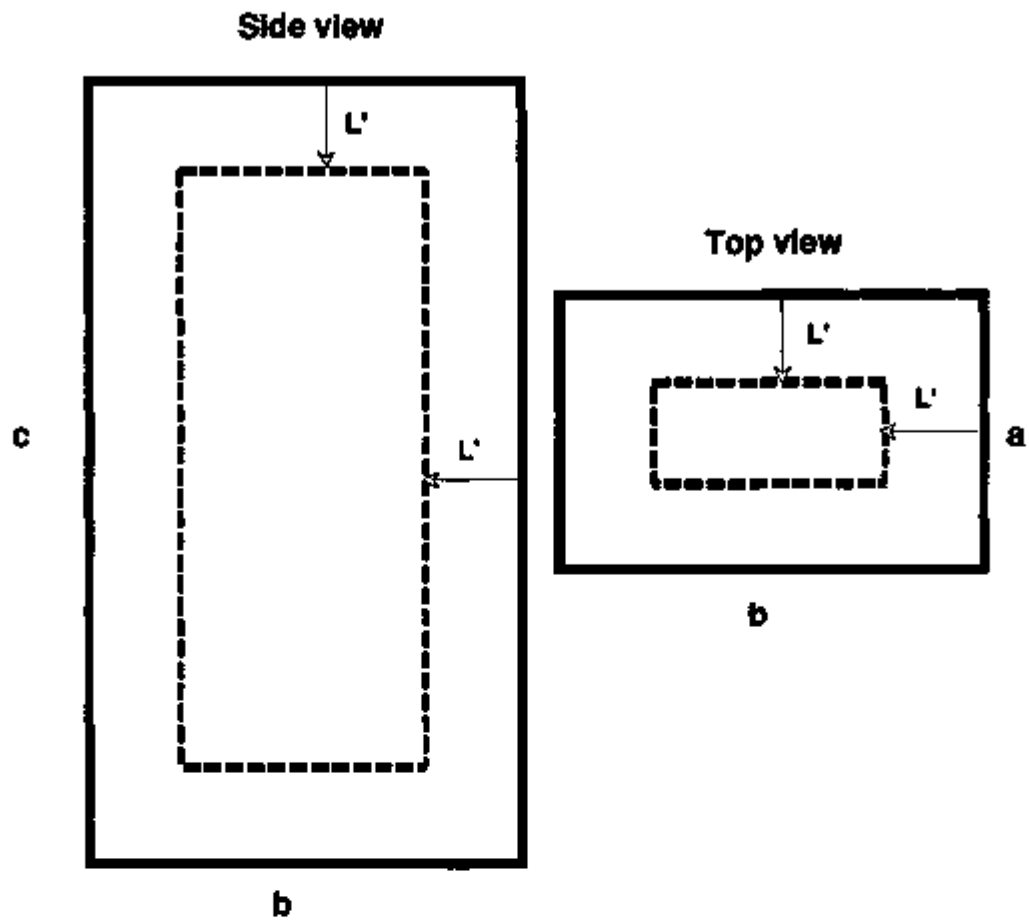
L': distance to imbibition front, 0 ≤ L' ≤ a/2

Fig. 2.2. Imbibition front within matrix block.
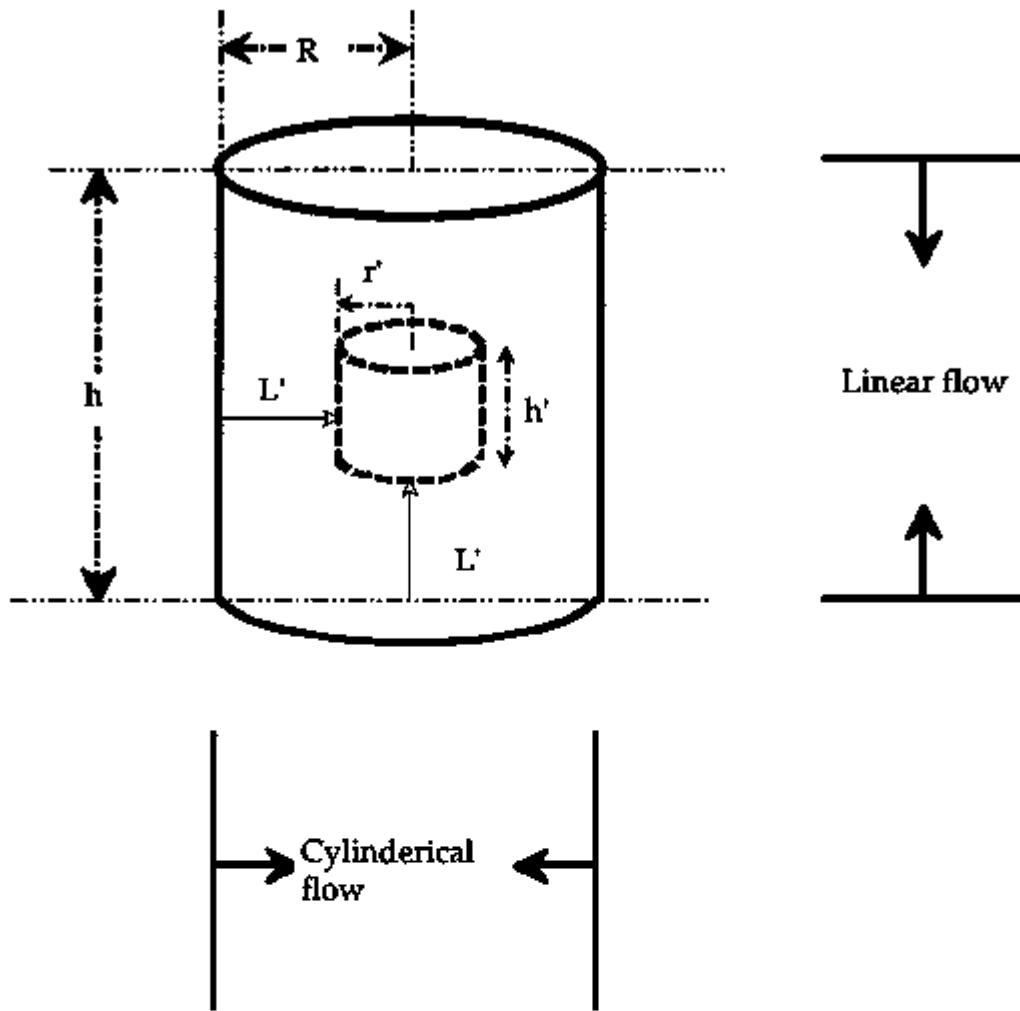
Fig. 2.3. Cylindrical matrix block with imbibition front.
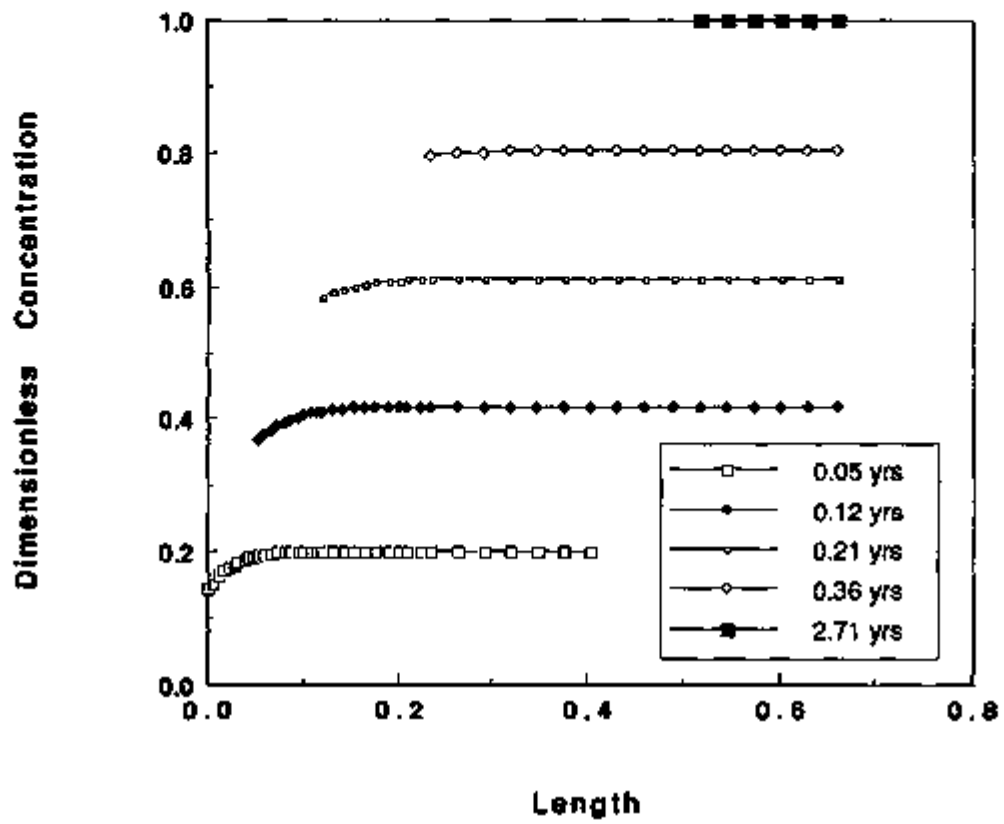
Fig. 2.4. Dimensionless gas concentration, 450 °F.
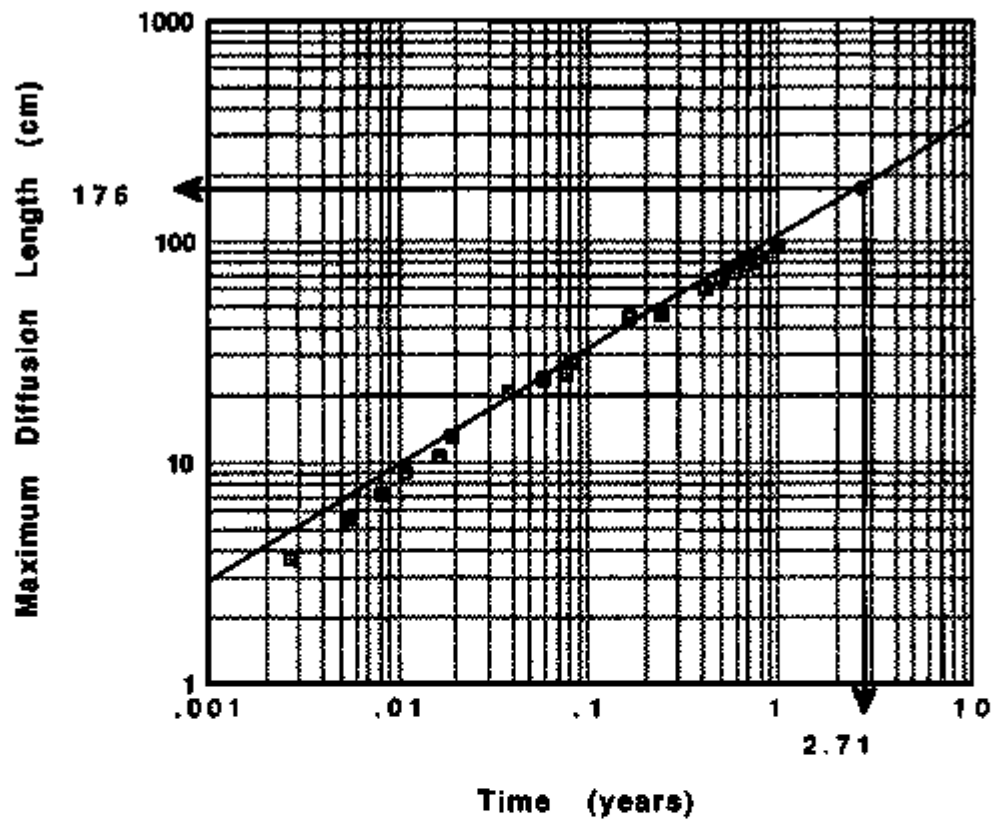
Fig. 2.5. Characteristic diffusion length for case 1.
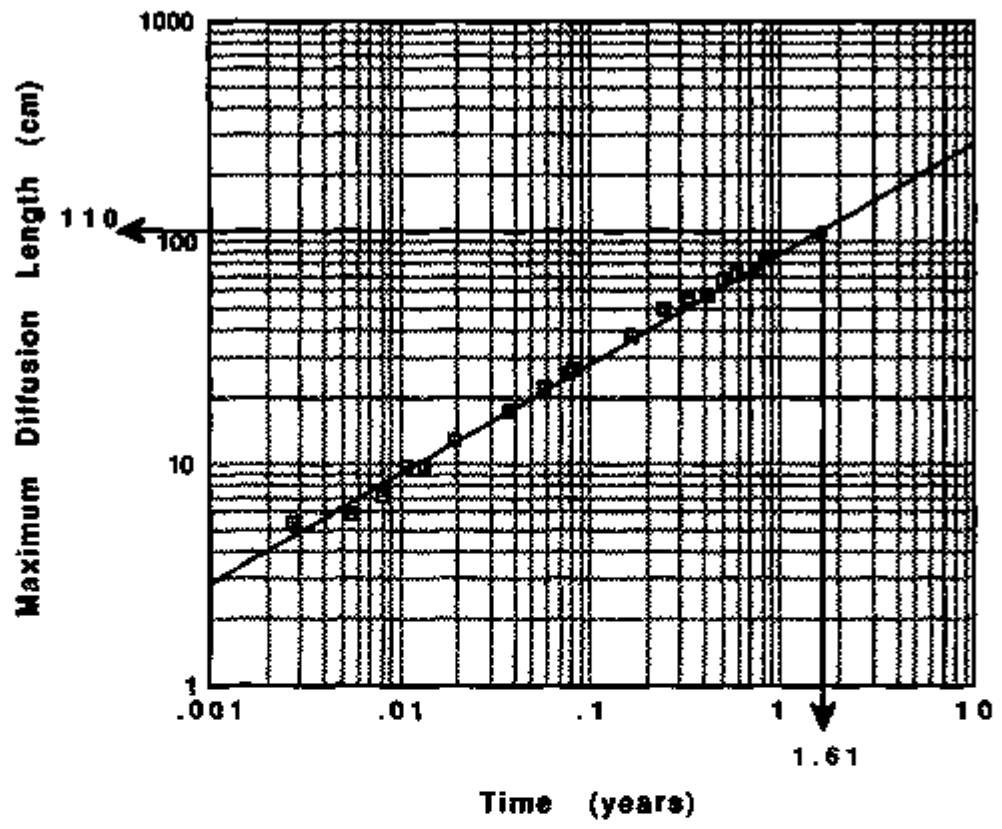
Fig. 2.6. Characteristic diffusion length for case 2.
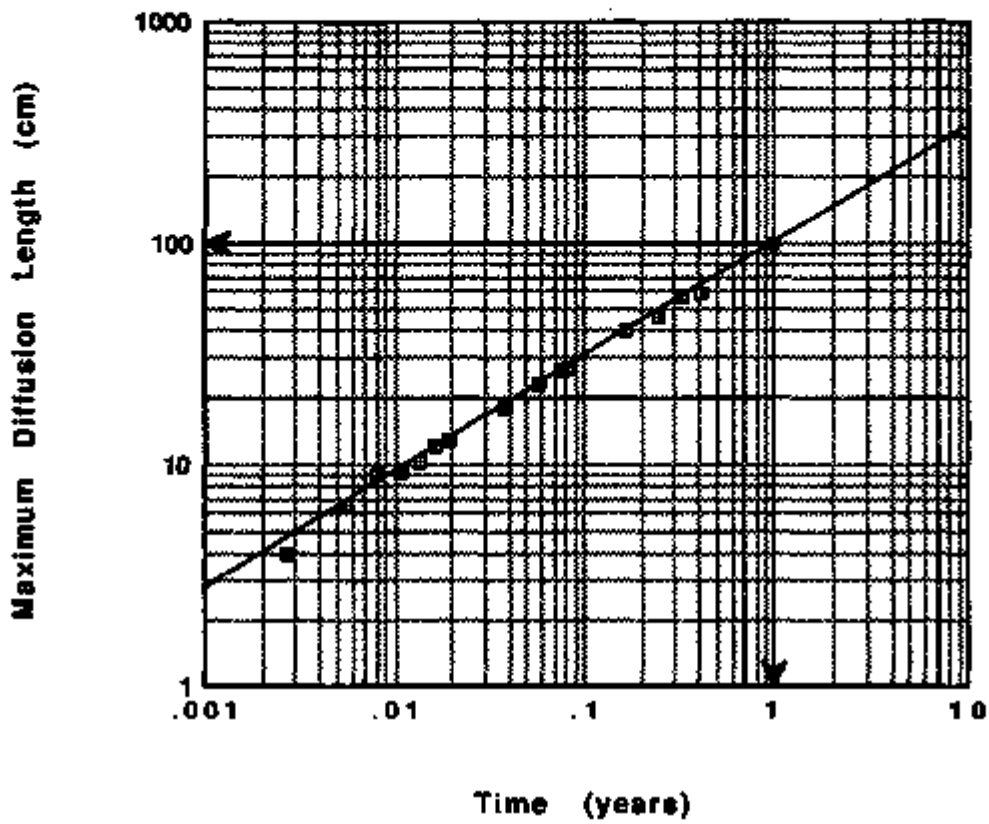
Fig. 2.7. Characteristic diffusion length for case 3.

Maximum Diffusion Length (mm)
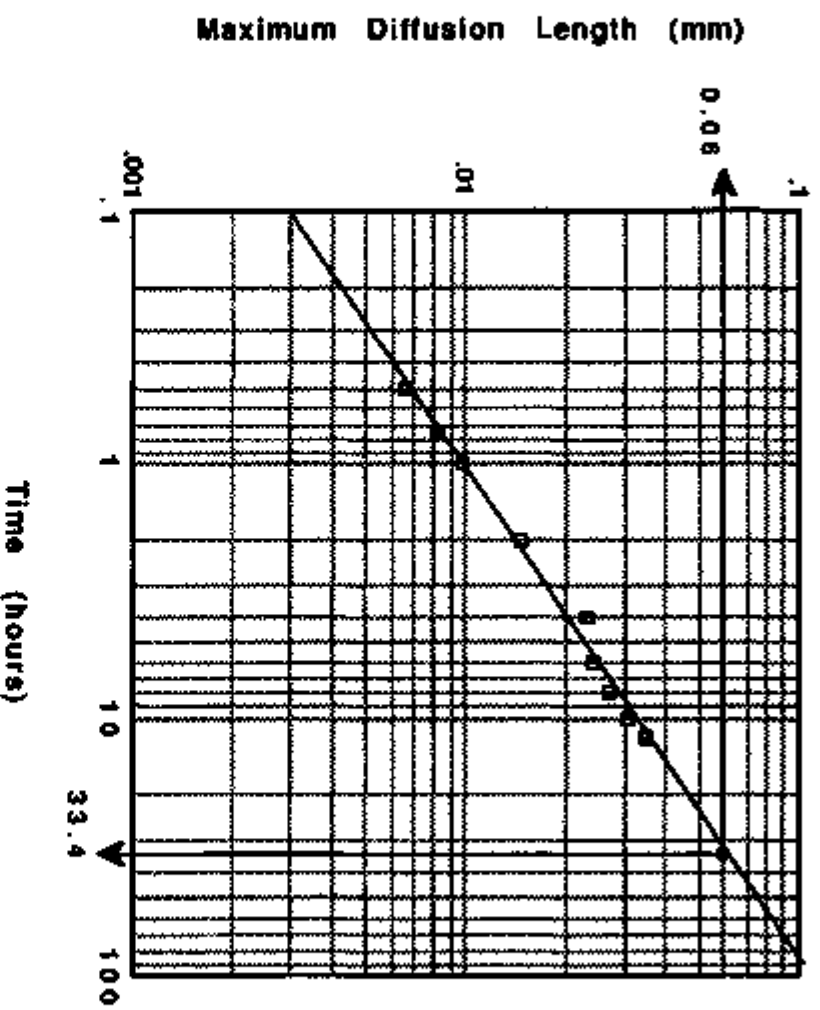
Fig. 2.8. Characteristic diffusion length for case 4.

Time (hours)

22

3.0 EXPERIMENTAL STUDIES

The primary objectives of the experimental studies have been to obtain data for testing the predictive models for capillary imbibition developed in this study and for predicting heat transport into matrix blocks.

3.1 CAPILLARY IMBIBITION MODELS

Experimental studies were conducted to test both the air/water and oil/water capillary imbibition models. The air/water models were found to successfully predict the measured behavior. Testing the oil/water models was difficult because of experimental repeatability caused from variations in core wettability. Those difficulties have been resolved and additional data are being obtained. In the following discussion, only the air/water imbibition data are presented.

Berea sandstone was used for these studies. Berea sandstone is known to be strongly water-wet. Cores with various sizes and dimensions were cut from the same rock block to have similar permeability and porosity. Water was used for cutting to make sure that the wettability characteristics of the cores were preserved. The cores were also fired to stabilize the water-sensitive clay particles and to remove contaminating materials from the rock surfaces. The physical characteristics of cores are given in Table 3.1.

The derivations of closed-form analytical models for counter-current imbibition, for this case are presented in Section 2 of this report. These models are summarized below:

For a rectangular matrix block, the normalized cumulative water imbibed is given by

$$\frac{Q_{water}}{Q_\infty} = L_D \left[\frac{(ab+bc+ac)}{bc} - \frac{a(a+b+c)}{bc} L_D + \frac{a^2}{bc} L_D^2 \right] \tag{3.1}$$

For a cylindrical matrix block, however, the normalized cumulative volume of water imbibed is given for two different cases depending on the aspect ratio of the cylinder.

For cylinders with a height to radius ratio of

$$\frac{h}{2R} \leq 1 \tag{3.2}$$

The cumulative imbibition is

$$\frac{Q_{water}}{Q_\infty} = L_D \left[(1+\frac{h}{R}) - \frac{h}{2R^2} (\frac{h}{2}+2R) L_D + \frac{h^2}{4R^2} L_D^2 \right] \tag{3.3}$$

while for cylinders with a height to radius ratio of

$$\frac{h}{2R} \geq 1 \tag{3.4}$$

$$\frac{Q_{water}}{Q_\infty} = L_D \left[\ 2(1+\frac{R}{h}) - (1+4\frac{R}{h})L_D + \frac{2R}{h}L_D^2\right] \tag{3.5}$$

The dimensionless distance, L_D is

$$L_D = \left[\frac{2\,k\,P_{c,swi}\,t}{(\frac{\mu_{gas}}{k_{rgas}} + \frac{\mu_{water}}{k_{rwater}})\,\phi\,\Delta S_{water}L^2}\right]^{1/2} \tag{3.6}$$

Expressions for two-dimensional imbibition, where one pair of core faces are rendered impermeable, can be found from Eqs. 3.1, 3.3 and 3.5 if one of the dimensions is assumed to go to infinity. For example, the expression for a rectangular matrix block for a two-dimensional water imbibition is

$$\frac{Q_{water}}{Q_\infty} = L_D \left[\frac{(b+a)}{b} - \frac{a}{b}L_D\right] \tag{3.7}$$

Similarly, for one-dimensional (linear) imbibition, the recovery is given as

$$\frac{Q_{water}}{Q_\infty} = L_D \tag{3.8}$$

3.2 WATER SATURATION BEHIND THE IMBIBITION FRONT

In developing the model for water imbibing into a gas saturated matrix block, the water saturation behind the imbibition front was assumed to be linear, e.g., piston-like displacement. To test this assumption, the location of the imbibition front was observed visually using cores with transparent casings on some sides. The three geometries studies are shown in Figs. 3.1 through 3.3.

Since the cumulative volume of water imbibed was also measured as a fraction of time, an approximate water saturation behind the imbibition front was calculated. Table 3.2 gives the water saturation just before the imbibition front, L' reaches the end of the matrix block, L, as well as the final average water saturation. The average saturation behind the front was nearly equal to the final saturation, which implies that the average saturation was nearly constant at its final volume.

Table 3.2 also shows that the recovery was around 95% when the imbibition front arrived at the end. This also indicated that water imbibition was nearly piston-like. Figure 3.4 shows that the saturation behind the imbibition front stays reasonably constant. This constancy further supports the assumption of piston-like displacement.

3.3 EFFECT OF GEOMETRY ON IMBIBITION

The effect of geometry on the imbibition rate was also studied. Figure 3.5 shows the recoveries from three-dimensional water-air imbibition experiments with various size cores. A description of these cores is given in Table 3.1.

If the recovery is assumed to be 100% when the imbibition front reaches the end (rather than the measured value of 95%), the equation for the position of the imbibition front can be rewritten as

$$L_D = \left[-\frac{Z_0}{2} + D \right]^{1/3} + \left[-\frac{Z_0}{2} - D \right]^{1/3} - \frac{a^2 + ab + ac}{3a^2} \tag{3.9}$$

where

$$Z_0 = \frac{1}{27} \left(-2 \left(\frac{a^2 + ab + ac}{a^2} \right)^3 - 9 \frac{(ab + bc + ac)(a^2 + ab + ac)}{a^4} - 27 \left(\frac{bc}{a^2} \right) \frac{Q_{water}}{Q_\infty} \right) \tag{3.10}$$

$$D = \sqrt{\left(\frac{Z_1}{3} \right)^3 + \left(\frac{Z_0}{2} \right)^2} \tag{3.11}$$

and

$$Z_1 = \frac{1}{3} \left(3 \left(\frac{ab + bc + ac}{a^2} \right) - \left(\frac{a^2 + ab + ac}{a^2} \right)^2 \right) \tag{3.12}$$

For a cubical core where all sides are equal, the equation further reduces to

$$L_D = 1 - \left(1 - \frac{Q_{water}}{Q_\infty} \right)^{1/3} \tag{3.13}$$

Equation 3.6 suggests that dimensionless penetration depth, L_D, depends only on the shortest distance to the center for various block geometries and varies as the square root of time, all other factors remaining unchanged. Figure 3.6 shows the calculated

dimensionless penetration depth obtained by using Eqs. 3.9 through 3.13. The x-axis, $\frac{\sqrt{t}}{L}$, was obtained by rearranging Eq. 3.6 as

$$L_D = \left[\frac{2\, k\, P_{c,swi}}{\left(\frac{\mu_{gas}}{k_{rgas}} + \frac{\mu_{water}}{k_{rwater}} \right) \phi\, \Delta S_{water}} \right]^{1/2} \frac{\sqrt{t}}{L} \qquad (3.14)$$

This figure shows that the curves collapse to a common trend line indicating that this model successfully scales the geometry of imbibition. Also shown in this figure is a straight line approximation to the data. It can be seen that the position of the imbibition front deviates somewhat from the predicted square root of time behavior late in the imbibition. An empirical model for the recovery is given by

$$L_o = 0.087 \frac{\sqrt{t}}{L} \qquad (3.15)$$

3.4 EFFECT OF TEMPERATURE ON IMBIBITION

The temperature is another factor that can significantly affect the recovery. Figure 3.7 shows the recovery rate for different temperatures for a single core. As can be seen, the imbibition rate increases with increasing temperature. Table 3.3 gives the other pertinent data for the experiment.

To examine the predicted temperature effects from the imbibition model, further simplifications on Eq. 3.6 are necessary. One of the unknowns in the model is the driving capillary pressure $P_{c,swi}$, this value can be estimated from the capillary tubes model. The capillary pressure in a capillary tube is expressed by

$$P_c = \frac{2\, \sigma\, \cos\theta}{r} \qquad (3.16)$$

and the permeability of a bundle of tubes is given by

$$k = \frac{\phi\, r^2}{8} \qquad (3.17)$$

The radius of the capillary tube can be eliminated by combining Eqs. 3.16 and 3.17 which results in the following approximation for the capillary pressure:

$$P_c = \sqrt{\frac{\phi}{2k}} \, (\sigma \cos\theta) \tag{3.18}$$

If this expression is substituted into Eq. 3.6 in place of $P_{c,swl}$, the resulting dimensionless

distance is

$$L_D = \left[\frac{\sqrt{\frac{2k}{\phi}} \, (\sigma \cos\theta)}{\left(\frac{\mu_{gas}}{k_{rgas}} + \frac{\mu_{water}}{k_{rwater}} \right) \Delta S_{water} L^2} \, t \right]^{1/2} \tag{3.19}$$

Owens and Archer (1966) reported that the mobilities of the imbibing water and expelled oil on the core surface stayed equal during a counter-current capillary imbibition. If this conclusion is assumed to be true for water-gas imbibition, the mobility terms in Eq. 3.19 can be expressed in terms of only one fluid, i.e., water, as

$$L_D = \left[\frac{\sqrt{\frac{2k}{\phi}} \, (\sigma \cos\theta)}{\left(2 \frac{\mu_{water}}{k_{rwater}} \right) \Delta S_{water} L^2} \, t \right]^{1/2} \tag{3.20}$$

Assuming a "zero degree" contact angle, the only parameter that is unknown is k_{rwater}.

Equation 3.20 can be re-casted in a such a way that the effect of temperature can be examined:

$$L_D = \sqrt{k_{rwater}} \, \psi \tag{3.21}$$

where

$$\psi = \left[\sqrt{\frac{k}{2\phi}} \, \frac{(\sigma \cos\theta)}{\mu_{water} \, \Delta S_{water} L^2} \, t \right]^{1/2} \tag{3.22}$$

Figure 3.8 shows a plot of L_D vs. ψ for different temperatures proving that the effect of temperature can be scaled if the correct viscosity and interfacial tension are used. Another conclusion that can be made from Fig. 3.8 is that the relative permeability, k_{rwater}, which is the square of the slope of curve, is essentially independent of temperature.

3.5 THERMAL CONDUCTIVITY MEASUREMENTS

Thermophysical properties such as thermal conductivity and thermal diffusivity are key parameters for describing heat flow. The thermal conductivity and thermal diffusivity values are important to determination of heat transfer to matrix blocks from steam-heated fractures.

Hundreds of studies have been reported on the measurement of thermal conductivities for metals and insulators, whose conductivity values lie at two extremes. However, only a few describe techniques for fluid saturated permeable media, having intermediate conductivity values. Both steady-state and transient methods in radial and axial geometries are commonly used for the measurement of conductivity. While simplicity has been emphasized in the design of many experiments, methods to account for heat losses are often complicated and have limited experimental procedures and theoretical calculations. In this study, specific attention is given to minimizing heat losses with the purpose of increasing the accuracy of the thermal conductivity and diffusivity values.

3.5.1 Experimental Apparatus

A steady-state axial heat flow method is commonly used to measure thermal conductivity. However, steady-state methods are prone to greater heat losses and therefore the main thrust in the design of this experiment is to minimize or account for heat losses. In the absolute method, the amount of heat supplied to the specimen must be measured. The goals in designing the steady-state apparatus are three-fold:

1)   High measurement accuracy.

2)   Capability for specified multiphase fluid saturations at various temperatures to 450°F.

3)   Capability for transient conductivity measurements with little modification.

A guarded hot plate method is the most widely used apparatus for determining the thermal conductivity of dry insulating materials (De Ponte *et al.*, 1974; Prats *et al.*, 1975; Standard, 1976; Woodside *et al.*, 1961; Woodside *et al.*, 1957). In this method a hot plate is surrounded by a guard ring to cause heat from the hot plate to pass axially through the test specimen with little or no radial heat transfer so that a one-dimensional steady-state heat flow equation can be applied to determine thermal conductivity. The specimen extends over the entire cross-section of hot plate and guard ring. The hot plate and the guard ring are wired such that their temperatures can be varied independently. Thermal guarding is achieved by maintaining the temperature of the guard ring as close as possible to the hot plate (*i.e.*, test area). Despite such guarding, isotherms and heat flow lines are distorted by heat losses at the outer edge of the guard material. Unidirectional heat flow may not occur in the test section of the specimen if the radial width of the guard ring is insufficient. This causes the measured thermal conductivity value to differ from the true value. The magnitude of the error is determined by relative heat losses, which depend on the geometry of the test assembly and the thermal conductivity of the test specimen.

For test specimens whose thermal conductivity is greater than 0.1442 W/m-K the British Standard recommends that a hot plate can be used without a guard ring (Pratt, 1962). This arrangement introduces a large correction for edge heat loss: approximately 12% for a 2 in. thick specimen and 7% for a 1.5 in. specimen (Pratt, 1962). Apart from the transient method, this method (*i.e.*, without a guard ring) has been widely used by the petroleum industry. A steady-state apparatus with guard rings to measure thermal

conductivity of fluid saturated reservoir rocks is new to the best of our knowledge. This apparatus is also different from a conventional guarded hot plate method.

The guarded hot plate method has been standardized by ASTM (Standard, 1976) and British Standards (1965), and has traditionally been used for less conductive materials. The design criteria require the diameter of the sample to be at least twice the thickness. Specimens sometimes have thicknesses exceeding the maximum permissible. In these cases, it is recommended that additional edge insulation be used to minimize measurement error. However, even with the additional insulation, errors in testing thick specimens may be large (Woodside, 1957).

When using a core sample from a reservoir rock, it is often inconvenient to obtain a sample with a diameter large enough to extend to the outer edge of the guard ring. Moreover, because the whole heater and specimen assembly is to be encapsulated for fluid pressure confinement purposes, simply adding thicker insulation at the edge may not be possible. One approach in improving the specimen size requirement is to reduce the overly conservative design criteria specified by ASTM (Standard, 1976) standards. This can be accomplished by using more realistic boundary conditions for the heat loss calculations. Such realistic boundary conditions are also essential to the overall apparatus design. Moreover, the standard guarded hot plate apparatus is designed for thermal conductivity of specimens at dry atmospheric conditions. A significant modification in design is warranted to accommodate fluid saturation and vacuum experiments. In this regard, this apparatus is very different from the standard guarded hot plate apparatus.

It was decided that the thermal conductivity would be measured by using a specimen as large as a core plug obtained from the field. Using realistic boundary conditions alone would not allow the implementation of guarded hot plate principle for a specimen of such a size (*i.e.*, diameter-to-length ratio). Therefore, a numerical investigation was conducted (Mohanty, 1993) to see if a separate guard material (having same properties as that of the specimen) could be used instead of having the specimen to extend over both guard and test region. The influence of using a low conducting sleeve was also investigated.

The thermal properties of the materials used for constructing the apparatus play a very important role. Therefore, a thorough survey was conducted to obtain proper materials for the thermal conductivity apparatus on the basis of availability, cost, temperature tolerance (to 450°F), pressure tolerance (to 500 psia), and opaqueness (to minimize the effect of radiative heat transfer). For these experiments, the requirement of fluid confinement required materials that were impermeable and insulating. Most insulating materials do not meet these requirements and hence warranted compromises. For example, the pressure vessel, which ideally should have been built with insulating materials, was built with type-304 stainless steel. Among the commercially available alloys, type-304 stainless steel has nearly the lowest thermal conductivity, approximately eight times lower than that of brass (material used to build the guard and main heater assemblies). Still, type-304 stainless steel is typically three times more conducting than wet Berea sandstone (Roy *et al.*, 1988). This is not expected to be a serious problem as the pressure vessel would not directly touch the heating and cooling blocks.

The apparatus has been designed based on maintaining less than a 1% theoretical heat loss. The schematic of the thermal conductivity apparatus is shown in Fig. 3.9. Heat loss calculations are based on a specimen size of 1 in. thick and 1.25 in. in diameter. Although it was desirable to maintain a specimen diameter of 1 in. (*i.e.*, the typical size of specimens from the field) it was decided to maintain the diameter at 1.25 in. because the smallest length of a heater commercially available was 1.25 in. long. Also, we would

normally want vertical heat losses, thus, longer cores might be possible. The test specimen and the heating block are surrounded by a rigid sleeve made of a low conductivity material (Torlon) in order to confine pressure.

Torlon completely separates the main section and the guard sections and thereby acts as a heat barrier. This also serves as a guide for proper axial alignment of the heating blocks and the specimen. The main heating block, the specimen, and the cooling end heating block have corresponding concentric main guard block, guard material, and cooling-end guard block, respectively. Alignment is ensured in the design such that the main guard circumscribes only the main heating block, the guard material circumscribes the specimen material, and so on. A heating plate (upper guard block) extends across the whole assembly of the main heater block, sleeve, and the main guard block, which is maintained at the same temperature as that of the main guard block. A low conductivity material (Kinel) 0.125 in. thick separates the upper guard from the main heating end heater assembly. Another insulating material (G-11) 0.5 in. thick prevents excessive heat loss from the upper guard to the upper flange. The conductivity values for various materials used in the apparatus are presented in Table .

A heater assembly similar to the main heating assembly is introduced at the lower temperature (cooling) end to maintain a low temperature gradient in the specimen. The low temperature gradient is required to minimize the nonlinearity in the temperature gradient and also permits the use of a guard material that is slightly different from the specimen material. A circulation chamber is attached at this end for cooling by circulating water or air. Radially, the cooling block extends to the edge of the lower radial guard thereby covering the cooling end heater block, sleeve, and the radial guard block. The cooling chamber consists of 1/4 in. grooves on two brass plates sandwiched together to form tube-like constrictions. Such constrictions uniformly distribute the coolant fluid across the whole cross-section flowing from the inlet to the outlet end. A 0.125 in. thick insulating material (Kinel) reduces heat transfer between the circulation chamber and the lower flange. Thermocouples, heaters, and tubing for fluid saturation pass through this chamber vertically and are protected from the circulating fluids using o-rings. As the cooling end heaters work in conjunction with fluid circulation, the experiment is not significantly affected by small fluctuations in the temperature of the circulation fluid. Also, by varying the rate of cooling water, some flexibility could be obtained in the downstream temperature.

Two thermocouple wells are drilled in the heating and cooling end pieces at both ends of the specimen, allowing the tip of the thermocouple to be positioned within 0.0625 in. from the interface. Two thermocouples are placed on each radial guard block, one near the outer edge and another right above the contact point between the heater and the brass block. One thermocouple is located at the center of the upper guard and the tip of this thermocouple lies very close to the insulating block that separates upper guard from the main heater block.

A guard material, preferably of the same material and with the same fluid saturation as the specimen, is used. Care is taken to polish the ends of the specimen and guard materials and to make the ends parallel to each other and perpendicular to the edge. This is done to maximize the contact between the specimen and guard material with the corresponding heating and cooling blocks.

The assembly is held together between two flanges tightened by means of three equally–spaced, threaded rods and nuts. The whole assembly rests on a wooden platform which is leveled horizontal so that it will aid in aligning the specimen as vertical as possible. The proper contact is ensured by tightening the bolts at opposite ends alternately such that the upper flange lowers uniformly from all directions. The bolts are tightened this

30

way until the insulating plate separating the upper guard and the radial guard become parallel with the upper edge of the radial guard, Fig. 3.10 shows the setup for the thermal conductivity apparatus.

The experiments are conducted at temperatures up to 400°F, where radiation can be neglected owing to the fact that the core is opaque and consists of capillary pores (Luikov, 1966). As the rock sample may contain fluid, therefore, the heater is placed on top of the core so that density gradients will align with the direction of the gravitational field and eliminate macroscopic convection.

3.5.1.1 Heat Sources

Four cartridge heaters and two band heaters are used for heating. A 100W cartridge heater embedded in the brass metering block is the main heating element. Another cartridge heater is embedded in the brass block at the cooling end. Two more cartridge heaters in parallel are embeded in a brass disc for the upper guard. Two band heaters tightly hold onto the brass guard blocks due to its own spring action to constitute the main guard and the cooling-end guards. The cooling block is identical to the metering block except that it uses a 80W cartridge heater. Figures 3.11 and 3.12 show the cartridge and band heaters. The roles played by these heaters will be discussed in the next section. Heater specifications are given in Appendix C. The guard heaters and the main heater are connected to a power supply through five relay switches. The electrical circuit diagram for the heater connections is shown in Fig. 3.13. The main heater is connected to a 50V DC power supply. The guard heaters and the cooling end heater are connected to a 110V AC power supply through a Variac so that more power can be supplied when larger heat losses are experienced. Relay switches are used for heater on-off control so that appropriate temperatures can be maintained. A current-measuring resistance is connected in series to the main heater. For experiments at higher temperature the 50V DC supply to the main heater is not adequate and one has to switch to AC supply. For AC supply, a redundant filtering device is installed parallel to the resistor to measure current. Room temperature is maintained at identical conditions for all runs.

3.5.1.2 Fluid Saturation

Separate provisions have been made for saturating the specimen and the guard. The schematic for the fluid saturation arrangement is shown in Fig. 3.14. This provides the capability to measure thermal conductivity at various fluid saturations. We desire to maintain similar thermal properties in the specimen as in the guard material. Hence while conducting the fluid saturated experiments, in addition to using the guard of the same material, we also wish to maintain the same saturating conditions as that of the specimen. To accomplish this, the apparatus has been arranged to simultaneously saturate the specimen and the guard material. Fluid is confined in the specimen by placing o-rings on the main heating and cooling blocks. To confine the fluid in the guard material a 304-stainless steel casing is used. O-rings on the guard blocks at the heating and cooling ends at the internal as well as the external diameters confine fluid in the guard material. Stainless steel tubing is connected to all the blocks as fluid inlet and outlet so that the saturation can be conducted with the specimen in-place. Only enough casing length was used to cover the guard material and the o-ring in order to simplify loading and unloading of the specimen. This also reduces the heat losses compared to the situation with the casing running all across the entire assembly.

3.5.2 Transient Measurements

The steady-state apparatus was modified for measurements using a transient method that does not need a hole to be drilled through the specimen as is needed in the widely-used probe method. This modification required capability for dynamically measuring the heat flux, which is accomplished by the use of a microfoil heat flux sensor.

3.5.2.1 Heat Flux Sensor

Most heat flux sensors are based on the measurement of temperature difference across an insulating layer. They employ the gradient layer principle used in direct calorimetry. The sensor uses differential thermocouples to measure the thermal gradient. Two dissimilar metal junctions are located across the insulating substrate material. When one junction is hotter than the other, a current flows in the circuit. The direction of the flow depends on the metals and the temperature of the junction. This is referred to as Seebeck effect. (CRC, 1982) The heat flow rate which is the consequence of the thermal gradient is then proportional to the voltage generated in the differential thermocouples.

The thermal resistance of the insulating substrate of the heat flow meter ought to be low to minimize the disturbance to the heat flow. Therefore the operation of such devices at very small temperature differences is desirable. In most cases a high-voltage output is also desired. This is accomplished by using a large number of differential thermocouples at the expense of heat flow efficiency. A series arrangement of the thermocouple junctions are formed by winding thin constantan wire around a mesh-like substrate and plating one half of each loop with copper or by soldering contacts between two dissimilar elements. Applying very small temperature difference across the substrate strip produces a voltage difference at each bimetallic junction. The more junctions, the smaller the temperature gradient is needed to generate a measurable voltage. A flux of $500W/m^2$ typically generates a signal of $1000\mu V$ (Shallcross and Wood, 1986). These thermocouple arrangements are protected with silicone rubber sheets on both of its sides. An additional thermocouple is present to measure the overall temperature of the sensor. The heat flux through the sensor q_s is represented by

$$q_s = \frac{e_s}{k_s}$$

(3.23)

where e_s is the output voltage and k_s is the sensor constant (Shallcross and Wood, 1986) or sensitivity (Herin and Thery, 1992). From this definition, the sensor sensitivity value does not depend on the measuring surface area and has units of $\mu V/W/m^2$. Sensitivity also depends on the amount of heat that deviates from the normal direction (Herin and Thery, 1992).

A schematic of the heat flux sensor is used in this study shown in Fig.3.15. The specifications for the sensor used in this experiment are shown in Table 3.5. The heat flux sensor is attached to the end of the metering block facing the specimen using RTV silastic, a high-temperature silicone rubber material. The sensor consists of about forty thermocouple pairs are arranged in four rows of ten in an area of 14x18 mm. The sensor is about 0.2 mm thick including the thickness of the protective silicone rubber sheet and is 19.2x22.2 mm. The manufacturer states that the sensor constant is a function of the sensor temperature, though the change is relatively small (about 1% change with 20°C temperature change).

3.5.3 Steady-State Experiments

In order to minimize the heat losses, initial experiments were conducted with the temperatures at the upper guard and the radial guards at exactly the main heater temperature. The cooling end guard and the cooling block are maintained at the same temperature. The temperatures at each face of the specimen and the guard material were maintained at their respective set values by turning heaters ON and OFF. A temperature tolerance to trigger the heater ON or OFF was determined by trial and error in order to maintain the average temperature as close as possible to the set-point temperature. Since the metering block is surrounded by heaters on all but one side, precise temperature control becomes crucial for proper heat flux control and measurement. Problems arose when the radial temperature difference was set at zero, especially when the guard heater voltage was set at relatively high values. There are two probable reasons for this.

1. Since heat losses take place from the guard heaters, those heaters turn ON-OFF more frequently than the heaters in the metering system. There are thus occasions when the guard temperature is higher than the metering system temperature.

2. The guard temperatures have large amplitude and cycle lengths during heating and cooling cycles.

With the purpose of avoiding the above effects, the apparatus was then tested by maintaining the upper two guard heaters at a specified temperature less than the set temperature. Thermal conductivity was calculated for each such radial temperature difference. This was done first with the pressure vessel removed and fiberglass wrapped around the guard assembly. Figure 3.16 is a plot of λ vs. ΔT_{radial} for $\Delta T_{axial}=22°F$ at a specimen midpoint temperature of 134°F. As expected, a straight line was observed. Extrapolating the straight line to a zero radial temperature difference thus yields a theoretical zero value of radial heat loss. This method of linear extrapolation gives much more accurate results than when it was attempted to maintain $\Delta T_{radial}=0$.

Through a diagnostic check, it was found that all the points on Fig. 3.16 may not fall on the straight line if the temperature of the guard heaters exceeds the temperature of the main heater. By plotting the corresponding temperature histories (Figs. 3.17 to 3.19) at all the thermocouples, it was seen that there was significant interference of guard heating in the metering system (i.e., temperature of the guard exceeding the temperature of the metering section). The amplitude of these temperature cycles and the cycle lengths increased with the increase in Variac setting. In all cases shown in Figs. 3.17 through 3.19, two hours time was allowed for the system to reach steady-state. The upper three curves are for the upstream end temperatures (i.e., main heater, main guard, and the upper guard) and the bottom two lines are for the downstream end temperatures (i.e., cooler and cooler guard), respectively. The three plots are for upstream end radial temperature differences of 5.00°F, 2.50°F, and 1.25°F, respectively, with a Variac setting of 50%. In all cases the cooling end guard- and the cooling end heaters are maintained at the same temperature. In Fig. 3.17, where the radial temperature difference is 5.00°F, it can be seen that the guard temperatures do not interfere with the temperature of the main heater, implying that the metering process is not affected by backflow of heat from the guard to the metering block. However, in Figs. 3.18 and 3.19, the temperature of the main guard heater clearly interferes with the temperature of the metering system. This corresponds to the observation that the heat flux value corresponding to a radial temperature difference of 1.25°F does not fall on the same straight line connecting values at 2.5°F and above.

33

Therefore it is recommended that if nonlinear behavior is observed in flux vs. radial temperature difference, then the temperature history should be plotted to ensure that the metering system is not influenced by the external heaters. Ideally, one should choose a low Variac setting for the guard heaters unless the experiments are run at high temperature where the heat loss is very high. In that case, to avoid the temperature interference, large ΔT_{radial} values should be used so that the crest of the temperature cycle does not exceed the trough temperature of the metering block, thereby ensuring linearity of the ΔT_{radial} vs. heat flow rate (q) plot. The main guard temperature variation has an amplitude of approximately 4°F and a cycle of 8 minutes at a Variac setting of 50%. A relationship between the amplitude and various Variac settings should be established to be used as a guideline for maintaining proper radial temperature differences in this apparatus. For example, at a Variac setting of 50% a minimum radial temperature difference of 4°F is needed to be maintained. Once such details are taken care of, then the extrapolation at various Variac settings should have the same intercept at a zero radial temperature difference. This is evident from Fig. 3.20 in which the extrapolation to zero radial temperature at Variac settings of 40% and 50% for dry limestone lead to the same intercept. The plots are obtained by using actual rather than the set radial temperature difference to obtain correct intercepts. The slope of the straight line changes with Variac settings.

It is established above that the large amplitude and the wavelength of the temperature cycles (*i.e.*, temperature overshoot) from heater ON-OFF are responsible for the guard heater temperatures exceeding the main heater temperature. Such large amplitudes are due to three reasons:

1.   The distance between the body of the heaters and the tip of the thermocouple.

2.   The large heat capacity of the material constituting the body of the guard heater.

3.   The large mass of the brass materials that hold the guard heaters in place.

A careful study was done to ensure that these large amplitudes and temperature cycles are not due to improper contact between the heaters and the brass body or due to excessive heat losses either from the brass block or from the thermocouples themselves. This problem of large amplitude and temperature cycles is typical of band heaters because of their large mass and heat capacity. The band heaters are used as radial guards, and cartridge heaters are used as main heaters, cooling end heaters, and upper guard heaters. We attempted to ensure proper contact between the band heaters and the brass blocks by using aluminum foil between them. No change in the amplitude was noticed, indicating that contact between the band heater and the brass block was adequate. This problem was not observed for the upper guard heaters where two cartridge heaters were used. These are very small in size and have very low heat capacity (*i.e.*, the heat transfers instantly from the heaters to the brass block).

To reduce the effect of temperature overshoot at the radial guards, two additional thermocouples were placed on the bodies of the band heater (to measure "guard heater temperature"). This indeed reduced the size of the temperature cycles, but then the temperature at the guards were consistently lower than obtained before. Although this may have affected the calculation of the thermal conductivities by contributing to larger heat losses from the guard heater block than actually used in the design calculation, still it allowed the maintenance of smaller amplitudes of temperature cycles.

Approximately half an hour was needed to heat the apparatus from room temperature to 245°F. However, the system was allowed to heat for two hours before data

34

acquisition was started. The initial heat-up period and the total length of the experiment may depend on the supplied power. However, the power must be supplied cautiously, as long as ON-OFF type controlling is used, to avoid inaccuracy in the heat flux measurements. The data acquisition was done over two hours for each radial temperature unbalance. A lesser time span could be used for more routine measurements.

3.5.4 Transient Experiments

The capability of this apparatus was extended to measure thermal conductivity under transient condition and diffusivity with some minor modification. The theoretical derivation for the transient experiment using above steady-state apparatus has been presented by Trevisan in Miller *et al.* (1992). In this method, a microfoil heat flux sensor is used to measure the heat input into the sample. The main advantage in using a heat flux sensor is that dynamically varying heat inputs can be measured. Along with the temperature readings by thermocouples, these data form the history of the test. The data treatment involves deconvolving the temperature and heat flux as functions of time, so that simpler models can be generated for the same physical configuration.

The experimental arrangement for the transient measurement is identical to the steady-state apparatus except that a heat flux sensor is attached to the end of the metering block facing the specimen. Contact resistance problems are reduced, since the sensor is sandwiched between the specimen and the metering block. However the possibility of compressing the sensor too much to the extent that substrate material is deformed cannot be ruled out. Therefore, it is recommended that the sensor is calibrated more frequently.

One way of obtaining the relationship between $q_0(t)$ and $T_0(t)$ is to treat the problem as two independent problems. Details of the method for solving the coupled differential equation with appropriate initial and boundary conditions can be found in Miller *et al.* (1992). When solved in Laplace space, the basic solutions are obtained as functions of s^*, the Laplace variable in dimensionless space. The problem is solved as two independent problems, as if they were simply two different interpretations of the same physical problem, and the two solutions are equated to obtain

$$\frac{\overline{\theta_0}}{\overline{q_0^*}} = \frac{\tanh\left(\sqrt{s^*}\right)}{\sqrt{s^*}} \tag{3.24}$$

where $\overline{\theta_0}$, and $\overline{q_0^*}$ are the dimensionless temperature and flux, respectively, in the Laplace space corresponding to time t. The limit for small values of s^* (t→∞) of the previous function is:

$$\lim_{s^* \to 0}\left(\frac{\overline{\theta_0}}{\overline{q_0^*}}\right) = 1 \tag{3.25}$$

While for large values of s^* (t→0),

$$\lim_{s^* \to \infty}\left(\frac{\overline{\theta_0}}{\overline{q_0^*}}\right) = \frac{1}{\sqrt{s^*}} \tag{3.26}$$

Figure 3.21 shows the characteristic curve of the functions in Eq. 3.24 vs. s*. At large s* (small t), the curve becomes a straight line of slope -1/2, corresponding to the transient period of heat conduction. The steady-state regime is characterized by the flat portion of the curve (small s* values). A type-curve match could be used by using Fig. 3.21 to verify the transition between regimes and to estimate both parameters of conductivity and diffusivity. The scale on the vertical coordinate of the real data plot would be $\overline{(T_o-T_i)}/\overline{q_o}$, which is related to the corresponding scale of the type-curve by

$$\frac{\overline{(T_o-T_i)}}{\overline{q_o}} = \frac{L}{\lambda A}\left(\frac{\overline{\theta_o}}{q_o^*}\right) \tag{3.27}$$

Once the steady-state plateau in Fig. 3.21 is reached, the thermal conductivity is determined by

$$\lambda = \frac{L}{A}\frac{\overline{q_o}}{\overline{(T_o-T_i)}} \tag{3.28}$$

As can be seen from Fig. 3.21, the steady-state regime is fully established for s* values less than 2.5×10^{-3}. In terms of real data calculations, the corresponding criterion for the Laplace variable in dimensional space, s, is

$$s = \frac{\alpha}{L^2}s^* < 2.5 \times 10^{-3}\frac{\alpha}{L^2} \tag{3.29}$$

Thermal diffusivity may be obtained from data gathered at earlier times, in other words for higher values of s. This is accomplished by observing that as $s^* \to \infty$,

$$\frac{\overline{\theta_o}}{q_o^*} = (s^*)^{-1/2} \tag{3.30}$$

or, in terms of dimensional data,

$$\frac{\overline{(T_o-T_i)}}{\overline{q_o}} = \frac{\sqrt{\alpha}}{\lambda A}s^{-1/2} \tag{3.31}$$

The coefficient on the right side of Eq. 3.31 can be determined from the slope of the plot of $(T_o-T_i)/\overline{q_o}$ versus $s^{-1/2}$. If the slope of the curve is β, then

$$\beta = \frac{\sqrt{\alpha}}{\lambda A} \tag{3.32}$$

The main advantage of the above method is that it allows one to conduct steady-state and transient runs using the same apparatus. This method avoids the use of a probe and therefore avoids problems due to poor thermal contact and machining. The heat capacity of the heating source need not be known as the heat flux is measured directly at the interface. As the heat flux and the temperatures are dynamically measured, the boundary condition restrictions such as constant heat input or constant temperature are not necessary.

36

3.5.4.1 Experimental Procedure

While conducting the experiments, the voltage leads from the heat flux sensor were connected to the voltage module of 2400B FLUKE data acquisition system, and the readings were directly recorded and then converted to heat flux values. The fastest rate at which the data acquisition could be accomplished by the Fluke system was around 0.8 sec per reading. Fast data acquisition was essential at the beginning of the temperature transient.

The transient method was tested at various operating conditions. In all cases, the system was maintained at a specified temperature until it reached a uniform temperature. This was done by allowing a one-hour stabilization time after all the thermocouples reached the designated base temperature. After that, the temperatures at the main heater as well as the upper guard heaters were raised 10° to 20°F above the stabilized uniform temperature. After the transient period has begun, the cooling end is maintained at the same temperature as the initial stabilized uniform temperature. The thermocouple readings and the heat flux meter readings were recorded at 0.8, 10, 20, and 30 seconds intervals for time period of 100, 500, 1000, and 7200 seconds, respectively. Sufficient time was allowed for the system to reach steady-state.

When the heaters were operating independently to reach the set temperatures, the heating rate was different by different heaters. For this method, however, it was desirable for the temperature of the guards and the metering block to increase at the same rate. Therefore the computer control program was modified to ensure that the temperature at the guards never exceeded the temperature of the main heater. When the guard temperature was used for the control, the guard temperature during its transient intermittently exceeded the main heater temperature because of the distance between these thermocouple locations and the band heater. Therefore, the guard heater temperature was used for control instead of the guard temperature. In the transient calculations, although this modification allowed the temperatures at all the heaters to rise at the same rate, it also prolonged the time needed to heat the system. As a typical example, with the temperature tracking option off, it takes about 30 minutes to reach the steady-state upstream temperature of 150°F at a Variac setting of 50%, whereas with this option ON, it takes about 1.25 hours to reach this temperature. Therefore, it is recommended that, to conduct a transient test, the option of the guard temperature tracking the metering system temperature should be engaged and while conducting steady-state experiments, it can be turned off.

At low temperatures, the use of a proper cooling fluid seems to play an important role. Most experiments can be run without having to run any cooling fluids. But because the transient model requires that the downstream end temperature be maintained at a designated temperature, a proper cooling fluid plays an important role. Test cases have been run without a circulating fluid, and with air and water as circulating fluids. Figure 3.22 shows the transient experiment with a set temperature 10°F above the room temperature with no fluid circulation. In Fig. 3.23, the experiment was run at 130°F as the base temperature. In Fig. 3.22, it is seen that the cooling end temperature rises because of the main heater and main guard heater, even while the cooling end heaters did not turn ON. In 1,800 seconds the cooling end temperature increased by 1.25°F above the cooling end set temperature without air circulation, whereas the temperature rose by 0.5°F with air circulation at 100 psia. In both cases it is apparent that the cooling system is not adequate for such runs. This is due to insufficient heat transfer between the brass block at the cooling end and the circulating air. Circulating water is the obvious next step, as water has much higher conductivity and heat capacity than air. To avoid the temperature build-up at the cooling end, the overall specified temperature of the system was increased to 130°F such that there is a large temperature difference between the cooling end and ambient

temperature or the circulating air temperature. This allowed us to maintain the experiment at a steady specified cooling end temperature. This is reflected in Fig. 3.23.

3.5.4.2 Calculation Procedure

The procedure to determine l and a via Eqs. 3.27 and 3.30 involves first recording the time evolution of $(T_o - T_i)$ and q_o from the very beginning of the experiment. The Laplace transform needed to deconvolve the temperature and heat flux functions is calculated numerically from both history data. This calculation yields the values necessary to plot a curve similar to Fig. 3.21. The Laplace transform is obtained by numerical integration of:

$$\overline{(T_o \cdot T_o)}(s) = \int_0^\infty e^{-st}(T_o \cdot T_i)\, t\, dt \tag{3.33}$$

This integral equation was evaluated numerically by using a Simpson adaptative numerical scheme (Cheney and Kincaid, 1980). A cubic-spline method of second order (Press *et al.*, 1989) was used for interpolation purposes. The upper limit of the integral in Eq. 3.33 depends on s and, for the purpose of this work, its numerical value is taken high enough so that there will be no alteration greater than 1×10^{-3}.

Figures 3.24 and 3.25 are plots of temperature and heat flux respectively vs. time with a heating end temperature of 145°F. The cooling end was maintained at 22°F below the heating end temperature. The upper and radial guards are maintained at the metering block temperature. The Laplace transform of the data presented in Figs. 3.24 and 3.26 are plotted in Figs. 3.26 and 3.27. The conductivity is calculated from the intercept of the flat portion of the log-log plot on Fig. 3.26 on the vertical axis. Diffusivity is calculated from the Cartesian plot of early time data presented in Fig. 3.27. The following intercepts for the flat region and slope of the early time regime are obtained, and then the conductivity and diffusivity values are determined.

$$\frac{\overline{(T_o \cdot T_i)}}{\overline{q_o}} = 12.3 \text{ °K/W}$$

$$\lambda = 2.31 \text{ W/mK}$$

$$\beta = 0.5896 \text{ °K/W}\sqrt{s}$$

$$\alpha = 1.04 \times 10^{-6} \text{ m}^2/\text{s}$$

Due to the non-smooth nature of the temperature and flux history data, the cubic spline may not always give a correct interpolation. Therefore, if the interpolation gives unreasonably large positive or negative values of $\theta_o / \overline{q_o}$ at a given s^* compared to the neighboring points, then that value is discarded. The initial temperature that is needed by the program should be judiciously selected. In the above calculations, the temperature data was first sorted to find the minimum temperature value and this temperature value was later used as the starting temperature. Otherwise, it was difficult to obtain the straight line

behavior at early time. Also, it is helpful to start with very large and very small s* values
to bracket the values of $\theta_o / \overline{q}_o$ which correspond to early time and late time. This
facilitates the determination of values in between these two extremes..

3.5.5 Fluid Saturation Experiments

Fluids saturation experiments were conducted by steady-state only because for the
transient experiment, the apparatus was not pressure tight. The experiments were run
under vacuum conditions, air saturation, and water saturation. For the vacuum
experiments, the specimen was evacuated using a vacuum pump for one hour due to the
small pore volume of the specimen. The vacuum pump was kept running throughout the
experiment. The high pressure runs were conducted with air at 100 psia and with nitrogen
at 300 psia. For tests with water as the saturating fluid, the specimen was evacuated for
one hour before saturating with deionized water. Water was then injected by only using the
gravity feed. The system was further evacuated for some time in a water-saturated
condition. Then the system was heated up to the temperature at which the experiment was
to be conducted and water circulation was resumed again, very slowly, for a short period
of time. This was done to drive out any air bubble that would have been trapped
accidentally and which expanded with increasing in temperature. This also eliminated the
pressure build-up in the system that would have taken place due to thermal expansion. In
all fluid experiments the safety valve was adjusted to bleed at pressures exceeding 350
psig. For the residual water saturation experiments, air at pressure less than 10 psig was
injected from the top of the specimen. Air was then injected at high rate to reduce the water
saturation to a reasonably lower value. The residual water saturation was determined
volumetrically.

3.5.6 Error Analysis

The accurate determination of heat flux is crucial to the steady state experiment.
Whether the data acquisition system is accurately computing the heat flux or not was
verified by using the chart recorder. The voltage drop across the current measuring resistor
was recorded vs. time over a 90 min interval. The last 26 temperature ON-OFF cycles
were used for data analysis purposes. Ideally, periodic ON-OFF cycle is expected after
steady-state has been reached. The data show no systematic deviation, but rather reflect
random fluctuation. The fraction of time the heater was ON in an average ON-OFF cycle
(t_{on}/t_{cycle})was 0.075. The voltage drop across the current measuring resistor was
essentially the same in all cycles considering the accuracy of the chart recorder. With the
average voltage drop of 47.968 volts across the heater and a drop of 2.6656 volts across
the resistor, the heat flow rate from the chart data was calculated to be 1.198 W compared
to the average over 7200 seconds by the data acquisition system of 1.225 W, a difference
of only around 2%.

In the standard guarded hot plate method, investigations have been conducted in the
past to quantify the effects of radial temperature unbalance. While using an 8"x8" hot plate
and testing 1" thick cork specimens, Gilbo (1951) observed that a 0.2°F temperature
difference between the metering section and the guard caused an error in the conductivity of
3%. He attributed the disagreement among results for the same standard material by
various investigators to such a possible temperature imbalance in the radial direction.
Pascal (1955) reported that the error due to the unbalance is a function of the specimen
conductivity, being greater with the decrease of conductivity. Though Woodside and
Wilson (1957) tested the effect of temperature imbalance only at room temperature, still
they found that a linear relationship does exist between temperature unbalance and the
measured thermal conductivity for various thickness of the specimen. The purpose of their

unbalanced temperature experiment was only to determine the error in guarded hot plate method that has been standardized by ASTM. But in our case, we deliberately use the unbalance as an accurate way of measuring thermal conductivity such that the temperature fluctuation due to ON-OFF control will not interfere with the heat flux measurement. In the standard guarded hot plate method, temperatures in the meter and the guard were maintained at the desired level by gradually and carefully adjusting the power supply either manually or automatically, which can be quite cumbersome. Woodside and Wilson (1957) suggested that the unbalance error decreases as the size of the plate is increased.

The following is an approximate calculation to demonstrate the effect of temperature unbalance. The total heat flow from the metering block in the directions other than the specimen can be represented as

$$q_t = q_r + q_{au} \tag{3.34}$$

where q_r is the radial heat flow rate from the metering block to the radial guard, q_{au} is the axial heat flow rate toward the upper guard, and q_t is the total heat loss. Under the steady-state heat transfer assumption,

$$q_t = \frac{2\pi \left(T_{meter} - T_{radial\ guard}\right)}{\frac{1}{\lambda_1} \ln \frac{r_2}{r_1} + \frac{1}{\lambda_2} \ln \frac{r_3}{r_2}} + \frac{\lambda_{Kinel}\ A \left(T_{meter} - T_{upper\ guard}\right)}{L} \tag{3.35}$$

where λ_1 and λ_2 are conductivities of sleeve and brass blocks respectively. r_1, r_2, and r_3 are the radii of the metering block, external sleeve, and the radial location of the guard thermocouple, respectively. The above equation calculated nearly 20% higher heat loss than what truly is experienced. This may be due to the complicated surface area of the metering block in the radial direction. In addition, the thickness of the layer of air at all interfaces and also the location of the o-rings in the radial direction were not taken into account that certainly offer more resistance to heat flow.

An error analysis was done for the above run by incorporating all available information. The length and diameter were measured using a slide calipers with a precision of 0.0005". The current measuring resistor was heated to 450°F and the change in its resistance was within its accuracy at the room temperature. The Fluke Manufacturing Co. has suggested the thermocouple accuracy at the data acquisition speed of 30 readings/sec to be ±0.5°C after one year of calibration. This includes all error sources: reference junction, conformity, A/D conversion. As the relationship between temperature vs. emf generated in the thermocouple is linear for the J-type thermocouple in the temperature range of interest, therefore, the linear extrapolation using the boiling and freezing point temperatures of water is not expected to include any additional error. In that case, the precision of the mercury thermometer, which is 0.1°C, can be used as the thermocouple error in the error analyses.

The resolution for voltage measurements is $1\mu V$ when the voltage range 0-0.1V is used and 1mV when the range 0-100V was used. For the steady-state experiments, the wider voltage range and for the transient experiment the narrower range was used. The time used for integrating the power supply for calculating the heat flux had a precision of ±10 milliseconds. For integration purposes, the voltage drops across the current measuring resistor and the heater are sampled as fast as possible by the 2400B. The average sampling interval was 0.8 seconds, which is essentially the time it takes to go

through one loop in the control program. Therefore, it is quite probable that the actual heater ON-OFF time is not accurately recorded. This amounts to a systematic error which eventually approaches zero at long time because this time lag influences the heater on time and off time equally. In the above experiment, more than 660 ON-OFF cycles were recorded, and therefore, the effect of the time lag is expected to be minimal. The average ON time covers approximately 8% of the ON-OFF cycle time, but the ratio of heater ON-OFF time increases with the increase of the conductivity of the specimen.

3.5.7 Results and Discussion

In this section, experimental results on thermal conductivity and thermal diffusivity obtained by using steady-state and transient methods are presented.

As discussed in previous sections, Austin limestone and Berea sandstone were used in this study as typical carbonate rock and sandstone specimens. On the other hand, the Berea sandstone is relatively clean from complex clay structures, has relatively simple structures, and is mineralogically well defined. Berea sandstone has also been widely used for measuring other petrophysical properties, so that the thermal properties can be related to those properties.

<u>3.5.7.1 Steady-State Measurements</u>

Steady-state thermal conductivity values for dry limestone and sandstone were obtained by using the extrapolation technique discussed in previous sections. In almost all cases a temperature gradient of 22°F/inch was imposed in the axial direction. The results have been reported here at the midpoint temperature of the specimen. The results for experiments with atmospheric air reported here have been obtained by averaging five runs whereas other results have been obtained by averaging two to three runs. Data were reproducible to within ±4% of the mean value.

The steady-state experiments were conducted with the limestone and sandstone specimens under vacuum conditions, air saturation, and water saturation. For the vacuum experiments, the specimen was evacuated using a vacuum pump for one hour before starting the experiment. The vacuum pump was kept running during the measurements. For measurements with air at atmospheric pressure, all valves were kept open. The flanges were adequately tightened by using the bolts so that the vertical strain caused by air in the high pressures experiments would not cause loss of contact between the specimen and the cooling/heating ends. In the case of water saturation, the specimen was evacuated for one hour before saturating with deionized water and the evacuation process was continued for some more time to allow the air bubbles that may have been accidentally trapped to escape.

The thermal conductivity of limestone at various conditions is presented in Table 3.6. As expected, the thermal conductivity with vacuum was less than that with air at atmospheric pressure. A few runs were also conducted at 100 psia air saturation pressure using limestone specimen. One run was conducted at 300 psia with nitrogen as the saturating fluid. The observed change in thermal conductivity with the above change in pressure was within the expected error margin of ±6.1%. This is consistent with data available in the literature (Woodside and Messmer, 1961). One test was done with water as the saturating fluid.

Similarly, the experiments were conducted on Berea sandstone with air at vacuum condition, 110 psi air pressure, 100% water saturation and irreducible water saturation. Results are presented in Table 3.7. The expected error for the results reported here is ±6.1%.

41

The thermal conductivity of Berea sandstone has been measured by many investigators in the past (Somerton and Boozer, 1960; Woodside and Messmer, 1961, Kunii and Smith, 1961). Berea sandstone is relatively clean and the grains are well sorted. However, there is still a wide variation (nearly 20% from the mean) in the conductivity values reported in the literature. Results from this study for Berea sandstone with atmospheric air and water as saturating fluids are compared against some of the published data in Tables 3.8 and 3.9, respectively.

It is difficult to quantify the significant variation in these data as numerous factors may have influenced the measurements. It is possible that the variation was due to normal petrophysical variability.

The effect of temperature on the thermal conductivity was studied using air-saturated Berea sandstone at atmospheric pressure. The effect of temperature was also studied at vacuum condition. Results are presented in Fig. 3.28. The decrease in thermal conductivity of Berea sandstone in vacuum condition is monotonic compared to with air. The trend of the conductivity with air at atmospheric pressure is different from the data presented in the past in the sense that in this study, the conductivity of sandstone with atmospheric air is a stronger function of temperature than has been reported in the past. This study also shows that the thermal conductivity of porous sandstone under vacuum conditions can be a strong function of temperature. There is no published data available which shows temperature behavior of sandstones in vacuum. Experiments need to be conducted at higher temperature to see if the rate of decrease in conductivity slows down at higher temperatures.

The thermal conductivity of Berea sandstone with 100% water saturation is almost twice that of the case where atmospheric air is the saturating fluid. The conductivity of air saturated sand is about 33% more than that of at vacuum condition. In case of limestone, the increase in conductivity with 100% water saturation is not as dramatic as that of sandstone.

Results for the dry limestone have been compared with the data published in the literature (Roy *et al.*, 1988) as shown in Fig. 3.29. The limestone used has a porosity of nearly 30% compared to <10% for the published data presented in this figure. This may explain why the results fall in the lower range of this figure.

3.5.7.2 Transient Method

The thermal diffusivity values measured by using the transient method are reported in Table 3.10 for limestone and sandstone specimens. The thermal conductivity value obtained from the heat flux sensor was 1.8 W/m-K for dry limestone at atmospheric pressure and 134°F average temperature compared to 1.6 W/m-K calculated by the steady-state method. The thermal conductivity values were first obtained from the late time data.

Our method of calculation of thermal diffusivity avoids knowing the specific heat, but instead requires the thermal conductivity value to be known. The measured thermal conductivity from the late time data seems to be higher than the value measured using the steady-state method. Differences between thermal conductivity data from steady-state and transient methods have been reported by previous investigators (Somerton, 1992). There has been a continuing effort to explain these difference. For the calculation of thermal diffusivity, we have used the thermal conductivity value obtained from the steady-state measurement which is considered to be more accurate than the value obtained from the transient method.

The conductivity value obtained for Berea sandstone with air at atmospheric condition is very close to the value presented by Messmer (1965) using a probe technique. However, the steady-state thermal conductivity is less than this value. In the literature most investigators have corrected their steady-state results to match this value. We believe that our steady-state method gives more accurate results, therefore, the thermal conductivity from the steady-state experiment was used to calculate thermal diffusivity data.

Similar to thermal conductivity, a wide variation in the thermal diffusivity is reported in the literature. In Table 3.11, results of some of the previous investigations are reported for comparison purposes.

Table 3.1. Physical characteristics of the cores.

Core	k, md	Porosity, %	Geometry	Core dimensions	Type of imbibition Experiments
SS#1	980	24.6	Cylinder	Diameter=1" L=3.65"	1-D through one face
SS#2	980	24.6	Cylinder	Diameter=2" L=1"	2-D through cylindrical face
SS#3	115	20.63	Cylinder	Diameter=2" L=3"	2-D through cylindrical face
SS#4	115	19.04	Rectangular	Dimensions a=0.3" b=2" c=4"	2-D through four faces
SS#5	115	18.28	Cylinder	Diameter=1" L=2"	1-D through one face
SS#6	115	18.05	Rectangular	Dimensions a=2.25" b=2.25" c=2.25"	3-D through all faces
SS#7	115	20.6	Rectangular	Dimensions a=2" b=2" c=2"	3-D through all faces
SS#8	115	20.63	Rectangular	Dimensions a=2" b=2" c=4"	3-D through all faces
SS#9	115	19.04	Rectangular	Dimensions a=2" b=2" c=3"	3-D through all faces
SS#10	115	19.28	Rectangular	Dimensions a=1" b=2" c=2"	3-D through all faces
SS#11	115	20.28	Cylinder	Diameter=2" L=1"	3-D through all faces
SS#12	115	20.00	Cylinder	Diameter=2" L=3"	3-D through all faces

Table 3.2. Fluid saturation data.

Core	Average Sw behind L' when L'< L	Final Average Sw	*Recovery at the time of L'=L, %*
SS#1	0.65	0.72	93
SS#2	0.60	0.66	95
SS#3	0.61	0.64	94
SS#4	0.61	0.64	95
SS#5	0.59	0.66	83

Table 3.3. Data on effect of temperature on imbibition.

Temperature, C	IFT (Water-air), dyne/cm	Water viscosity, cp	ΔS_{water}
1	75.83	1.728	0.64
23	72.43	0.9325	0.64
43	69.50	0.6178	0.63
60	66.97	0.4665	0.63
81	62.50	0.3503	0.65

Table 3.4. Thermal conductivity of materials used in this study.

Material	Temperature (°C)	Thermal Conductivity (W.m-°K)
Brass	20	111
G-11 composite	140	0.259
Teflon	27	0.25
Kinel-5504	27	0.499
Dry Air	27	0.0263
Fiberfrax	204	0.06
Water (liquid)	27	0.613
	127	0.688
	227	0.642
Berea sandstone (air-filled (approx.)	27	3

Table 3.5. Heat flow sensor specifications.

RdF Part No.	20457-2(SP) Serial No. 91D0100
Output at 70°F	3.31 µvolts/Btu-Ft^{-2}-Hr^{-1}
Polarity: (For heat flow into surface)	White - Positive (+) Red - Negetive (-)
Temperature Multi- plication Factor:	See attached graph
Thermal resistance	0.005 °F/Btu-Ft^{-2}-Hr^{-1} (Typ)
Heat Capacity	0.02 Btu-Ft^{-2}/°F (Typ)
Response time	0.06 sec (62% response to step function) (Typ)
Thermocouple	Type T (Copper-Constantan)

Table 3.6. Thermal conductivity values with various pore fluids in limestone at a midpoint temperature of 134°F.

Saturating fluid	Thermal conductivity at 134°F (W/m-K)
Vacuum	1.147
Atmospheric air	1.577
Air @ 100 psig	1.524
Nitrogen @ 300 psig	1.485
Deionized water	2.208

Table 3.7.   Thermal conductivity values with various pore fluids in Berea sandstone at a midpoint temperature of 134°F.

Saturating fluids	Thermal conductivity (W/m-K)
Vacuum condition	1.62
Atmospheric air	2.13
Air (110 psi)	2.35
Deionized water (S_w=0.29)	3.90
Deionized water (S_w=1.0)	4.25

Table 3.8.   Comparison of thermal conductivity measurements of Berea sandstone with atmospheric air by various investigators.

Investigator(s)	Temperature (°F)	Thermal conductivity (W/m-K)
Somerton & Boozer (1960)	200	1.575
Kunii & Smith (1961)	—	1.731
Woodside & Messmer (1961)	—	2.39
Messmer (1965)	165	2.357
Somerton & Gomma (1973)	68	2.33 and 2.09
This study	134	2.13±6.1%

Table 3.9.   Comparison of thermal conductivity values for Berea sandstone saturated with 100% water by various investigators.

Investigators	Temperature (°F)	Thermal conductivity (W/m-K)
Woodside and Messmer (1961)	—	4.48
Ozbek (1972)	—	4.10
This study	134	4.25±6.1%

Table 3.10. Thermal diffusivities and conductivities from transient method.

Medium	α (m^2/sec)	λ (W/m-K)
Austin limestone	0.49×10^{-6}	1.8
Berea sandstone	1.04×10^{-6}	2.31

Table 3.11.   Comparison of thermal diffusivity values for Berea sandstone with atmospheric air by various investigators.

Investigators	Temperature (°F)	α (m^2/s)
Somerton & Boozer (1960)	200	0.8825×10^{-6}
Edmondson (1960)	---	0.800×10^{-6}
Somerton (1972)	—	1.414×10^{-6}
This study	**134**	**1.04 $\times$ 10^{-6}**
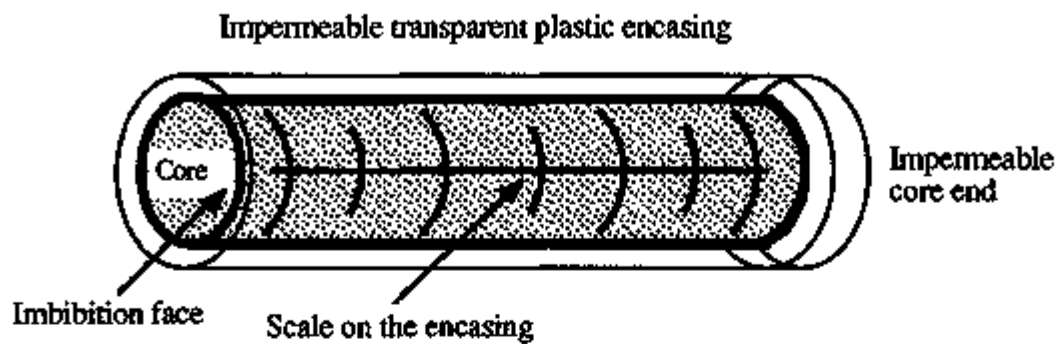
Fig. 3.1. Core geometry for one-dimensional linear imbibition.
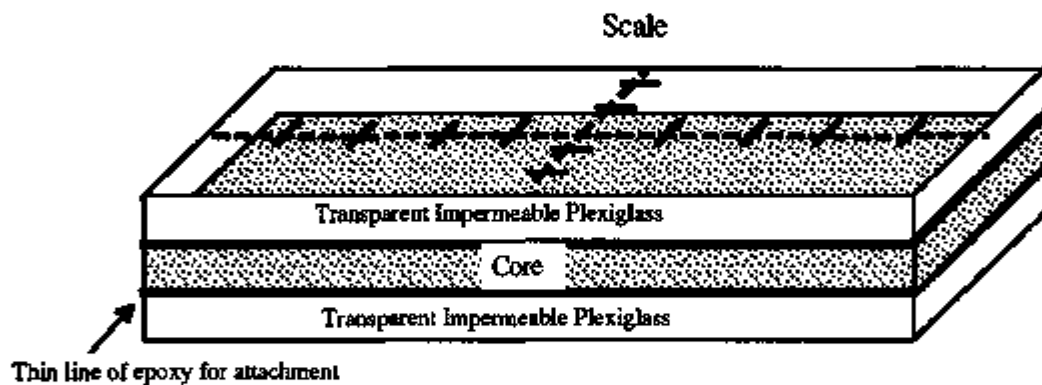
Fig. 3.2. Core geometry for two-dimensional linear imbibition.
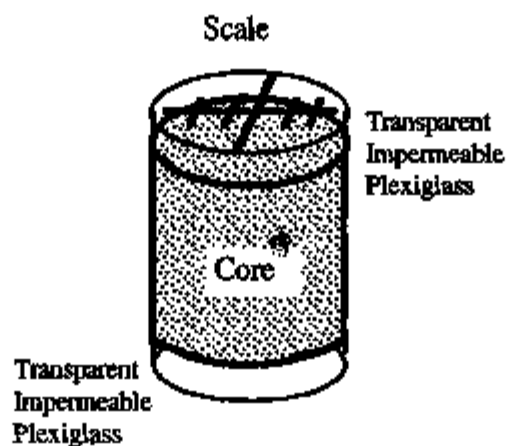
Scale

Fig. 3.3. Core geometry for radial imbibition.
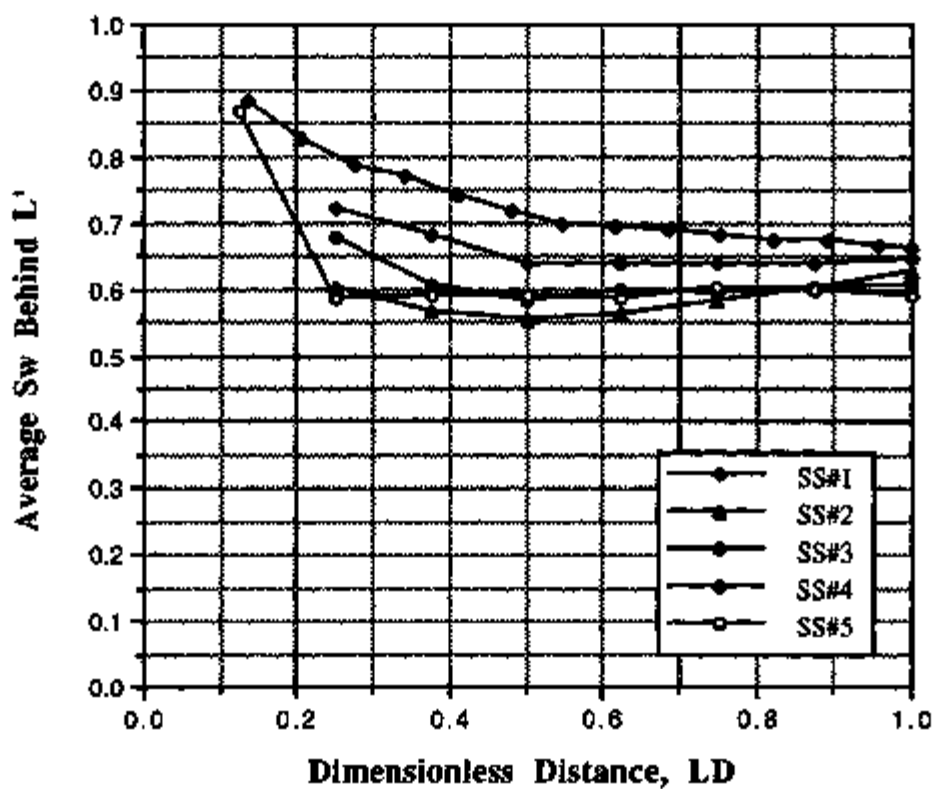
Fig. 3.4. Average saturation behind imbibition front.
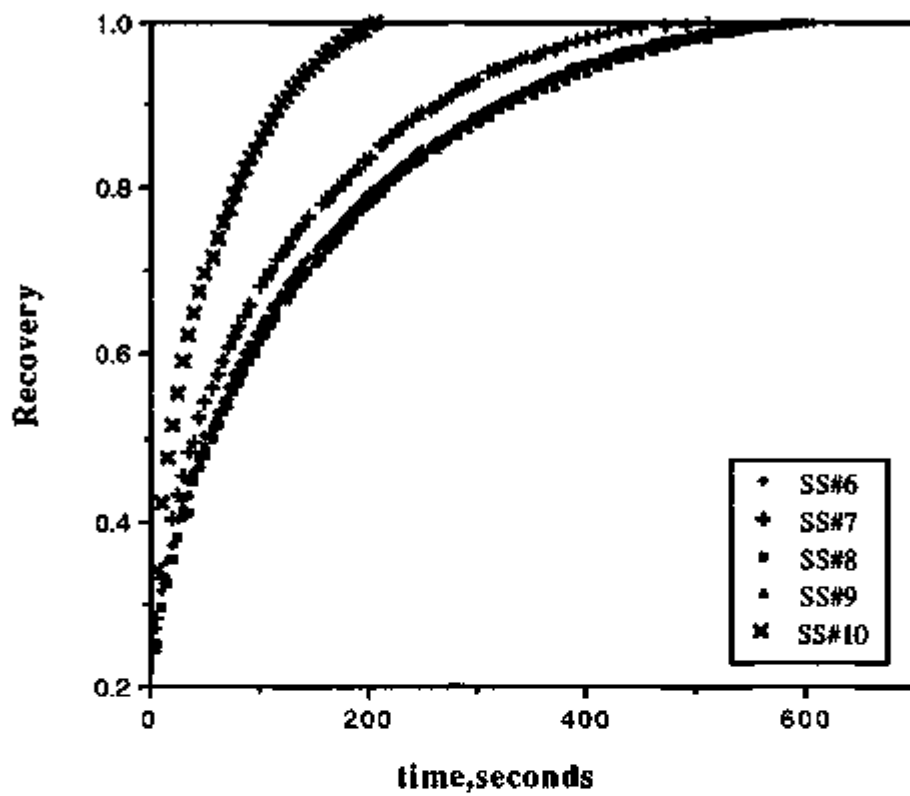
Fig. 3.5. Imbibition data from various sized cores.
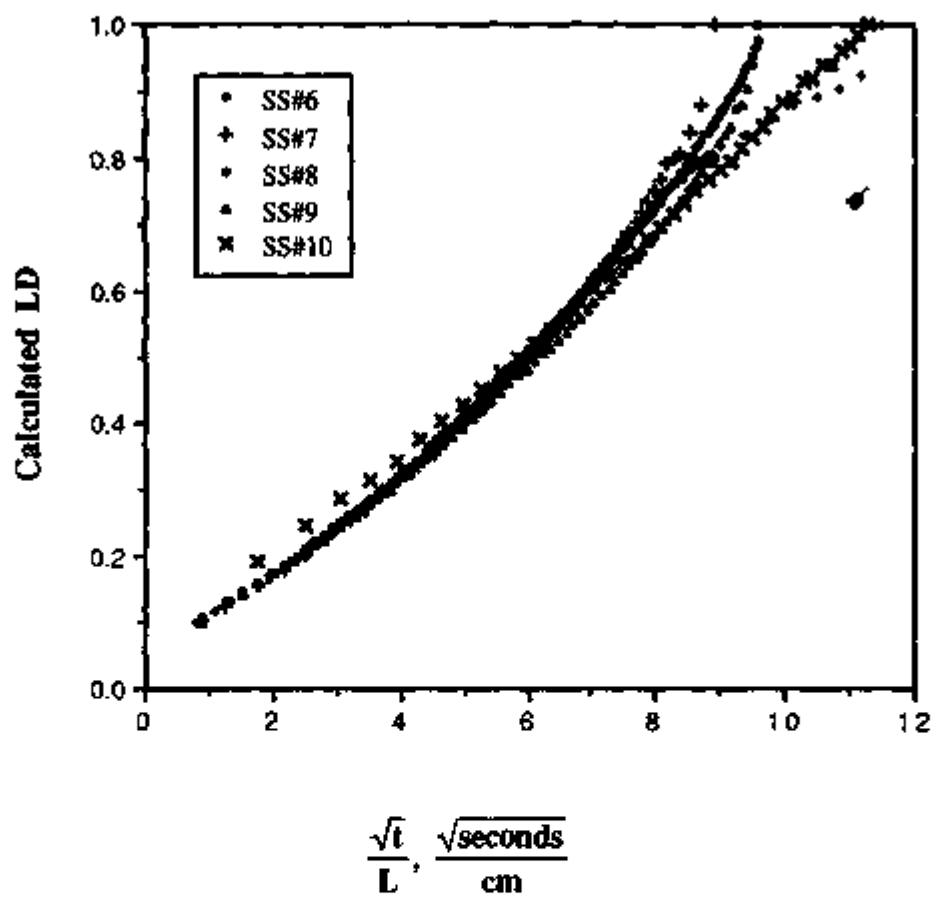
Fig. 3.6. Geometrically scaled imbibition data.
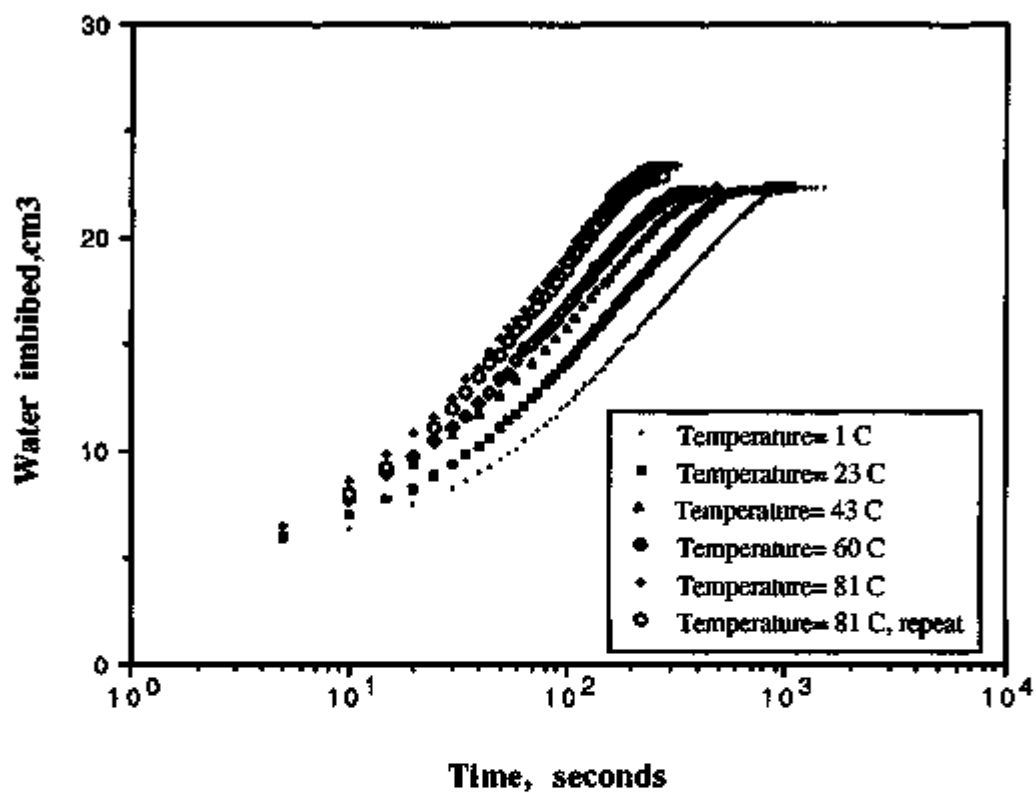
Fig. 3.7. Countercurrent imbibition at various temperatures.
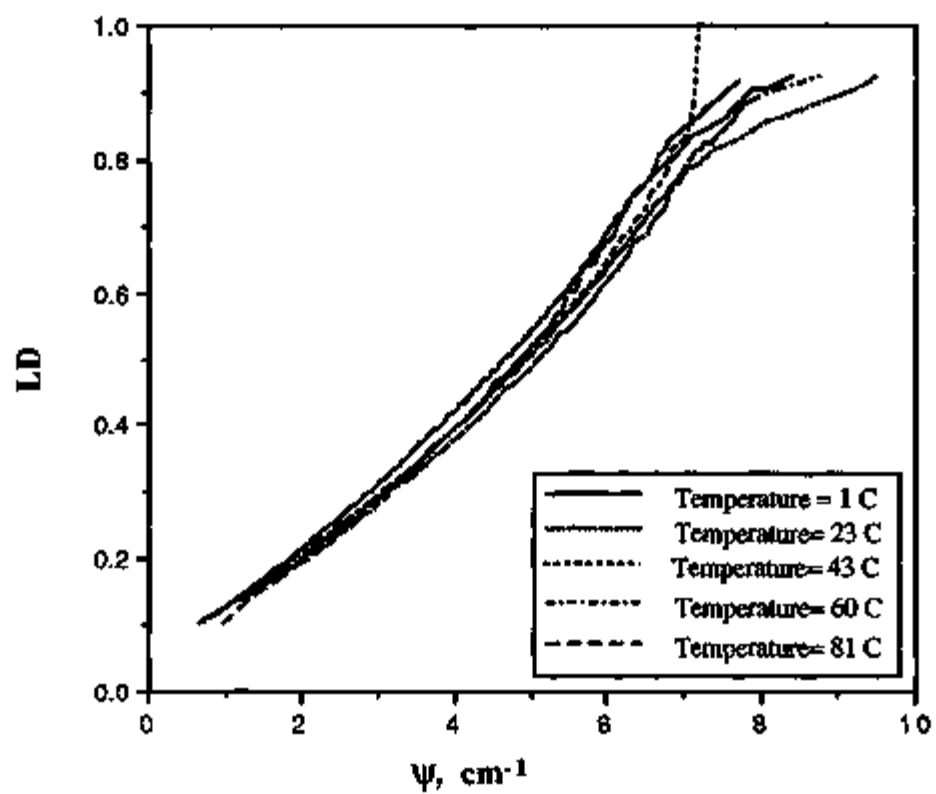
Fig. 3.8. Effect of temperature on imbibition.
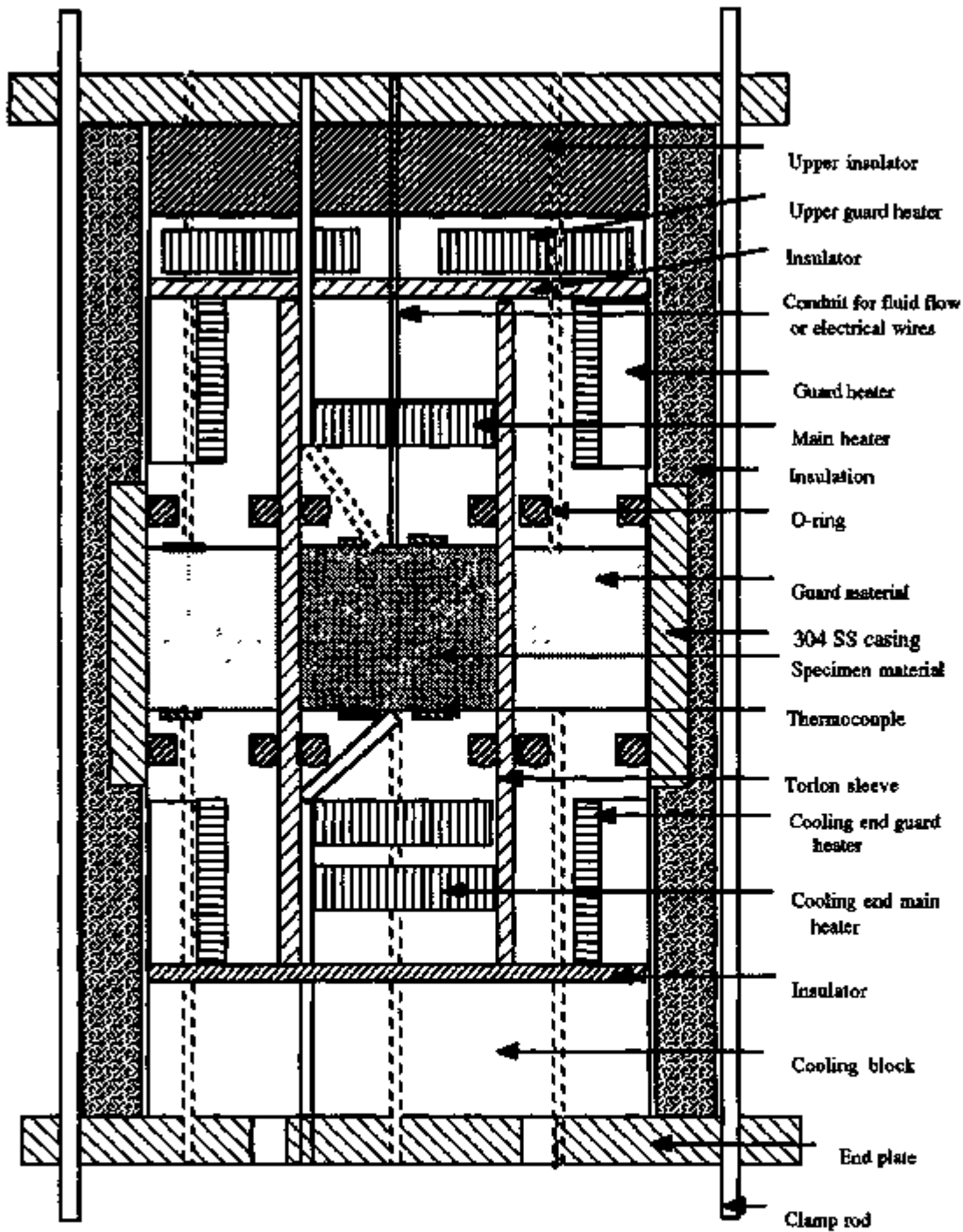
Fig. 3.9. Detailed schematic of steady-state thermal conductivity cell.

Upper insulator

Upper guard heater

Insulator

Conduit for fluid flow or electrical wires

Guard heater

Main heater

Insulation

O-ring

Guard material

304 SS casing

Specimen material

Thermocouple

Torlon sleeve

Cooling end guard heater

Cooling end main heater

Insulator

Cooling block

End plate

Clamp rod

Fig. 3.10. Apparatus for steady-state thermal conductivity measurements.
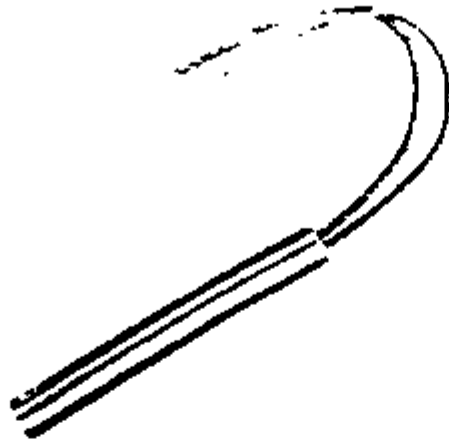
Fig. 3.11. Cartridge heaters used as the main heater, upper guard heaters, and cooling end heaters.

Fig. 3.12. Band heaters used as the main guard and cooling guard heaters.
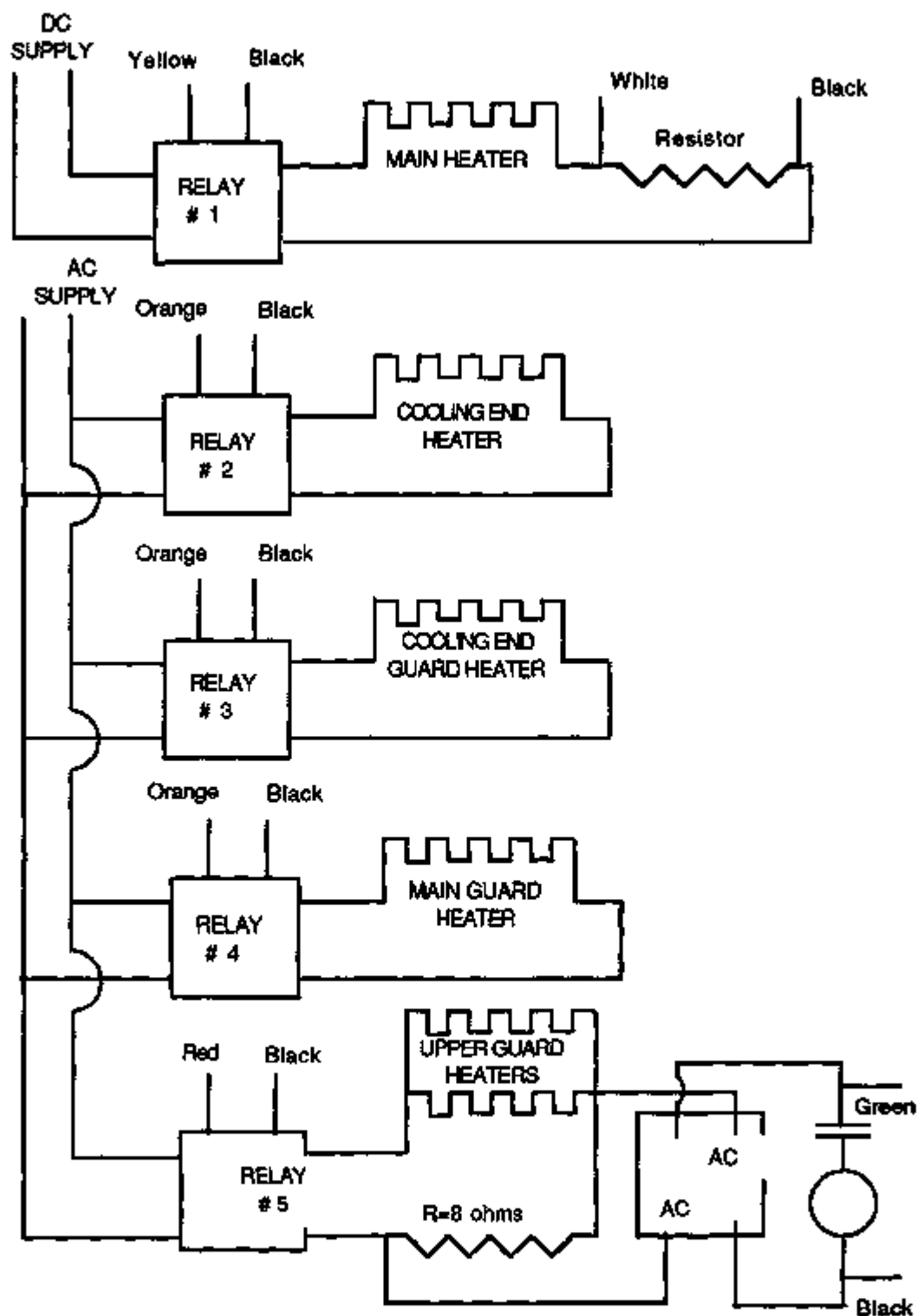
Fig. 3.13. Electrical circuit diagram for the thermal conductivity apparatus.
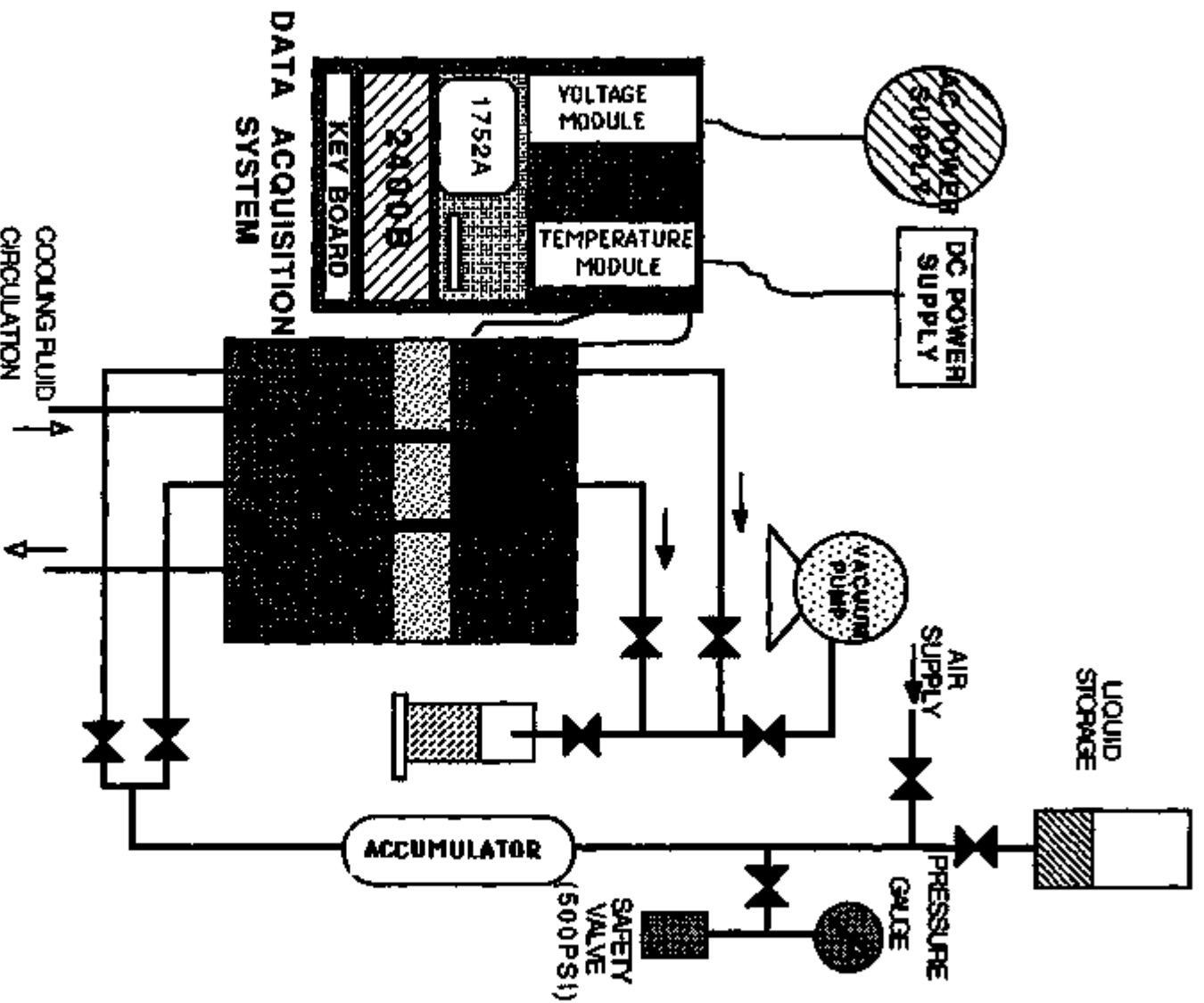
Fig. 3.14. Schematic of the apparatus including fluid saturation system.
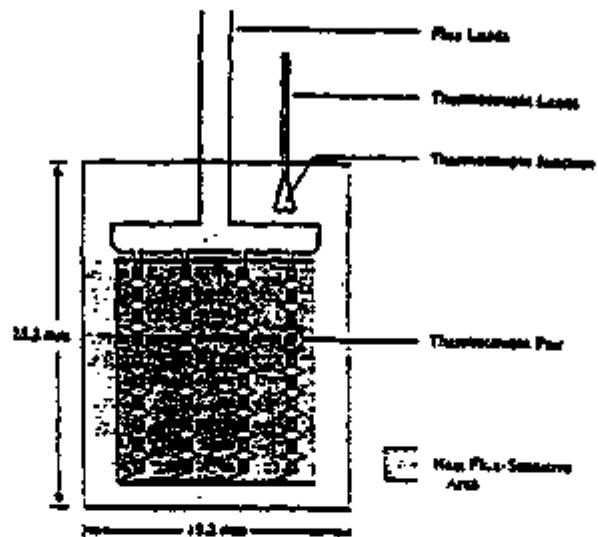
Fig. 3.15. Heat Flux Sensor Schematic (Shallcross and Wood, 1990).
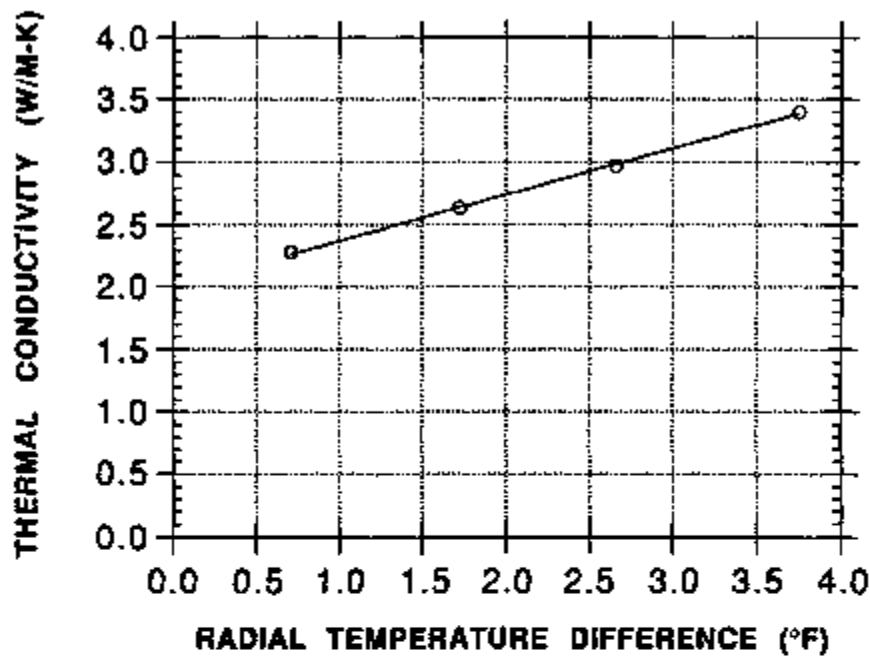
Fig. 3.16.   Thermal conductivity vs. radial temperature difference for the case of $\Delta T_{axial} = 22°F$ and $T_{midpoint} = 134°F$ at Variac setting=60%. Experiment was run using limestone with air at atmospheric pressure.
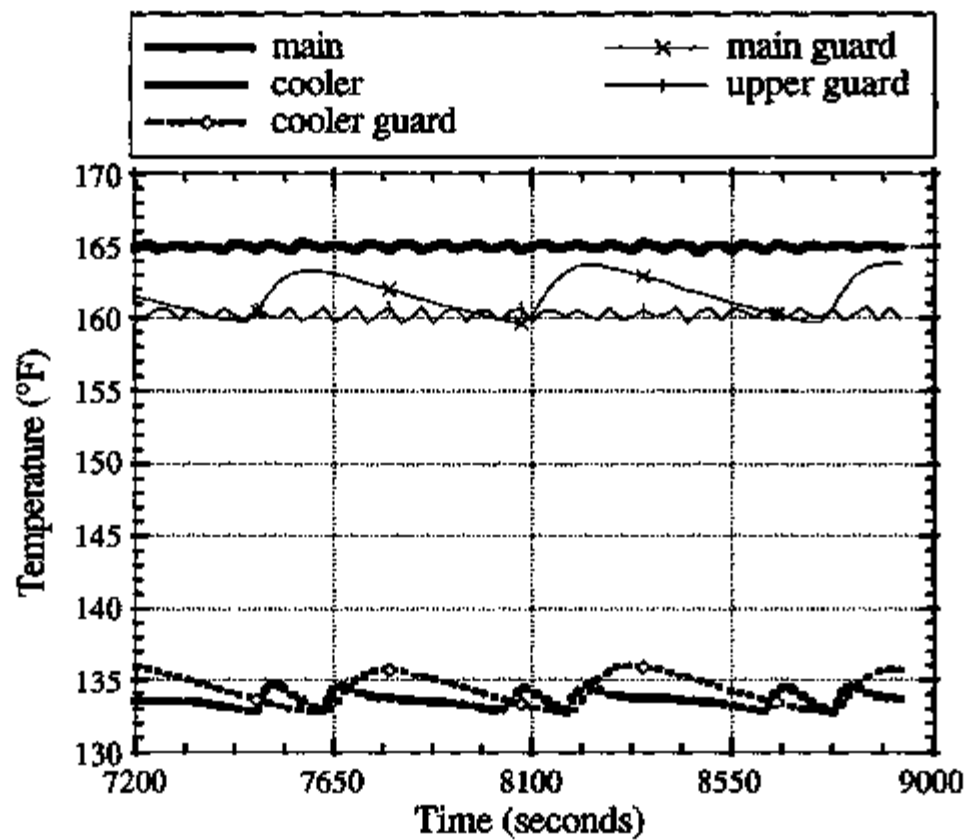
Fig. 3.17.   Temperature history of steady-state run for ΔT_{radial}=5.0°F at a Variac setting of 50% of full scale.
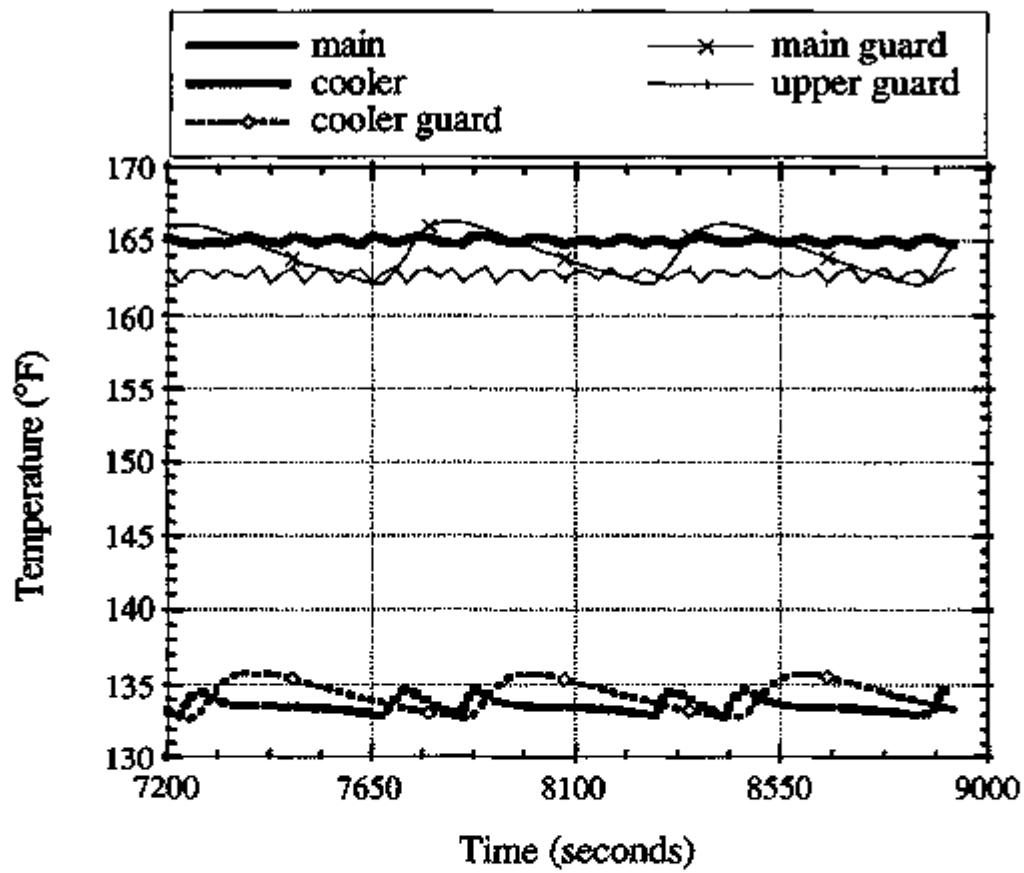
Fig. 3.18.   Temperature history of steady-state run for ΔT_{radial}=2.50°F at a Variac setting of 50% of full scale.
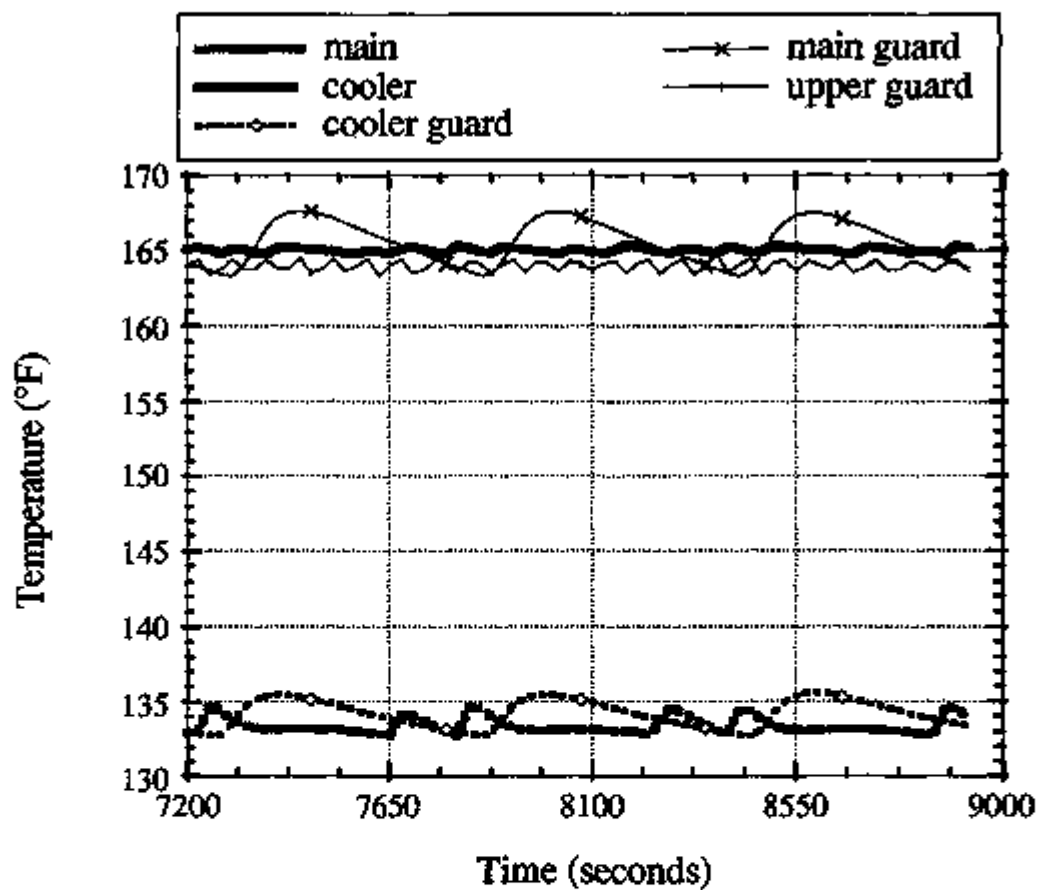
Fig. 3.19.   Temperature history of steady-state run for ΔT_{radial}=1.25°F at a Variac setting of 50% of full scale.

64
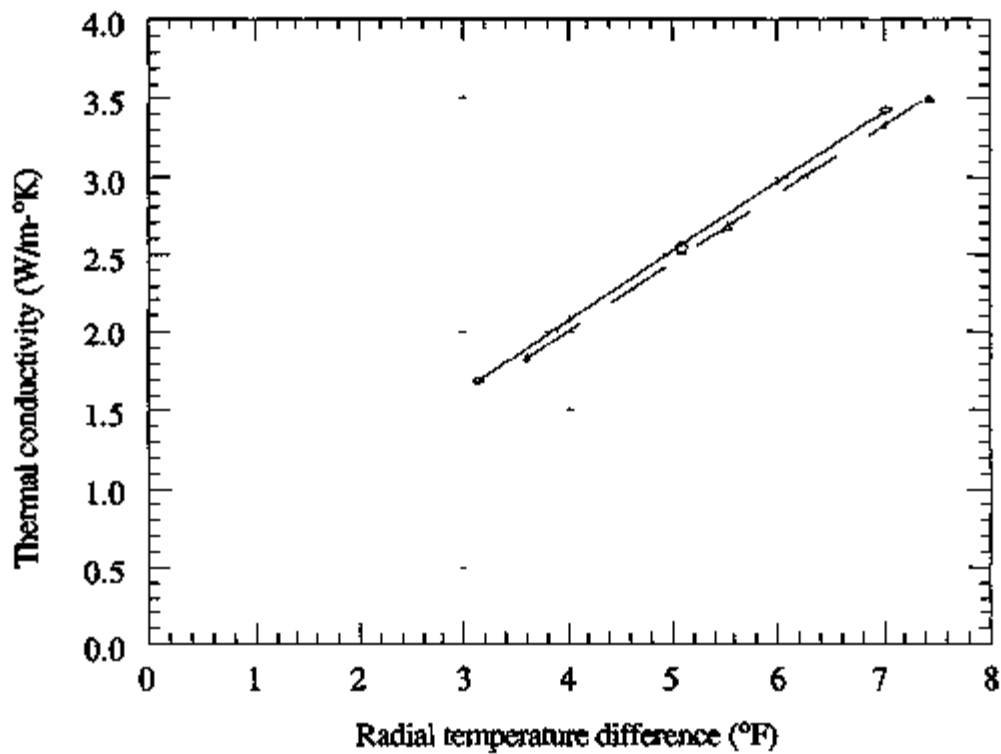
Fig. 3.20.   Comparison of linear extrapolation at two different Variac settings at 350°F average temperature (Variac settings at 40% and 50%).
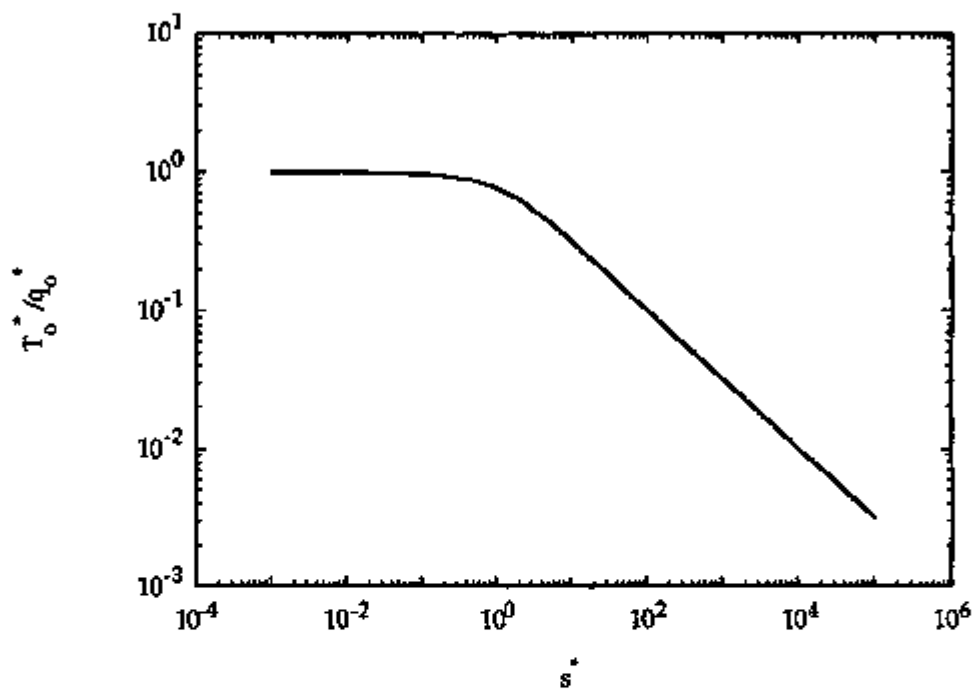
Fig. 3.21. Type-curve for constant heat flux boundary in Laplace space.
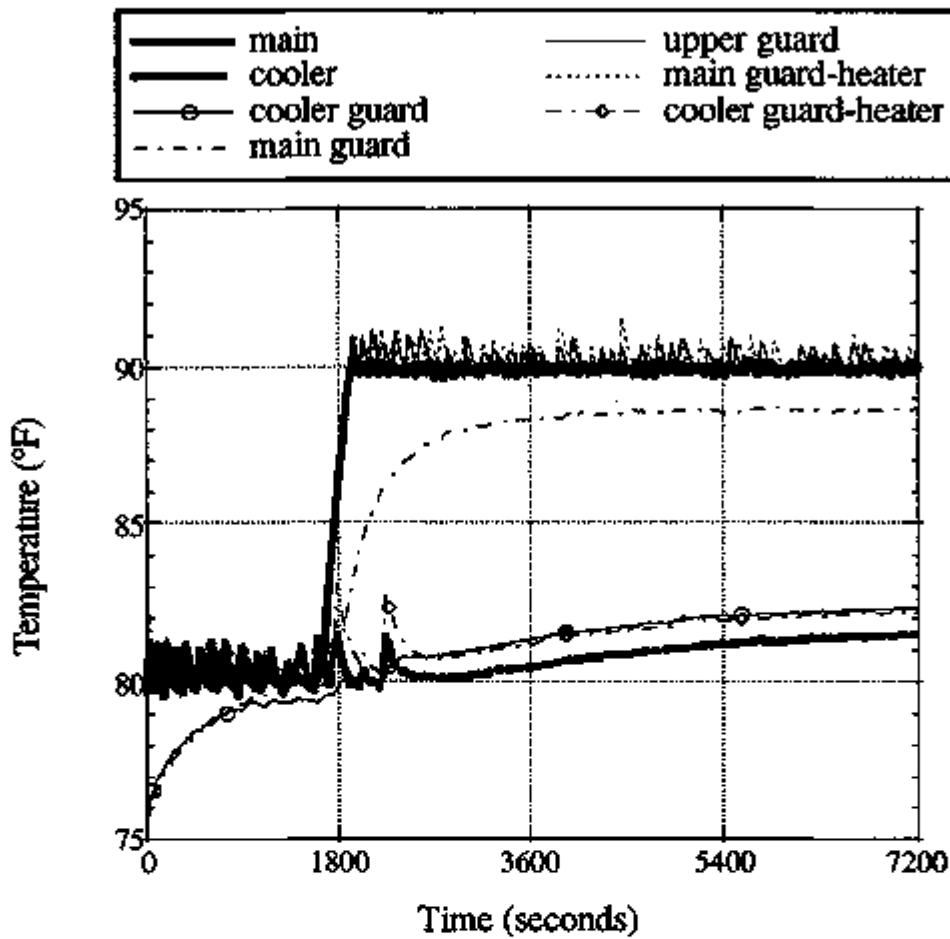
Fig. 3.22.   Temperature history of the transient measurement at the set axial temperature difference of 10°F and the cooler end temperature maintained at the room temperature. Air was used as the circulating fluid.
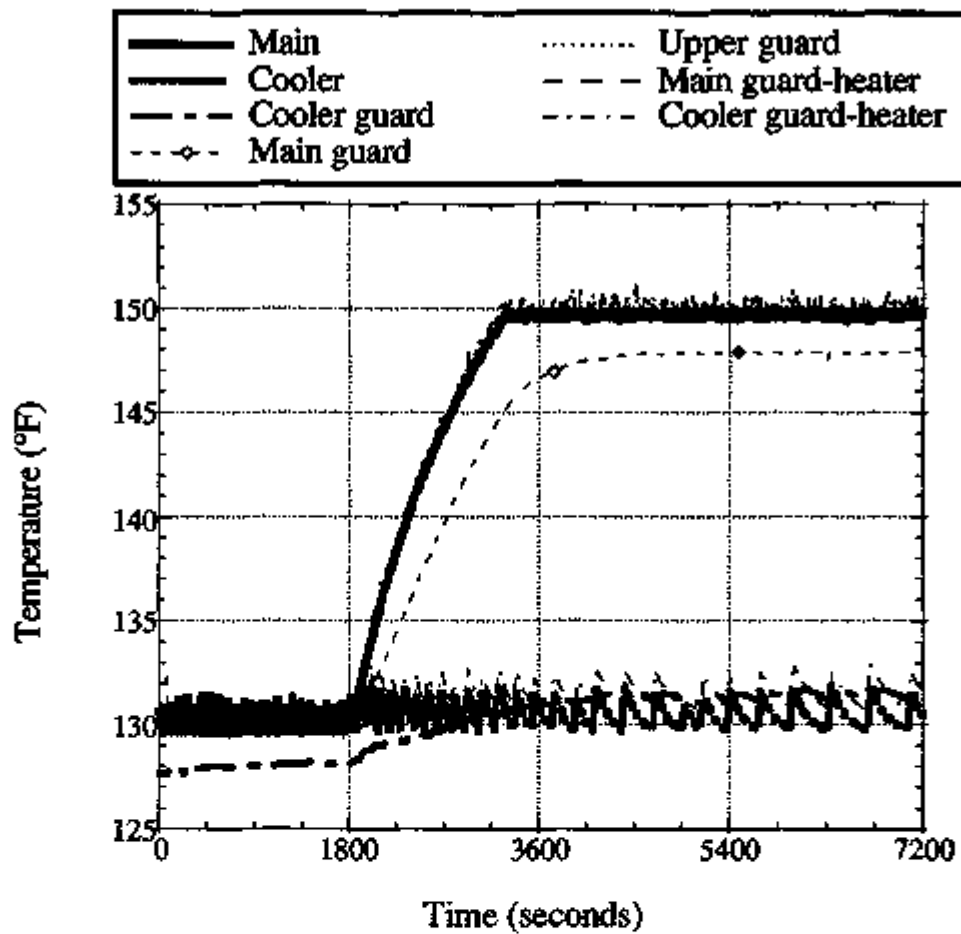
Fig. 3.23.   Temperature history of the transient measurement at the set axial temperature difference of 20°F. No coolant was circulated.

68
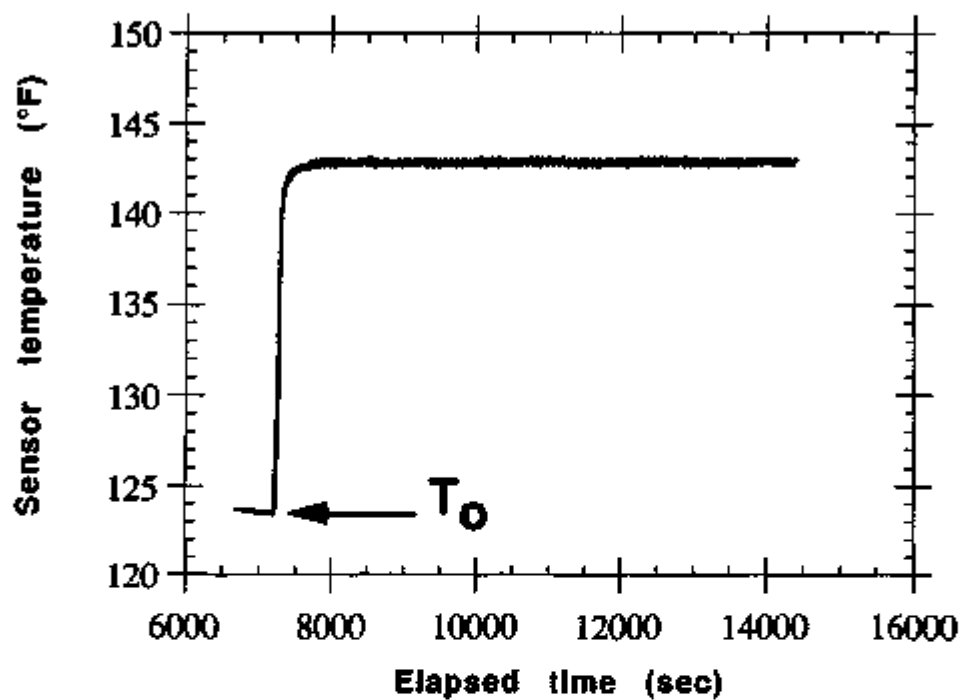
Fig. 3.24. Temperature behavior with time at the heat flux sensor at 145°F.
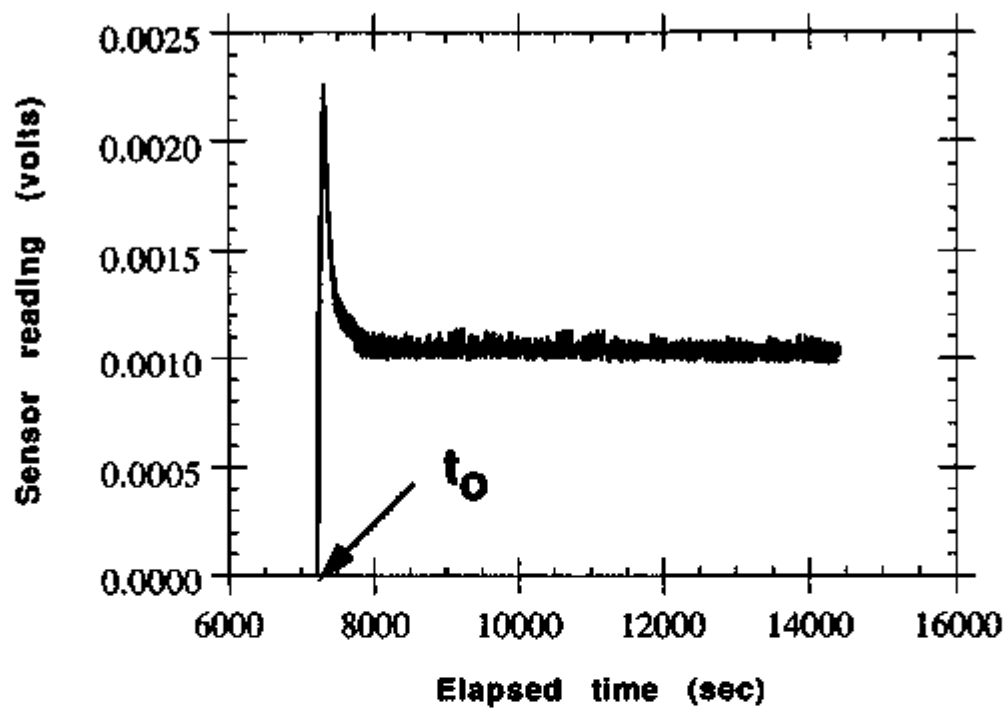
Fig. 3.25. Heat flux sensor reading with respect to time corresponding to the temperature behavior on Fig. 3.24.
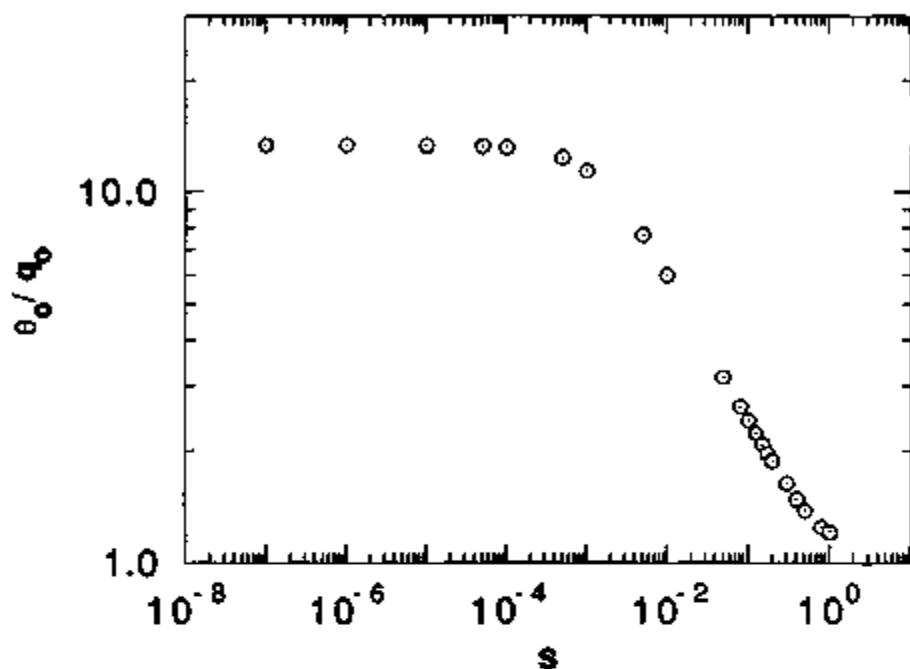
Fig. 3.26. Constant heat flux solution at 145°F from deconvolved data.
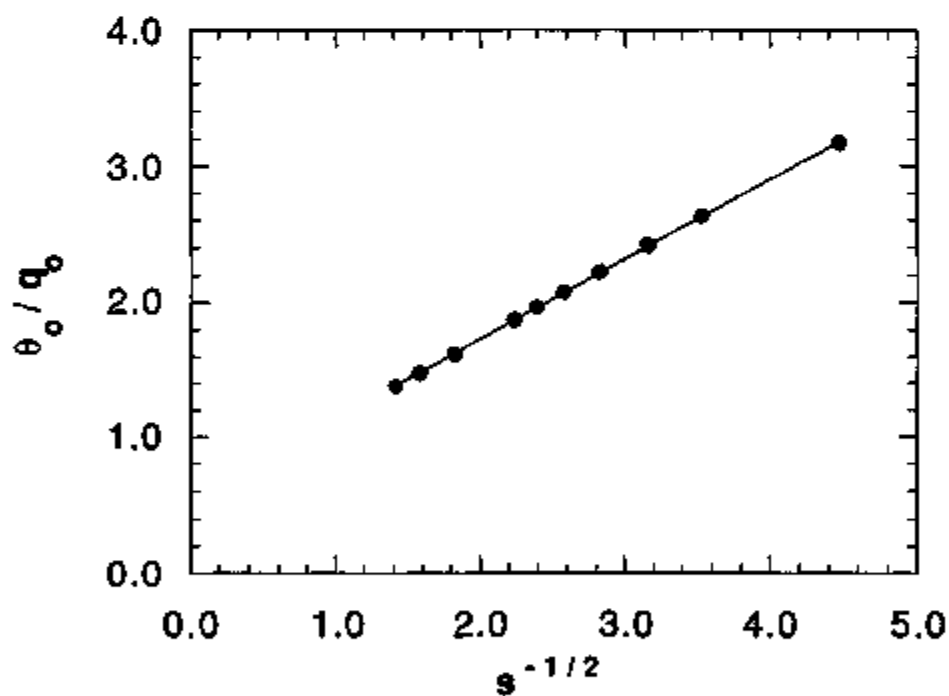
Fig. 3.27.   Early transient solution from the data collected at 145°F after data deconvolution.
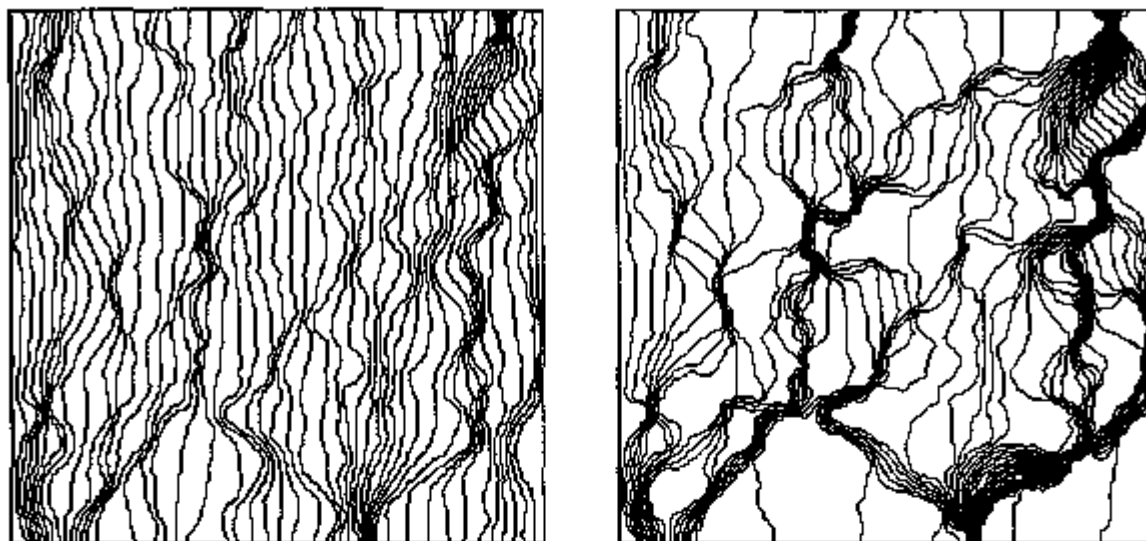
Fig. 3.28a.   Contour map of the flux values on a thin section of Berea sandstone reduced from 512x512 pixels to 128x128 pixels.
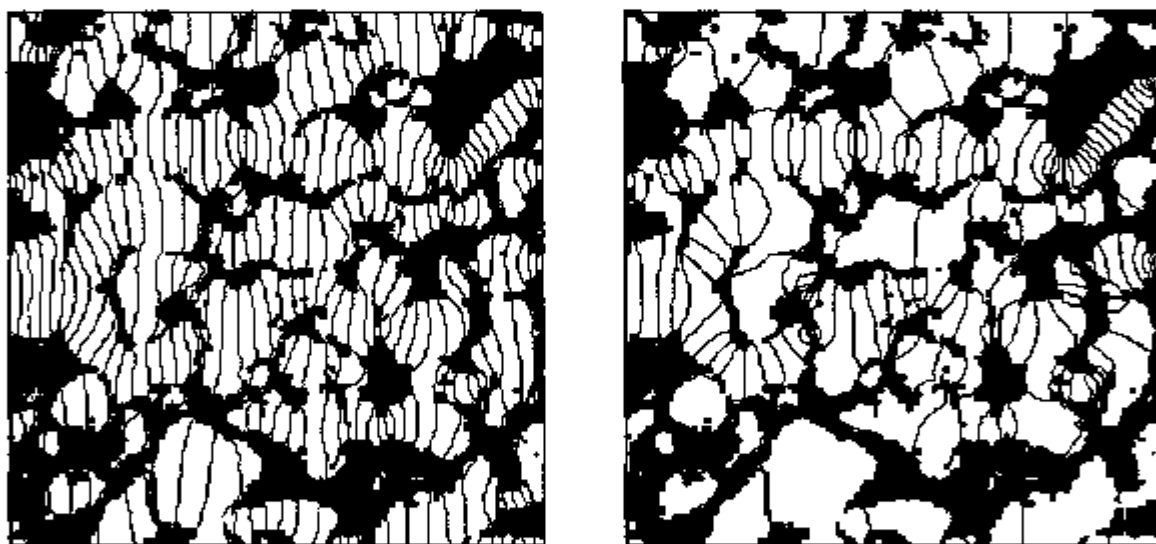
Fig. 3.28b.   Superposition of contour maps of the flux values on the rock matrix with water (cond ratio=.103278) and air (cond. ratio=0.00426) respectively. The field is a reduced field from 512x512 to 128x128 pixels. The white region represents grains.
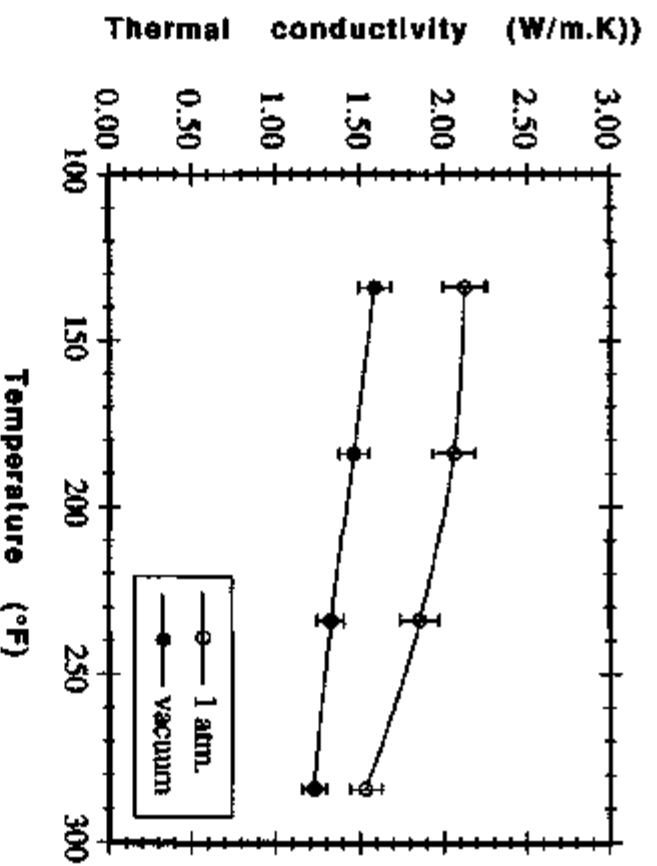
Fig. 3.29. Thermal conductivity data for the Berea sandstone at various temperatures.

73
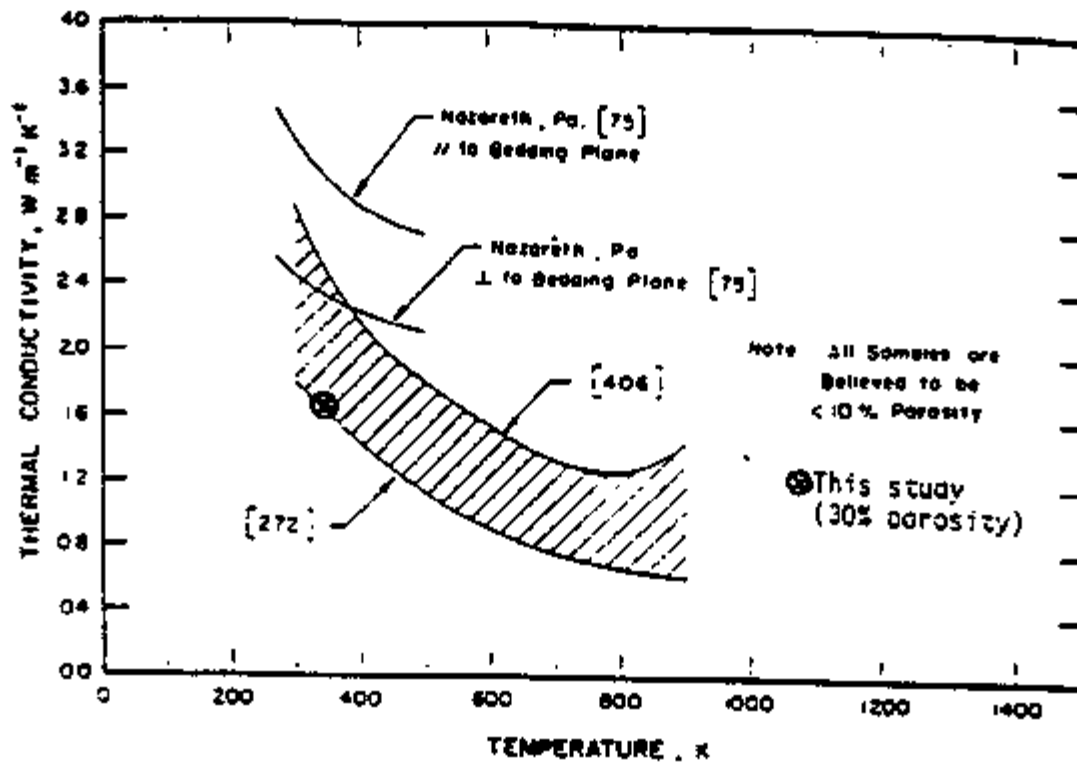
Fig. 3.30.   Thermal conductivity data for the limestone used (ϕ=30%) compared to the previously published data (Roy, Beck, and Touloukian, 1988).

4.0 NUMERICAL STUDIES

Numerical studies on this project included five main activities. First, a new dual porosity simulation approach was developed as a means to easily implement dual porosity behavior in existing (e.g., thermal) single porosity model. This appproach was tested on isothermal water imbibtion. Second, studies were conducted to investigate matrix-fracture transfer flow with a fine-grid model of a single matrix block. Third, a method of easily modeling gas generation effects was developed and tested. Fourth, an investigation of methods to calculate over- and underburden heat losses was conducted. And lastly, a new dual porosity thermal simulation was developed and preliminary testing conducted.

4.1 A NEW DUAL POROSITY SIMULATION APPROACH

In this section, the development of an accurate and computationally efficient isothermal dual porosity simulator (UTDUAL) for naturally fractured reservoirs and its applications to modeling fluid flow in fractured reservoirs are described. This work formed the basis for development of an efficient technique for implementing dual porosity effects into an existing single porosity simulator. Implementation of this approach in a thermal (steam) model is given in Section 4.4. This work can provide the basis for others to implement dual porosity behavior into any existing thermal simulation model.

In UTDUAL, the basic assumption of dual porosity model is adopted, namely, that fracture networks can be modeled by a continuous porous medium and matrix blocks act much like sources or sinks. The finite-difference equations for the fracture system are treated implicitly and solved using Newton's method.

Three different options were developed for UTDUAL to model flow within matrix blocks and matrix/fracture transfer flow: (1) an IMPES method, (2) diffusion methods, and (3) results from single matrix block studies. In the first two options, the matrix blocks are discretized into subgrids to enhance pressure and saturation resolution. The equations for matrix/fracture transfer flow are formulated in such a way that they are mathematically decoupled, and the resulting fracture equations are the same as for a single porosity model except for explicit matrix source and/or sink terms for each fracture gridblock. This option allows an existing single porosity model to easily be made into a dual porosity code. The third option requires fine-grid simulation studies of a representative matrix block under totally immersed conditions, but with computation time almost the same as for a single porosity system.

4.1.1 General Descriptions and Assumptions

This section presents a general description of the new dual porosity simulator (UTDUAL) developed for naturally fractured reservoirs including its capabilities and limitations. Basic assumptions are also described.

UTDUAL can simulate oil recovery by fluid expansion, displacement, and capillary/gravity imbibition mechanisms in naturally fractured reservoirs. Some typical field production problems which can be handled by UTDUAL include primary depletion, pressure maintenance by water injection, evaluation of secondary recovery waterflooding, and displacement operations. The main improvements of UTDUAL over existing dual

porosity simulators in the literature are the accuracy and efficiency of the matrix/fracture transfer flow calculations, and the availability of three different options.

Technically, UTDUAL is a multidimensional, isothermal, black oil, dual porosity simulator. Therefore, all basic assumptions for black oil simulators apply. Usually, water is the wetting phase and oil is the nonwetting phase. Oil and water are assumed to be immiscible and they do not exchange mass. Furthermore, it is assumed that fluids are at constant temperature and in thermodynamic equilibrium throughout the system.

In UTDUAL, fractured reservoirs are idealized as a set of discontinuous parallelepipeds within a continuous fracture system. The fracture system can be modeled much like a single porosity reservoir. Since matrix blocks are usually small compared to the finite-difference gridblocks of the fracture system, each fracture gridblock may encompass a number of matrix blocks. Another assumption is that the matrix blocks in a fracture grid can be modeled by a representative block. Therefore, the total matrix/fracture transfer rate is the summation of contributions from each of these matrix blocks. Figure 4.1 shows a schematic of the assumptions of the dual porosity model and the relationship between matrix blocks and fracture gridblocks.

UTDUAL was developed on the VAX-6520 in the Dept. of Petroleum Engineering. With minor modifications it also runs on the Cray Y-MP/8 at the UT System Center for High Performance Computing. The fracture part of the simulator and all PVT and rock property calculations are largely vectorized.

The following is a partial list of UTDUAL's capabilities:

(1)   Multiple sets of PVT and rock data are allowed within different reservoir regions. However, at least two sets of data, one for matrixes and another for fractures, are required.

(2)   Variable numbers of gridblocks, with either point-centered or block-centered grid distributions are allowed. A radial flow option is also available for single well studies.

(3)   Constant time step size and automatic time step size selection are available.

(4)   Constant reservoir parameters, such as permeability and porosity, or distributions of these parameters, can be chosen.

(5)   Both compressible and incompressible systems can be modeled.

(6)   Tabular relative permeability or fitted equations of relative permeability can be used. Capillary pressure data is tabular.

(7)   PVT properties are tabular.

(8)   Various well control schemes, such as total oil production rate, total liquid production, constant injection rate, constant bottomhole pressure production and constant pressure injection, can be chosen.

(9)   Matrix option can be turned on and off to simulate fractured and unfractured reservoirs. Detailed formulations for some of these capabilities are covered in the following sections.

76

4.1.2 Fracture Equations and Solution Method

In this section, the implicit finite-difference fracture equations are described, including the initial and boundary conditions. The Newton-Raphson method is used to linearize these equations. For the convenience of following discussions, the transfer flow rates, $\tau_{\alpha m\text{-}f}$, are treated much like source/sink terms.

c4.4.1.2.1 Implicit Fracture Equations

The standard dual porosity flow equations for modeling naturally fractured reservoirs in finite-difference form can be written as

Fracture equations:

$$\Delta\left[T_{\alpha f}\left(\Delta \, p_{\alpha f} - \gamma_{\alpha f} \, \Delta \, D_f\right)\right] - \tau_{\alpha m\text{-}f} + q_{\alpha f} = \frac{V_b}{5.615 \, \Delta t} \, \Delta_t\left(\frac{\phi_f \, S_{\alpha f}}{B_{\alpha f}}\right) \tag{4.1}$$

Matrix flow equations:

$$\tau_{\alpha m\text{-}f} = \frac{V_b}{5.615 \, \Delta t} \, \Delta_t\left(\frac{\phi_m \, S_{\alpha m}}{B_{\alpha m}}\right) \tag{4.2}$$

where α denotes either oil or water phase, and other terms are defined in Chapter 1 and the Nomenclature section. UTDUAL is currently for oil and water flow only. However, inclusion of a gas phase flow equation is straightforward. Transmissibility for fracture-fracture flow, $T_{\alpha f}$, is defined as

$$T_{\alpha f \, i+1/2 \, j \, k} = 0.001127 \frac{k_{xf \, i+1/2 \, j \, k} \, \Delta Y_j \, \Delta Z_k}{0.5\left(\Delta X_i + \Delta X_{i+1}\right)} \lambda_{\alpha f \, i+1/2 \, j \, k} \tag{4.3a}$$

for flow in the x-direction, where the mobility, $\lambda_{\alpha f \, i+1/2}$, is

$$\lambda_{\alpha f \, i+1/2} = \omega_{\alpha f}\left(\frac{k_r}{\mu \, B}\right)_{\alpha f \, i} + (1 - \omega_{\alpha f})\left(\frac{k_r}{\mu \, B}\right)_{\alpha f \, i+1} \tag{4.3b}$$

Similar terms can be defined in the y- and z-directions. The term $\omega_{\alpha f}$ is the upstream weighting factor and is either one or zero depending on the flow direction of phase α. In UTDUAL, only one-point upstream weighting is evaluated.

The first term on the left-hand side of Eq. 4.1 can be expanded to

$$\Delta T \Delta \, (p - \gamma D) = \Delta_x T_x \Delta_y \, (p - \gamma x) + \Delta_y T_y \Delta_y \, (p - \gamma y) + \Delta_z T_z \Delta_z \, (p - \gamma z) \tag{4.4}$$

where, for example,

$$\Delta_z T_z \Delta_z (p - \gamma z) = T_{z\,k+1/2} \left[p_{k+1} - p_k - \gamma_{k+1/2} \left(z_{k+1} - z_k \right) \right]$$
$$+ T_{z\,k-1/2} \left[p_{k-1} - p_k - \gamma_{k-1/2} \left(z_{k-1} - z_k \right) \right] \tag{4.5}$$

Similar expressions can be written for the x- and y-directions. Figure 4.2 illustrates the coordinate and node locations used in the three-dimensional formulation. $\gamma_{k+1/2}$ is the average specific gravity between neighboring gridblocks

$$\gamma_{k+1/2} = \frac{\gamma_{k+1} + \gamma_k}{2} \tag{4.6}$$

A radial coordinate of system is also implemented in UTDUAL. This option is useful for single well studies. Figure 4.3 illustrates a radial grid geometry. Normally, smaller grid increments are necessary near the well in order to maintain uniform accuracy (Aziz and Settari, 1979).

Inter-grid transmissibility is calculated by

$$T_{\alpha\,i+1/2} = 2\pi \; r^L_{i+1/2} \frac{\Delta z}{r_{i+1} - r_i} \lambda_{\alpha\,i+1/2} \tag{4.7}$$

and the bulk volume of a gridblock is:

$$V_{b\,i} = \pi \left(r^2_{i+1/2} - r^2_{i-1/2} \right) \Delta z \tag{4.8}$$

where,

$$r^2_{i+1/2} = \frac{r^2_{i+1} - r^2_i}{\ln \left(\frac{r_{i+1}}{r_i} \right)^2} \tag{4.9}$$

and

$$r^L_{i+1/2} = \frac{r_{i+1} - r_i}{\ln \left(\frac{r_{i+1}}{r_i} \right)} \tag{4.10}$$

Aziz and Settari (1979) provide detailed derivations of the above formulations.

4.1.2.2 Initial and Boundary Conditions

Initial conditions are set by specifying two independent variables (p_{of} and S_{wf}) at each gridblock node throughout the solution domain (the reservoir) at time zero. Since it is assumed that the reservoir is initially at static equilibrium throughout the domain, it is only necessary to specify the oil-phase pressure at one elevation (datum) in the domain. Values at other points are calculated from hydrostatics:

$$p_{of\,k} = p^0 + \gamma_{o k} \left(z_k - z^0 \right) \tag{4.11}$$

where p^0 is the pressure specified at datum z^0.

Initial water saturation can be obtained by gravity and capillary pressure equilibrium:

$$S_{wfk} = P_c^{-1} (p_{ofk} - p_{wfk}) \tag{4.12}$$

In the case of zero capillary pressure in the fracture system, initial fluid segregation is assumed.

No-flow boundary conditions for the mass conservation equations (Eq. 2.1) are given by:

$$\vec{n} \cdot \vec{u_\alpha} = 0 \tag{4.13}$$

For finite-difference equations (Eq. 4.1), the no-flow boundary conditions (Eq. 4.12) are implemented by setting transmissibilities to zero.

4.1.2.3 Solution Method

The linearization of Eq. 4.1 using the Newton-Raphson method is described in this section. Equation 4.1 can be expressed in terms of residuals:

$$R(X) = 0 \tag{4.14}$$

where X and R are arrays, and x_{ijk}, the ijkth gridblock in the X array has two components:

$$x_{ijk} = \begin{bmatrix} p_{of} \\ S_{wf} \end{bmatrix}_{ijk} \tag{4.15}$$

and the corresponding residual R_{ijk} is a two-component vector:

$$R_{ijk} = \begin{bmatrix} R_o \\ R_w \end{bmatrix}_{ijk} \tag{4.16}$$

R_{oijk} and R_{wijk} are functions of p_{of} and S_{wf} in gridblock ijk and the six surrounding blocks (Fig. 4.2), and take the following forms:

Oil :

$$R_{o\ ijk} = \Delta_x T_x \Delta_x (p_{of} - \gamma_o x_f) + \Delta_y T_y \Delta_y (p_{of} - \gamma_o y_f) + \Delta_z T_z \Delta_z (p_{of} - \gamma_o z_f)$$
$$- \frac{V_{b\ ijk}}{\Delta t} \left[\left(\frac{\phi S_o}{B_o} \right)^{n+1} - \left(\frac{\phi S_o}{B_o} \right)^n \right]_{ijk} - q_{o\ ijk} + \tau_{o\ m-f} \tag{4.17}$$

Water:

$$R_{w\ ijk} = \Delta_x T_x \Delta_x (p_{wf} - \gamma_w x_f) + \Delta_y T_y \Delta_y (p_{wf} - \gamma_w y_f) + \Delta_z T_z \Delta_z (p_{wf} - \gamma_w z_f)$$
$$- \frac{V_{b\ ijk}}{\Delta t} \left[\left(\frac{\phi S_w}{B_w} \right)^{n+1} - \left(\frac{\phi S_w}{B_w} \right)^n \right]_{ijk} - q_{w\ ijk} + \tau_{w\ m-f} \tag{4.18}$$

79

Equation 4.14 can be linearized using Newton-Raphson method. If X^c is an approximation to $X^{t+\Delta t}$, the approximation to $\Delta X = X^{t+\Delta t} - X^c$ is

$$\Delta X = -J^{-1} R(X^c) \qquad (4.19)$$

where each element of the Jacobian J is a 2×2 submatrix:

$$J_{ij} = \frac{\partial R_i}{\partial X_j} = \begin{bmatrix} \dfrac{\partial R_{oi}}{\partial p_{oj}} & \dfrac{\partial R_{oi}}{\partial S_{wj}} \\ \dfrac{\partial R_{wi}}{\partial p_{oj}} & \dfrac{\partial R_{wi}}{\partial S_{wj}} \end{bmatrix} \qquad (4.20)$$

A summary the procedure for obtaining the solution at time $t + \Delta t$ follows:

(1)   Obtain an estimate of the solution X^c at time $t + \Delta t$.

(2)   Solve Eq. 4.19.

(3)   Update the solution vector $X^c <- X^c + \Delta X$.

(4)   Compute the new residual $R(X^c)$.

(5)   If the residual in Step 4 is sufficiently small, set $X^{t+\Delta t} = X^c$; otherwise resolve Eq. 4.19 with the new value of X^c.

4.1.3 Special Topics

In this section, several special topics are described including well models, automatic time step size selection, material balance calculation, solvers, and vertical equilibrium capillary pressure curve.

4.1.3.1 Well Models

Wells in a fractured reservoir are assumed to be connected to the fracture system only. Well models are used to set the source/sink terms to mimic actual well operations. The relationship between flow rate, flowing bottomhole pressure and gridblock pressure can be expressed as

$$q_{ock} = PI_k \, \lambda_{ock} \, (p_{wf\,k} - p_{ok}) \qquad (4.21)$$

where PI_k is the productivity index for layer k and can be calculated by:

$$PI_k = \frac{\sqrt{k_{xf} \, k_{yf}} \; \Delta z_k}{\left[\ln\!\left(\dfrac{r_o}{r_w}\right) + S \right]} \qquad (4.22)$$

where r_o is determined by the method suggested by Peaceman (1983):

$$r_o = 0.28 \frac{\left[\left(\frac{k_{yf}}{k_{xf}}\right)^{1/2} \Delta x^2 + \left(\frac{k_{xf}}{k_{yf}}\right)^{1/2} \Delta y^2\right]^{1/2}}{\left(\frac{k_{yf}}{k_{xf}}\right)^{1/4} + \left(\frac{k_{xf}}{k_{yf}}\right)^{1/4}}$$ (4.23)

where gridblock indices are omitted for convenience. To use Eq. 4.23, a well is assumed to be located at the center of the gridblock.

A variety of well control schemes are implemented in UTDUAL. Details of all these options are described in the next section. Similar formulations can be found in a paper by Fanchi *et al.* (1982).

4.1.3.2 Rate Constraint Representations

In these representations, rates are specified for producers and injectors. These can be oil production rate or total liquid (oil plus water) production rates for producers, and water injection rates for injectors.

Case 1-Oil Production Rate Specified

Assuming that a well is completed in K layers, the production rate of layer k can be calculated by

$$q_{ok} = Q_o \frac{[(PI) \lambda_o]_k}{\sum_{k=1}^{K} [(PI) \lambda_o]_k}$$ (4.24)

The water production rate for layer k is determined according to the mobility ratio:

$$q_{wk} = q_{ok} \frac{\lambda_{wk}}{\lambda_{ok}}$$ (4.25)

Case 2-Total Production Rate Specified

In this case, total mobility ratios are first computed, followed by calculation of flow rates for each layer:

Oil mobility ratio

$$\alpha_{oT} = \sum_{k=1}^{K} \frac{\lambda_{ok}}{\lambda_{ok} + \lambda_{wk}}$$ (4.26)

Water mobility ratio

$$\alpha_{wT} = \sum_{k=1}^{K} \frac{\lambda_{wk}}{\lambda_{wk} + \lambda_{ok}}$$ (4.27)

Based on α_{wT} and α_{oT}, the total oil rate for a well can be calculated by

$$Q_o = \frac{\alpha_{oT}}{\alpha_{oT} + \alpha_{wT}} Q_I \qquad (4.28)$$

Once Q_o is known, the oil and water production rates (q_{ok}, q_{wk}) for each layer can be determined by Eqs. 4.24 and 4.25.

Case 3-Injection Rate Specified

If a well is a water injector, the water injection rate, Q_w, must be specified. The injection rate for each layer is allocated as follows:

$$q_{wk} = Q_w \frac{WI_k (\lambda_o + \lambda_w)_k}{\sum\limits_{k=1}^{K} \left[WI_k (\lambda_o + \lambda_w)_k \right]} \qquad (4.29)$$

It is important that the allocation of injection fluids be based on total mobilities, and not simply injected fluid mobility. This is necessary for the following reason. If an injector is placed in a block where the relative permeability to the injected fluid is zero, then using the injection fluid mobility would prohibit fluid injection, even though a real well would allow fluid injection into a block containing oil and irreducible water. To avoid these unrealistic cases, the total mobility of the block should be used. For most cases, the error in this method only persists for a few time steps. The mobile fluid saturation in the block will be dominated by the injected fluid after these few steps (Fanchi et al., 1982).

Case 4-Bottomhole Well Pressure Specified

In this case, the source/sink terms in the fluid flow equations are:

$$q_{ok} = PID \left(\lambda_o\right)_k^{n+1} \left(p_\alpha^{n+1} - p_{wf}\right) \qquad (4.30)$$

where

$$PID = PI, \ p_\alpha^{n+1} > p_{wf} \text{ for a producer}$$

and

$$PID = WI, \ p_\alpha^{n+1} < p_{wf} \text{ for a injector}$$

Thus, the source/sink terms, q_{ok}, can be replaced by an implicit pressure term.

4.1.3.2 Automatic Time Step Selection

Two options for time step size control are implemented in UTDUAL: manual and automatic time step size selections. Proper selection of time step size will ensure stability of the solution and acceptable truncation errors. Manual selection during a simulation study can be frustrating, particularly when well rates change drastically during a simulation run.

82

Since UTDUAL is an implicit simulator, theoretically it is unconditionally stable. However, to ensure acceptable truncation errors, the following algorithm is implemented for the automatic time step size selection (Aziz and Settari, 1979):

1. Input maximum allowable pressure and saturation changes over a time step: Δp_{lim} and ΔS_{lim}.

2. Compute

$$\Delta S_{max}^n = \max\left(\left|\Delta_t S_{ijk}^n\right|\right) \qquad (4.31a)$$

$$\Delta p_{max}^n = \max\left(\left|\Delta_t p_{ijk}^n\right|\right) \qquad (4.31b)$$

3. Calculate Δt^{n+1} as

$$\Delta t^{n+1} = \min\left(\Delta t_s, \Delta t_p\right) \qquad (4.32)$$

where,

$$\Delta t_s = \Delta t^n \frac{\Delta S_{lim}}{\Delta S_{max}^n}$$

and

$$\Delta t_p = \Delta t^n \frac{\Delta p_{lim}}{\Delta p_{max}^n}$$

4. After time step $n + 1$ is completed, calculate Δp_{max}^{n+1} and ΔS_{max}^{n+1}. The step is accepted if:

$$\Delta p_{max}^{n+1} \leq C_1 \Delta p_{lim} \qquad (4.33a)$$

$$\Delta S_{max}^{n+1} \leq C_2 \Delta S_{lim} \qquad (4.33b)$$

where C_1 and C_2 are constants greater than one. Otherwise, calculate Δt^* as:

$$\Delta t^* = \min\left(\Delta t_s, \Delta t_p\right) \qquad (4.34)$$

where

$$\Delta t_s = \Delta t^{n+1} \frac{\Delta S_{lim}}{\Delta S_{max}^{n+1}}$$

and

$$\Delta t_p = \Delta t^{n+1} \frac{\Delta p_{lim}}{\Delta p_{max}^{n+1}}$$

Set Δt^{n+1} to Δt^* and resolve the equations for time step $n+1$.

This algorithm will maintain pressure and saturation changes close to Δp_{lim} and ΔS_{lim}, but will not exceed $C_1 \Delta p_{lim}$ or $C_2 \Delta S_{lim}$.

4.1.3.3 Material Balance

In UTDUAL, two levels of material balance calculations are performed. The first level is differential material balance calculation. The volumes of oil and water in place at the beginning of a time step are compared to their respective values at the end of the time step with injected and produced fluids, being taken into account. The percentage change over the time step is calculated for each phase. The second level is cumulative material balance. This calculation compares the initial amount of oil and water to their respective values at the end of the time step, considering cumulative production.

4.1.3.4 Solvers

In UTDUAL, the linear system of equations (Eq. 4.19) can be solved by one of two solvers: an iterative, the bi-conjugate gradient method by Oppe *et al.* (1988), or a direct symbolic factorization of Gaussian Elimination by Cotner (1990). Details of this method can be found in Woo *et al.* (1973).

4.1.3.5 Vertical Equilibrium Capillary Pressure Curves

Laboratory rock capillary pressure (P_c) curves reflect the relationship between capillary pressure and saturation at a point (e.g. the gridblock center). The vertical equilibrium (VE) (1971) curve relates P_c at the point to the average saturation over the entire gridblock height encompassing the point. The VE capillary pressure curve can be obtained be integrating the laboratory curve over a capillary pressure increment equal to the product of block height times water-oil density difference. Thus each gridblock has a different VE capillary pressure curve, and the curve changes with time reflecting changes in fluid densities.

Coats (1989) and Coats *et al.* (1971) have extensively studied the effects that VE capillary pressure curves have on initialization and simulation results. In the equilibration of reservoirs having initial water-oil contacts, the VE capillary pressure curves give the exactly correct initial volumes in places while use of rock capillary pressure curves result in errors in these quantities which increase with the ratio of block thickness to transition zone thickness increases. Under dynamic conditions, the VE capillary pressure curves reflect the underlying equilibrium state without assuming that the dynamic fluid distribution is segregated, or, in any sense, in equilibrium (coats, 1989).

In the dual porosity case, the capillary pressure is usually assumed to be zero in fractures. The VE capillary pressure for each fracture gridblock can easily be derived.

Fluid potentials for the oil and water phases are defined as

$$\Phi_{of} = P_{of} - z\, \gamma_o \tag{4.35a}$$

and

$$\Phi_{wf} = p_{wf} - z\,\gamma_w \tag{4.35b}$$

Since potentials are equal at equilibrium, differentiating Eq. 4.35 with respect to z gives

$$\frac{dP_{cf}}{dz} + (\gamma_w - \gamma_o) = 0 \tag{4.36a}$$

The integration of Eq. 4.36a over gridblock thickness, assuming fluid segregation, gives the VE capillary pressure:

$$\widetilde{P}_{cf} = (1 - 2\,S_{wf})(\gamma_w - \gamma_o)\frac{h}{2} \tag{4.36b}$$

This fracture VE capillary pressure curve is used for equilibration and interblock flow and plays no role in matrix/fracture transfer calculations.

4.1.4 Decoupling Method

In this section, a mathematical method for decoupling the fracture equation from the matrix equation is described using single-phase flow as an example. This numerical technique was first used by Douglas *et al.* (1989) to simulate two-phase, incompressible fluid flow in a dual porosity system. This formulation requires that the matrix flow equation in finite-difference form be linear over a time step. To demonstrate the concept, the following assumptions are made for the single phase finite-difference equations: (a) diffusivities are constant, and (b) the gravity is negligible. With these assumptions, the finite-difference equations for a slightly compressible, single-phase dual porosity model are

Fracture equation:

$$\Delta T_f \Delta p_f^{n+1} = \frac{(\phi\,\mu\,c_t)_f}{k_f}\frac{V_b}{\Delta t}\Delta_t p_f + \tau_{m\text{-}f} \tag{4.38}$$

Matrix equation for each fracture grid:

$$\Delta T_m \Delta p_m^{n+1} = \frac{(\phi\,\mu\,c_t)_m}{k_m}\frac{V_{bm}}{\Delta t}\Delta_t p_m \tag{4.39}$$

with a pressure continuity boundary condition:

$$p_m^{n+1} = p_f^{n+1} \tag{4.40}$$

The transfer flow term, $\tau_{m\text{-}f}$, is calculated as

$$\tau_{m\text{-}f} = NM\sum_{l=1}^{N_b} T_{m\text{-}f\,l}\left(p_{m\,l}^{n+1} - p_f^{n+1}\right) \tag{4.41}$$

85

where NM is the total number of matrix blocks within a fracture gridblock, and N_b is the number of matrix grids which have surfaces exposed to fractures. The T_{m-f1} are the transmissibilities depending on the matrix subgrid geometry. T_{m-f1} is not pressure-dependent in this case.

One obvious way to solve Eqs. 4.38 and 4.39 coupled by Eq. 4.41 is to solve them simultaneously. This approach may require large computer resources, especially for multiphase flow problems. Alternatively, the matrix equation can be decoupled from the fracture equation by recognizing that Eq. 4.39 is linear in p_m^{n+1}. Equation 4.39 can be solved by finding a particular solution without satisfying of Eq. 4.40, and then adding a solution to the problem not containing the term p_m^{n+1}, but satisfying the boundary conditions. Therefore, the matrix equations can be solved by the following two steps.

First, solve for p_m^{n+1} from:

$$\Delta T_m \Delta \bar{p}_m^{n+1} = \frac{(\phi \mu c_t)_m}{k_m} \frac{V_{bm}}{\Delta t} \Delta_t \bar{p}_m \qquad (4.42)$$

with boundary condition given by:

$$\bar{p}_m^{n+1} = p_f^0 \qquad (4.43)$$

and then solve for $\tilde{p}_m^{n+1}$ satisfying:

$$\Delta T_m \Delta \tilde{p}_m^{n+1} = \frac{(\phi \mu c_t)_m}{k_m} \frac{V_{bm}}{\Delta t} \tilde{p}_m^{n+1} \qquad (4.44)$$

with boundary condition:

$$\tilde{p}_m^{n+1} = 1 \text{ at boundary} \qquad (4.45)$$

Both of these problems can be solved without knowing p_f^{n+1}. Clearly, we have

$$p_m^{n+1} = \bar{p}_m^{n+1} + \left(p_f^{n+1} - p_f^0\right) \tilde{p}_m^{n+1} \qquad (4.46)$$

It is simple to show that the solutions of Eqs. 4.42 and 4.44 with Eq. 4.46 satisfy Eqs. 4.39 and 4.40. However, p_m^{n+1} cannot be obtained without knowing p_f^{n+1} from the fracture equations.

In terms of $\bar{p}_m^{n+1}$ and $\tilde{p}_m^{n+1}$, the matrix/fracture transfer rates (Eq. 4.41) can be expressed as

$$\tau_{m-f} = NM \sum_{i=1}^{N_b} T_{m-fi} \left[p_f^{n+1}\left(\tilde{p}_{mi}^{n+1} - 1\right) + \bar{p}_{mi}^{n+1} - p_f^n \tilde{p}_{mi}^{n+1}\right] \qquad (4.47)$$

For time level $n+1$, the only unknown in Eq. 4.47 is p_f^{n+1}. Substituting this into the fracture equation (Eq. 4.38) results in a fracture equation with fracture unknowns only, which can be solved implicitly. In summary, solving the coupled fracture and matrix equations can be done by solving two small systems (Eqs. 4.42 and 4.44) once. Equation 4.38 can then be solved with Eq. 4.47 without knowing the matrix pressures at the new time level. After the fracture pressures are known, the matrix pressures can be updated according to Eq. 4.46. As noted, the key to this decoupling approach is that the matrix equations are linear over a time step. The fracture equations, however, do not necessarily have to be linear. If the fracture equation is nonlinear, iterations are required.

4.1.5 IMPES Formulation for Matrix Blocks

In this section, the first of the three options of matrix/fracture transfer flow calculations is described. This method involves the subgridding of matrix blocks and solving the resulting finite-difference equations using an IMPES method. The equations are first derived in terms of flow potentials following the formulations used in BOAST simulation model (Fanchi *et al.*, 1982) since in this formulation no iterations are required to solve the pressure equations. A subgrid system is described followed by a derivation of the finite-difference equations. The decoupled equations are also described.

4.1.5.1 Fluid Flow Equations

The two-phase flow equations in terms of flow potentials can be written for each phase as

$$\nabla \cdot \left[\lambda_{\alpha m} \nabla \Phi_{\alpha m} \right] = \frac{\partial}{\partial t} \left(\phi \frac{S_\alpha}{B_\alpha} \right)_m \tag{4.48}$$

where the phase potentials are defined as

$$\Phi_{\alpha m} = p_{\alpha m} - \gamma_{\alpha m} z_m \tag{4.49}$$

No source or sink terms are included in the above equations since wells are assumed to be connected only to the fracture system.

The derivation of the finite-difference equation for this IMPES formulation follows Fanchi *et al.* (1982). The right-hand sides of Eq. 4.48 can be expanded for each phase as:

$$\frac{\partial}{\partial t} \left(\phi \frac{S_\alpha}{B_\alpha} \right)_m = \left(\phi \frac{S_\alpha}{B_\alpha} \right)_m \left[\frac{1}{\phi} \frac{d\phi}{dp_\alpha} - \frac{1}{B_\alpha} \frac{dB_\alpha}{dp_\alpha} \right]_m \frac{\partial p_{\alpha m}}{\partial t} + \frac{\phi_m}{B_{\alpha m}} \frac{\partial S_{\alpha m}}{\partial t} \tag{4.50}$$

Multiplying the oil equation by B_o and adding the water equation multiplied by B_w yields

$$B_{om} \frac{\partial}{\partial t} \left(\phi \frac{S_o}{B_o} \right)_m + B_{wm} \frac{\partial}{\partial t} \left(\phi \frac{S_w}{B_w} \right)_m = \left(\phi c_t \right)_m \frac{\partial p_{om}}{\partial t} \tag{4.51}$$

where c_t is the total compressibility defined as

$$c_{tm} = S_{om} c_{om} + S_{wm} c_{wm} + c_{rm} \tag{4.52}$$

87

In Eq. 4.52, c_o, c_w, and c_r are the oil, water, and rock compressibilities, respectively, and are defined as follows:

$$c_{\alpha m} = -\frac{1}{B_{\alpha m}} \frac{dB_{\alpha m}}{dp_{\alpha m}},$$ (4.53)

and

$$c_{rm} = \frac{1}{\phi_m} \frac{d\phi_m}{dp_{om}}$$ (4.53c)

Finally, the final equation can be derived by multiplying Eq. 4.48 for oil by B_o and adding Eq. 4.48 for water multiplied by B_w:

$$B_{om} \nabla \cdot \left[\lambda_{om} \nabla \Phi_{om}\right] + B_{wm} \nabla \cdot \left[\lambda_{wm}\left(\nabla \Phi_{om} - \nabla \Phi_{cowm}\right)\right] = \left(\phi c_e\right)_m \frac{\partial \Phi_{om}}{\partial t}$$ (4.54)

where Φ_{cowm} accounts for the interplay of capillary pressure and gravitational forces, and is given by

$$\Phi_{cowm} = P_{cowm} + \left(\gamma_{wm} - \gamma_{om}\right) z_m$$ (4.55)

and

$$c_{em} = \frac{c_{rm}}{1 - \gamma_{om} z_m c_{om}}$$ (4.56)

The initial condition for matrix blocks is simply uniform phase potentials throughout. Initial saturations are determined according to gravity/capillary pressure equilibrium.

The boundary condition for matrix blocks is continuity of flow potentials between matrix blocks and fractures:

$$\Phi_{\alpha m} = \Phi_{\alpha f}$$ (4.57)

which also leads to capillary potential continuity:

$$\Phi_{cowm} = \Phi_{cowf}$$ (4.58)

4.1.5.2 Subgrid System

Before deriving the finite-difference equations for matrix blocks, the subgrid system will be described. In the discussion of the decoupling method (section 4.4), there are no specific requirements as to how matrix blocks are discretized. In fact, the only requirement is that the matrix equations be linear over a time step.

We adopted Beckner *et al.* (1991) approach to discretize parallelepiped matrix blocks into rectangular rings and layers as shown in Fig. 4.4. The lateral subgrid system

is similar to the MINC (multiple interacting continua) approach (Pruess and Narasimhan, 1985; Wu and Pruess, 1986). In the vertical direction, matrix blocks are sliced into layers. In the lateral direction, the model partitions a matrix block into subgrids in such a way that interfaces between volume elements in the block are parallel to the nearest fracture. This choice of gridding assumes that the equipotential surfaces are characterized by having a constant distance from the nearest fracture. This subgrid model in the lateral direction is adequate for modeling uniform boundary problems, which is normally the case in a fracture gridblock. Subgrids in the vertical direction are designed to model gravitational effects. This approach also models fluid segregation in surrounding fractures by imposing different boundary conditions at different elevations. Therefore, a three-dimensional problem is modeled by a two-dimensional problem to reduce computer resources while at the same time maintaining adequate accuracy.

4.1.5.3. Finite-Difference Equations

The basic assumptions are those of a standard IMPES model (Chen, 1993). However, in this formulation, iterations are not required since all coefficients are evaluated at the old time level. Using the sub-grid system described above, detailed transmissibility calculations, especially those related to geometry, are described as follows.

The discretized matrix equations can be written as:

$$
\left\{ \left[B_o \, \Delta TH_o + B_w \, \Delta TH_w \right]_m^n \Delta \Phi_{om}^{n+1} \right\}_{jk} + \left\{ \left[B_o \, \Delta TV_o + B_w \, \Delta TV_w \right]_m^n \Delta \Phi_{om}^{n+1} \right\}_{jk}
$$
$$
= C_{owm\,jk}^n + \left(\phi \, c_e \right)_{m\,jk}^n \frac{V_{bm\,jk}}{5.615 \, \Delta t} \Delta_t \Phi_{om\,jk}
\tag{4.59}
$$

TH_α and TV_α are the horizontal and vertical transmissibilities, respectively. For flow between matrix subgrids, one-point upstream weighting is used:

$$
TH_{\alpha\,j+1/2\,k} = TH_{j+1/2\,k} \left[\omega_{m\alpha} \left(\frac{k_r}{\mu\,B} \right)_{m\alpha\,j+1\,k} + (1 - \omega_{m\alpha}) \left(\frac{k_r}{\mu\,B} \right)_{m\alpha\,jk} \right]
\tag{4.60}
$$

For flow between the matrix block surfaces and fractures, the transmissibilities are defined by

$$
TH_{m\text{-}f\,\alpha} = S_{wf}\,TH_{m\text{-}f} \left[\omega_{m\text{-}f\,\alpha} \left(\frac{k_r}{\mu\,B} \right)_{m\,\alpha\,N_{sub}-1} + (1 - \omega_{m\text{-}f\,\alpha}) \frac{k_{m\,ro}(S_{m\,wf})}{(\mu\,B)_{m\,\alpha\,N_{sub}}} \right]
\tag{4.61}
$$

where $TH_{m\text{-}f}$ is the geometrical part of the transmissibility. The modification by S_{wf} is for the partial coverage of a matrix by water in the fracture (Thomas et al., 1983). $\omega_{m\text{-}f\alpha}$ is the upstream weighting factor. $\omega_{m\text{-}f\alpha}$ is equal to one for flow from matrix to fracture, and normal matrix mobility is used. $\omega_{m\text{-}f\alpha}$ is equal to zero for flow from fracture to matrix, and relative permeability is evaluated at S_{mwf}. In the vertical direction, the transmissibilities $TV_{m\text{-}f\alpha}$ are calculated similarly.

The first term on the right-hand side of Eq. 4.59, C_{owm}, is due to capillarity and gravity:

$$C_{owm} = \left[B_w \, \Delta TH_w \, \Delta\Phi_{cow} + B_w \, \Delta TV_w \, \Delta\Phi_{cow} \right]_m \tag{4.62}$$

The boundary conditions for Eq. 4.59 can be obtained by requiring matrix/fracture potential continuity along the matrix surfaces:

$$\Phi_{om}^{n+1} = \Phi_{of}^{n+1} \tag{4.63}$$

where Φ_{of} is the fracture potential. Since fluid equilibrium is assumed within a fracture gridblock, fracture potentials are constant along the matrix surfaces. This is another reason why the matrix equations are expressed in terms of potentials rather than pressures.

Once the potentials for matrix subgrids are known, water and oil saturations for each subgrid can be calculated according to the following equations:

Water saturation:

$$\frac{V_{bm\,jk}}{5.615 \, \Delta t} \left[\left(\frac{\phi}{B_w} \right)^{n+1} S_w^{n+1} - \left(\frac{\phi}{B_w} \right)^n S_w^n \right]_{m\,jk} = \left\{ \left[\Delta TH_w + \Delta TV_w \right]^n \Delta\Phi_w^{n+1} \right\}_{m\,jk} \tag{4.64}$$

Oil saturation:

$$S_{o\,m\,jk}^{n+1} = 1 - S_{w\,m\,jk}^{n+1} \tag{4.65}$$

The matrix/fracture fluid transfer rates can be computed from:

$$\begin{aligned}
\tau_{m\text{-}f\,\alpha} = NM \sum_{j=1}^{N_{sub}} TV_{m\text{-}f\,\alpha\,j\,1/2} \left(\Phi_{m\,\alpha\,j1}^{n+1} - \Phi_{\alpha f}^{n+1} \right) \\
+ NM \sum_{j=1}^{N_{sub}} TV_{m\text{-}f\,\alpha\,j\,M_{sub}+1/2} \left(\Phi_{m\,\alpha\,jM_{sub}}^{n+1} - \Phi_{\alpha f}^{n+1} \right) \\
+ NM \sum_{k=1}^{M_{sub}} TH_{m\text{-}f\,\alpha\,N_{sub}+1/2\,k} \left(\Phi_{\alpha\,m\,N_{sub}k}^{n+1} - \Phi_{\alpha f}^{n+1} \right)
\end{aligned} \tag{4.66}$$

where NM is number of matrix blocks in a fracture gridblock, and N_{sub} and M_{sub} are the number of subgrids in the lateral and vertical directions, respectively. The first term on the right-hand side of Eq. 4.66 represents the summation of matrix/fracture flow through the top face of a block. Similarly, the second term is the summation of matrix/fracture flows through the bottom faces, and the last term is for the four vertical faces of each layer.

4.1.5.4 Geometrical Part of Transmissibilities

As discussed, the subgrid geometry reduces a three-dimensional problem to a two-dimensional problem (see Fig. 4.4). Therefore, the formulations for the lateral transmissibilities are different from those for the vertical direction. The internal subgrid

transmissibilities within the matrix blocks are slightly different from those between matrix subgrids and fractures.

Figures 4.5 and 4.6 show the subgrid indices and dimensions for the lateral and vertical directions, respectively. In UTDUAL, the input data required are the matrix block dimensions (L_x, L_y, and L_z), the number of subgrids in the lateral and vertical directions (N_{sub} and M_{sub}), and volume fraction (f_j) of each subgrid in the lateral direction.

The volume fraction, f_{jk}, for the jth ring and kth layer is defined by

$$f_{jk} = \frac{L_{x\,jk}\, L_{y\,jk}\, h_k}{V_{b\,m}}\, j = 1, ..., N_{sub} \tag{4.67}$$

where V_{bm} is the bulk volume of the matrix block. We have:

$$\sum_{j=1}^{N_{sub}} f_{jk} = 1, k = 1, ..., M_{sub} \tag{4.68}$$

From Eqs. 4.67 and 4.68, the dimensions for each subgrid can be computed by

$$L_{x\,j+1/2k} = L_x \left[\sum_{i=1}^{j} f_{ik} \right]^{1/2} k = 1, ..., M_{sub} \tag{4.69a}$$

and

$$L_{y\,j+1/2k} = L_y \left[\sum_{i=1}^{j} f_{ik} \right]^{1/2} k = 1, ..., M_{sub} \tag{4.69b}$$

The geometrical part of the transmissibilities for subgrid jk in the lateral direction can be calculated as:

$$TH_{j+1/2k} = 8 \times 0.001127 \left(\frac{L_{yjk}\, h_k\, k_{xj+1/2k}}{L_{x\,j+1k} - L_{x\,jk}} + \frac{L_{xjk}\, h_k\, k_{yj+1/2k}}{L_{y\,j+1k} - L_{y\,jk}} \right) \tag{4.70a}$$

For the innermost subgrid:

$$TH_{1/2k} = 4 \times 0.001127 \left(\frac{L_{y1/2k}\, h_k\, k_{1/2k}}{L_{x1/2k}} + \frac{L_{x1/2k}\, h_k\, k_{y1/2k}}{L_{y1/2k}} \right) \tag{4.71b}$$

For the outmost subgrid, N_{sub} (i.e., between the matrix subgrid and fractures):

$$TH_{N_{sub}k} = 8 \times 0.001127 \left(\frac{L_{yN_{sub}k}\, h_k\, k_{xN_{sub}k}}{L_x - L_{xN_{sub}-1k}} - \frac{L_{xN_{sub}k}\, h_k\, k_{yN_{sub}k}}{L_y - L_{yN_{sub}-1k}} \right) \tag{4.71c}$$

in which fracture aperture is assumed negligible.

The geometrical part of the internal subgrid transmissibilities in the vertical direction are relatively simple (Fig. 4.6):

$$TV_{jk+1/2} = 0.001127 \frac{2 f_j L_x L_y k_{myk+1/2}}{h_{k+1} + h_k} \tag{4.72a}$$

For top and bottom subgrids, the transmissibilities are:

$$TV_{j1/2} = 0.001127 \frac{2 f_j L_x L_y k_{my1/2}}{h_1} \tag{4.72b}$$

and

$$TV_{jM_{sub}+1/2} = 0.001127 \frac{2 f_j L_x L_y k_{myM_{sub}}}{h_{M_{sub}}} \tag{4.72c}$$

Again, in Eqs. 4.72a and 4.72b, fracture aperture is assumed to be negligible compared to $h_k/2$.

4.1.5.5 Decoupled Equations

Equation 4.59 can be rewritten in the form of a linear system of equations:

$$TT_{jk} \Phi_{om\,jk-1}^{n+1} + TI_{jk} \Phi_{om\,j-1k}^{n+1} + TC_{jk} \Phi_{om\,jk}^{n+1} + TO_{jk} \Phi_{om\,j+1k}^{n+1} + TB_{jk} \Phi_{om\,jk+1}^{n+1}$$
$$= C_{cow}^n + \left(\phi\, c_e\right)_{jk}^n \frac{V_{mb\,jk}}{5.615\,\Delta t}\left(\Phi_{om\,jk}^{n+1} - \Phi_{om\,jk}^n\right) \tag{4.73}$$

where

$$TC = -TI - TT - TB - TO \tag{4.74}$$

The transmissibilities, TI, TT, TB, and TO, can be computed by

$$TT_{jk} = B_{om\,jk}^n TV_{o\,jk-1/2}^n + B_{wm\,jk}^n TV_{w\,jk-1/2}^n , \tag{4.75a}$$

$$TB_{jk} = B_{om\,jk}^n TV_{o\,jk+1/2}^n + B_{wm\,jk}^n TV_{w\,jk+1/2}^n, \tag{4.75b}$$

$$TI_{jk} = B_{om\,jk}^n TH_{o\,j-1/2k}^n + B_{wm\,jk}^n TH_{w\,j-1/2k}^n, \tag{4.75c}$$

$$TO_{jk} = B_{om\,jk}^n TH_{o\,j+1/2k}^n + B_{wm\,jk}^n TH_{w\,j+1/2k}^n \tag{4.75d}$$

Since the coefficients in Eq. 4.73 are treated explicitly, the decoupling idea discussed in Section 4.4 can be applied to solve for the matrix variables. The following two systems of equations can be solved independent of the fracture potential or saturations at the new time level:

92

$$TT_{jk} \overline{\Phi}_{om\,jk-1}^{n+1} + TI_{jk} \overline{\Phi}_{om\,j-1k}^{n+1} + TC_{jk} \overline{\Phi}_{om\,jk}^{n+1} + TO_{jk} \overline{\Phi}_{om\,j+1k}^{n+1} + TB_{jk} \overline{\Phi}_{om\,jk+1}^{n+1} \tag{4.76}$$
$$= C_{cow}^{n} + \left(\phi\,c_{e}\right)_{jk}^{n} \frac{V_{mb\,jk}}{5.615\,\Delta t} \left(\overline{\Phi}_{om\,jk}^{n+1} - \Phi_{om\,jk}^{n}\right)$$

with boundary conditions

$$\overline{\Phi}_{om\,jk}^{n+1} = \Phi_{of\,j}^{n} = N_{sub}, k = 1,...,M_{sub} \tag{4.77}$$

$$j = 1, N_{sub}, k = 1, M_{sub}$$

and

$$TT_{jk} \widetilde{\Phi}_{om\,jk-1}^{n+1} + TI_{jk} \widetilde{\Phi}_{om\,j-1k}^{n+1} + TC_{jk} \widetilde{\Phi}_{om\,jk}^{n+1} + TO_{jk} \widetilde{\Phi}_{om\,j+1k}^{n+1} + TB_{jk} \widetilde{\Phi}_{om\,jk+1}^{n+1} \tag{4.78}$$
$$= \left(\phi\,c_{e}\right)_{jk}^{n} \frac{V_{mb\,jk}}{5.615\,\Delta t} \left(\widetilde{\Phi}_{om\,jk}^{n+1}\right)$$

with

$$\widetilde{\Phi}_{om\,jk}^{n+1} = 1j = N_{sub}, k = 1,...,M_{sub}$$

$$j = 1, N_{sub}, k = 1, M_{sub} \tag{4.79}$$

Once the fracture potentials are known, the matrix potential for each subgrid can be updated by:

$$\Phi_{om}^{n+1} = \overline{\Phi}_{om}^{n+1} + \left(\Phi_{of}^{n+1} - \Phi_{of}^{n}\right)\widetilde{\Phi}_{om}^{n+1} \tag{4.80}$$

This is hoe the matrix potential, Φ_{om}^{n+1}, is related to the fracture potential, Φ_{of}^{n+1}. Substituting Eq. 4.80 into 4.66, we arrive at equations for the matrix/fracture transfer rates ($t_{m-f\,\alpha}$) with only fracture unknowns.

4.1.6 Formulation for Matrix Subgrids Using Diffusion Equation

In this section, the second of the three options of matrix/fracture transfer flow calculations is described. This approach involves numerically solving the capillary diffusion equation for matrix blocks. The subgrid system for the IMPES method (Section 4.5) is also adopted here. The major issue is to implement physically correct boundary conditions for the matrix blocks. Partial immersion of matrix blocks is taken into account by modifying the diffusion coefficient at matrix/fracture interfaces.

4.1.6.1 General Formulation

The capillary diffusion equation in finite-difference form using the subgrid system shown in Fig. 4.4 can be easily derived as

$$TT_{jk} \, S^{n+1}_{wm \, jk-1} + TI_{jk} \, S^{n+1}_{wm \, j-1k} + TC_{jk} \, S^{n+1}_{wm \, jk} + TO_{jk} \, S^{n+1}_{wm \, j+1k} + TB_{jk} \, S^{n+1}_{wm \, jk+1}$$ (4.81)

$$= \frac{\phi_m \, V_{mb \, jk}}{5.615 \, \Delta t} \left(S^{n+1}_{wm \, jk} - S^{n}_{wm \, jk} \right)$$

where TC is the summation of TT, TI, TO, and TB. Calculation of these coefficients is fairly straightforward, for example, TT can be computed by

$$TT_{jk} = TV_{jk-1/2} \, D(S_{wm})_{jk-1/2}$$ (4.82)

The remaining coefficients, TI, TO, TB, can be calculated similarly. The geometrical parts of the transmissibilities are exactly the same as those given by Eqs. 4.70 through 4.72. In Eq. 4.82, $D(S_{wm})_{jk-1/2}$ is computed by

$$D(S_{wm})_{jk-1/2} = \frac{k_{rom \, jk-1/2}}{\mu_{om}} \, f_{w \, jk-1/2} \left(\frac{dP_{cowm}}{dS_{wm}} \right)_{jk-1/2}$$ (4.83)

To evaluate $D(S_{wm})_{jk-1/2}$, one-point upstream weighted relative permeability is used. Since fluid potential is not solved for, capillary pressure is used instead to determine the upstream weighting.

The initial condition for matrix blocks is fairly simple. If a matrix subgrid is below the oil-water contact, the subgrid has a water saturation of one. For those subgrids above the oil-water contact, the water saturation is distributed according to capillary pressure.

The physically correct boundary condition for matrix blocks is potential continuity, which results in water saturation equal to $1 - S_{or}$ ($= S_{wJ}$) at the matrix/fracture interface if no capillarity is assumed for fractures:

$$S_{wm \, jk} = S_{wm \, 1j} = N_{sub}, \, k = 1,...., \, M_{sub}$$

$$j = 1, \, N_{sub}, \, k = 1, \, M_{sub}$$ (4.84)

To take the partial immersion of matrix blocks into account, the diffusion coefficient at matrix block surfaces is modified by S_{wf}:

$$D_{m-f \, jk} = S_{wf \, k} \, D(S_{wm})_{jk}$$ (4.85)

where $S_{wfk} = S_{wf}$ if no fluid segregation is assumed in the fractures. Details of the S_{wfk} calculations due to fluid segregation in fractures will be given later in this section. Verification of the modified diffusion coefficient will be described in Section 4.10, where the results of modeling an ideal fractured reservoir are described.

Matrix/fracture transfer flow rates can be computed by:

$$\tau_{w\,m\text{-}f} = NM\,S_{wf1}\sum_{j=1}^{N_{sub}} D(S_{wm})_{j1/2}\frac{S_{wmJ} - S_{wmj1}}{h_1/2}$$

$$+ NM\,S_{wfM_{sub}+1}\sum_{j=1}^{N_{sub}} D(S_{wm})_{jM_{sub}+1/2}\frac{S_{wmJ} - S_{wmjM_{sub}}}{h_{M_{sub}}/2}$$

$$+ NM\sum_{k=1}^{M_{sub}} S_{wf\,k}D(S_{wm})_{N_{sub}+1/2k}\frac{S_{wmJ} - S_{wmN_{sub}-1}}{h_k/2}$$

(4.86)

The three terms on the right-hand side of Eq. 4.86 are for matrix/fracture transfer flow through top, bottom, and vertical faces, respectively. Specifics about the implicitness of the diffusion coefficients are presented in the following two sections.

4.1.6.2 Explicit Diffusion Coefficient

The easiest way to solve Eq. 4.81 with boundary conditions given by Eq. 4.84 is to evaluate $D(S_{wm})$ at the old time level. Subsequently, we have a linear system of equations with $(N_{sub} \times M_{sub})$ unknowns, which can be solved easily. No iterations are necessary if S_{wf} at the old time level is used in the $D(S_{wm})_{m\text{-}f}$ calculations. Otherwise, iterations are required.

In order to ensure stability, this option of solving diffusion equation require somewhat smaller time step sizes compared to those of the implicit method described below.

4.1.6.3 Implicit Diffusion Coefficient

A more stable approach is to implicitly solve Eq. 4.81 using the Newton-Raphson method. Equation 4.81 can be rewritten in terms of residuals:

$$R(S_{wm}) = 0 \tag{4.87}$$

where R and S_{wm} are arrays with $N_{sub} \times M_{sub}$ elements. Applying the Newton-Raphson method to Eq. 4.87, we have the following linear system of equations:

$$\Delta S_{wm} = J^{-1}\,R(S_{wm}^c) \tag{4.88}$$

where J is the Jacobian matrix. Each element of J is evaluated as:

$$J_{ij} = \frac{\partial R_i}{\partial S_{wm\,j}} \tag{4.89}$$

Since the number of subgrids used for matrix blocks is usually small to moderate, a direct solver is preferred to solve Eq. 4.88.

4.1.6.4 Gravitational Effect

Compared to capillary pressure, the gravitational effects are normally small in a oil/water countercurrent imbibition process (Chen, 1993). However, gravity has a larger effect on the fluid segregation within fractures, which consequently affects the oil/water imbibition through the boundary conditions.

The first option in UTDUAL is to assume that oil and water in the fracture system are dispersed and that there is no sharp fluid interface within the fracture grid. Therefore, all surface subgrids experience the same imbibition process, and only one value of fracture water saturation is needed in Eqs. 4.85 and 4.86.

The second option is that fluid segregation is assumed to occur in the fracture system and that there exists a sharp fluid interface within the fracture. To implement this option, we first calculate the oil-water contact in a fracture gridblock:

$$h_{woc} = S_{wf} L_z \tag{4.90}$$

The water saturation in a fracture at an elevation corresponding to a matrix subgrid can be determined by:

$$S_{wfk} = \begin{cases} 1 & L_z - \sum_{j=1}^{k} h_j > h_{woc} \\ 0 & L_z - \sum_{j=1}^{k} h_j < h_{woc} \end{cases} \tag{4.91}$$

With this option, surface subgrids in the vertical direction experience a different imbibition processes, and imbibition takes place only in those subgrids below the oil-water contact.

4.1.7 Results from Single Matrix Block Studies

In UTDUAL, the third option of calculating matrix/fracture transfer flow is to incorporate the results from single matrix block studies. The motivation to this approach is that any single porosity simulator can easily be modified to model a dual porosity system, and very accurate results (analytical or numerical) can be obtained from single matrix block studies. Details of this option are described in this section.

In Chapter 3, the average water imbibition into a matrix block under totally immersed condition is analyzed in terms of elapsed time. Two flow periods are identified to characterize the imbibition process. To incorporate these flow characteristics into UTDUAL, the average water imbibition rate is instead expressed in terms of average water saturation in the matrix block:

$$u_{w\,m\text{-}f} = f(S_{wm\,ave}) \tag{4.92}$$

To account for the partial immersion of a matrix block, $u_{wm\text{-}f}$ is corrected by S_{wf}:

$$\tau_{w\,m\text{-}f} = NM\, A_{m\text{-}f}\, S_{wf}\, f(S_{wm\,ave}) \tag{4.93}$$

where $A_{m\text{-}f}$ is the total surface area of a matrix block exposed to fracture flow.

Additional flow rate due to compressibility can be calculated by assuming that the matrix pressure changes at the same rate as that in the fracture. In other words, instantaneous pressure equilibrium between matrix blocks and fracture is assumed. Dutra and Aziz (1991) calculated the time required to reach pressure equilibrium to be less than a minute for a matrix block with dimension of 10 ft, compressibility of 10^{-5} psi^{-1}, porosity of 0.30, permeability of 10 md, and fluid viscosity of 1.0 cp. For most simulation purposes, this can be considered instantaneous.

4.1.8 Model Verification

In this section, several test cases are shown to verify the mathematical formulations derived earlier in this chapter. These cases are also used to ensure the correctness of coding. The first case is the Buckley-Leverrett (1942) problem. This case is to ensure the accuracy of the single porosity part of UTDUAL. For a single phase problem, the results of UTDUAL are compared with Warren and Root's (1963) analytical solution in which pseudosteady-state matrix/fracture transfer flow is assumed. The new transient solution developed in Appendix D is also used to test UTDUAL for the accuracy of the subgrid geometry for transient flow in matrix blocks.

4.1.8.1 Single Porosity Waterflooding

Without capillary pressure, the one-dimensional incompressible waterflooding case is the well-known Buckley-Leverrett (1942) problem. To simulate this problem, only the fracture system of UTDUAL is used. Table 4.1 lists the input data for the simulation run. Figure 4.7a shows the fractional flow curve and its derivative with respect to water saturation used to generate the analytical solution. The comparison between the Buckley-Leverrett solution and the simulation results is shown in Fig. 4.7b for dimensionless time equal to 0.1 and 0.175. Using 500 gridblocks, the simulation results match the analytical solution well except at the displacement front, where numerical smearing occurs.

4.1.8.2 Warren and Root (1963) Solution

Warren and Root (1963) were first to introduce the dual porosity model to the oil industry. All subsequent models (Gringarten, 1982; Kazemi et al., 1976) for both pressure transient analyses and simulation have been modifications of this model. In Warren and Root's model, fluid flow between matrix blocks and fractures is treated by a pseudosteady-state model. A detailed derivation of this analytical solution is given in Chen (1993). In additional to permeability and skin, two parameters defined by Warren and Root to characterize transient flow in a dual porosity reservoir are called the storativity ratio (ω) and interporosity parameter (λ) defined by

$$\omega = \frac{(\phi c)_f}{(\phi c)_m + (\phi c)_f} \tag{4.94}$$

and

$$\lambda = \sigma \frac{k_m}{k_f} r_w^2 \tag{4.95}$$

where r_w is the wellbore radius. According to Eq. 4.94, ω equal to one represents that single porosity reservoir with only fracture properties, and zero with only matrix properties. The value of λ is usually very small because k_m is usually several orders of magnitude smaller than k_f. Both ω and λ have large effect on the performance of a dual porosity reservoir. Figure 4.8 shows a typical pressure drawdown curve of Warren and Root's (1963) model in dimensionless space. The skin factor and wellbore storage are set to zero. As shown in Fig. 4.10, the two parallel straight lines represent the early and late time behavior of a dual porosity system. During the early flow period, only fractures affect reservoir behavior, while contributions from the matrix blocks are minimal. After a transition time, the reservoir again behaves as a single porosity reservoir with total system properties.

Table 4.2 lists the variables used in Warren and Root's pressure buildup studies. To obtain proper parameters for simulation runs, the following assumptions are made: the matrix blocks and fracture have equal compressibilities ($c_m = c_f$), and the matrix blocks have dimensions of $10 \times 10 \times 10$ ft^3. Based on these assumptions, calculated matrix and fracture porosities are listed in Table 4.3. The shape factor, σ, is calculated according to Eq. 2.10 to be 0.12 ft^{-2} and the matrix permeability is 0.0167 md from Eq. 4.95.

Figure 4.10 shows a comparison between Warren and Root's solution and the results of UTDUAL with the radial flow option. No matrix subgridding was used in order to mimic Warren and Root's model. As shown, excellent agreement is reached for storativity ratios ranging from 0 to 1. The agreement between the analytical and numerical solutions for the case of $\omega = 1$ further proves the accuracy of the single porosity part of the simulator.

4.1.8.3 New Analytical Solution

It has long been known (Gringarten, 1982) that Warren and Root's (1963) model is not capable of modeling transient flow within matrix blocks. Gringarten (Gringarten, 1982) summarized some of the analytical solutions which account for transient matrix flow within one-dimensional and spherical matrix blocks. A general form of the analytical solution for a dual porosity model with matrix blocks of any geometry is derived in Chen (1993). This solution reduces to Warren and Root's model if their assumptions are made. It can easily be proven that the solution also reduces to those of Gringarten (1982) for the same matrix geometries.

The average pressure in matrix blocks is first expressed in terms of a convolution integral between the solution of the diffusivity equation for matrix blocks with unit boundary condition and rate of the pressure change in the fractures. The diffusivity equation for a slightly compressible for the fracture system is then solved using Laplace transform. The solution is expressed in the general form for two different cases: infinite and finite reservoirs with no-flow or constant outer pressure boundary conditions. Stehfest's (1970) algorithm is used to convert the solution in Laplace space to real time.

In the case of square matrix blocks, the diffusivity equation for a matrix block with unit boundary condition is solved using separation of variables (Chen, 1993). Coupling with the general solution of the fracture equation results in a solution for an infinite reservoir with no wellbore storage and skin effects. Figures 4.10a and 4.10b ($\lambda = 10^{-3}$ and 10^{-6}) show comparisons of the dimensionless pressure drawdown between

98

Warren and Root's model and those with transient flow in square matrix blocks. The curves between $\omega = 0$ and $\omega = 0.001$ are not distinguishable because in those cases fracture storativity is extremely small and matrix transient flow dominates the early time flow period. The long transition flow period dominates the pressure drawdown curve. After a transition flow period, the reservoir behaves as a homogeneous system with the total reservoir property $[(\phi c_t)_{m+f}]$. The pressure derivative curves shown in Fig. 4.10c also support these observations.

Figure 4.11 compares the analytical solution with transient flow in matrix blocks and the results from UTDUAL. In the UTDUAL runs, the properties listed in Tables 4.2 and 4.3 are used. To model transient flow in matrix blocks, eight matrix subgrids are used. As shown in Fig. 4.11, excellent agreement between the analytical solution and that of UTDUAL is achieved. The small difference at small horner time is due to finite time step and gridblock sizes. However, these differences disappear after a very short period of time.

4.1.8.4 The Sixth SPE Comparative Solution Project

UTDUAL is also applied to the Society of Petroleum Engineers (SPE) Comparative Solution Project for the simulation of a naturally fractured reservoir, and for the case of waterflooding. This is a five-layer cross-sectional problem with 10 horizontal grids and two wells (one producer and one injector). The basic rock and fluid data are given in Firoozabadi and Thomas (1989).

Figure 4.12 shows a comparison of the results of UTDUAL and those of simulation of the participating companies. In this case, no matrix subgrid is used because the majority of the simulators used by the participating companies did not have this option. As shown in Fig. 4.12, UTDUAL's results fall within the band of the SPE results except for a small discrepancy at late time.

4.1.8.5 Comparison with Commercial Simulator, VIP-DUAL

VIP-DUAL is a black oil, dual porosity model by Western Atlas. The problem tested was Kazemi et al.'s (1976) quarter of five-spot reservoir (Section 4.10.2). Since VIP does not allow matrix subgridding, only no matrix subgridding is used in UTDUAL runs. Figures 3.13a to 3.13c show the comparisons of producing water-oil ratio and water saturation profiles (for both matrix and fracture) among three models. As expected, results are identical.

4.1.9 Simulation Studies of an Ideal Fractured Reservoir

In this section, the results of simulation studies of an ideal fractured reservoir are presented. The ideal fractured reservoir is configured in such a way that the properties of individual fractures are known. Two different methods are used in the simulation studies. The first method used is the IMPES model developed for single matrix block studies to conduct fine-grid simulations by discretizing both the fractures and matrix blocks. This study also serves as a comparison standard for verifying the dual porosity concept for modeling fractured reservoirs. The second method is to model the same reservoir using UTDUAL. Sensitivity studies describing the effects of different parameters have on fractured reservoir are also presented.

4.1.9.1 Problem Description

Figure 4.14 shows the configuration of the ideal fractured reservoir, in which two sets of fractures with known properties are orthogonal. This resembles a quarter five-spot reservoir with two wells (one injector and one producer).

Matrix blocks are assumed to be uniform throughout the whole reservoir and have dimensions of $10 \times 10 \times 10$ ft. The fracture capillary pressure is assumed to be zero, and the relative permeability curves are straight lines with zero residuals. Other reservoir data are listed in Table 4.4. All data are adopted from Beckner *et al.* (1988) except for the fracture permeability and reservoir size.

In this reservoir, 97.4% of the pore volume is in the matrix, typical of a fractured reservoir. The system is assumed to be incompressible. Therefore, the main oil recovery mechanism is countercurrent imbibition. Since the reservoir size is fairly small, the injection rate is set to 0.25 STB/D. Constant bottomhole pressure equal to the initial pressure is assigned to the production well.

4.1.9.2 Fine-Grid Simulation Results

The reservoir is first simulated using a single porosity model by discretizing both the fractures and matrix blocks (so-called fine-grid single porosity simulation). The IMPES model developed for single matrix block studies is used for this purpose. This simulation serves as a comparison standard for dual porosity results since all recovery mechanisms are taken into account. However the major disadvantage of this simulation approach is the amount of detail required, as well as a large cost in computer time.

In all fine-grid simulation runs, the fractures are only discretized in the longitudinal direction while matrix blocks are discretized into a two-dimensional grid system. Figure 4.15 illustrates a typical grid arrangement in which each matrix block is discretized into 3×3 grids.

To ensure accuracy, grid refinement studies are first conducted. The simulation result (oil recovery) is shown in Fig. 4.16 for matrix grids ranging from 1×1 to 7×7. The total number of grids used for the reservoir ranges from 121 to 1681. As shown in these figures, there is significant improvement from 121 grids to 441 grids while only small changes occur in the oil recovery between 441 and 1681 grids.

The case with a 1×1 matrix grid corresponds to a conventional dual porosity model with no matrix subgridding. Oil recovery and water cut are shown in Figs. 4.17a and 4.17b for matrix permeabilities ranging from 0.02 to 20 md. These figures demonstrate the effect that matrix permeability has on oil recovery and water breakthrough time of a fractured reservoir. These results are also used for comparing results with the dual porosity (UTDUAL) runs.

4.1.9.3 Dual Porosity Studies

The same reservoir as in the previous section with identical matrix subgridding is simulated using UTDUAL. The equivalent permeability ($\bar{k}_f$, see Table 4.4) for the fracture system is calculated using Parsons' (1966) formulation, and an equivalent porosity (ϕ_f) is computed by dividing the fracture pore volume by the reservoir bulk

volume. No modification of matrix block properties was made. In all runs, 5×5 fracture grids are used to ensure that each gridblock encompasses at least one matrix block. All three options of calculating matrix/fracture transfer flow are used.

IMPES Option

The IMPES method option to calculate matrix/fracture flow is first used to model the ideal fractured reservoir.

For the case of one matrix subgrid, UTDUAL reduces to a conventional dual porosity model. Figures 4.18a and 4.18b show comparisons of oil recovery and water cut from runs made using UTDUAL vs. fine-grid single porosity simulations for matrix permeabilities ranging from 0.02 to 20.0 md. The water saturation profiles along a line between the production well and the injection well are shown in Figs. 4.18c and 4.18d. As shown in these figures, excellent agreement between the two approaches is obtained.

Similar results are shown in Figs. 4.19a to 4.20b for runs corresponding to with 3×3 and 7×7 matrix grids in fine-grid simulations, respectively. Again, excellent agreement is achieved between runs by UTDUAL and fine-grid ones for the same level of accuracy.

Diffusion Methods

UTDUAL with the diffusion equation option is also used to model the ideal fractured reservoir. Figures 4.21a and 4.21b show comparisons between results of the IMPES option and the diffusion equation option, for cases with one and four matrix subgrids. Again, the case with one matrix subgrid corresponds to a standard dual porosity model. The case with four subgrids produces more accurate results. As shown in these figures, excellent agreement is obtained.

If saturation continuity between matrix blocks and fractures is used as the matrix boundary conditions, considerable differences in oil recovery and water cut are introduced as shown in Figs. 4.22a through 4.23b for different numbers of matrix subgrids. With this method, the water relative permeability at the matrix/fracture interface is equal to S_{wf} which is considerably smaller than k_{wm} at S_{wmj} at early time. Consequently, water imbibition rates into the matrix blocks are small, which results in earlier water breakthrough and low recovery.

Results from Single Matrix Block Studies

The third option in UTDUAL, using the results of single matrix block studies to calculate matrix/fracture transfer flow, is also applied to model the ideal fractured reservoir. Before describing the simulation results, we will examine the water saturations and matrix/fracture transfer rates calculated by UTDUAL with the capillary diffusion option. Figure 4.24a shows the fracture water saturation for each gridblock along the diagonal line connecting the injector and producer as a function of the displaceable pore volumes injected. Note that the saturation in each gridblock increases in a similar pattern. The matrix/fracture transfer rate (q_{wm-f}) in each fracture gridblock divided by the fracture water saturation (S_{wf}) in that grid versus the average water saturation in matrix blocks is shown in Fig. 4.24b. The agreement of all curves in Fig. 4.24b proves that every gridblock experiences a similar imbibition process. A comparison of the transfer rate in grid (1,1) with that of a single matrix block under totally immersed conditions is shown in Fig. 4.24c. As expected, both agree very well.

Results of the UTDUAL simulation with this option are shown in Fig. 4.25 in terms of water cut versus displaceable pore volumes injected. Two different runs with results from single matrix block studies using 40 grids are shown in this figure.

Further Results

For the rest of this section, we turn our attention to the accuracy and efficiency of UTDUAL in further modeling the same ideal fractured reservoir. The results of grid refinement studies (for subgrids ranging from 1 to 8) are shown in Figs. 4.26 to 4.27 for a matrix permeability of 2.0 md. Oil recovery and water breakthrough time converge rapidly as the number of subgrids increases. The curves for oil recovery and water cut with 4 and 8 subgrids are almost indistinguishable (Figs. 4.26 and 4.27). Note that the fine-grid simulation requires finer subgridding to achieve the same level of results as the dual porosity model.

In the fractured reservoir under consideration, each matrix block experiences three different flow periods. The first period is single phase flow before injected water reaches the matrix block. The number of matrix blocks undergoing this flow period decreases as the water front advances from the injector to the producer. The second flow period is from the time when the injected water first contacts the block surface to the time when the water front within the matrix block reaches the block center. This flow period corresponds to the infinite-acting flow period in single matrix block studies. A large number of grids is needed to obtain good accuracy. The last flow period corresponds to late flow in the matrix block. It can be observed that the water saturation within the matrix block during the late flow period changes fairly uniformly throughout the whole block. Therefore, only a small to moderate number of grids are needed to reach accurate results. The number of matrix blocks undergoing the second flow period is relatively small compared to the other two flow periods. Therefore, overall accuracy is controlled by those matrix blocks undergoing the first and third flow periods, during which only a small to moderate numbers of matrix subgrids are required.

However, matrix subgridding may still be necessary for low permeability reservoirs. Figure 4.27 shows the relative difference between UTDUAL runs with matrix subgrids and without subgrids. It is noted that the difference decreases as matrix permeability increases. For a matrix permeability of 0.02 md, the maximum error without matrix subgrids is over 30%.

As shown in Fig. 4.29, computer time increases linearly as the number of subgrids increases. Figure 4.30 shows the computer time comparison between two different options in UTDUAL. The diffusion option is about one-third faster than the IMPES option while using single matrix block results is almost as fast as single porosity simulation.

4.1.9.4 Sensitivity

In this section, we study the effects of several variables on the performance of fractured reservoirs. These variables include Coats' (1989) pseudo-capillary pressure for the fracture system, fracture porosity and permeability, matrix permeability and capillary pressure, matrix block size, matrix boundary conditions, and injection rate. The effects of some of the variables, such as matrix permeability and matrix block boundary conditions, were studied earlier. For the following studies, the base case is the ideal fractured reservoir described in Section 4.1.9.1. Two matrix subgrids are used to minimize computational cost.

Coats' (1989) pseudo-capillary pressure curve for the fracture system is used to account for phase segregation due to gravity. Figures 4.31a and 4.31b show differences with and without the pseudo-curves in terms of the oil recovery and water cut. As shown, there are no substantial differences between the two.

The effect of matrix block size on fractured reservoir performance is similar to those of matrix permeability. Since permeability and gridblock size are inversely proportional in the calculation of transmissibilities, higher recovery and later breakthrough time result from smaller matrix block sizes, as shown in Figs. 4.32a and 4.32b.

Normally, higher injection rates result in lower recovery and faster water breakthrough. These situations are more drastic in fractured reservoirs. As shown in Figs. 4.33a and 4.33b, an injection rate of 25 STB/D results in nearly instantaneous water breakthrough and a lower recovery curve. Clearly, for fractured reservoirs, low injection rate is desired to reach high oil recovery since all injected water is imbibed into matrix blocks to displace oil.

The effect of fracture porosity on reservoir performance is obvious. Higher porosity results in higher recovery and slower water breakthrough (Figs. 4.34a and 4.34b).

To study matrix capillary pressure effects on fractured reservoir behavior, the base case capillary pressure is multiplied by 10 and 0.1, which results in two different P_{cm} curves. Oil recovery and water cut with these P_{cm} curves are shown in Figs. 4.35a and 4.35b. It is obvious that higher P_{cm} results in higher oil recovery and slower water breakthrough, since more water is imbibed into matrix blocks with higher P_{cm}.

In general, to waterflood a fractured reservoir, it is desirable that the reservoir has high matrix permeability and capillary pressure, and small matrix block size. To maintain a long water-free production period, a lower injection rate is desired to ensure that all injected water is imbibed.

4.1.10 Simulation Studies of Fractured Reservoirs

In this section, the results of modeling Kleppe and Morse's (1974) waterflooding experiments on a fractured core and Kazemi *et al.* (1976) quarter five-spot reservoir are presented.

4.1.10.1 Kleppe and Morse's Experimental Data

Kleppe and Morse (1974) reported imbibition oil recovery data for a single cylindrical matrix block with an annular vertical fracture. The matrix block was 9.87 cm in diameter and 122.8 cm in height. Table 4.5 lists the rest of their data. The relative permeability and capillary pressure data in Kleppe and Morse's paper are tabulated in (Beckner *et al.*, 1987). The constant water injection rate at the bottom of the core was 3.3 and 35 cm^3/min for their low- and high-rate tests, respectively.

Kleppe and Morse's experimental data have been modeled by several researchers using either fine-grid single porosity simulation or the dual porosity models. Beckner *et al.* (1987) simulated these experiments using a single porosity simulator. Straight-line relative permeability and zero capillary pressure were assigned to fracture gridblocks. No specifics about the matrix/fracture interface condition were given. Their results agreed

well with the low-rate experimental data but showed almost none of the rate dependency necessary to match the high-rate test. Coats' (1989) fine-grid simulation results, on the other hand, showed significant rate dependency. Theoretically, the imbibition process is independent of the flow rate in the adjacent fractures as long as there is sufficient water available for imbibition. However, the availability of water in the fracture depends on the injection rate. Dual porosity models were also used by Beckner *et al.* (1988) and Coats to model the experimental data. The results did not agree with the experimental data except for the early time results of the low-rate case reported by Coats.

Before presenting the results of modeling these experiments using UTDUAL , a brief discussion of flow characteristics is in order. It is obvious that matrix/fracture transfer flow is capillary-dominated, and the gravity contribution is negligible for such a small system. If piston-like displacement (at the critical rate defined by Mattax and Kyte (1962)) in both the matrix and fracture is assumed, the water advance velocities are 0.236 cm/min (11.1 ft/D) for low injection rate case and 2.508 cm/min (118.5 ft/D) for high injection rate, respectively. These velocities would be constant before injected water breaks through at the top of the core. For the low-rate case, the velocity is close to that calculated by Coats from Kleppe and Morse's data (11.0 ft/D). However, there is a considerable difference for the high injection rate (118.5 vs. 140 ft/D calculated by Coats). The water advance velocity in the matrix block is thus lower than that in the fracture for the high-rate case. However, from the straight line of Kleppe and Morse's data (Fig. 4.36a), one could easily conclude that a stationary saturation profile is developed as the injected water progresses along the fracture for both cases. Beckner *et al.* (1987) also reached the same conclusion from single porosity modeling.

The results of UTDUAL modeling Kleppe and Morse's data are shown in Fig. 4.36a using $1 \times 1 \times 20$ fracture grids and one matrix subgrid for both the low- and high-rate cases. As shown, good agreement is reached for both cases. The slight difference between the simulation and experimental data for the high-rate case is believed to be the effect of transient flow in the matrix block. The comparison between the high-rate data and the results with two matrix subgrids is shown in Fig. 4.36b. Better agreement is achieved. Figures 4.36c and 4.36d illustrate the stationary saturation profiles from the simulation results, which agree with the observations of the experimental data (cumulative recovery from cure is a linear function of injection rate).

4.1.10.2 Modeling of Kazemi *et al.* (1976) Quarter Five-Spot Reservoir

The results of modeling Kazemi *et al.* (1976) quarter five-spot reservoir are described in this section. The matrix and fracture relative permeability and capillary pressures are given in (1976) along with the relevant fluid properties. Matrix blocks are $10 \times 10 \times 30$ ft. A total of 64 (8×8) fracture gridblocks are used with $\Delta x = \Delta y = 75$ ft. Water is injected into the fracture at 200 STB/D at the injector and oil is produced at 210 STB/D at the producer.

With one subgrid and using the dispersed fracture fluid option, the formulation of UTDUAL with the IMPES matrix option reduces to that used by Kazemi *et al.* Figures 4.37a and 4.37b show comparisons of the producing water-oil ratio and water saturation profiles (matrix and fracture) for the results of UTDUAL and Kazemi *et al.* (1976). As expected, the results are essentially identical.

The effect of matrix subgrids on this five-spot simulation is shown in Figs. 4.37c and 4.37d. There are substantial differences in the water breakthrough time and oil recovery between run with one matrix subgrid and two subgrids. However, not much

improvement is observed when increasing number of subgrids from two to four. This conclusion agrees with that made from the results of the ideal fractured reservoir in Section 4.9. This field scale modeling of fractured reservoir also suggests that matrix subgrid is absolutely necessary to accurately model matrix/fracture transfer flow, but only small to moderate number of subgrids is required.

4.1.11 Summary

A dual porosity simulator (UTDUAL) has been developed to model fluid flow in naturally fractured reservoirs. Applications of UTDUAL to this type of reservoir are also described.

UTDUAL is a two-phase, three-dimensional dual porosity simulator designed to model waterflooding in fractured reservoirs. UTDUAL can also be used to model nonfractured reservoirs without code modification. Numerous well control schemes and automatic time step selection are implemented. The simulator is largely vectorized to take advantage of vector computers such as the CRAY at the Center for High Performance Computing at the University of Texas at Austin.

Three different options were developed to model matrix/fracture transfer flow. The first option models fluid flow in matrix blocks using an IMPES method. The resulting matrix equations are mathematically decoupled from the implicit fracture equations, while implicitness between the matrix pressure and fracture variables is retained. This scheme greatly reduces the coding and computational effort. The second option employs a diffusion equation in which the primary variable is the matrix water saturation rather than pressure. The matrix equation is also decoupled from the fracture equations. For these two options, a subgrid system for matrix blocks is adopted to model a three-dimensional problem as a two-dimensional one. The third option uses the results of single matrix block studies, and is useful when such results are available. An instantaneous pressure equilibrium between matrix blocks and fracture is assumed for this option as well as for the option using the diffusion equation. These two options are most applicable for cases with high matrix permeability and/or small matrix block sizes.

This section also presented model verification results. These included the single porosity Buckley-Leverett (1942) waterflooding case, Warren and Root' (1963) single-phase dual porosity solution, and a new analytical solution developed in this study that include transient flow in matrix blocks. UTDUAL was also compared to the SPE Sixth Comparative Project and commercial simulator (VIP-DUAL). Favorable results were obtained.

An ideal fractured reservoir with known individual fracture properties was designed to test the accuracy of UTDUAL comparing fine-grid single porosity simulation results in which both matrix blocks and fractures are discretized. Sensitivity studies were also performed to study the effects of several variables on fractured reservoir behavior. These variables include fracture permeability and porosity, matrix capillary pressure and permeability, matrix block size, pseudo-capillary pressure, and injection rate.

UTDUAL was also used to model Kleppe and Morse's (1974) waterflooding experimental data on fractured cores. For the first time, these experiments were successfully modeled by a dual porosity model for both the low- and high-rate cases. The results of modeling Kazemi et al. (1976) quarter five-spot reservoir showed that UTDUAL reduces to their model without matrix subgridding.

4.2 MATRIX-FRACTURE TRANSFER DURING STEAMFLOODING NATURALLY FRACTURED RESERVOIRS

The purpose of the study presented in this section of the report was to perform a preliminary investigation of the rate of oil expulsion from matrix blocks by thermal expansion and capillary imbibition, in order to determine the apparent dominant transfer mechanism for inclusion into the dual porosity thermal model.

4.2.1 Single Matrix Model

The physical system considered in this study is formed by a parallelepiped matrix block surrounded by fractures on all sides. Only two phases, oil and water, are considered in this first approach. Both matrix and fractures are initially at equilibrium, with the matrix block at a given connate water saturation and the fractures completely oil-filled. Oil-phase pressure is constant throughout. Water pressure in the matrix is lower than the oil pressure by the level of capillary pressure corresponding to the connate water saturation. Capillary pressure in the fracture is assumed to be zero at all times, as the characteristic capillary length for the fracture is much larger than that for the matrix.

At time zero, the fractures are totally flooded by hot water and steam. Because of the high permeability of the fracture network, the hot fluid invasion is assumed instantaneous. The pore volume of the fractures is filled with hot fluid and the temperature is uniform along the fracture. The temperature difference at the fracture-matrix interface will cause thermal energy to diffuse into the matrix, thus beginning to heat this portion of the system. Water only imbibes from the fracture into the matrix block, aided by the viscosity reduction from the temperature increase. Convection at this point augments the heat flow to the matrix. At the same time, oil is displaced to the fracture by both thermal expansion and capillary imbibition.

4.2.2.1 Mathematical Formulation

The single matrix study is carried by a fine-grid simulation on a regular geometry with fracture and matrix represented by two regions with different petrophysical properties. Figure 4.38 shows a schematic of the physical configuration considered.

The governing equations from the conservation laws are

Oil:

$$\nabla \bullet [\lambda_o (\nabla P_o - \gamma_o \nabla z)] = \frac{\partial}{\partial t}\left(\frac{\phi S_o}{B_o}\right) + q_o \tag{4.96}$$

Water:

$$\nabla \bullet [\lambda_w (\nabla P_w - \gamma_w \nabla z)] = \frac{\partial}{\partial t}\left(\frac{\phi S_w}{B_w}\right) + q_w \tag{4.97}$$

Energy:

106

$$V\{\lambda_o B_o \rho_o h_o(\nabla P_o - \gamma_o \Delta z) + \lambda_w B_w \rho_w h_w(\nabla P_w - \gamma_w \nabla z)\} =$$
$$\frac{\partial}{\partial t}\{\phi[\rho_o S_o u_o] + (1-\phi)\rho_r u_r\} - \nabla(\lambda_t \nabla T) + q_h \qquad (4.98)$$

where the mobility terms are given by

$$\lambda_\alpha = \frac{k_{r\alpha} k}{\mu_\alpha B_\alpha} \qquad (4.99)$$

applied to both the matrix and the fracture systems. In writing the above equations the following assumptions were implicitly assumed:

1.   The flux of each phase is given by the multiphase extension of Darcy's law.

2.   Dispersion of mass and heat are negligible.

3.   Energy contributions from kinetic, gravitational, and viscous dissipation are negligible.

4.   Local thermal equilibrium between phases is reached instantly.

5.   No radiative heat transfer is present.

6.   No chemical reactions occur.

The normal constraint equations must also be satisfied to complete the flow description:

$$S_O + S_w = 1$$
$$P_{c_{ow}} \approx P_O - P_w \qquad (4.100)$$

As stated in Eqs. 4.96 through 4.98, the primary variables in the formulation adopted are oil pressure, water saturation, and temperature. Fluid and petrophysical properties do vary with these variables. Table 4.6 summarizes the property dependence used in this model.

The boundary conditions applied to the governing differential equations are

$$P_o \text{ (fracture)} = P_{oi}$$
$$S_w \text{ (fracture)} = S_{wf}$$
$$T \text{(fracture)} = T_h \qquad (4.101)$$

$$\frac{\partial P_o}{\partial n} = \frac{\partial S_w}{\partial n} = \frac{\partial T}{\partial n} = 0 \quad \text{in the center of the block.} \qquad (4.102)$$

Initial conditions are

$$P_o\,(t=0) = P_{oi}$$
$$S_w\,(t=0) = S_{wi}$$
$$T(t=0) = T_i \tag{4.103}$$

where P_{oi} is the constant pressure in the fracture and initial pressure in the matrix. S_{wf} is the saturation of the water-invaded fracture and S_{wi} is the water saturation in the matrix when the flooding process begins. S_{wf} will be typically 100% while S_{wi} will correspond to the irreducible water saturation. T_i is the initial reservoir temperature, prior to any thermal activity, and T_h is the temperature of the injected hot water and steam. The boundary conditions in terms of derivatives are due to the lines of symmetry within the block. Symmetry is such that only one-quarter of a parallelepiped need to be considered for the solution of the entire block.

Equations 4.96 through 4.98 along with the boundary conditions and constitutive relations presented in the previous section were solved numerically. The finite-difference versions of the equations were derived using a fully implicit formulation. The discretization in space was obtained using a first-order finite-difference in a point-distributed grid. Discretization in time was carried out by a forward-difference first-order scheme. The interblock permeabilities, in the transmissibility terms, were calculated using a harmonic average, while the interblock conductivity was obtained by arithmetic average. Relative permeabilities are evaluated at upstream gridblock saturations.

Since a fully implicit solution technique is employed, all terms were calculated at the new time level except for part of the accumulation terms. Solution is accomplished by Newton's method.

Other features of the simulator include:

- Both compressible and incompressible systems can be modeled, including thermal and mechanical compressibilities.
- It accepts boundary conditions of constant potential or specified flux.
- Both constant timestep and optimized variable timestep schemes can be used.
- Petrophysical properties like porosity and permeability can be entered by field distributions.
- Number of gridblocks is variable and block sizes can be entered in both point-distributed or block-centered grid distributions.
- The code is largely vectorized, so as to improve computation performance in computers equiped with vector facilities.

4.2.2 Results

The numerical simulator was tested on a unidimensional base case. A parallelepiped matrix block of $1 \times 0.1 \times 0.1$m ($3.2 \times 0.32 \times 0.32$ ft) is considered in the preliminary simulations. The matrix block is open along the longest direction to fracture flow. The fracture open surface is represented by a constant potential boundary, regarding temperature, saturation and pressure. No-flow boundaries are imposed on the

symmetry planes and the remaining two surfaces are held at constant potential. The petrophysical and fluid PVT data used are summarized in Tables 4.7 and 4.8.

A first set of runs was conducted to find out the proper mesh for the grid. Figure 4.39 illustrates the influence of the grid size on the accuracy of the solution. The curves show the distribution of water saturation along the matrix, which is the most sensitive of the primary variables. Results shown in the remainder of this report were obtained using a $150 \times 1 \times 1$ grid. This mesh was found to yield solutions reasonably insensitive to further refinement.

In order to investigate the interplay between different recovery mechanisms, runs were made according to the presence or absence of thermal expansion, capillary imbibition and convective flow of energy.

Figure 4.40 shows the oil production rate at the block-matrix interface. All cases in the graph were run taking into account the expansion of oil, water, and rock. The four curves come from the combination of effects caused by heat convection and capillary imbibition. It is clear from Fig. 4.40 that heat convection does not affect oil production. The difference between the two curve-envelopes is caused by water imbibition. Imbibition was inhibited in the simulator by setting capillary pressure values to low levels. We arbitrarily set the capillary pressure curve as the values given in Table 4.7 multiplied by a factor of 10^{-8}. Not too suprisingly, convection does not seem to play a significant role in the recovery process. Its effects as a heat transfer mechanism are not significant, as illustrated in Fig. 4.41. The conclusion that convection does not affect the matrix-fracture interaction is important as it allows the development of heat transfer functions based entirely on heat conduction. The results in Figs. 4.40 and 4.41 were obtained for a particular set of property values, as specified before. More case runs are needed to support the above conclusion, as well as to state the range of its validity.

In the next set of runs we separate the effects of expansion and imbibition as oil recovery mechanisms. Figure 4.42 depicts the oil production rate at the surface of our 1x0.1x0.1 matrix block for possible combinations of these mechanisms. No oil production is possible if none of these mechanisms is active. The curve at the bottom of the graph reflects the fact that we used a very low (but not zero) capillary pressure to simulate lack of imbibition. All the other curves fall closely together, meaning that the two recovery mechanisms have overall effects that are of the same order of magnitude. This is less true for the late-time period, where imbibition seems to take over as the dominant mechanism.

Since energy transfer is dominated by conduction and neither expansion nor imbibition interfere significantly with conduction, the energy flux will remain the same as in Fig. 4.41. Water invasion into the matrix presents a pattern very similar to oil production. As Wolff (1987) has pointed out, the pressure compressibility has little significance in these flows since pressure differences are relatively small. Figure 4.43 shows the water inflow rate history according to the combination of expansion/imbibition mechanisms. Expansion contributes negatively to water invasion, being responsible for the difference in the two upper curves. The difference in volume alteration expels both oil and water from the matrix block to the fracture. Otherwise the curves in Fig. 4.43 closely follow the oil production curves.

Another interesting point to address is how much the imbibition process is affected by matrix heating. This question is important since imbibition and expansion have similar impact on oil recovery. Figure 4.44 shows the rates of water imbibition into

the matrix for three cases. For comparison purposes, we simulated imbibition-only drive with cold water injected into cold matrix (cold case), with hot water imbibing into a hot matrix (hot case), and with hot water brought in contact with a cold matrix (process case). It appears that imbibition drive in the normal hot water-cold matrix situation can be handled as if the process had occurred with a completely hot matrix. This can be explained by the higher characteristic time that imbibition presents compared to the heat diffusion time. Given this, it appears that the imbibition-driven oil flux can be calculated by the schemes used to estimate cold water imbibition with properties evaluated at the hot fluid temperature.

4.2.3 Analytical Approximations

The simplicity of the heat-driven mechanism suggests that some approximate analytical approaches can be used to estimate matrix-fracture transfer flow. Considering only conduction in the matrix, the energy equation can be written as

$$\nabla(\lambda_t \Delta T) = \frac{\partial}{\partial t}[\phi(\rho_o s_o u_o) + (1-\phi)\rho_r u_r] \tag{4.104}$$

which can be approximated by

$$\nabla^2 T = \frac{1}{\alpha_t}\frac{\partial T}{\partial t} \tag{4.105}$$

where

$$\alpha_t = \frac{\lambda_t}{\phi(\rho_o S_o C_o + \rho_w S_w C_w) + (1-\phi)\rho_r C_r} \tag{4.106}$$

Boundary conditions to Eq. 4.105 in the matrix are as stated in Eqs. 4.101 through 4.103. The temperature distribution resulting from the mathematical problem stated in Eq. 4.105 can be expressed in two different ways (Carslaw and Jaeger, 1959):

$$\frac{T(x,t)-T_i}{T_h - T_i} = 1 - \frac{4}{\Pi}\sum_{n=0}^{\infty}\frac{(-1)^n}{(2n+1)}e^{\frac{-\alpha_t(2n+1)^2\Pi^2 t}{4l^2}}\cos\left[\frac{(2n+1)\Pi x}{2l}\right] \tag{4.107}$$

or

$$\frac{T(x,t)-T_i}{T_h - T_i} = \sum_{n=0}^{\infty}(-1)^n\left[\text{erfc}\frac{(2n+1)(l-x)}{2\sqrt{\alpha_t t}} + \text{erfc}\frac{(2n+1)(l+x)}{2\sqrt{\alpha_t t}}\right] \tag{4.108}$$

The energy transfer rate between the matrix and the fracture is given by

$$q_h = -\lambda_t A\frac{\partial T}{\partial x}\bigg|_{x=l} \tag{4.109}$$

where A is the matrix-fracture interface area. Notice that in order to be used as heat transfer functions in the energy governing equation for the fracture system, q_h in Eq. 4.109 needs to be volume specific.

$$q_h = q'/v \tag{4.110}$$

110

From Eqs. 4.107 through 4.110

$$q_h = \frac{2\lambda_t \Delta T}{l^2} \sum_{n=0}^{\infty} e^{\frac{-\partial (2n+1)^2 \Pi^2 t}{4l^2}} \tag{4.111}$$

or

$$q_h = \frac{\lambda_t \Delta T}{l^2} \left\{ \left(\frac{\alpha_t t}{l^2}\right)^{\frac{1}{2}} \left[\Pi^{\frac{1}{2}} + 2\sum_{n=1}^{\infty} (-1)^n \, \text{ierfc}\left(n\sqrt{\frac{l^2}{\alpha_t t}}\right) \right] + 2\frac{l^2}{\alpha_t t} \sum_{n=1}^{\infty} (-1)^n \, n \, \text{erfc}\left(n\sqrt{\frac{l^2}{\alpha_t t}}\right) \right\} \tag{4.112}$$

The series in Eq. 4.111 converges rapidly for large values of $\alpha_t t/l^2$, while the series in Eq. 4.112 converges for small values of the same group. Figure 4.45 illustrates the convergence of the series in Eq. 4.111 for the transport properties values used in the simulation. Similarly, Fig. 4.46 shows the convergence for Eq. 4.112. The first term in each series is sufficient to accurately represent the solution in different ranges , i.e., where

$\frac{\alpha_t t}{l^2}$ is either more than or less than one. For this corresponds to the time for temperature diffusion to reach the center of the matrix block. This early time, the heat transfer function can be described by

$$q_h = \frac{\lambda_t \Delta T}{l^2} \left[\Pi^{-\frac{1}{2}} \left(\frac{\alpha_t t}{l^2}\right)^{\frac{1}{2}} \left(1 + 2e^{-\frac{l^2}{\alpha_t t}}\right) \right], \quad \frac{\alpha_t t}{l^2} \leq 1 \tag{4.113}$$

while for times after the heat front reaches the center of the block,

$$q_h = \frac{2\lambda_t \Delta T}{l^2} e^{\frac{-\Pi^2 \alpha_t t}{4l^2}}, \quad \frac{\alpha_t t}{l_2} \geq 1 \tag{4.114}$$

For $t_D \leq 0.1$ Eq. 4.113 can also be simplified to

$$q_h = \frac{\lambda_t}{l^2} \Pi^{-\frac{1}{2}} \left(\frac{\alpha_t t}{l^2}\right)^{\frac{1}{2}} \Delta T \tag{4.115}$$

with accuracy within 0.01%.

Figure 4.47 shows a comparison in terms of heat flux rate between the analytical solution given by Eqs. 4.114 and 4.115 and the numerical results obtained from simulation. All parameters in the analytical expressions were evaluated at the initial temperature of the matrix block. The agreement between the solutions is remarkable, given that no adjustments were made in either the analytical model or the simulator.

4.2.3.1 Oil Transfer Functions

Expansion is one of the most important mechanisms of oil recovery from the matrix. Upon heating, the matrix block is pressurized by the differential thermal expansion between the fluids and the rock. The fluids are then expelled to the fracture

because of the pressure difference that is generated. Two transport processes occurs as this mechanism acts: heat diffusion into the matrix and the oil flow out of the block. For the range of parameters usually found in field applications, hydrodynamic diffusivity is much higher than thermal diffusivity. It is thus reasonable to assume that the pressure increases from heating are essentially instantaneously propagated throughout the matrix. Figure 4.48 illustrates the evolution of pressure profiles along the block as the heat advances. At early times there is a pressure buildup close to the boundary. The pressure increase is quickly propagated to the entire block. After this short buildup period, the pressure profiles show a diffusion pattern with a much slower rate. In fact, the characteristic time for the pressure depletion is the same as the characteristic time for the heat diffusion. This is a definite indication that oil expulsion is controlled by the slower transport process, which is heat transport.

Assuming instantaneous propagation of thermally-created pressure differences, the oil expelled from the matrix is locally given by

$$dq_o = \beta v \phi \frac{dT}{dt} \tag{4.116}$$

For the whole matrix block, we integrate in space

$$dq_o = \beta v \phi \frac{d\overline{T}}{dt} \tag{4.117}$$

where β is an effective differential thermal expansion coefficient for the matrix block.

From Eq. 4.107, the average temperature in the matrix is

$$\frac{\overline{T} - T_i}{T_h - T_i} = 1 - \frac{8}{\Pi^2} \sum_{n=0}^{\infty} \frac{1}{(2n+1)^2} e^{\frac{-(2n+1)^2 \Pi^2 \alpha_t t}{4 l^2}} \tag{4.118}$$

and the expulsion rate for the expansion mechanism becomes as

$$q_o = 8 \phi \beta v \Delta T \sum_{n=0}^{\infty} e^{\frac{-(2n+1)^2 \Pi^2 \alpha_t t}{4 l^2}} \tag{4.119}$$

The expression given in Eq. 4.119 is adequate for the late-time solution. As before, an alternative expression can be used for the early-time period.

There is a relation, implicit in the model, between the energy input into the matrix and the oil output:

$$q_o(t) = \frac{\alpha_t \beta \phi}{\lambda_t} q_h(t) \tag{4.120}$$

Associated with the oil production is a pressure gradient in the system. The overall pressure difference necessary to drive the oil out can be estimated from the expulsion rate, and is related to the temperature difference by

$$\Delta P = \frac{\alpha_t \beta \mu \phi}{K} (T_h - T_i) \tag{4.121}$$

112

Figure 4.49 shows a comparison between the analytical solution and the simulation results for the case when expansion is allowed only in the matrix block.

4.3 MODELING GAS GENERATION BY CHEMICAL REACTION

Gas generation can be an important mechanism of oil recovery from naturally fractured reservoirs by steam injection. The significance of gas generation lies in that it can recover oil that otherwise cannot be recovered by capillary imbibition and thermal expansion.

Gas can be generated in several ways: solution gas vaporization, in-situ steam generation and gas generation by chemical reaction (Reis, 1990). Generally, gas generation by chemical reaction occurs after solution gas vaporization and before in-situ steam generation. If solution gas vaporization does not happen during a recovery process, gas generation by chemical reactions will have increasing importance. Hence, gas generation by chemical reaction should be considered in the modeling of oil recovery from naturally fractured reservoirs by steam injection. The following sections describe how gas generation by chemical reactions is treated in the single matrix thermal recovery model. This same approach can be used for dual porosity modeling.

4.3.1 Kinetics of Gas Generation

Akstinat's study (1983) shows that many reactions concerning gas generation happen in reservoir fluids and between reservoir fluids and rocks during steam flooding. The reactions that happen in reservoir fluids are aquathermolysis of oil and thermal cracking of heavy hydrocarbons (Meyer *et al.*, 1982; Monin and Audibert, 1984). In water, the primary reaction is the dissolution of reservoir rocks. In both the cases, CO_2 is the major product. But these reactions happen at different conditions. Aquathermolysis and thermal cracking of heavy hydrocarbons proceed at relatively high temperatures, in most cases above 300°C. Dissolution of reservoir rocks can proceed at an appreciable rate at temperature as low as 200°C in acidic environments (Briggs *et al.*, 1989). At thermal recovery conditions, CO_2 is more likely produced by reactions between reservoir water and rocks (Cathles *et al.*, 1987; Gunter and Bird, 1988).

4.3.2 Rate of Gas Generation

Chemical reactions in geothermal systems convert unstable reservoir minerals to stable minerals. The stability of a reservoir mineral depends on temperature and other minerals existing in the system (Giggenbach, 1981). Carbonates, kaolinite and quartz become unstable at high temperature and low CO_2 pressure when they exist simultaneously in a geothermal system. Carbonates dissolve in water to produce CO_2 and quartz dissolves to buffer the pH. The reaction proceeds until one of the reactants is consumed completely.

Gunter (1988) conducted the experiment of CO_2 production in tar sand containing calcite at 265°C, he got maximum CO_2 concentration of 0.15 mole/kg water. In Dreher's (1986) experiment, approximately one mole of CO_2 was produced for each mole of water injected at 150°C. These studies suggest that the rates of reactions are high compared to fluid flow in reservoirs.

Gunter (1988) proposed a kinetics to interpret his experiment results. He assumed the dissolution of quartz to be the rate controlling reaction and obtained a rate equation

for quartz dissolution. Cathes *et al.* (1987) developed a rate law for CO_2 generation during steamflooding of Chevron's Buena Vista Hills reservoir. This rate law takes a similar form as Gunter's, and a complete set of kinetic parameters was given. We use their model to calculate the rates of gas generation in matrix blocks during steam injection into a naturally fractured reservoir.

The reaction is assumed to be a first-order reversible reaction. The rate of reaction is calculated by:

$$\phi r_{co_2} = \rho_w k_0 \exp(-E/RT)(C_{eq1} - C) \qquad (4.122)$$

The activation energy, E, given by Cathles is 15,000 cal/mole. The kinetic pre-exponential coefficient, k_0, ranges from 0.025 to 0.3 sec^{-1}.

The solubility of reservoir rocks, C_{eq1}, is originally given by Giggebach (1981):

$$\log C_{eq1} = 6.491 - 6332.3/T + 0.00745\ T \qquad (4.123)$$

4.3.3 Gas Saturation

The CO_2 concentration in water at chemical equilibrium generally increases as temperature increases. However, the solubility of CO_2 gas in water decreases as temperature increases and increases as pressure increases. At relatively high temperature and low pressure, the sum of CO_2 partial pressure at chemical equilibrium and saturated water vapor pressure can be greater than the reservoir pressure. In this case, a gas mixture of CO_2 and steam will exist in the matrix blocks. To calculate gas saturation, the following assumptions are made:

1. During formation of the gas phase, reservoir fluids are at phase equilibrium.

2. CO_2 and steam form an ideal mixture.

3. The oil vapor pressure is zero.

In a given time interval, Δt, the change of amount of CO_2 in a unit volume is

$$\Delta m_{co_2} = \Delta[C(\rho_w S_w + f_{ow}\rho_o S_o)] + r_{co_2}\Delta t \qquad (4.124)$$

Where C is the concentration of CO_2 in water, f_{ow} is the equilibrium concentration ratio of CO_2 in oil and water. f_{ow} can be estimated to be in the range of 1.0-5.0 (Sayegh, 1990; Chung, 1986).

At vapor-liquid phase equilibrium, the partial pressure of CO_2 in the gas phase, P_{co2}, is

$$P_{co2} = P_g - P_s \qquad (4.125)$$

where steam vapor pressure, P_g, can be approximated by (Elder, 1981)

$$P_s = 0.085 - 0.794(T/100) + 2.203(T/100)^2$$
$$-1.976(T/100)^3 + 1.503(T/100)^4 \tag{4.126}$$

At vapor-liquid phase equilibrium, the concentration of CO_2 in water is related to the partial pressure of CO_2 in the gas by Henry's law:

$$C_{eq2} = P_{co2}/K_H \tag{4.127}$$

where Henry's constant, K_H, is given by

$$\log K_H = 8.769 - 0.00745\, T - 1517.7/T \tag{4.128}$$

At vapor-liquid equilibrium, the amount of CO_2 in water and oil can be calculated by

$$m_l = C_{eq2}(\rho_w S_w + f_{ow}\rho_o S_o) \tag{4.129}$$

The amount of CO_2 in the gas phase, m_g, is then

$$m_g = m_{co2} - m_l \tag{4.130}$$

If $m_g < 0$, the gas phase does not exist:

$$S_g = 0 \tag{4.131}$$

When $m_g > 0$, the gas phase saturation is:

$$S_g = m_g\, zRT/P_{co2} \tag{4.132}$$

If the gas saturation exceeds its critical value, the gas phase will flow. However, since the rate of gas generation is slow and its viscosity is much lower than water or oil, gas saturation will not be appreciably higher than its critical value, S_{gc}. We have thus assumed that the maximum gas saturation attainable is S_{gc}.

4.3.4 Single Matrix Block Thermal Recovery Model

With the formation of gas phase, gas expels liquid to the surrounding fractures and fluid in matrix blocks becomes three-phase. Equations describing fluid flow in matrix blocks should consider gas flow when the gas phase is formed. However, because the matrix blocks are heated from a fracture, the gas begins to be generated from the fracture first. So, gas flow does not influence oil and water at the centers of matrix blocks where a gas phase has not yet been generated. Furthermore, due to the slow rate of generation and high mobility of the gas, gas flow has negligible influence on the flow of oil and water after the gas saturation reaches its critical value. Practically, it may thus not be necessary to consider flow of the gas phase. The flow equations for two phase flow can still be used in case of gas generation. The effect of gas generation can be treated by including the gas saturation in a three-phase relative permeability relationship.

4.3.5 Equations of Fluid Flow and Heat Transfer in A Single Matrix Block

The equations for oil and water flow are:

$$\nabla \cdot \left[\lambda_o\left(\nabla P_o - \gamma_o \nabla z\right)\right] = \frac{\partial}{\partial t}\left(\frac{\phi S_o}{B_o}\right)$$

(4.133)

and

$$\nabla \cdot \left[\lambda_w\left(\nabla P_w - \gamma_w \nabla z\right)\right] = \frac{\partial}{\partial t}\left(\frac{\phi S_w}{B_w}\right)$$

(4.134)

The energy equation is:

$$\nabla \cdot \left[\lambda_o h_o \rho_o B_o\left(\nabla P_o - \gamma_o \nabla z\right) + \lambda_w h_w \rho_w B_w\left(\nabla P_w - \gamma_w \nabla z\right)\right]$$
$$= \frac{\partial}{\partial t}\left\{\phi\left[\rho_o S_o u_o + \rho_w S_w u_w\right] + \left(1-\phi\right)\rho_r u_r\right\} - \nabla\left(\lambda_t \nabla T\right) + q_h$$

(4.135)

Where mobility λ_α is:

$$\lambda_\alpha = \frac{k_{r\alpha} k}{\mu_\alpha B_\alpha}$$

Oil and water pressure are related by capillary pressure between oil and water P_{cow}:

$$P_{cow} = P_o - P_w$$

(4.136)

The heat of vaporization for gas is not included in the equation because the rate of gas generation is slow and the rate of heat transfer is high.

4.3.6 Three-Phase Relative Permeabilities

Three-phase relative permeabilities are calculated by Stone's model I (Stone, 1970):

$$k_{rw} = k_{rw}(S_w)$$

(4.137)

$$k_{ro}(S_w, S_g) = \frac{S_o^* k_{row} k_{rog}}{\left(1-S_w^*\right)\left(1-S_g^*\right)}$$

(4.138)

where,

$$S_o^* = \frac{S_o - S_{om}}{1-S_{wc} - S_{om}}$$

(4.139)

$$S_w^* = \frac{S_w - S_{wc}}{1-S_{wc} - S_{om}}$$

(4.140)

$$S_g^* = \frac{S_g}{1-S_{wc} - S_{om}}$$

(4.141)

116

Two phase permeabilities k_{rw}, k_{row} and k_{rog} are calculated by the following correlations:

$$k_{rw} = k^o_w S^*_w{}^{nw} \qquad (4.142)$$

$$k_{row} = k^o_{ow} S^*_{ow}{}^{now} \qquad (4.143)$$

$$k_{rog} = k^o_{og} S^*_{og}{}^{nog} \qquad (4.144)$$

$$S^*_w = \frac{S_w - S_{wr}}{1 - S_{wr} - S_{orw}} \qquad (4.145)$$

$$S^*_{ow} = \frac{S_o - S_{orw}}{1 - S_{wr} - S_{orw}} \qquad (4.146)$$

$$S^*_{og} = \frac{S_o - S_{org}}{1 - S_{gr} - S_{org}} \qquad (4.147)$$

The three saturations obey the relation:

$$S_w + S_o + S_g = 1 \qquad (4.148)$$

4.3.7 Results

Equations 4.122 through 4.132 are used to calculate example times for gas to reach the critical saturation in the matrix blocks as a function of temperature at CO_2 partial pressure of 2 bars, 5 bars and 10 bars, respectively. Initial CO_2 concentrations are assumed to be zero. Results are plotted in Fig. 4.50. Parameters used in the calculations are listed in Table 4.9.

Figure 4.50 clearly shows that the time for the gas phase to be generated is very sensitive to temperature. At temperatures below 250°C, the gas phase cannot be generated, even at a CO_2 partial pressure of 2 bars. The three curves at different pressures indicate that the time increases greatly as CO_2 pressure increases.

Equations 4.122 through 4.141 are used in our single matrix block thermal recovery model to simulate the process of gas generation in a single matrix block. The fractures are one dimensional with a fracture spacing of 4 m.

Figure 4.51 shows the oil recovery for residual oil saturation of 0.1, 0.15, and 0.2. The enhanced recovery is nearly proportional to the decrease of three phase residual oil saturation.

Figure 4.52 shows oil recovery and gas saturation in the matrix blocks vs. time for gas generation in a single matrix block at temperatures of 275, 280 and 290. Although the rate of gas generation strongly depends on temperature, the final recoveries are the same. Comparing the recovery and gas generation curves, it is easy to find that the rates of recovery are slower than the rate of gas generation. This means that gas phase expels both oil and water out of the matrix blocks. When oil saturation is high, gas primarily expels oil into the fractures. When oil saturation is low, gas primarily expels water into the fractures, and then oil is imbibed by water into the fracture. In both the cases, gas

117

occupies the pore volume originally occupied by residual oil and makes a fraction of residual oil flowable.

Similar to Fig. 4.52, Fig. 4.53 indicates that the final recovery is not influenced by pressure but by the rate of gas generation.

4.4 HEAT LOSSES TO OVERBURDEN AND UNDERBURDEN

In thermal reservoir simulation, the energy balance equation is solved over the entire overburden-reservoir-underburden system. Heat losses to the overburden and underburden are by conduction only. Computing energy transfer for this entire system, however, can be very computationally expensive, as the temperature profile extends for a long distance from the reservoir.

To solve this problem, Weinstein (1972) introduced a semianalytic method for thermal coupling of the reservoir and overburden, and extended this method for increasing and decreasing boundary temperature (Weinstein, 1974). Chase and O'Dell (1973) applied variational principles for heat loss calculations to the overburden and underburden. Incorporating this method into a thermal simulator, only a system of two nonlinear ordinary differential equations must be solved for each gridblock at the interface of the reservoir and overburden. Vinsome and Westerveld (1980) presented a simpler method by using a fitting function for the temperature profile into the overburden or underburden. This method is used extensively in current thermal simulation models.

Although the Vinsome and Westerveld method has been shown to work very well for steamflooding applications, these applications have high rates of convective energy transfer within the reservoir. However, in the case of naturally fractured reservoirs, energy transfer through the reservoir is primarily by conduction, at a much slow rate than convection in conventional steamflood operations. We were thus concerned that the relative amount of heat conduction to the overburden and underburden would be high, and that perhaps the Vinsome and Westerveld method might not work as well.

To test this out, we modeled two separate cases. Both were of a constant temperature fracture conducting heat into a reservoir (Fig. 4.54). The first model was a complete heat conduction calculation, numerically solving the thermal diffusivity equation in 2D for the combined reservoir, overburden, underburden system. The second model did a thermal diffusivity calculation into the reservoir, but used the Vinsome and Westerveld method to calculate heat transfer from the reservoir to the overburden and underburden.

Figures 4.55 and 4.56 show the results of these runs. In these figures heat efficiency is defined as the amount of heat remaining in the reservoir as a fraction of the total amount of heat conducted from the fracture. Figure 4.55 shows cumulative heat efficiency vs. time. Figure 4.56 shows an instantaneous rate efficiency vs. time. Note that the complete finite difference result and the Vinsome and Westerveld method give essentially identical results.

It should be noted that this test included heat conduction in both the longitudinal and transverse directions. The Vinsome and Westerveld method has often been compared against the Marx and Langenheim (1959) result, which neglected heat conduction parallel to heat flow in the reservoir. This test was thus more rigorous than has usually been applied to the Vinsome and Westerveld method.

4.5 NEW DUAL POROSITY THERMAL SIMULATOR

A new 3D dual porosity simulator has been developed in this research. Both single porosity reservoirs and fractured reservoirs can be simulated using this simulator. Different options in handling fluids and heat transfer between matrix and fracture are also included in the new simulator.

The new simulator can simulate typical field production problems such as primary depletion, pressure maintenance, evaluation of oil recovery by waterflooding, steamflooding, and steam stimulation. The oil recovery mechanisms of fluid displacement, capillary imbibition, gravity drainage, mechanical and thermal expansion of fluids in naturally fractured reservoirs, heat losses to the overburden and underburden all can be handled by the simulator.

Using the dual porosity concept, a fractured reservoir is idealized as a discontinuous matrix system and a continuous fracture system. The fracture system is modeled much like a single-porosity reservoir. The difference is that there are fluids and energy source/sink terms for each gridblock that reflect the fluids and heat transfer from and to the matrix.

Numerical instability is often encountered in simulating thermal processes in petroleum engineering. Therefore, a fully implicit scheme is used in both the fracture system and matrix systems in order to ensure stability.

4.5.1 Mathematical Formulation

The dual porosity concept assumes that the fractured reservoir is represented by a continuous fracture system and a discontinuous matrix system. The fracture system and the matrix system occupy the same computational grid-block. Applying material and energy balances to these two systems yield two groups of equations which are coupled by so-called transfer functions. The transfer functions characterize fluid and energy flow between the fracture and matrix blocks.

The following are major assumptions incorporated into the simulator:

1.   Darcy's law applies to all fluids.

2.   Injection and production wells are all in the fracture system.

3.   Heat losses to the overburden and underburden are from the matrix system. There is no heat loss directly from the fracture system due to the small area in contact with the overburden and underburden.

4.   There is no steam generation in the matrix system, i.e., there are only water and oil phases in matrix.

Applying material balance and Darcy's law to each phase in a 3D control volume of the fracture system, the following continuity equations for each phase are obtained:

119

Oil:

$$\nabla\left[\frac{kk_{ro}}{\mu_o B_o}(\nabla P_o - \rho_o \nabla z)\right]_f + q_o - \tau_{omf} = \frac{\partial}{\partial t}\left[\frac{S_o \phi}{B_o}\right]_f \tag{4.149}$$

Water:

$$\nabla\left[\frac{kk_{rw}}{\mu_w B_w}(\nabla P_w - \rho_w \nabla z)\right]_f + q_w + q_{sw} - \tau_{wmf} = \frac{\partial}{\partial t}\left[\frac{S_w \phi}{B_w}\right]_f \tag{4.150}$$

Steam:

$$\nabla\left[\frac{kk_{rs}}{\mu_s B_s}(\nabla P_s - \rho_s \nabla z)\right]_f + q_s - q_{ws} = \frac{\partial}{\partial t}\left[\frac{S_s \phi}{B_s}\right]_f \tag{4.151}$$

where the terms τ_{omf} and τ_{wmf} are the oil and water transfer rates between the fracture and matrix. The terms q_{sw} and q_{ws} represent the volumetric rates of condensation of steam per unit of reservoir volume. These two terms are canceled by the multiplication of the water and steam continuity equations by the water and steam densities respectively and adding the two equations in solving the fracture system. This approach has been shown to improve stability in the modeling of steam injection processes.

For the same control volume in the fracture, the energy conservation equation accounts for energy transferred and stored in the fluids and in the porous medium. Convection and conduction of thermal energy are two main mechanisms of energy transfer.

$$\nabla\left[\frac{kk_{ro}}{\mu_o}\rho_o h_o(\nabla P_o - \rho_o \nabla z) + \frac{kk_{rw}}{\mu_w}\rho_w h_w(\nabla P_w - \rho_w \nabla z) + \frac{kk_{rs}}{\mu_s}\rho_s h_s(\nabla P_s - \rho_s \nabla z)\right]_f$$

$$+k_M \nabla T_f + Q_h - \tau_{hmf} = \frac{\partial}{\partial t}\left[\phi(S_o\rho_o U_o + S_w\rho_w U_w + S_s\rho_s U_s) + (1-\phi)\rho_r U_r\right]_f \tag{4.152}$$

where ρ_α is the density, h_α is the enthalpy and U_α is the internal energy with $\alpha = o$ (oil), w (water), s (steam), and r (rock). k_M is the thermal conductivity of rock and fluids and T is the temperature. Q_h is the injected or produced energy. τ_{hmf} is the energy transferred between the fractures and matrices.

Another governing equation is an equation of state for the steam/water mixture.

$$T = T(P_{sat}) \text{ when } p = p_{sat} \tag{4.153a}$$

$$S_s = 0 \text{ and } \frac{dS_s}{dT} = 0 \text{ when } T < T_{sat} \tag{4.153b}$$

These equilibrium equations state that the temperature of saturated steam is dependent upon the saturation pressure and that there is no steam phase when the temperature is lower than the saturation temperature.

Using the same method as for the fracture system, we can obtain similar equations for the matrix system. In naturally fractured reservoirs, the matrix permeability is very low in comparison with the fracture. As before, the convection terms in the matrix system are neglected. Therefore the simplified equations become

Oil:

$$\tau_{omf} = \frac{\partial}{\partial t}\left[\frac{\phi S_o}{B_o}\right]_m \tag{4.154}$$

Water:

$$\tau_{wmf} = \frac{\partial}{\partial t}\left[\frac{\phi S_w}{B_w}\right]_m \tag{4.155}$$

Neglecting the contribution of convection to energy transfer yields the simplified energy balance equation:

$$k_{hm}\nabla T_m + Q_l + \tau_{hmf} = \frac{\partial}{\partial t}\left[\phi(S_o\rho_o U_o + S_w\rho_w U_w + S_s\rho_s U_s) + (1-\phi)\rho_r U_r\right]_m \tag{4.156}$$

where Q_l is the heat loss to the overburden and underburden. The Vinsome and Westerveld (1980) method is used to calculate heat losses.

The initial values of pressure, saturation and temperature are specified at each point in the reservoir. Also we assume that the reservoir is initially at static equilibrium throughout the reservoir. Therfore we only need to specify the oil phase pressure at one elevation. Values of oil pressure at other points are then calculated from hydrostatics:

$$P_{ok} = P^o + \rho_o g(z_k - z^o) \tag{4.157}$$

where P^o is the pressure specified at elevation z^o.

The basic boundary conditions are given by

$$\bar{n}\cdot\bar{u}_\alpha = 0 \quad \alpha = o,w,s \tag{4.158}$$

where $\bar{n}$ is the unit vector normal to the boundary. Equation 4.158 assumes that there is no mass flow through impermeable boundaries.

121

For the heat loss calculations, the boundary is at infinity with the condition being

$$T_\infty = T^i \tag{4.159}$$

where T^i is the initial reservoir temperature.

To complete the governing equations for the fracture and matrix, the following constraints must be added to the system:

$$\sum_l S_{lj} = 1 \tag{4.160}$$

where $j = f$ (fracture) or m (matrix), $l = o, w, s$ (oil, water, steam).

$$P_{cgo} = P_g - P_o \tag{4.161}$$

$$P_{cow} = P_o - P_w \tag{4.162}$$

where P_{cgo} and P_{cow} are gas-oil and oil-water capillary pressures.

4.5.2 Finite Differencing

The Cartesian coordinate system is used to describe the simulated spatial domain. A block-centered finite-difference grid is employed and is numbered from (1,1,1) to (N_x, N_y, N_z) or from 1 to $N_x N_y N_z$, where $N_x, N_y,$ and N_z correspond to the number of gridblocks in each direction. The discretization in space is obtained using first-order finite differencing. Thus for the node i,j,k:

$$\Delta_x f = f^n_{i+\frac{1}{2},j,k} - f^n_{i-\frac{1}{2},j,k} \tag{4.163}$$

The delta operator in the y and z directions are similar to that for the x direction. The descretization in time is carried out using a first-order forward difference scheme:

$$\Delta_t f = f^{n+1}_{i,j,k} - f^n_{i,j,k} \tag{4.164}$$

Employing the above operators to the oil conservation equation:

$$[\Delta_x TX_{of} \Delta_x P_o + \Delta_y TY_{of} \Delta_y P_o + \Delta_z TZ_{of} \Delta_z (P_o - \gamma_o Z)]_f + q_o - \tau_{omf} \tag{4.165}$$

$$= \frac{V}{\Delta t} \Delta_t \left[\frac{\phi S_o}{B_o} \right]_f$$

For the mass balance of water and steam, the equations are similar, simply replacing the subscripts o with w or s. The transmissibilities for fracture-fracture flow, $TX_{\alpha f}, TY_{\alpha f}, TZ_{\alpha f}$, are defined as:

$$TX_{\alpha f_{i+\frac{1}{2},j,k}} = \frac{\Delta Y_j \Delta Z_k}{\Delta X_{i+\frac{1}{2}}}\left[k_{xf}\lambda_{\alpha f}\right]_{i+\frac{1}{2},j,k} \tag{4.166a}$$

$$TY_{\alpha f_{i,j+\frac{1}{2},k}} = \frac{\Delta X_i \Delta Z_k}{\Delta Y_{j+\frac{1}{2}}}\left[k_{yf}\lambda_{\alpha f}\right]_{i,j+\frac{1}{2},k} \tag{4.166b}$$

$$TZ_{\alpha f_{i,j,k+\frac{1}{2}}} = \frac{\Delta X_i \Delta Y_j}{\Delta Z_{k+\frac{1}{2}}}\left[k_{zf}\lambda_{\alpha f}\right]_{i,j,k+\frac{1}{2}} \tag{4.166c}$$

where α denotes w, o, or s.

The mobility $\lambda_{\alpha f_{i+\frac{1}{2}}}$ is:

$$\lambda_{\alpha f_{i+\frac{1}{2}}} = \omega_{\alpha f}\left(\frac{k_r}{\mu B}\right)_{\alpha f_i} + (1-\omega_{\alpha f})\left(\frac{k_r}{\mu B}\right)_{\alpha f_{i+\frac{1}{2}}} \tag{4.167}$$

Similar equations for mobility in the y and z directions are straightforward. The paramete $\omega_{\alpha f}$ is the upstream factor and is either one or zero depending on the flow direction of phase α.

The energy conservation equation discretizes as:

$$\begin{aligned}
&\Delta_x TXH_{of}\Delta_x P_o + \Delta_y TYH_{of}\Delta_y P_o + \Delta_z TZH_{of}\Delta_z(P_o - \gamma_o Z)\\
&+\Delta_x TXH_{wf}\Delta_x P_w + \Delta_y TYH_{wf}\Delta_y P_w + \Delta_z TZH_{wf}\Delta_z(P_w - \gamma_w Z)\\
&+\Delta_x TXH_{sf}\Delta_x P_s + \Delta_y TYH_{sf}\Delta_y P_s + \Delta_z TZH_{sf}\Delta_z(P_s - \gamma_s Z)\\
&+\Delta_x TXC_f\Delta_x T_f + \Delta_y TYC_f\Delta_y T_f + \Delta_z TZC_f\Delta_z T_f + Q_h - \tau_{hmf}
\end{aligned} \tag{4.168}$$

$$=\frac{V}{\Delta t}\left[\phi(\rho_o S_o U_o + \rho_w S_w U_w + \rho_s S_s U_s) + (1-\phi)\rho_r U_r\right]_f$$

The transmissibilities of energy by convection are:

$$TXH_{\alpha f_{i+\frac{1}{2},j,k}} = \frac{\Delta Y_j \Delta Z_k}{\Delta X_{i+\frac{1}{2}}}k_{x_{i+\frac{1}{2},j,k}}\left[\dot{\omega}_{\alpha f}\left(\frac{k_r \rho h}{\mu}\right)_{i,j,k} + (1-\omega_{\alpha f})\left(\frac{k_r \rho h}{\mu}\right)_{i+1,j,k}\right]_{\alpha f} \tag{4.169a}$$

123

$$TYH_{of_{i,j+\frac{1}{2},k}} = \frac{\Delta X_i \Delta Z_k}{\Delta Y_{j+\frac{1}{2}}} k_{y_{i,j+\frac{1}{2},k}} \left[\omega_{of} \left(\frac{k_r \rho h}{\mu} \right)_{i,j,k} + (1 - \omega_{of}) \left(\frac{k_r \rho h}{\mu} \right)_{i,j+1,k} \right]_{of} \quad (4.169b)$$

$$TZH_{of_{i,j,k+\frac{1}{2}}} = \frac{\Delta X_i \Delta Y_j}{\Delta Z_{k+\frac{1}{2}}} k_{z_{i,j,k+\frac{1}{2}}} \left[\omega_{of} \left(\frac{k_r \rho h}{\mu} \right)_{i,j,k} + (1 - \omega_{of}) \left(\frac{k_r \rho h}{\mu} \right)_{i,j,k+1} \right]_{of} \quad (4.169c)$$

One-point upstream weighting is also used in calculating heat transfer by convection. The transmissibilities of energy by conduction are calculated by:

$$TXC_f = \frac{\Delta Y_j \Delta Z_k}{\Delta X_{i+\frac{1}{2}}} k_{Nf_{i+\frac{1}{2},j,k}} \quad (4.170a)$$

$$TYC_f = \frac{\Delta X_i \Delta Z_k}{\Delta Y_{j+\frac{1}{2}}} k_{Nf_{i,j+\frac{1}{2},k}} \quad (4.170b)$$

$$TZC_f = \frac{\Delta X_i \Delta Y_j}{\Delta Z_{k+\frac{1}{2}}} k_{Nf_{i,j,k+\frac{1}{2}}} \quad (4.170c)$$

The arithmetic average is used to calculate the interblock thermal conductivity.

There are four finite-difference equations and one equilibrium equation at each gridpoint. The water condensation term can be canceled by adding the water and steam equations together. The auxiliary relationships help us to reduce the number of primary variables to four. We choose P_o, S_w, S_s and T_f as primary variables. The remaining variables are all dependent variables.

4.5.2.1 Solution Method

By moving the right hand side of the governing equations, the finite-difference equations can be expressed in the form of residuals:

$$R(X) = 0 \quad (4.171)$$

where X is vector of the primary variables:

$$x_{ijk} = \begin{bmatrix} P_{of} \\ S_{wf} \\ S_{sf} \\ T_f \end{bmatrix}_{ijk} \quad (4.172)$$

The nonlinear equations can be linearized and solved using the Newton-Raphson method. The iteration is defined by:

$$J\Delta X = -R \quad (4.173)$$

124

where **J** is the Jacobian matrix formed by differentiating the nonlinear residual equations with respect to the primary variables:

$$J_{ij} = \begin{bmatrix} \dfrac{\partial R_{oi}}{\partial P_{oj}} & \dfrac{\partial R_{oi}}{\partial S_{wj}} & \dfrac{\partial R_{oi}}{\partial T_{fj}} & \dfrac{\partial R_{oi}}{\partial S_{sj}} \\[2mm] \dfrac{\partial R_{wi}}{\partial P_{oj}} & \dfrac{\partial R_{wi}}{\partial S_{wj}} & \dfrac{\partial R_{wi}}{\partial T_{fj}} & \dfrac{\partial R_{wi}}{\partial S_{sj}} \\[2mm] \dfrac{\partial R_{Ti}}{\partial P_{oj}} & \dfrac{\partial R_{Ti}}{\partial S_{wj}} & \dfrac{\partial R_{Ti}}{\partial T_{fj}} & \dfrac{\partial R_{Ti}}{\partial S_{sj}} \\[2mm] \dfrac{\partial R_{si}}{\partial P_{oj}} & \dfrac{\partial R_{si}}{\partial S_{wj}} & \dfrac{\partial R_{si}}{\partial T_{fj}} & \dfrac{\partial R_{si}}{\partial S_{sj}} \end{bmatrix} \qquad (4.174)$$

The Jacobian matrix and the residual equations are updated after each iteration. The iteration continues until the relative changes in primary variables are smaller than given tolerance criteria.

An iterative solver is recommended here in solving the problem because the Jacobian matrices in multidimensional problems have large bandwidth. Even though direct solvers can also be employed in such problems, the low efficiency of calculation makes the application of the simulator limited.

4.5.2.2 Time Stepping Algorithms

Two time step options are implemented in the simulator — automatic time step control or constant time step size can be specified in the input data file. Although fully implicit solution techniques make the numerical solution stable under general conditions, there are, however, other limitiations that should be considered. In some thermal processes, arbitrary time step sizes may not ensure solution stability, or even convergence. Truncation error is also controlled by time step size. Also, some important physical phenomena may be missed by using arbitrarily large time steps.

The automatic time step algorithm implemented in the simulator uses the relative changes in primary variables to determining the time step size. The time step size is calculated from the most recent iteration and user-specified maximum time step size (Δt_{max}) minimum time step size (Δt_{min}), and allowable changes in primary variables ($\Delta P_{olim}, \Delta S_{wlim}, \Delta S_{slim}, \Delta T_{flim}$). The time step procedure is as follows. First calculate the maximum changes in the primary variables from the previous time step:

$$\Delta P_{o\,max}^{n} = \max_{ijk}\left\{\left|\Delta_t P_{o\,ijk}^{n}\right|\right\} \qquad (4.175a)$$

$$\Delta S_{w\,max}^{n} = \max_{ijk}\left\{\left|\Delta_t S_{w\,ijk}^{n}\right|\right\} \qquad (4.175b)$$

$$\Delta S_{s\,max}^{n} = \max_{ijk}\left\{\left|\Delta_t S_{s\,ijk}^{n}\right|\right\} \qquad (4.175c)$$

$$\Delta T^n_{f_{max}} = \max_{ijk}\left\{\left|\Delta_t T^n_{f_{ijk}}\right|\right\} \tag{4.175d}$$

Then adjust the current time step size for the next time step by:

$$\Delta t^{n+1} = \Delta t^n \cdot max\left\{\frac{\Delta P_{olim}}{\Delta P^n_{o_{max}}}, \frac{\Delta S_{wlim}}{\Delta S^n_{w_{max}}}, \frac{\Delta S_{slim}}{\Delta S^n_{s_{max}}}, \frac{\Delta T_{flim}}{\Delta T^n_{f_{max}}}\right\} \tag{4.176}$$

The new time step size is further checked after the current time step is finished. The new time step size and the results of iteration are accepted if the following conditions hold:

$$\Delta P^{n+1}_{omax} \leq C_1 \Delta P_{olim} \tag{4.177a}$$

$$\Delta S^{n+1}_{wmax} \leq C_2 \Delta S_{wlim} \tag{4.177b}$$

$$\Delta S^{n+1}_{smax} \leq C_3 \Delta S_{slim} \tag{4.177c}$$

$$\Delta T^{n+1}_{fmax} \leq C_4 \Delta T_{flim} \tag{4.177d}$$

where C_1, C_2, C_3 and C_4 are given constants greater than one. Otherwise, the time step size is recalculated using the same equations but with the current values of the primary variables.

A constant time step size requires a smaller time step size to guarantee convergence. And although smaller time steps take more computer time, sometimes readjusting the time step size takes even more time.

4.5.3 Matrix System Formulation

Fluids and energy flow between matrix blocks and the fracture within the same grid. This flow is expressed in terms of the flow from a representative matrix block multiplied by the number of matrix blocks in the grid. The representative matrix block can either be treated as a single block or divided into small cells (subgriding). Only the outer cells of the block exchange fluid and energy with the fracture system.

4.5.3.1 Subgriding

Matrix blocks are discretized in such a way that the matrix block can be divided into rectangular rings in ther lateral direction and layers in the vertical direction as shown in Fig. 4.57. In the lateral direction, the interfaces between volume elements are parallel to the nearest fracture. This choice of gridding assumes that the equipotential surfaces are characterized by having a constant distance from the nearest fracture. In the vertical direction, the matrix block is sliced into layers to model gravitational effects. Fluid segregation can also be simulated by imposing different boundary conditions at different elevations around the fracture. This scheme is the same as Beckner *et al.*'s (1991) and has features similar to the MINC (multiple interacting continua) approach (Pruess and Narasimhan, 1985; Wu and Pruess, 1986).

4.5.3.2 Transfer Flow Using Diffusion Equation

The two-dimensional diffusion equation can be used to describe the mass and energy flow in the matrix:

$$\frac{\partial}{\partial X}\left(D_{fx}\frac{\partial S_{wm}}{\partial X}\right)+\frac{\partial}{\partial Z}\left(D_{fz}\frac{\partial S_{wm}}{\partial Z}\right)=\frac{\partial S_{wm}}{\partial t} \tag{4.178}$$

$$\frac{\partial}{\partial X}\left(D_{Tx}\frac{\partial T_{m}}{\partial X}\right)+\frac{\partial}{\partial Z}\left(D_{Tz}\frac{\partial T_{m}}{\partial Z}\right)=\frac{\partial T_{m}}{\partial t} \tag{4.179}$$

where D_f and D_T are diffusion coefficients defined respectively by:

$$D_{fx}=\frac{K_{xm}K_{rom}}{\phi_{m}\mu_{o}B_{o}}f_{wx}\frac{\partial P_{cm}}{\partial S_{wm}} \tag{4.180}$$

$$D_{Tx}=\frac{\lambda_{mx}}{m_{r}} \tag{4.181}$$

$$m_{r}=(1-\phi_{m})\rho_{rm}C_{rm}+\phi_{m}(S_{wm}\rho_{w}C_{wm}+S_{om}\rho_{o}C_{om}) \tag{4.182}$$

No-flow boundary conditions are along the centerline of the block. The continuity of capillary pressure implies saturation along the matrix surface equal to S_{wf}. Heat conduction within the matrix is assumed to be the controling method of energy transfer. Thus the temperature at the matrix surface is equal to the temperature of the fluids T_f.

The finite-difference form of the diffusion equation in a subgrid can be easily derived as

$$\left[TT_{i,k}\,\Psi_{i,k-1}+TI_{i,k}\,\Psi_{i-1,k}+TC_{i,k}\,\Psi_{i,k}+TO_{i,k}\,\Psi_{i+1,k}+TB_{i,k}\,\Psi_{i,k+1}\right]^{n+1}$$

$$=\frac{V_{mi,k}}{\Delta t}\left(\Psi_{i,k}^{n+1}-\Psi_{i,k}^{n}\right) \tag{4.183}$$

where Ψ represents S_{wm} and T_{m}. TC is the summation of TT, TI, TO, and TB which are calculated as follows:

$$TT_{i,k}=TV_{i,k-\frac{1}{2}}D_{i,k-\frac{1}{2}} \tag{4.184a}$$

$$TB_{i,k}=TV_{i,k+\frac{1}{2}}D_{i,k+\frac{1}{2}} \tag{4.184b}$$

$$TI_{i,k}=TH_{i-\frac{1}{2},k}D_{i-\frac{1}{2},k} \tag{4.184c}$$

$$TO_{i,k}=TH_{i+\frac{1}{2},k}D_{i+\frac{1}{2},k} \tag{4.184d}$$

where *TH* and *TV* are geometrical coefficients and are given below.

The subgrid system reduces a 3D problem to a 2D problem. Therefore the formulations for the transmissibilities are different from the common form.

The volume fraction, $f_{i,k}$, for the i_{th} ring and k_{th} layer is defined by:

$$f_{i,k} = \frac{L_{xi,k}L_{yi,k}h_k}{V_{bm}} \quad j = 1, ..., N_{sub} \tag{4.185}$$

where V_{bm} is the bulk volume of the matrix block with dimensions of L_x, L_y, and L_z. We thus have:

$$\sum_{i=1}^{N_{sub}} f_{i,k} = 1 \quad k = 1, ..., M_{sub} \tag{4.186}$$

The dimensions for each subgrid then can be computed by:

$$L_{xi+\frac{1}{2},k} = L_x \left[\sum_{j=1}^{i} f_{j,k} \right]^{\frac{1}{2}} \quad k = 1, ..., M_{sub} \tag{4.187}$$

and

$$L_{yi+\frac{1}{2},k} = L_y \left[\sum_{j=1}^{i} f_{j,k} \right]^{\frac{1}{2}} \quad k = 1, ..., M_{sub} \tag{4.188}$$

The geometrical part of the transmissibilities for subgrid (i,k) in the lateral direction can be calculated by:

$$TH_{i+\frac{1}{2},k} = 8 \cdot \left(\frac{L_{yi,k}h_k}{L_{xi+1,k} - L_{xi,k}} + \frac{L_{xi,k}h_k}{L_{yi+1,k} - L_{yi,k}} \right) \tag{4.189}$$

For the innermost subgrid:

$$TH_{\frac{1}{2},k} = 8 \left(\frac{L_{y\frac{1}{2},k}h_k}{L_{x\frac{1}{2},k}} + \frac{L_{x\frac{1}{2},k}h_k}{L_{y\frac{1}{2},k}} \right) \tag{4.190}$$

For the outermost subgrid:

$$TH_{N_{sub},k} = 8 \left(\frac{L_{yN_{sub},k}h_k}{L_x - L_{xN_{sub}-1,k}} + \frac{L_{xN_{sub},k}h_k}{L_y - L_{yN_{sub}-1,k}} \right) \tag{4.191}$$

In the vertical direction, the geometrical part of the internal subgrid transmissibilities are computed by:

$$TV_{i,k+\frac{1}{2}} = 2f_i \frac{L_x L_y}{h_{k+1} + h_k} \qquad (4.192)$$

For the top subgrids:

$$TV_{i,\frac{1}{2}} = 2f_i \frac{L_x L_y}{h_1} \qquad (4.193)$$

For the bottom subgrids:

$$TV_{i,M_{ab}+\frac{1}{2}} = 2f_i \frac{L_x L_y}{h_{M_{ab}}} \qquad (4.194)$$

The diffusion coefficient D can be either D_f or D_T:

$$D_{Tmi,k-\frac{1}{2}} = \frac{k_{hmi,k-\frac{1}{2}}}{m_{ri,k-\frac{1}{2}}} \qquad (4.195)$$

$$D_{fmi,k-\frac{1}{2}} = \frac{k_m k_{romi,k-\frac{1}{2}}}{\phi_m \mu_{om}} f_{wi,k-\frac{1}{2}} \left(\frac{dP_{cowm}}{dS_{wm}} \right)_{i,k-\frac{1}{2}} \qquad (4.196)$$

where $D_{Ti,k-\frac{1}{2}}$ is arithmetically averaged. One-point upstream weighted relative permeability is used to evaluate $D_{fi,k-\frac{1}{2}}$. Since fluid potential is not solved in the matrix system, capillary pressure is used to determine the upstream weighting.

If no capillary pressure is assumed in the fracture, the saturation boundary condition is simply:

$$S_{wm} = 1 - S_{or} \qquad (4.197)$$

Since partial immersion of matrix blocks is possible, the diffusion coefficient at the block surface is modified by fracture water saturation:

$$D_f \big|_{surface} = D_f \cdot S_{wf} \qquad (4.198)$$

The finite-difference equations are solved implicitly using a scheme similar to that discussed for the fracture system. The matrix-fracture transfer flow can then be computed by:

$$\tau_{wmf} = N_m \left[\sum_{i=1}^{N_{mi}} TV_{i,\frac{1}{2}} k_{hmi,\frac{1}{2}} (T_f - T_{mi,\frac{1}{2}}) + \sum_{i=1}^{N_{mi}} TV_{i,M_{ab}+\frac{1}{2}} k_{hmi,M_{ab}+\frac{1}{2}} (T_f - T_{mi,M_{ab}+\frac{1}{2}}) \right]$$

$$+ \sum_{k=1}^{M_{st}} TH_{N_{sb}+\frac{1}{2},k} k_{hmN_{sb}+\frac{1}{2},k}(T_f - T_{mN_{sb}+\frac{1}{2},k}) \Bigg] \tag{4.199}$$

$$\tau_{wmf} = N_{in}\Bigg[\sum_{i=1}^{N_{sb}} TV_{i,\frac{1}{2}} D_{wmi,\frac{1}{2}}(S_{wf} - S_{wmi,\frac{1}{2}}) + \sum_{i=1}^{N_{sb}} TV_{i,M_{sb}+\frac{1}{2}} D_{wmi,M_{sb}+\frac{1}{2}}(S_{wf} - S_{wmi,M_{sb}+\frac{1}{2}})$$

$$+ \sum_{k=1}^{M_{st}} TH_{N_{sb}+\frac{1}{2},k} D_{wmN_{sb}+\frac{1}{2},k}(S_{wf} - S_{wmN_{sb}+\frac{1}{2},k}) \Bigg] \tag{4.200}$$

The three terms on the righthand side of the above equations represent the matrix-fracture transfer flow through the top, bottom, and vertical surfaces, respectively.

4.5.4 Well Model

Wells are assumed to be connected to the fracture system only. The flow rate, bottomhole pressure and gridblock pressure have the relationship

$$q_{ok} = PI_k \lambda_{ok}(P_{wfk} - P_{ok}) \tag{4.201}$$

where the PI_k is the productivity index for layer k.

There are four well models implemented in the simulator. Similar formulations can be found in a paper by Fanchi *et al.* (1982).

It is assumed that the well is completed in K layers.

4.5.4.1 Injection Rate Specified

In this case the total water and/or gas injection rate (Q_w and Q_g) and well injectivity index (WI) must be specified for each layer. The injection rate for each layer is then allocated as follows:

Water injection rate:

$$Q_{wk} = Q_w \frac{\left[WI(\lambda_o + \lambda_w + \lambda_g)\right]_k}{\sum_{k=1}^{K}\left[WI(\lambda_o + \lambda_w + \lambda_g)\right]_k} \tag{4.202}$$

Gas injection rate:

$$Q_{gk} = Q_g \frac{\left[WI(\lambda_o + \lambda_w + \lambda_g)\right]_k}{\sum_{k=1}^{K}\left[WI(\lambda_o + \lambda_w + \lambda_g)\right]_k} \tag{4.203}$$

4.5.4.2 Oil Production Rate Specified

In this case, the oil production rate, Q_o , is specified. The production rates of layer k are:

Oil:

$$Q_{ok} = Q_o \frac{\left[(PI)\lambda_o/B_o\right]_k}{\sum\limits_{k=1}^{T}\left[(PI)\lambda_o/B_o\right]_k} \tag{4.204}$$

Water:

$$Q_{wk} = Q_{ok}\left(\frac{\lambda_w/B_w}{\lambda_o/B_o}\right)_k \tag{4.205}$$

Gas:

$$Q_{gk} = Q_{gk}\left(\frac{\lambda_g/B_g}{\lambda_o/B_o}\right)_k \tag{4.206}$$

4.5.4.3 Total Production Rate Specified

When the total reservoir production rate, Q_T , is specified, we first compute the phase mobility ratio for each layer:

Oil mobility ratio:

$$\alpha_{oT} = \sum\limits_{k=1}^{K}\left[\frac{\lambda_o}{\lambda_o + \lambda_w + \lambda_g}\right]_k \tag{4.207}$$

Water mobility ratio:

$$\alpha_{wT} = \sum\limits_{k=1}^{K}\left[\frac{\lambda_w}{\lambda_o + \lambda_w + \lambda_g}\right]_k \tag{4.208}$$

Gas mobility ratio:

$$\alpha_{gT} = \sum\limits_{k=1}^{K}\left[\frac{\lambda_g}{\lambda_o + \lambda_w + \lambda_g}\right]_k \tag{4.209}$$

The total oil rate then can be computed by

131

$$Q_o = \frac{Q_T}{\overline{B}_o}\left(\frac{\alpha_{oT}}{\alpha_{oT} + \alpha_{wT} + \alpha_{gT}}\right) \tag{4.210}$$

where

$$\overline{B}_o = \frac{1}{K}\sum_{k=1}^{K}(B_o)_k \tag{4.211}$$

is the average oil formation volume factor for all layers in which the well is completed.

4.5.4.4 Bottomhole well pressure specified

In this case, the injection or production rate for each layer is:

$$Q_{\alpha k} = PID \cdot \left[\lambda_\alpha \left(P_\alpha - P_{wf}\right)\right]_k \tag{4.212}$$

where *PID* is production index for a producer and injection index for a injector.

4.5.5 Simulator Verification

As mentioned earlier, the simulator can simulate both single-porosity and dual porosity reservoirs. Both cases are verified in this section.

4.5.5.1 Single Porosity Waterflooding

The Buckley-Leverrett problem is a typical one-dimensional incompressible waterflooding case. No capillary pressure is considered. To simulate this problem, only the fracture system of the simulator is used. The input data is listed in Table 4.13. Figure 4.58 shows a comparison of the analytical solution with the simulation results. A linear model with 500 gridblocks is used. The simulation results match the analytical solution well except for some numerical smearing at the displacement front.

4.5.5.2 Single Porosity Hot Waterflooding

Lauwerier (1955) considered a situation in which hot water is injected into a cold reservoir. As the hot water flow through the reservoir, heat is lost to the overburden and underburden as shown in Fig. 4.59. In this case, it is assumed that there are no vertical temperature gradients in the reservoir. Hot water is injected at a constant rate and temperature. Table 4.14 gives the input data.

Figure 4.60 illustrates a comparison of the results. Simulated results match the analytical solution very well. Two hundred gridblocks were used in this calculation.

4.5.5.3 Single Porosity Steamflooding

Marx and Langenhiem (1959) solved the problem of a growing steam zone with heat losses to an overburden and underburden. As steam is injected into a lateral formation, the steam zone spreads laterally. Injected heat increases the heat either stored in the steam zone or is lost to the overburden and underburden. A thermal efficiency factor is used to indicate steam zone growth. Heat lost from the reservoir varies over a

large range with dimensionless time as shown in Fig. 4.62. 100% quality steam was used in this simulation. Two hundred blocks of size 0.2x2.0x0.5 (m^3) were used in simulating the one-dimensional case. Two-dimensional modeling is shown in Fig. 4.62. 10 by 10 gridblocks with block sizes of 1.0x1.0x1.0 (m^3) were used. We see that the analytical solutions are matched in both 1D and 2D cases. The late-time deviation from the analytical solution is because of the breakthrough of steam because of limited reservoir size.

4.5.5.4 Dual Porosity Waterflooding

Waterflooding of an ideal fractured reservoir was also simulated. A detailed description of the case is listed in Table 4.15. Other data are adopted from Beckner *et al.* (1988). The gridblocks are 5 by 5. No subgridding is used in the matrix. The system is assumed to be incompressible. Therefore the main oil recovery mechanism is countercurrent imbibition. An excellent match was obtained compared to the results of the dual porosity simulator developed for this study. Figure 4.63 shows the water cut obtained from the two simulators.

4.5.5.5 Comparison of Thermal and Isothermal Process in Fractured Reservoir

To investigate the efficiency of thermal process in fractured reservoir, the comparision runs was performed. The comparison between thermal process and isothermal process is shown in Figure 4.64. The two isothermal cases were simulated in two different temperatures. One is at the initial temerature of the thermal simulation and the other is near the final reservoir temperature of the thermal simulation. It is seen that the recovery of thermal process is higher than both of the isothermal processes. Therefore it can be concluded that not only does the oil viscosity lowered by thermal processes increase oil viscosiry, but also the thermal expansion is a big contribution.

4.5.5.6 Effects of Matrix Block Size

The effects of matrix block size was investigated. Four different simulation runs were performed with the blocks of 1, 4, 8 and 16 in rach grid. The results are shown in Figure 4.65. For the smaller block size, the matrix can be heated faster and the flow path of oil from matrix to fracture is shorter, therefore, a higher oil recovery is resulted.

Table 4.1. Input data for Buckley-Leverett problem.

Parameters	Values
Reservoir length, L	2.0 ft
Reservoir thickness, h	0.1 ft
Reservoir width, W	0.1 ft
Porosity, ϕ	0.20
Permeability, k	500 md
Oil viscosity, μ_o	20.0 cp
Water viscosity, μ_w	1.0 cp
Initial water saturation, S_{wI}	0.20
Final water saturation, S_{wJ}	0.65
Exponent of k_{ro}	1.0
Exponent of k_{rw}	0.2
End-point k_{ro}	1.0
End-point k_{rw}	0.2
Injection rate, q_{winj}	0.01 ft^3/D

Table 4.2. Warren and Root's data (1963) for pressure buildup test.

Parameters	Values
Fracture permeability, k_f	40 md
Reservoir thickness, h	20 ft
Outer reservoir radius, r_e	∞
Wellbore radius, r_w	0.316 ft
Reservoir storativity, $\phi_m c_m + \phi_f c_f$	2.64×10^{-6} psi^{-1}
Oil viscosity, μ_o	2.0 cp
Oil formation volume factor, B_o	1.23
Initial pressure, p_I	4000 psia
Production rate, q_o	115 STB/D
Production time, t_s	21 days
Interporosity parameter, λ	5×10^{-6}

Table 4.3. Calculated input data for simulation runs based on Warren and Root's data (1963).

Storativity ratio	0.0	0.0010	0.010	0.10	1.0
Fracture porosity	0.0	0.0002	0.002	0.02	0.2
Matrix porosity	0.2	0.1998	0.198	0.18	0.0

135

Table 4.4. Parameters for ideal fractured reservoir.

Parameters	Values
Reservoir size	$50 \times 50 \times 10$ ft
Matrix block size	$10 \times 10 \times 10$ ft
Matrix porosity, ϕ_m	0.30
Fracture aperture, W_f	0.0339 ft
Fracture porosity, ϕ_f	1.00
Equivalent fracture porosity, $\bar{\phi}_f$	0.0081
Fracture permeability, k_f	100.0 d
Equivalent fracture permeability, $\bar{k}_f$	405.1 md
Injection rate, q_{inj}	0.25 STB/D
Oil viscosity, μ_o	1.0 cp
Water viscosity, μ_w	0.8 cp

Table 4.5. Kleppe and Morse's (1974) experimental data.

Parameters	Values
Matrix permeability, k_m	290 md
Matrix porosity, ϕ_m	0.225
Core diameter	9.87 cm
Inside diameter of tube	10.39 cm
Core height, h	122.8 cm
Oil viscosity, μ_o	2.3 cp
Water viscosity, μ_w	1.0 cp
Oil density, ρ_o	0.811 g/cm^3
Water density, ρ_w	1.02 g/cm^3
Pore volume of core	2114 cm^3
Pore volume of fracture	1017 cm^3
Low injection rate	3.3 cm^3/min
High injection rate	35 cm^3/min

Table 4.6. Property dependence on primary variables of single matrix block thermal code.

	P_o	S_w	T
$\rho_o(B_o)$	X		X
$\rho_w(B_w)$			X
ρ_r			
μ_o	X		X
μ_w			X
ϕ	X		X
K_r		X	
P_c		X	
h_o			X
h_w			X
u_o	X		X
u_w	X		X
u_r			X
λ_t		X	X

Table 4.7. Relative permeability and capillary pressure used in single matrix block thermal studies.

S_w	k_{ro}	k_{rw}	P_c (psi)
0.350	0.7500	0.0000	5.65
0.375	0.5580	0.0007	3.95
0.400	0.4050	0.0039	2.91
0.425	0.2860	0.0110	2.31
0.450	0.1950	0.2200	1.88
0.475	0.1280	0.0380	1.54
0.500	0.0800	0.0600	1.27
0.525	0.0470	0.0880	1.04
0.550	0.0250	0.1230	0.84
0.575	0.0120	0.1660	0.66
0.600	0.0050	0.2160	0.50
0.625	0.0016	0.2740	0.36
0.650	0.0003	0.3400	0.23
0.675	0.00002	0.4150	0.11
0.700	0.0000	0.5000	0.00

Note: These data for relative permeability can be reproduced by taking $k^o_{rw}=0.50$, $k^o_{ro}=0.75$, $n_w \approx 3.2$ and $n_o \approx 1.8$.

Table 4.8. Petrophysical and PVT data used in single matrix block thermal studies.

Porosity:		
Initial	17.6	%
Compressibility C_r	5.076×10^{-10}	Pa^{-1}
Thermal Expansion β_r	9.72×10^{-5}	K^{-1}
Rock Density	2643.045	kg/m3
Oil Density at 60°F (328K)	816.94	kg/m^3
Oil Viscosity at 80°F (310K)	4.6×10^{-3}	Pa.s
Thermal exponent b	3.73	
Initial Pressure	11.72	MPa
Rock Conductivity (constant)	2.0	W/m.K
Matrix Permeability	0.0553	μm^2
Fracture Permeability	537	μm^2
Irreducible Water Saturation	35	%
Residual Oil Saturation	30	%
Initial Reservoir Temperature	27	°C
Hot Water Temperature	127	°C

Table 4.9. Parameters used in Fig. 4.50.

Activation energy, E	62,700 J/mole
Kinetic exponential coefficient, k_0	0.025 sec^{-1}
Concentration ratio of CO_2 in oil vs. water, f_{ow}	2.0
Critical gas saturation, S_{gc}	0.2
Water saturation, S_w	0.5
Oil saturation, S_o	0.5
Porosity, ϕ	0.2
CO_2 compressibility factor, z	1.0

Table 4.10. Parameters used in Figs. 4.51 through 4.53.

Initial temperature, T_i	50°C
Initial water saturation, S_{wi}	0.35
Initial oil saturation, S_{oi}	0.65
Critical gas saturation, S_{gc}	0.2
Fracture spacing, d	4 m
Matrix block porosity, ϕ	0.2
Matrix block permeability, k_x	55.3 md
Activation energy, E	62,700 J/mole
Kinetic pre-exponential coefficient, k_0	0.025 sec^{-1}
CO_2 compressibility factor, z	1.0
Concentration ratio of CO_2 in oil and water, f_{ow}	1.0

Table 4.11. Relative permeability parameters used in Figs. 4.51 through 4.53.

k°_{rw}	0.50	S_{wi}	0.35	n_w	3.2
k°_{row}	0.75	S_{orw}	0.30	n_{ow}	1.8
k°_{rog}	0.50	S_{org}	0.35	n_{og}	3.2
k°_{rg}	0.75	S_{gr}	0.20	n_g	1.8
S_{wc}	0.35				

Table 4.12. Capillary pressure vs. oil saturation used for Figs. 4.51 through 4.53.

S_o	P_{cow} (kPa)
0.0	37.9
0.1	30.3
0.2	23.4
0.3	17.2
0.4	11.7
0.5	6.89
0.6	3.45
0.7	2.07
0.8	1.38
0.9	0.69

Table 4.13. Input data for the Buckley-Leverett problem.

Reservoir length	20 m
Reservoir thickness	1 m
Reservoir width	1 m
Porosity	0.10
Permeability	100 md
Oil viscosity	3 cp
Water viscosity	1 cp
Initial water saturation	0.0
Final water saturation	1.0
Exponent of kro	2.0
Exponent of krw	2.0
Endpoint kro	1.0
Endpoint krw	0.0

Table 4.14. Input data for Lauwerier (1955) problem.

Reservoir length	305 m
Reservoir thickness	3.048 m
Reservoir width	3.048 m
Porosity	0.35
Permeability	10.0 d
Thermal conductivity	2.524 w/m K
Vol. heat capacity	2.35 mJ $/m^3$K
Initial temperature	288.7 K
Hot water temperature	366.48 K
Injection rate	7.36×10^{-5} m^3/s

Table 4.15. Isothermal dual porosity simulation input data.

Reservoir size	50x50x10 ft^3
Matrix block size	10x10x10 ft^3
Matrix porosity	0.30
Fracture porosity	0.0081
Fracture permeability	405 md
Matrix permeability	2 md
Water injection rate	0.25
Oil viscosity	1.0 cp
Water viscosity	0.8 cp
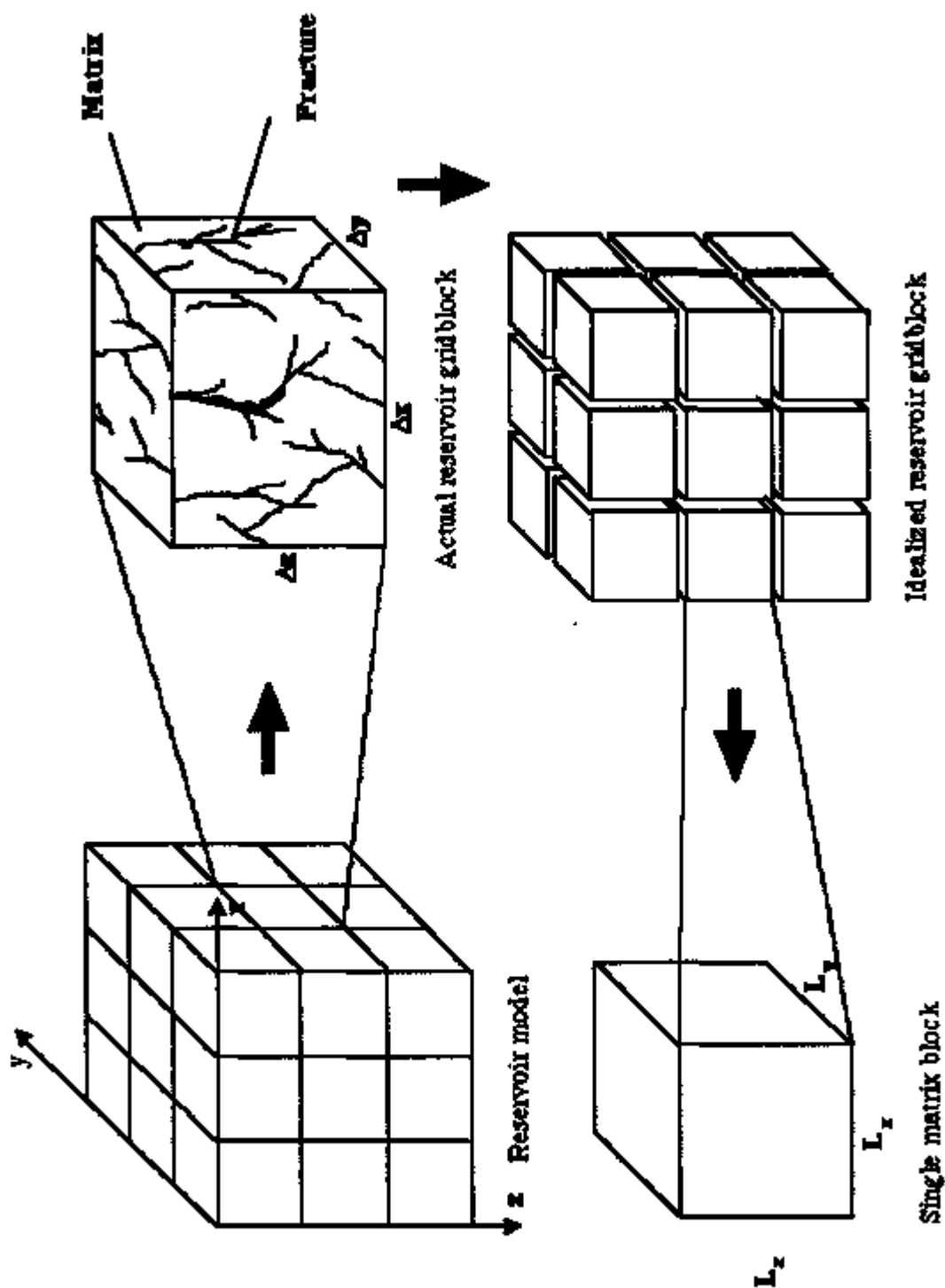
Fig. 4.1. Idealization of a naturally fractured reservoir by dual porosity model.
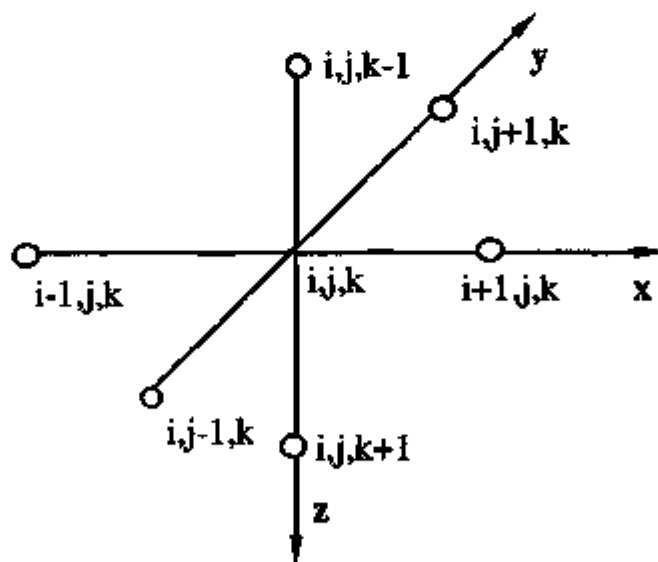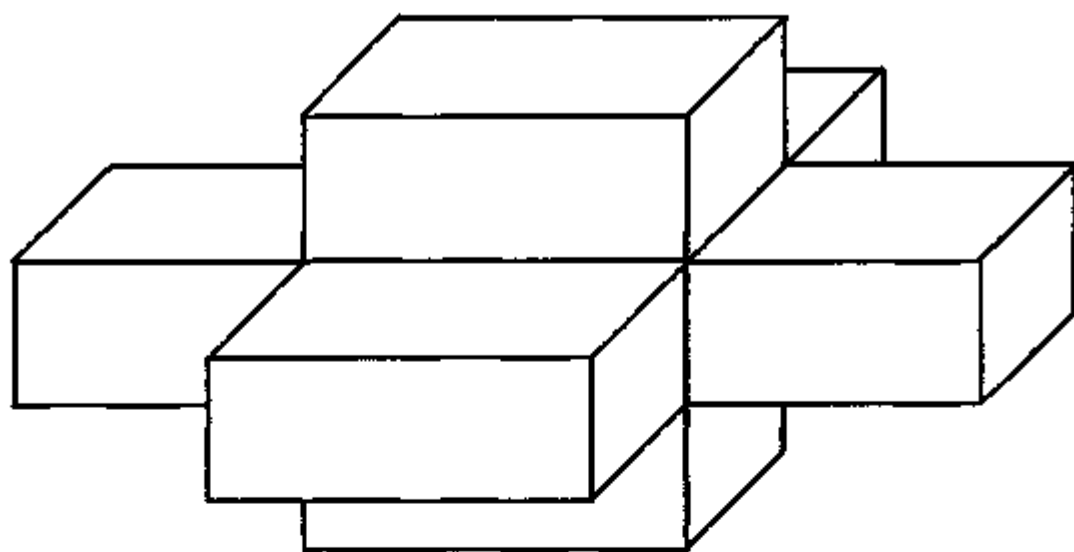
Fig. 4.2. Nodal representation of a three-dimensional array of reservoir gridblocks.

144
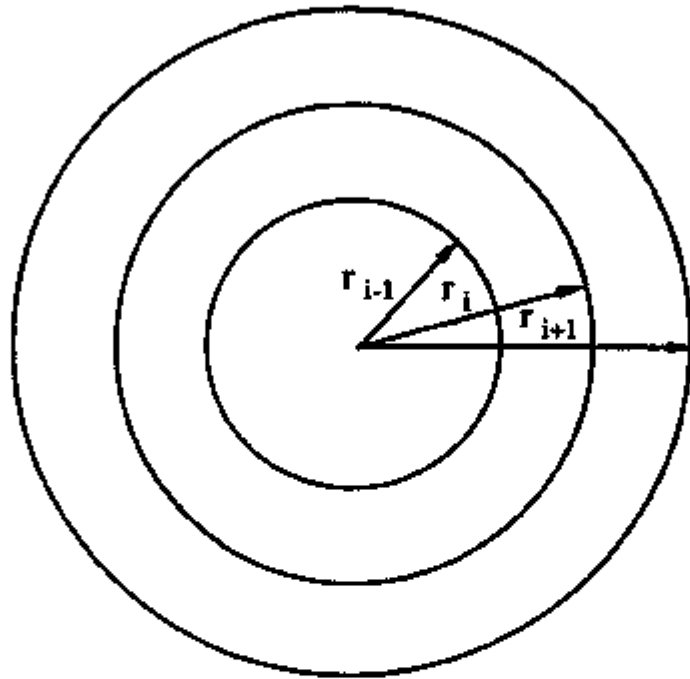
Fig. 4.3. Radial grid system.
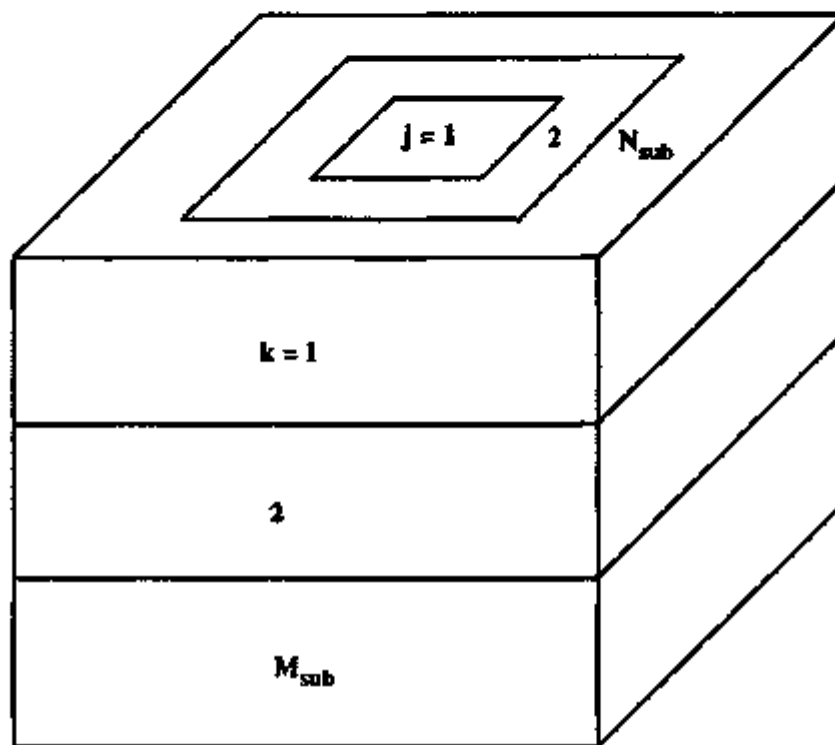
Fig. 4.4. Schematic of matrix block subgrids.
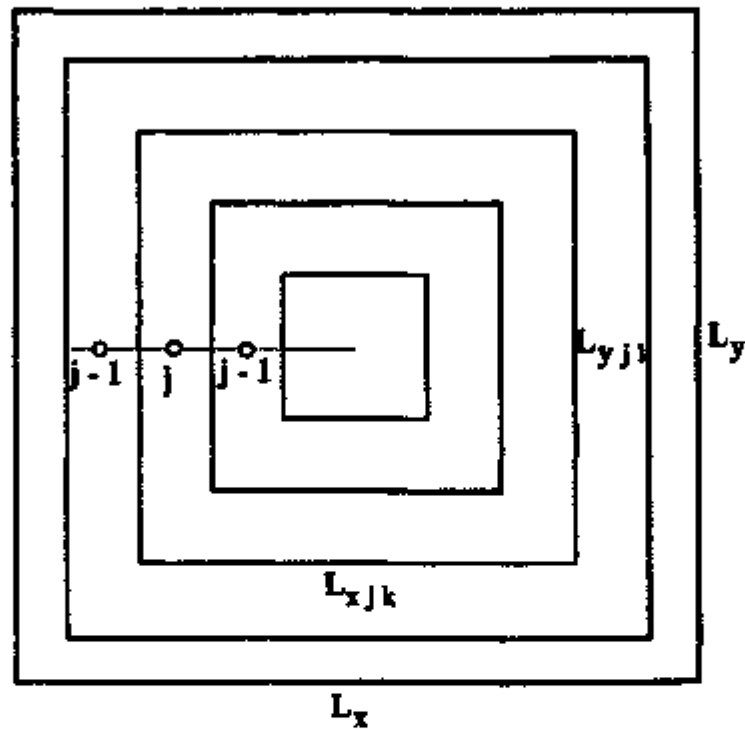
Fig. 4.5. Schematic of matrix subgrids in the lateral direction.
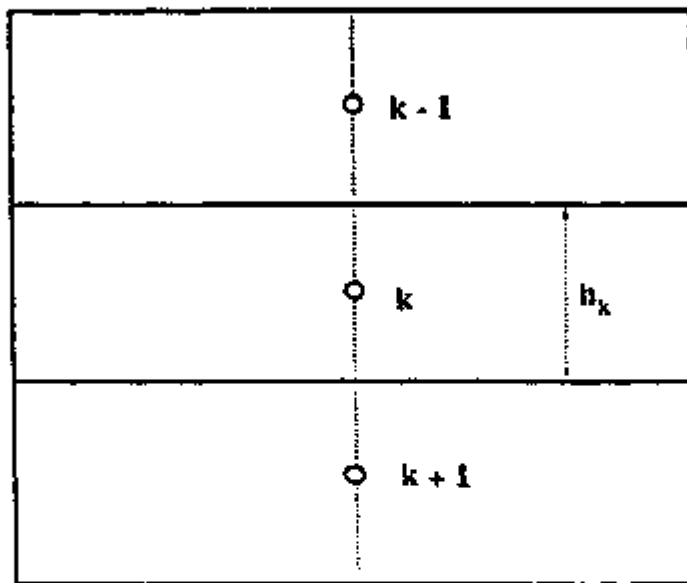
Fig. 4.6. Schematic of matrix subgrids in the vertical direction.
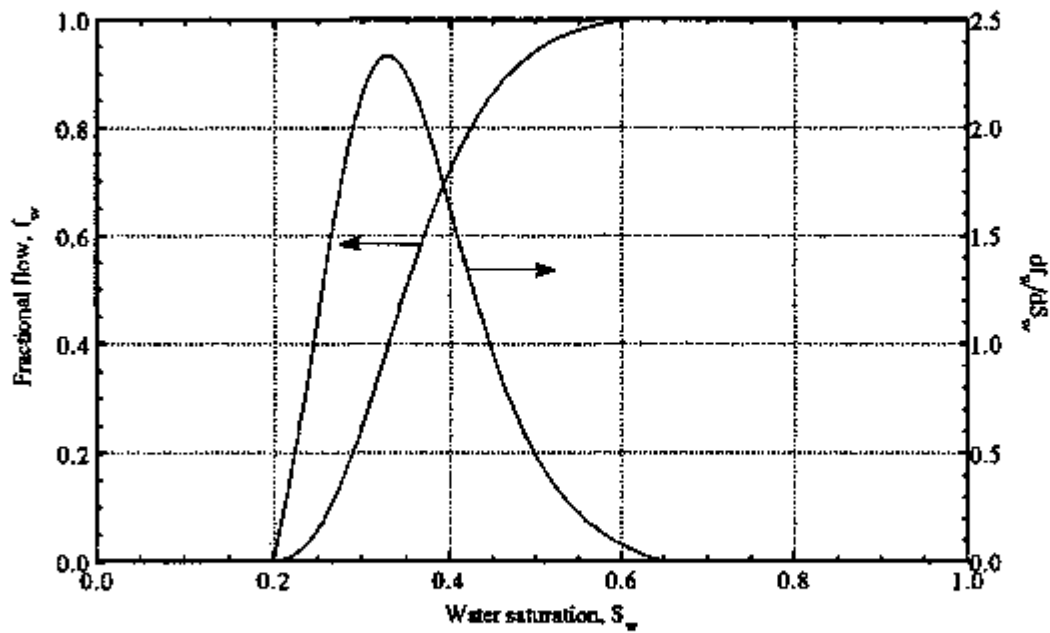
Fig. 4.7a Fractional flow and its derivative with respect to saturation.
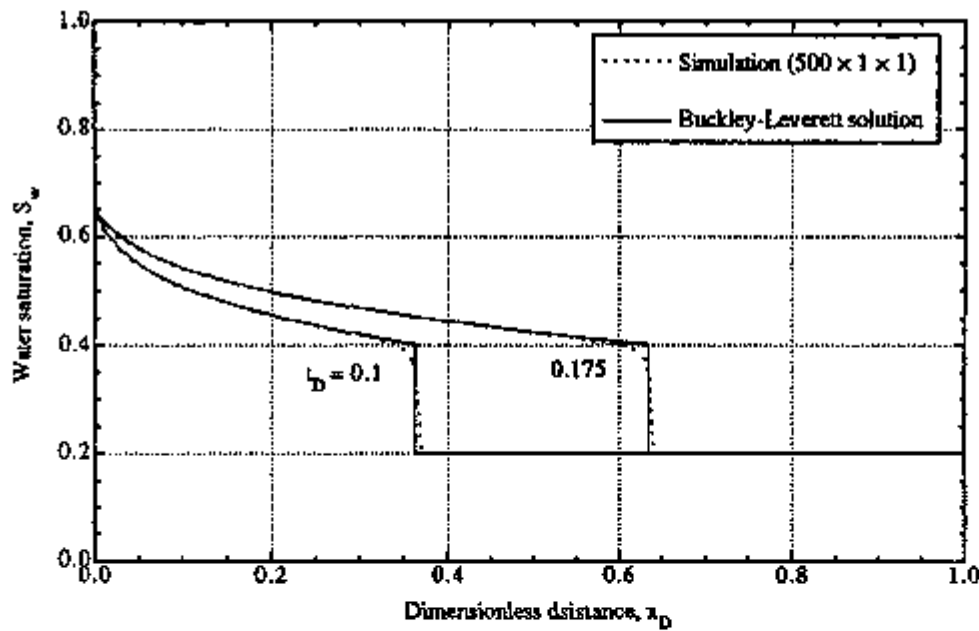
Fig. 4.7b   Comparison of water saturation profile of the Buckley-Leverett solution and UTDUAL results with a fracture system using 500 gridblocks.
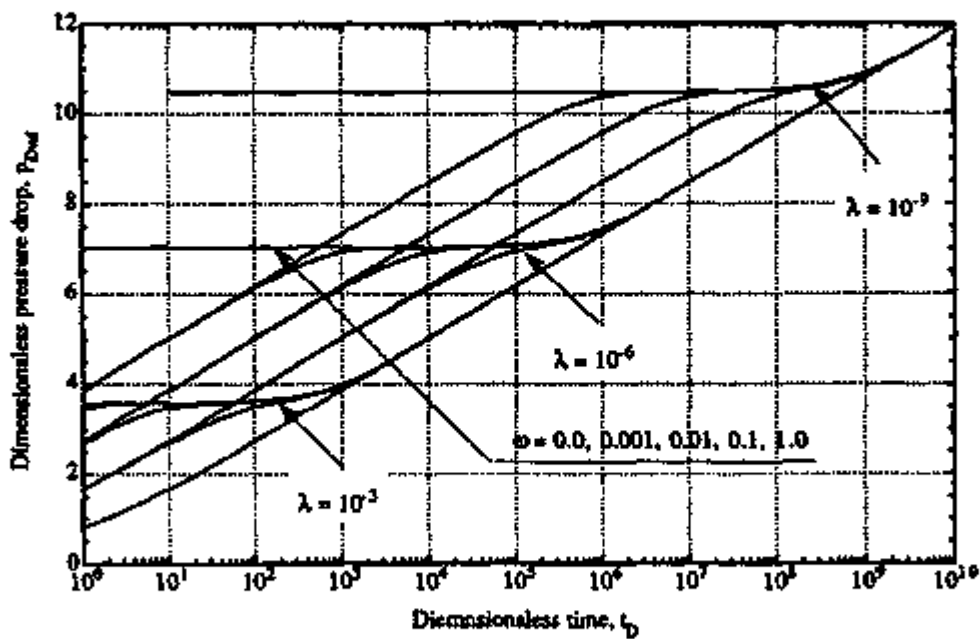
Fig. 4.8 Dimensionless pressure drop of Warren and Root's (1963) model.
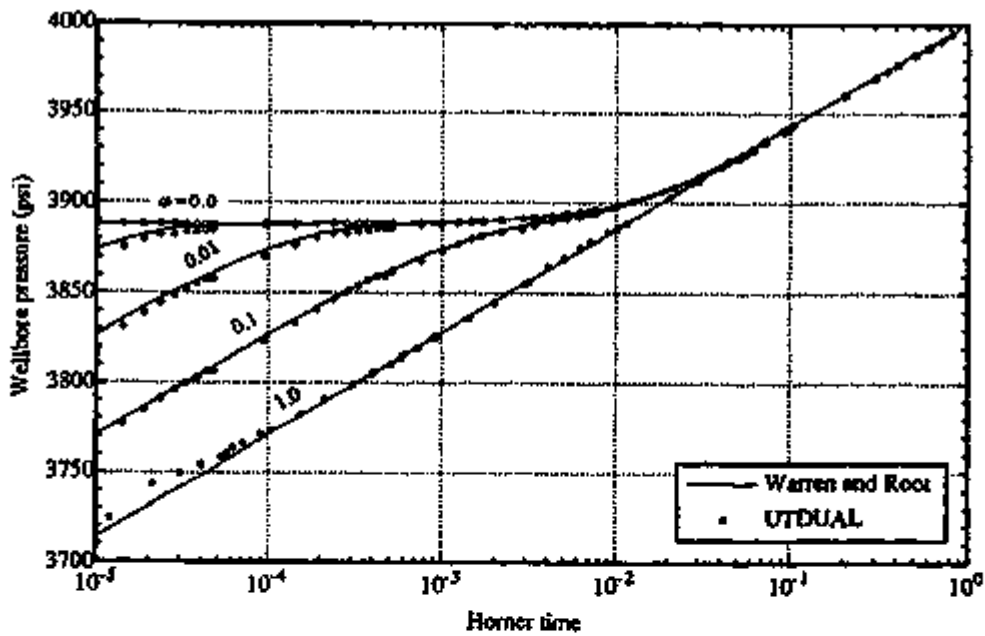
Fig. 4.9   Comparison of Warren and Root's solution (1963) and UTDUAL results.

150
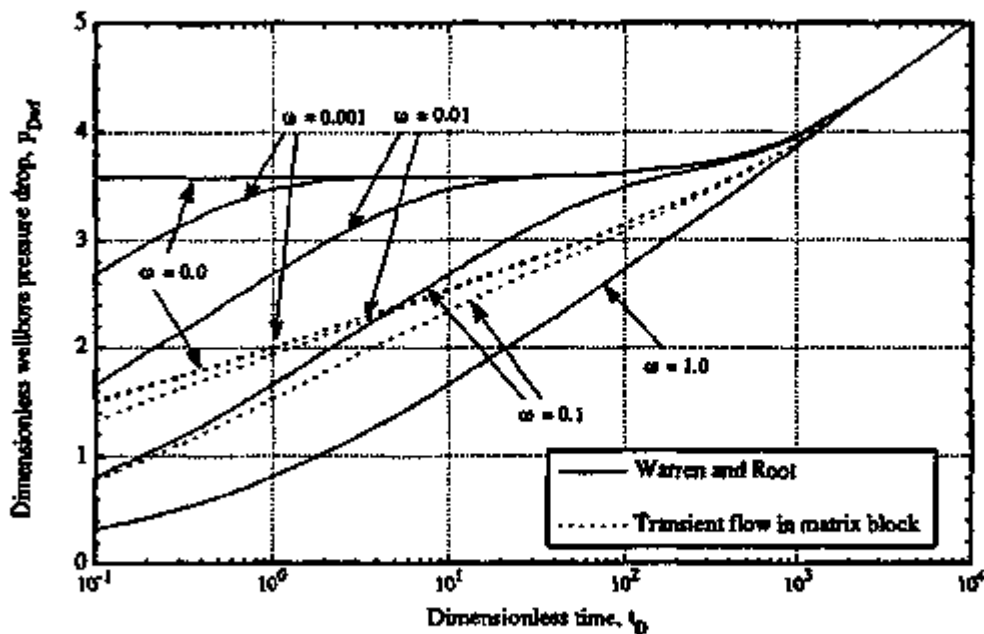
Fig. 4.10a Comparison of Warren and Root's (1963) solution and new transient solution
with square matrix blocks and $\lambda = 10^{-3}$.
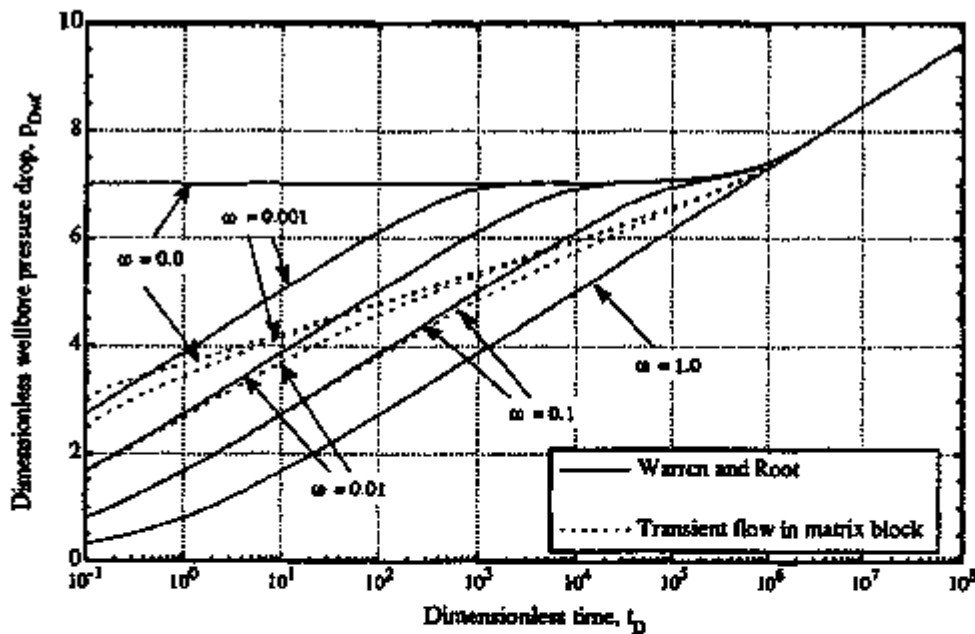
Fig. 4.10b Comparison of Warren and Root's (1963) solution and new transient solution
with square matrix blocks and $\lambda = 10^{-6}$.

151
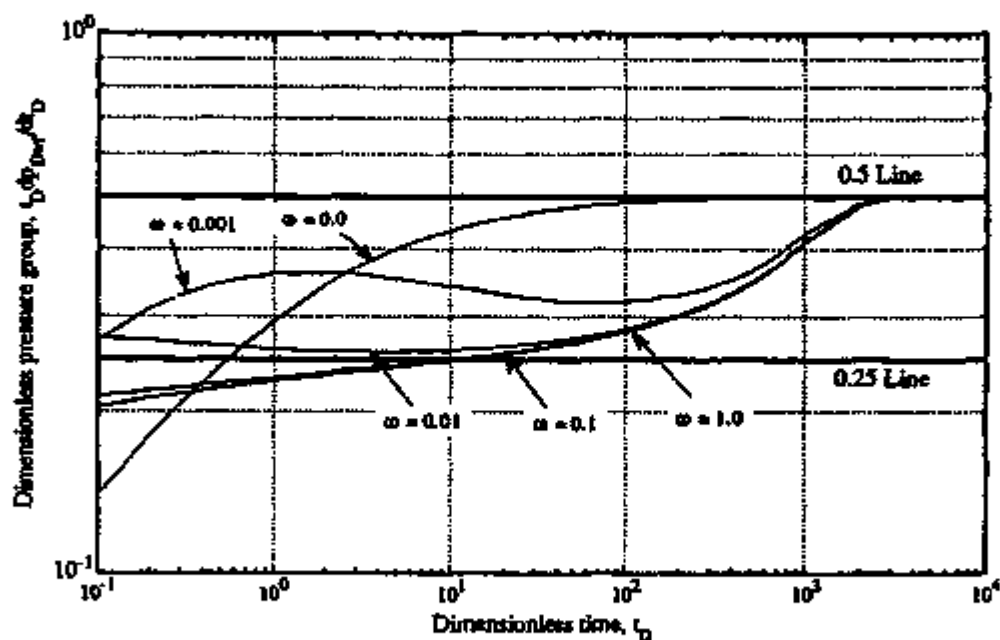
Fig. 4.10c Derivative curves of new transient solution with square matrix blocks and
$\lambda = 10^{-3}$.
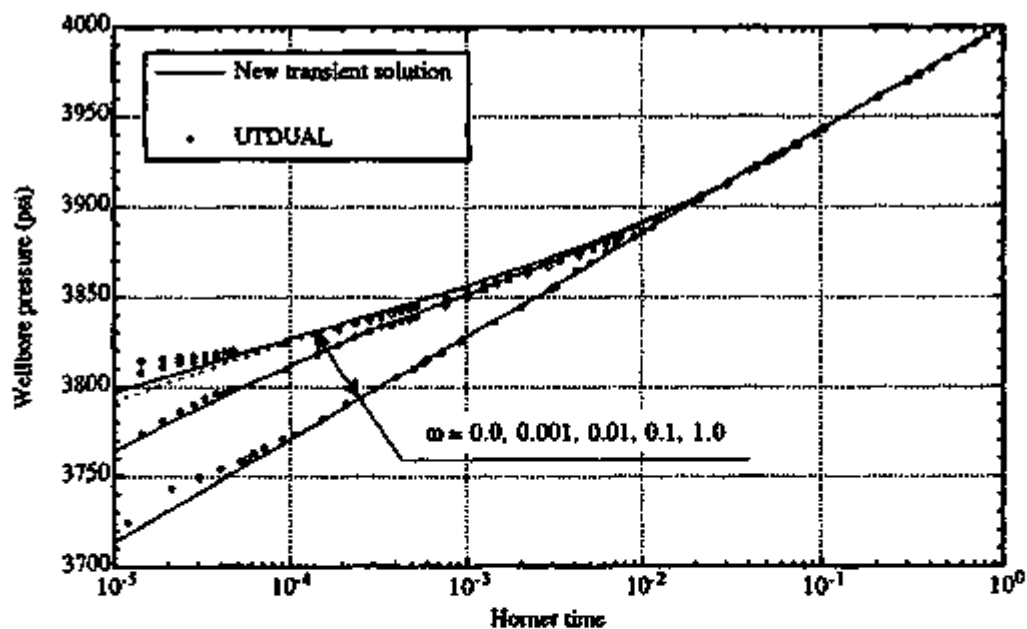
Fig. 4.11 Comparison of new transient solution with square matrix blocks and
UTDUAL results with 8 matrix subgrids.
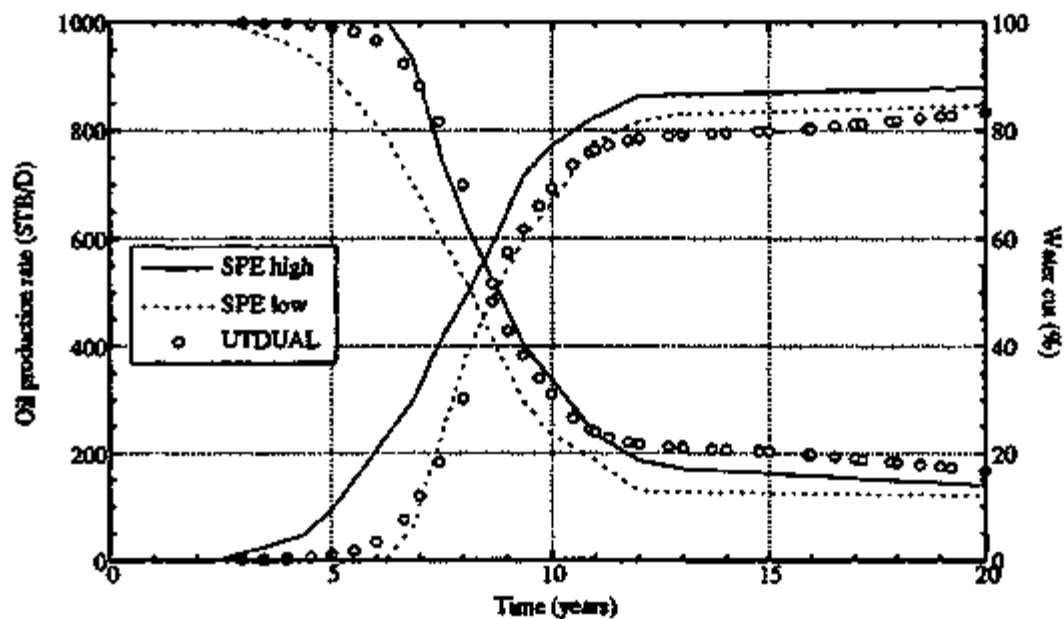
Fig. 4.12   UTDUAL results of the SPE sixth Comparative Project, water injection case.
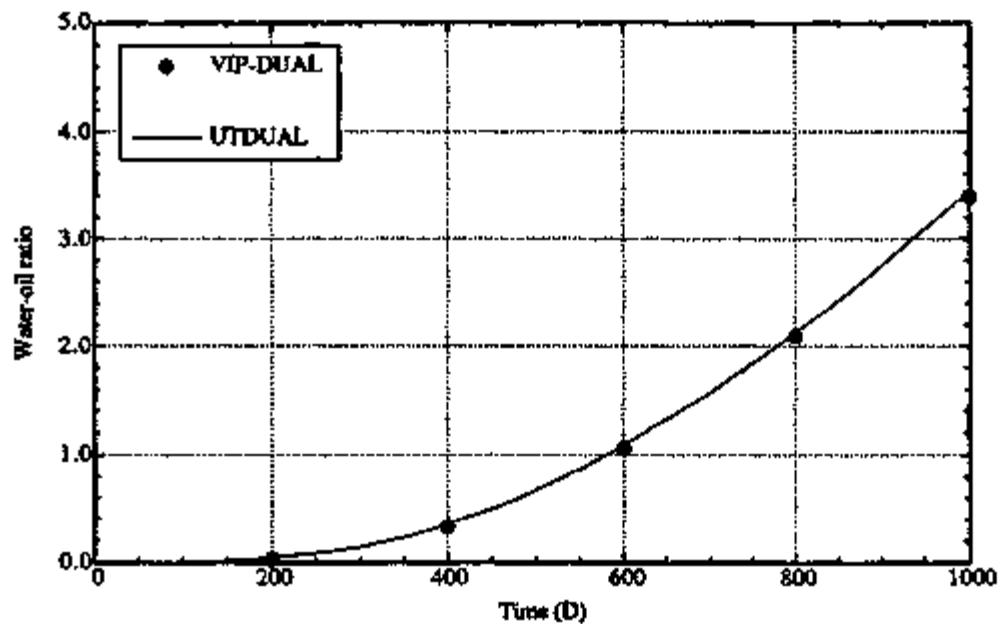
Fig. 4.13a Comparison between VIP-DUAL and UTDUAL for Kazemi *et al.'s* (1976) five-spot reservoir.

153
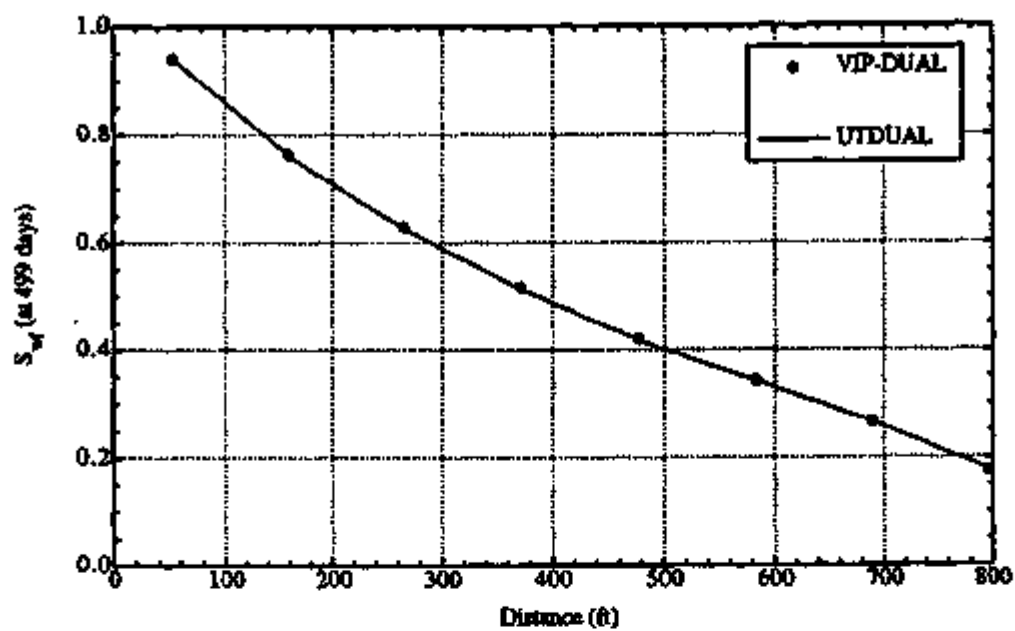
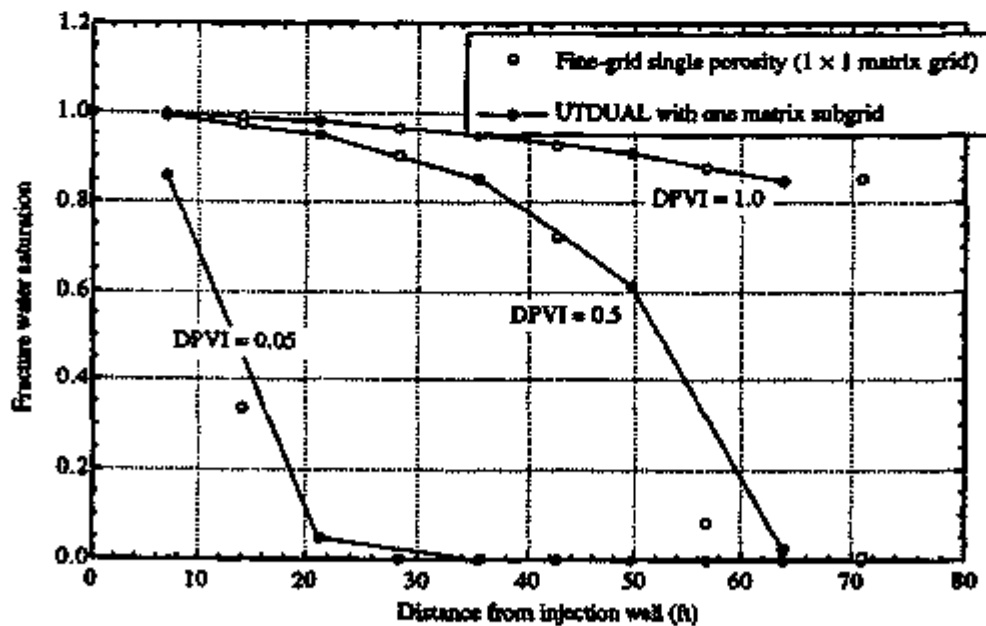Fig. 4.13b Fracture water saturation profile along the diagonal line connecting two wells.
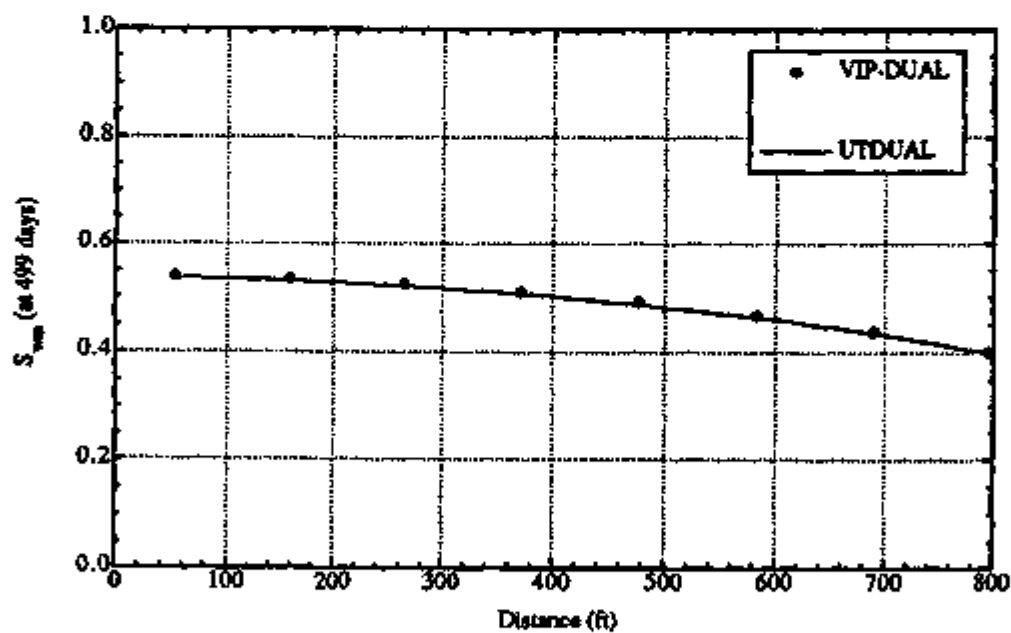
Fig. 4.13c Matrix water saturation profile along the diagonal line connecting two wells.

154
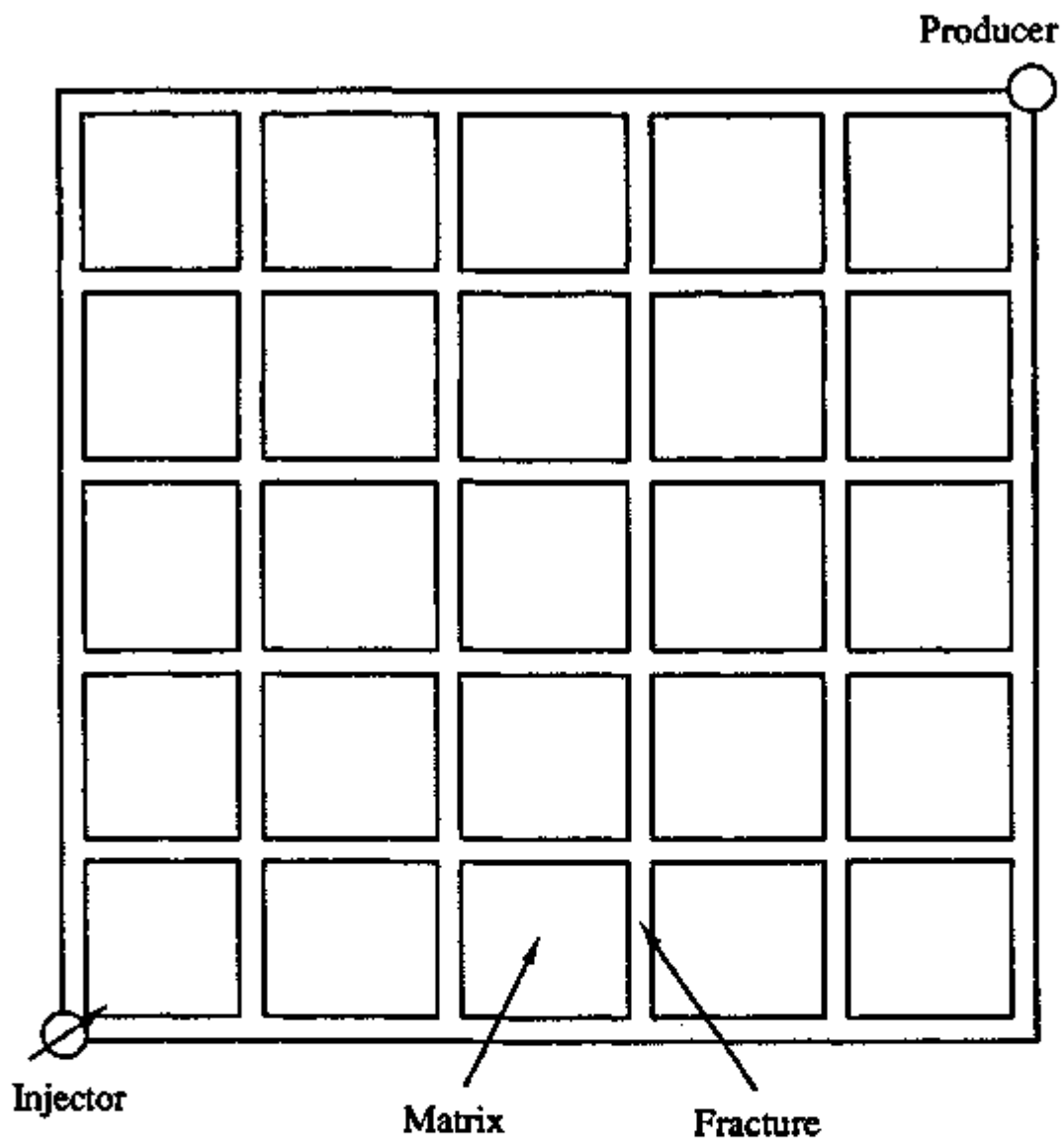
Fig. 4.14. Schematic of ideal fractured reservoir.
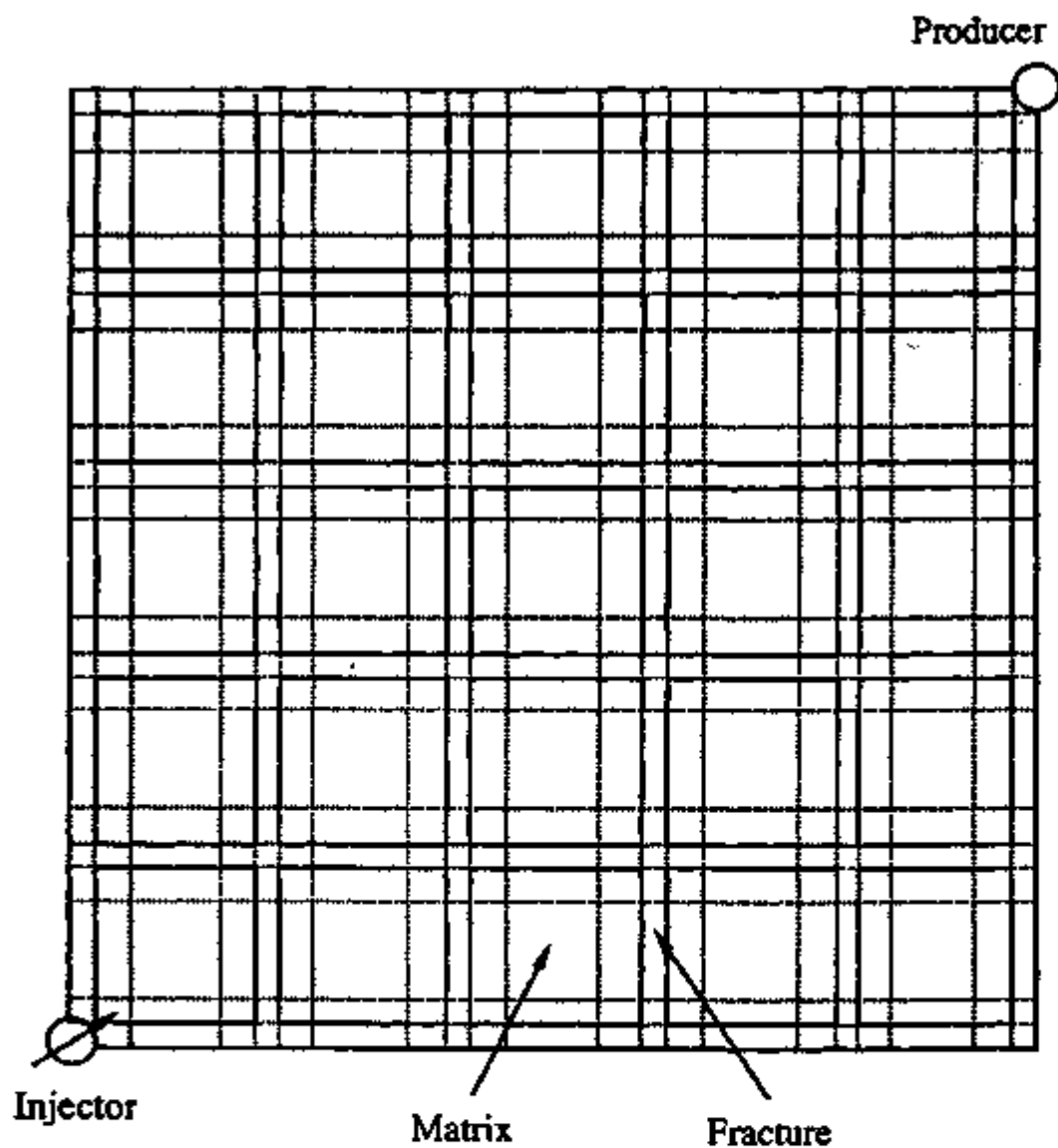
Fig. 4.15. Grid system for fine-grid simulation of an ideal fractured reservoir.
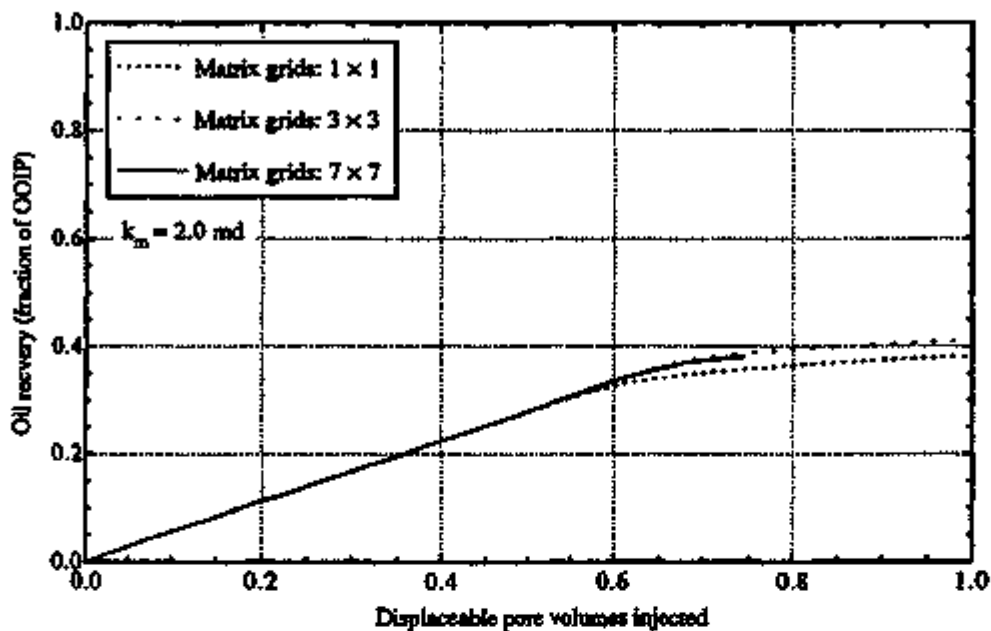
Fig. 4.16 Oil recovery of an ideal fractured reservoir by fine-grid simulation.
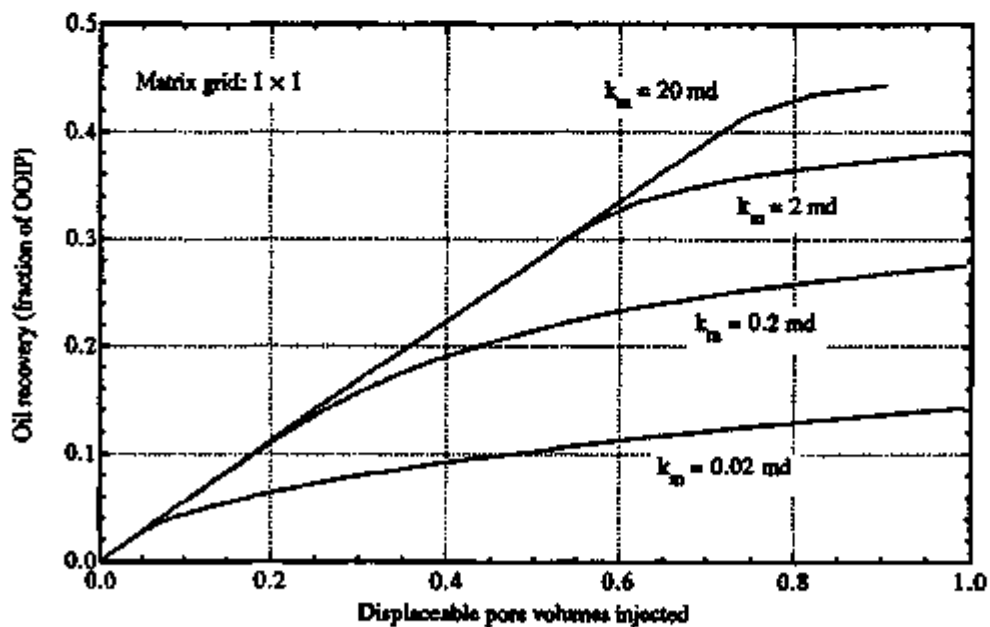
Fig. 4.17a Oil recovery from ideal fractured reservoir with different matrix
permeabilities by fine-grid single porosity method.

157
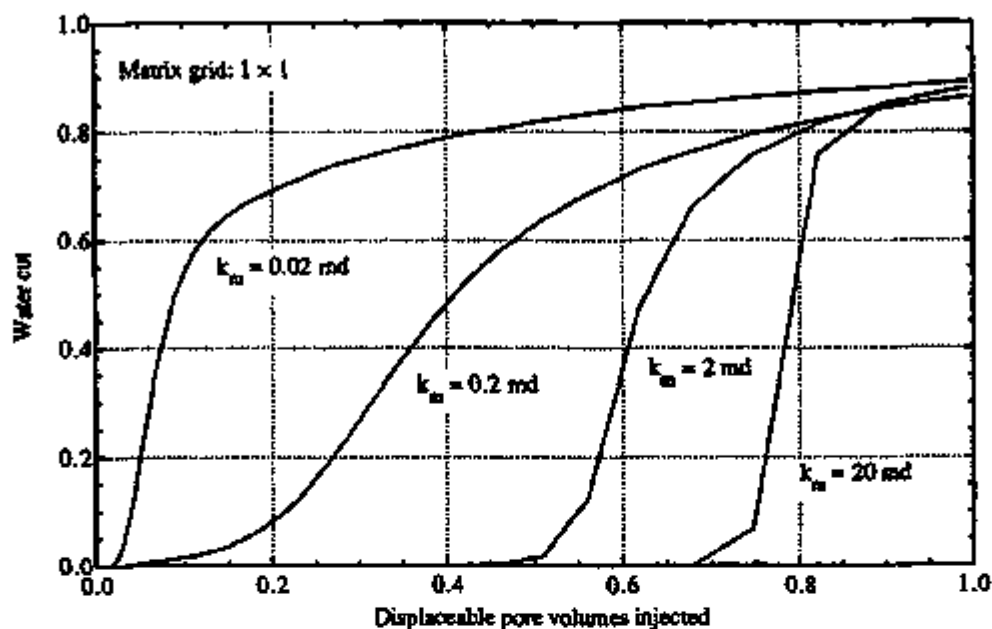
Fig. 4.17b Water cut from ideal fractured reservoir with different matrix permeabilities by fine-grid single porosity method.
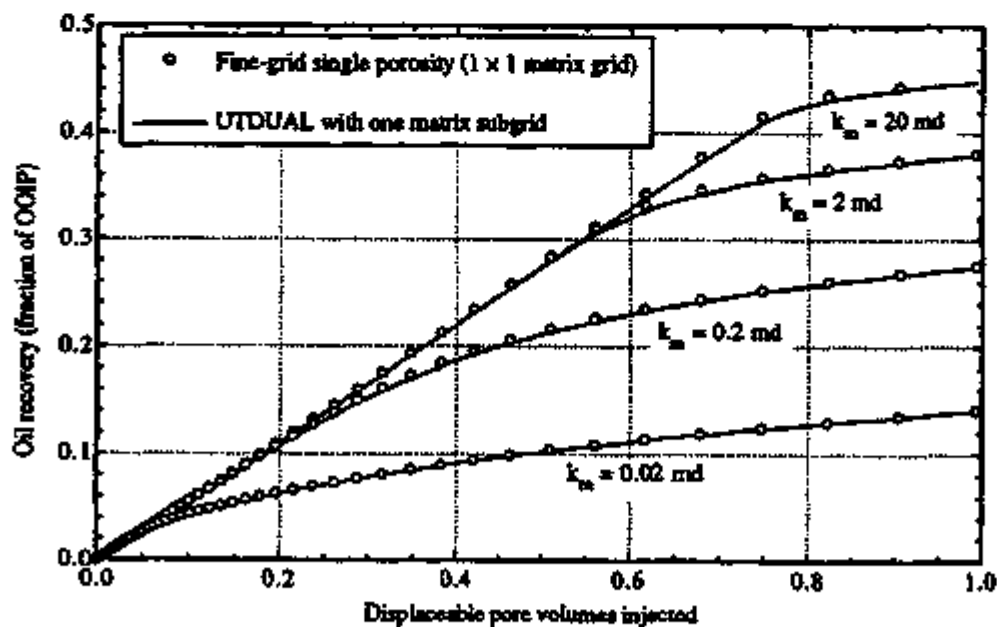
Fig. 4.18a Comparison of fine-grid single porosity simulation with UTDUAL results (IMPES option) of ideal fractured resevoir with different matrix permeabilities.

158
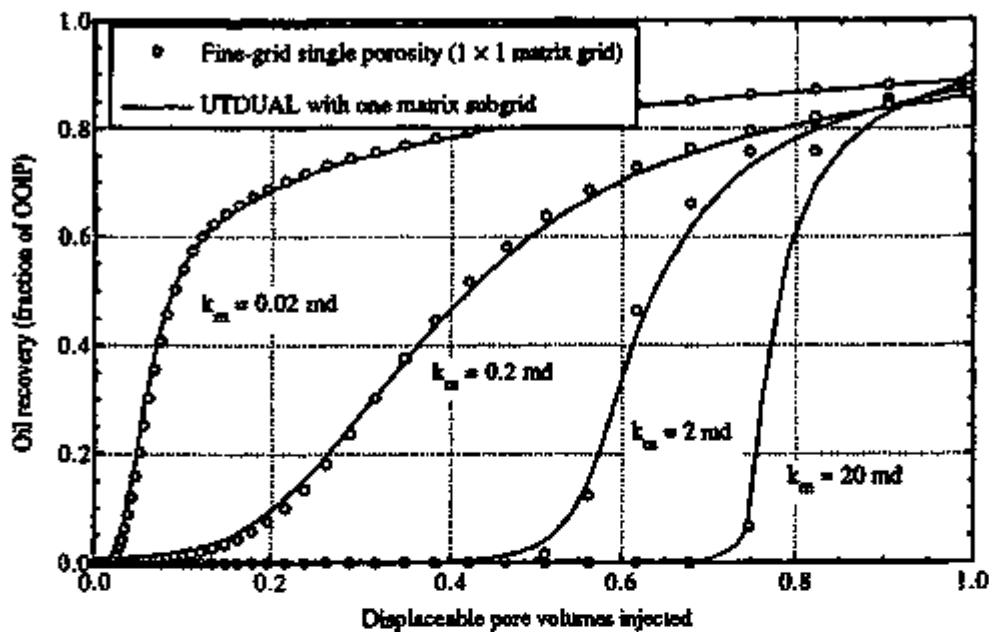
Fig. 4.18b Comparison of fine-grid single porosity simulaiton with UTDUAL results (IMPES option) for ideal fractured reservoir with different matrix permeabilities.

Fig. 4.18c Fracture water saturation profiles along the diagonal line connecting two wells for the case of $k_m = 2$ md.
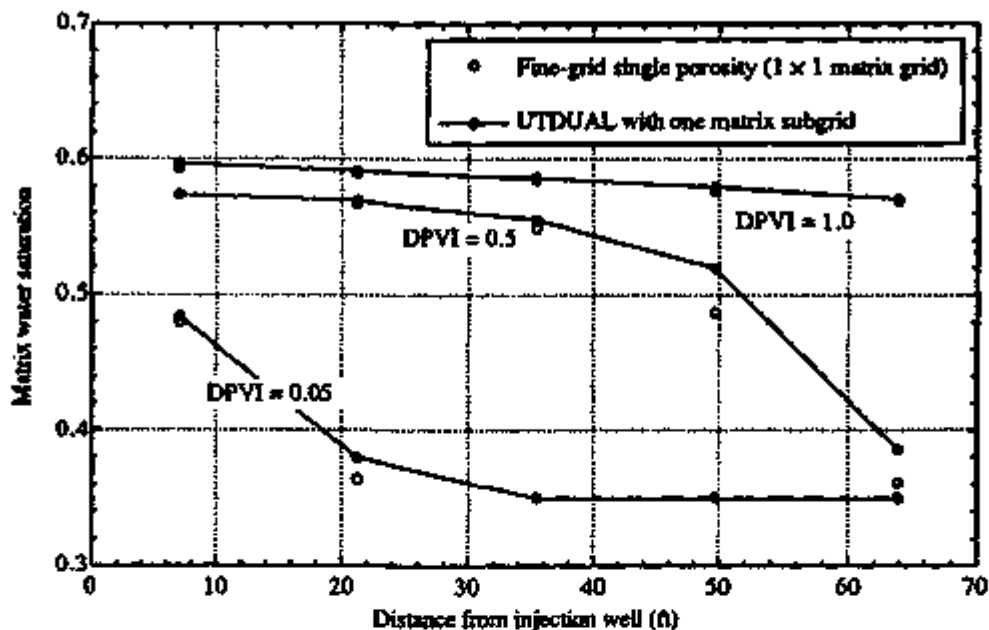
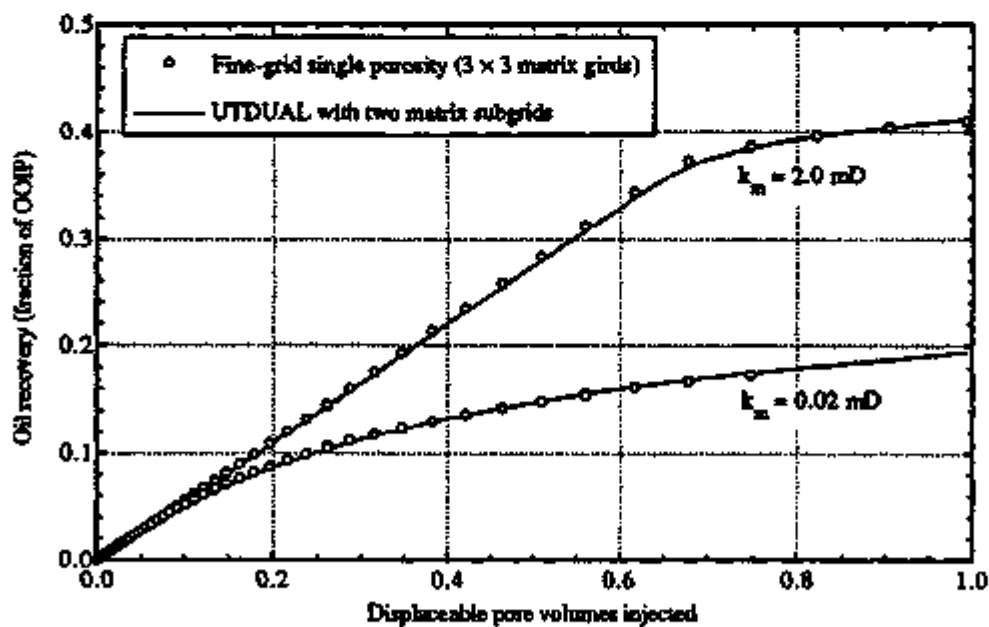Fig. 4.18d Matrix water sautration profiles along the diagonal line connecting two wells for the case of $k_m = 2$ md.

Fig. 4.19a Comparison of fine-grid single porosity simulation with UTDUAL results (IMPES option) for ideal fractured reservoir with different matrix permeabilities.
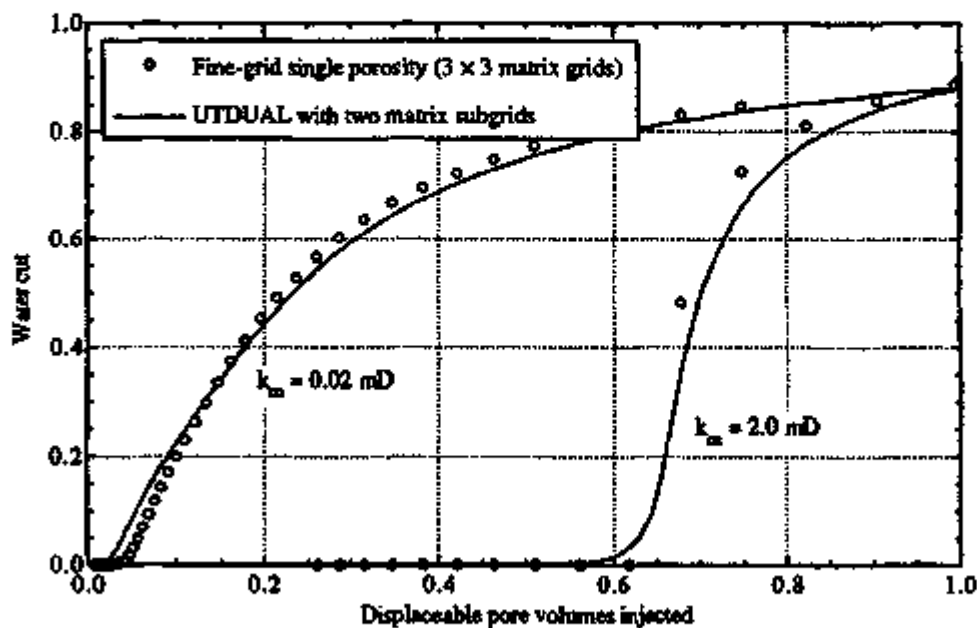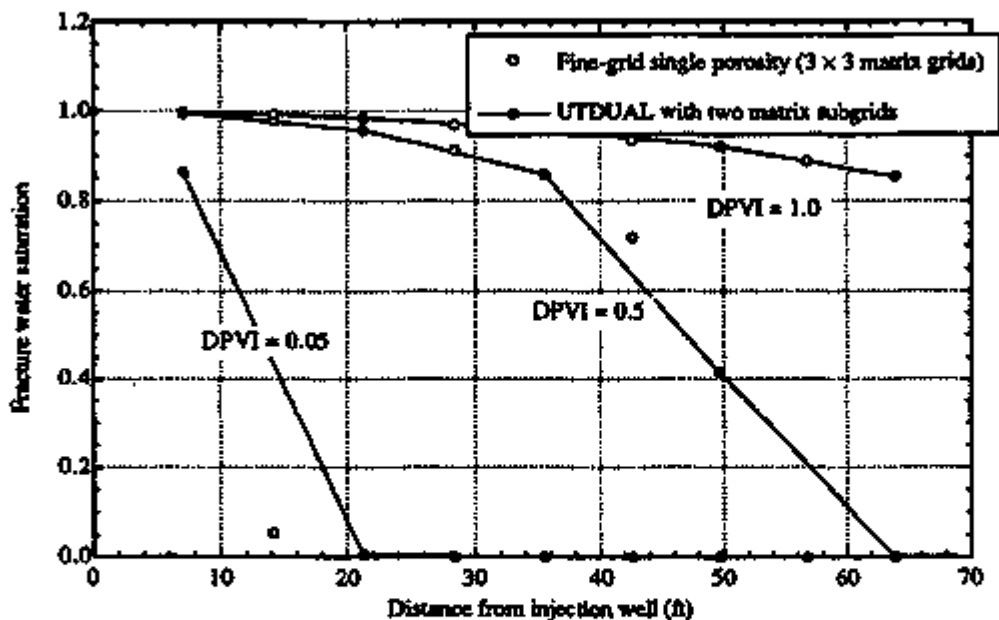
Fig. 4.19b Comparison of fine-grid single porosity simulation with UTDUAL results (IMPES option) for ideal fractured reservoir with different matrix permeabilities.

Fig. 4.19c Fracture water saturation profiles along the diagonal line connecting two wells for the case of $k_m = 2$ md.
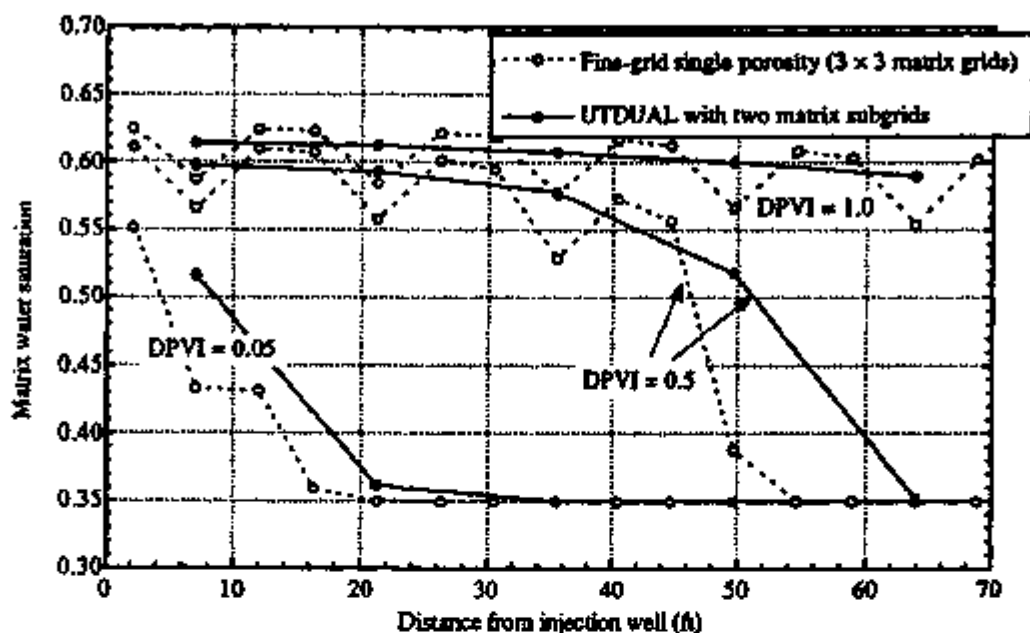
Fig. 4.19d Matrix water saturation profiles along the diagonal line connecting two wells for the case of $k_m = 2$ md.
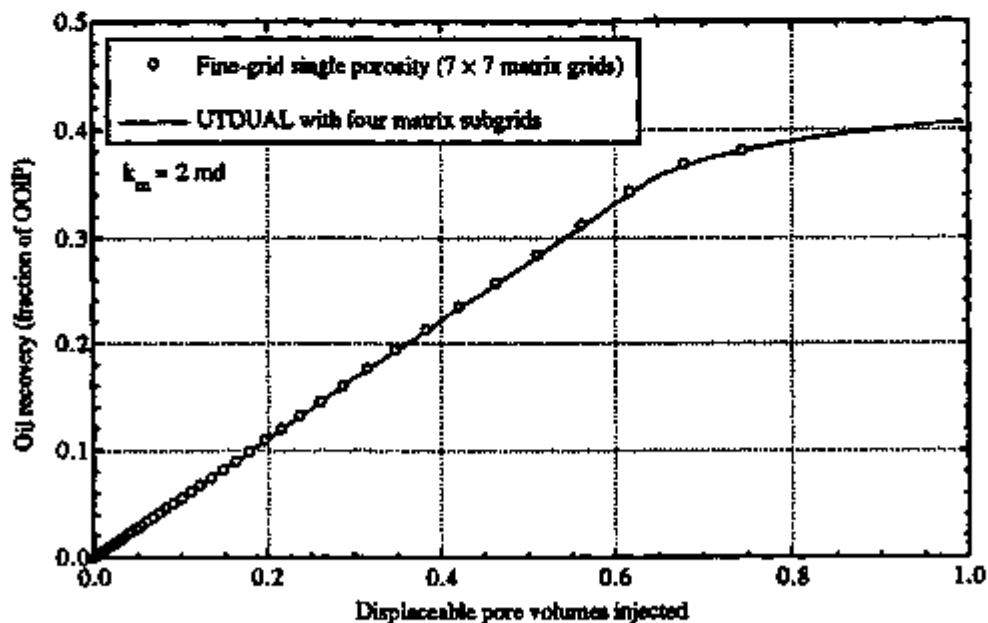

Fig. 4.20a Comparisons of fine-grid single porosity simulation with UTDUAL results (IMPES option) for ideal fractured reservoir.
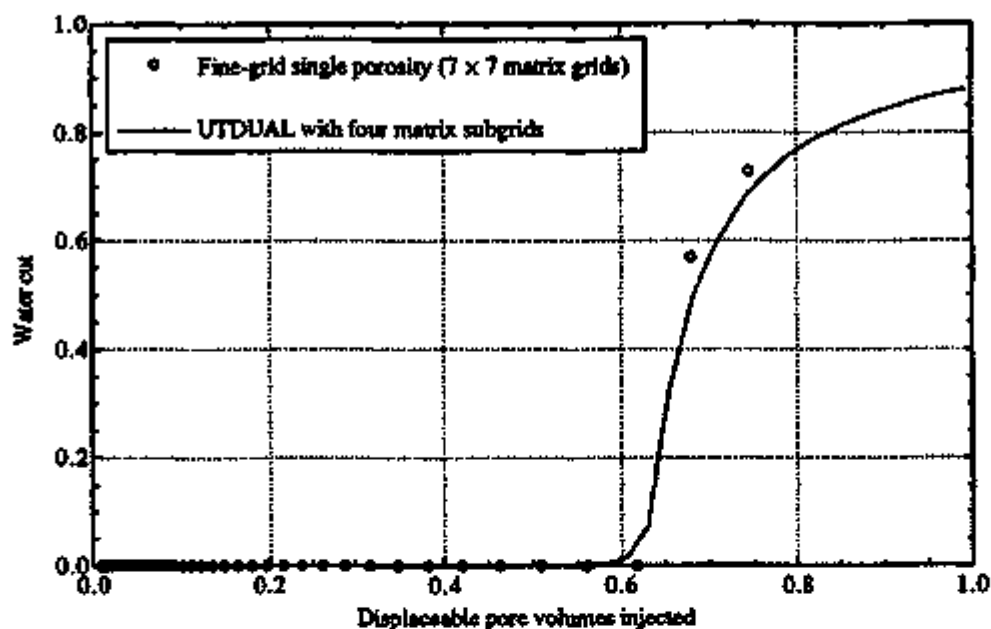
Fig. 4.20b Comparisons of fine-grid single porosity simulation with UTDUAL results
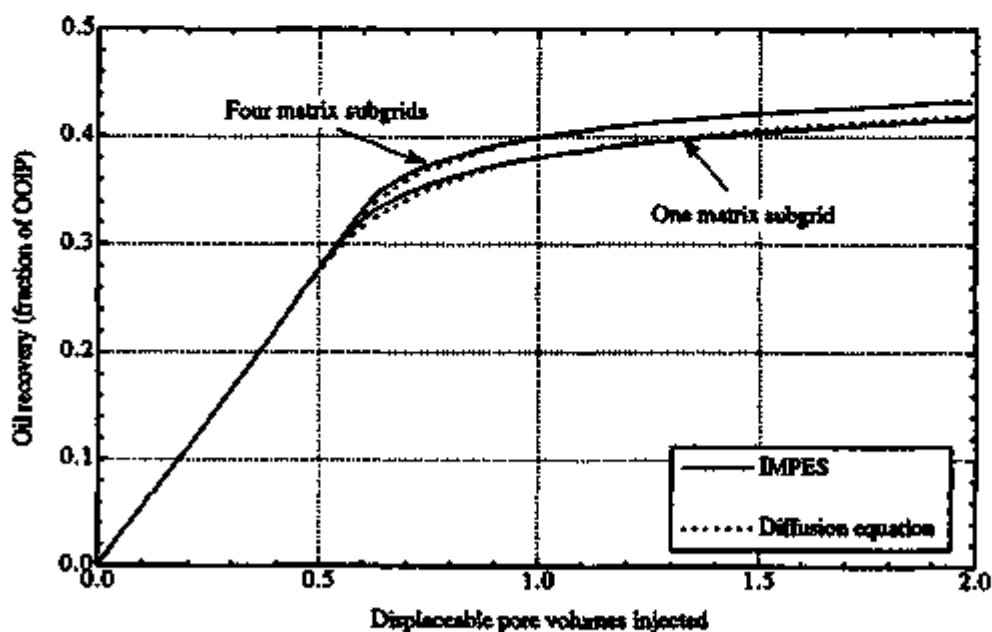(IMPES option) for ideal fractured reservoir.

Fig. 4.21a Comparison of two matrix/fracture transfer flow calculations: IMPES and
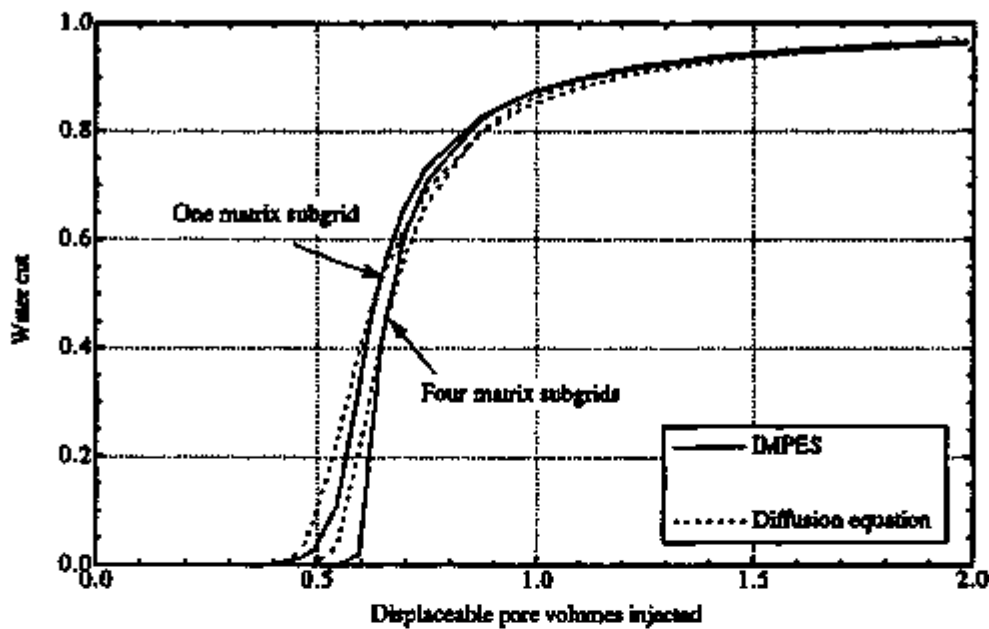diffusion equation for an ideal fractured reservoir with $k_m = 2$ md.

Fig. 4.21b Comparison of two matrix/fracture transfer flow calculations: IMPES and diffusion equation for an ideal fractured reservoir with $k_m = 2$ md.

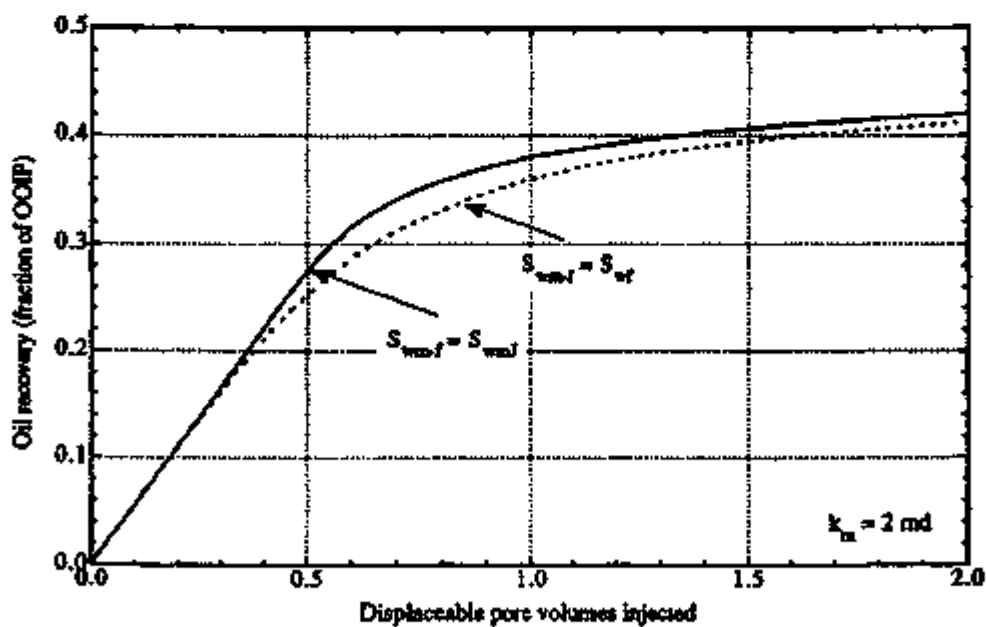Fig. 4.22a Effect of matrix boundary condition on oil recovery, UTDUAL runs with diffusion equation option and one matrix subgrid.

Fig. 4.22b Effect of matrix boundary condtion on water cut, UTDUAL runs with diffusion equation option with one matrix subgrid.

Fig. 4.23a Effect of matrix boundary condition on oil recovery, UTDUAL runs with diffusion equation option and four matrix subgrids.

165
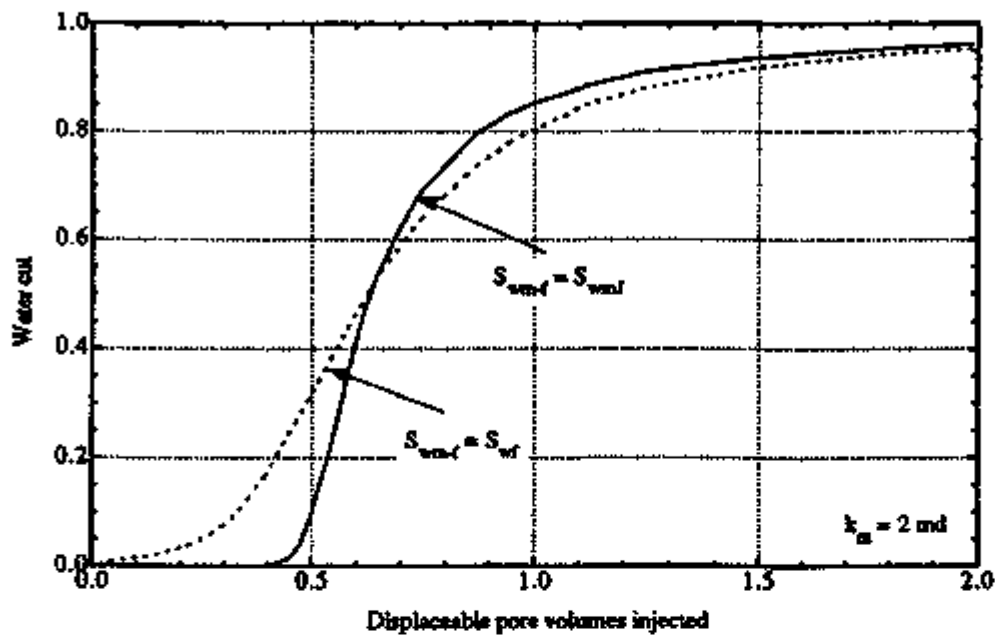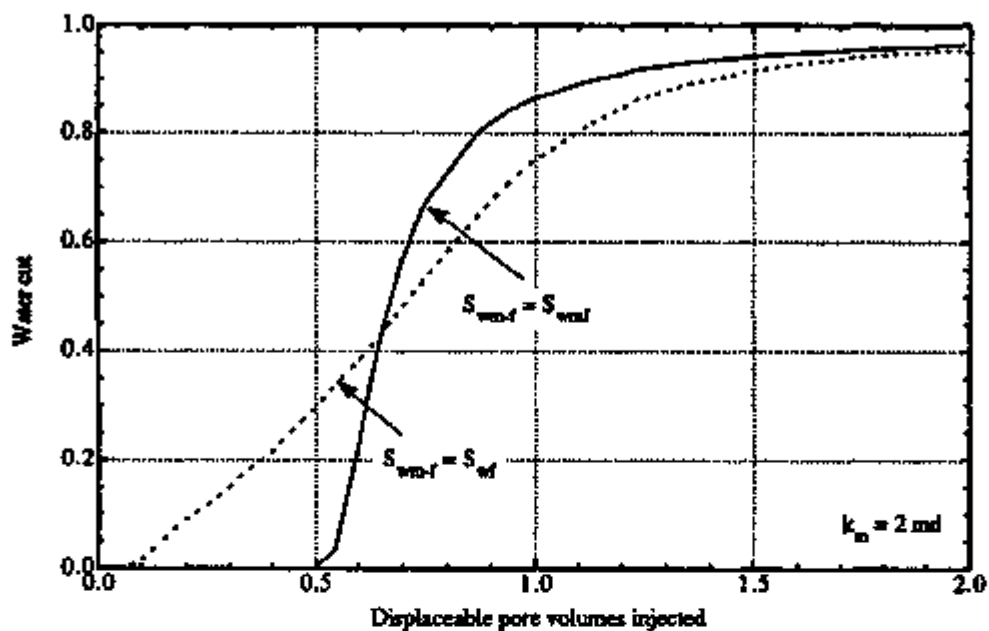
Fig. 4.23b Effect of matrix boundary condition on water cut, UTDUAL runs with diffusion equation option and four matrix subgrids.
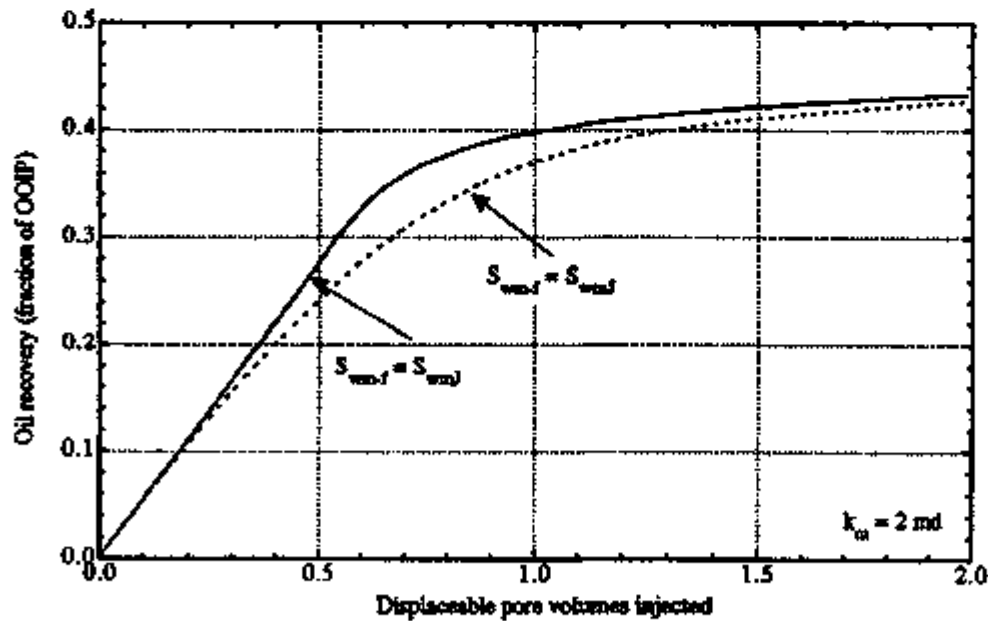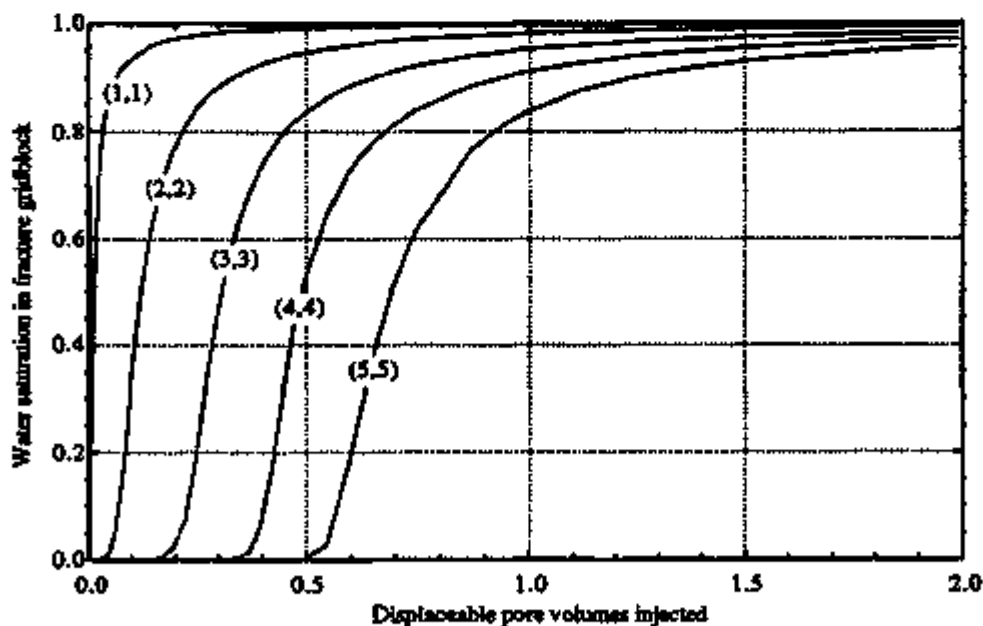

Fig. 4.24a Water saturation in each fracture gridblock along the diagonal line connecting two wells of ideal fractured reservoir with $k_m = 2$ md.
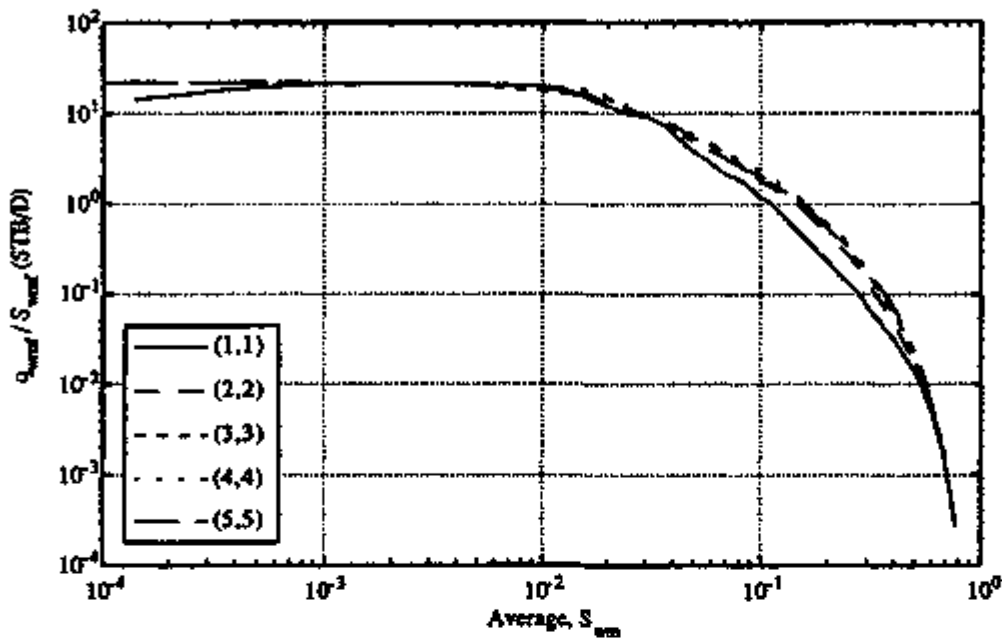
Fig. 4.24b Matrix/fracture transfer rate divided by S_{wf} for each gridblock along the diagonal line connecting two wells of ideal fractured reservoir with $k_m = 2$ md.
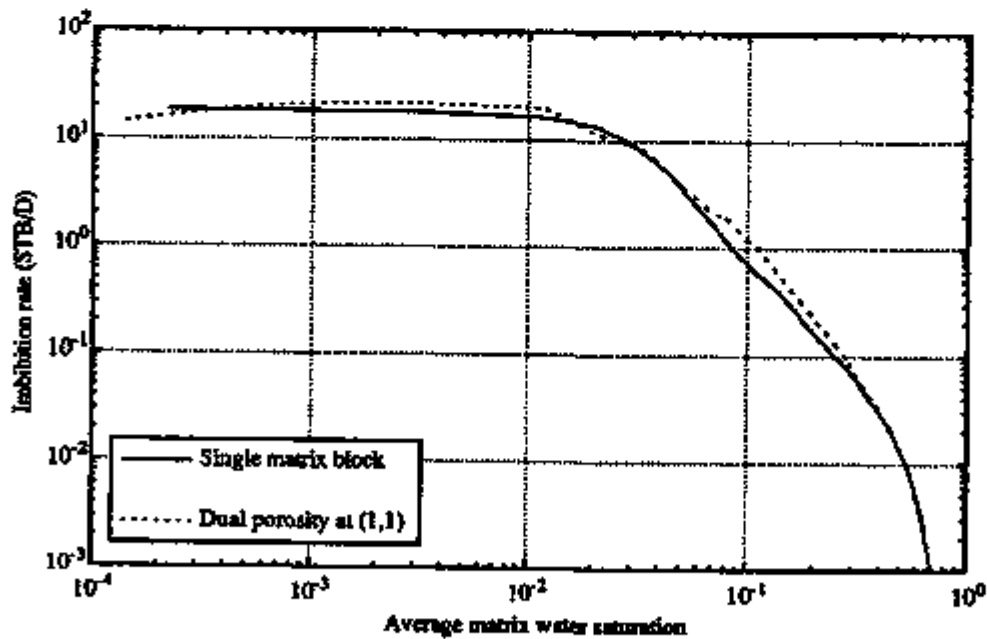
Fig. 4.24c Comparison of imbibition rate into single matrix block under totally immersed conditions and matrix/fracture transfer rate from UTDUAL simulation of ideal fractured reservoir.
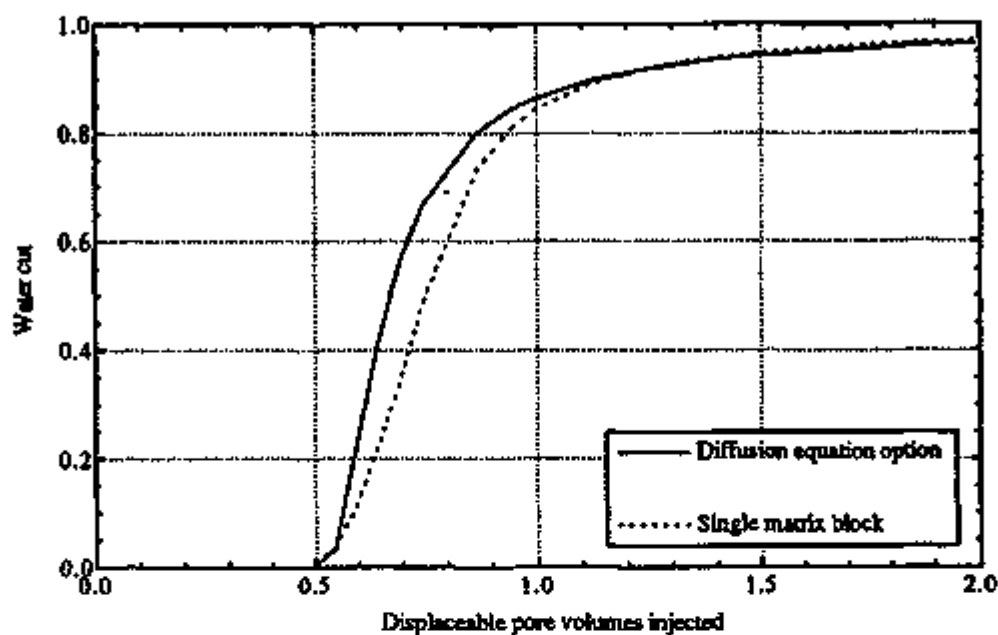
Fig. 4.25   Comparison between diffusion equation option and the option using results from single matrix block studies.
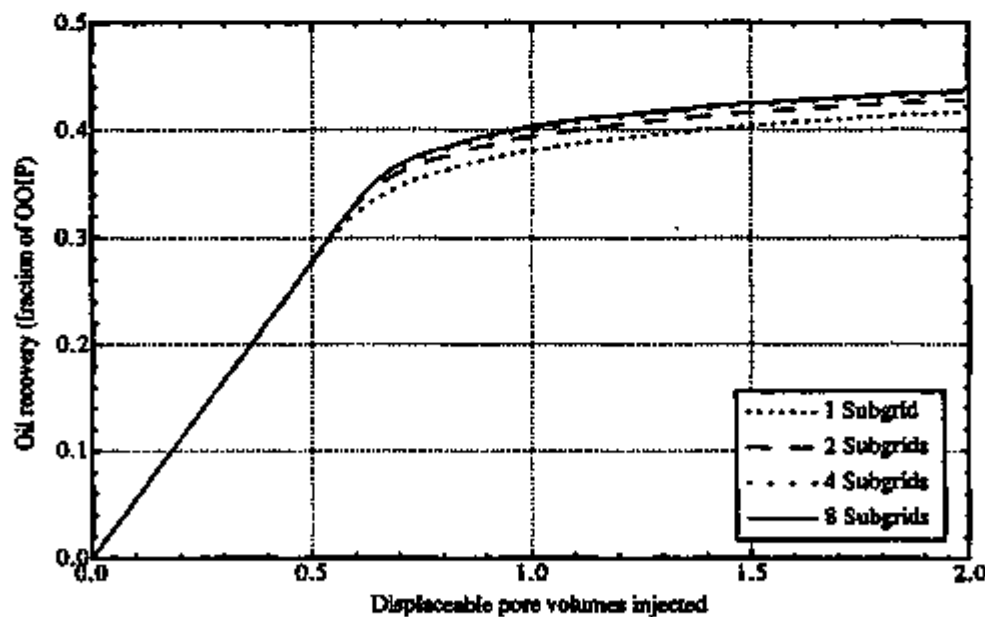
Fig. 4.26 Grid refinement studies of ideal fractured reservoir with $k_m = 2$ md.
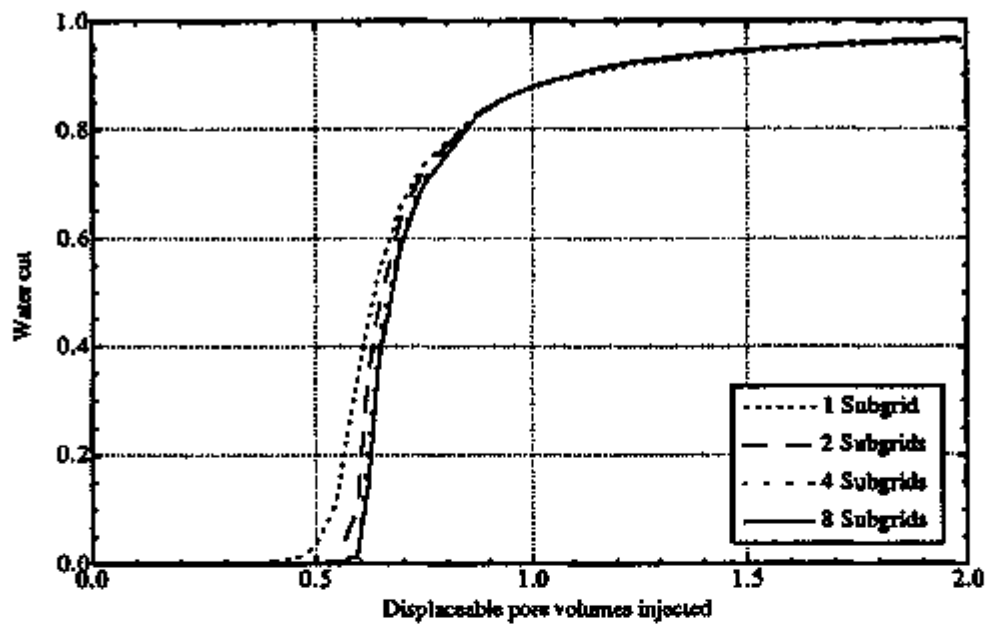
Fig. 4.27 Grid refinement studies of ideal fractured reservoir with $k_m = 2$ md.
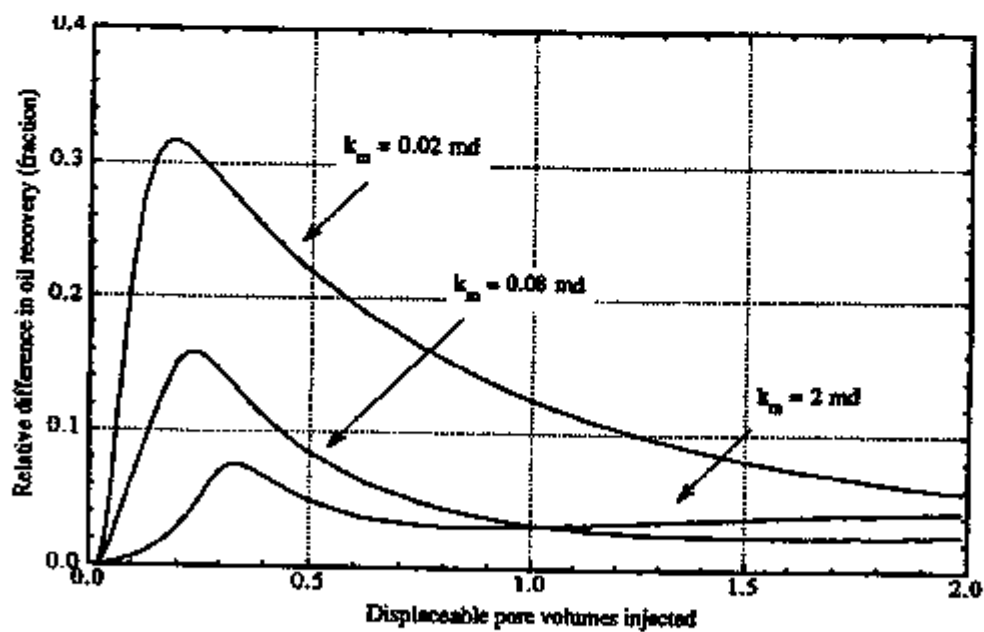
Fig. 4.28 Difference in oil recovery between results with/without subgrids.
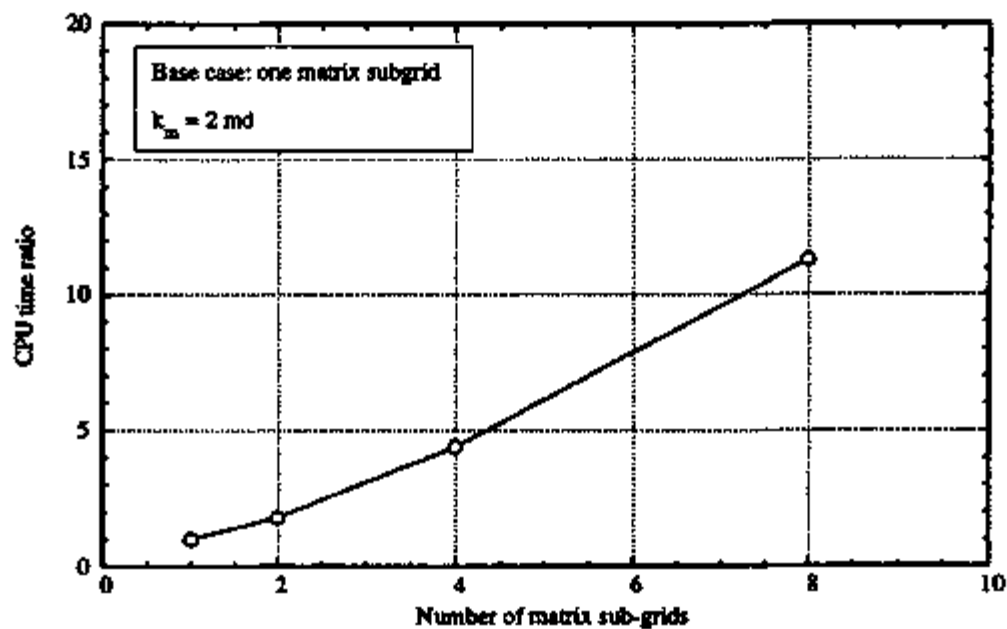
Fig. 4.29 CRAY Y-MP CPU time ratio versus the number of subgrids.
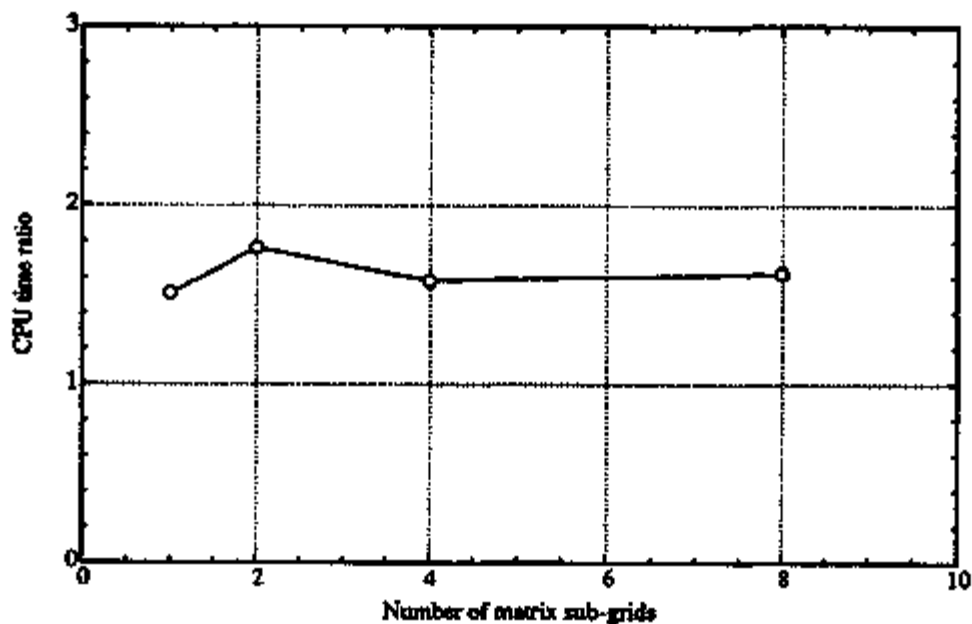
Fig. 4.30   Computer time ratio between IMPES and diffusion equation options of
UTDUAL.
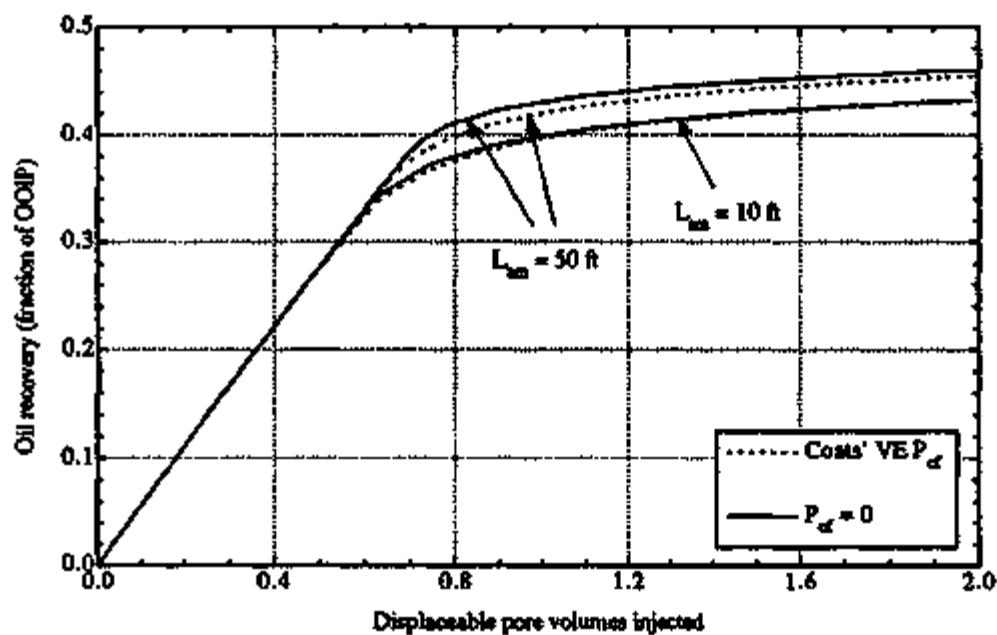
Fig. 4.31a Effects of Coats' (1989) pseudo-capillary pressure on oil recovery of ideal fractured reservoir.
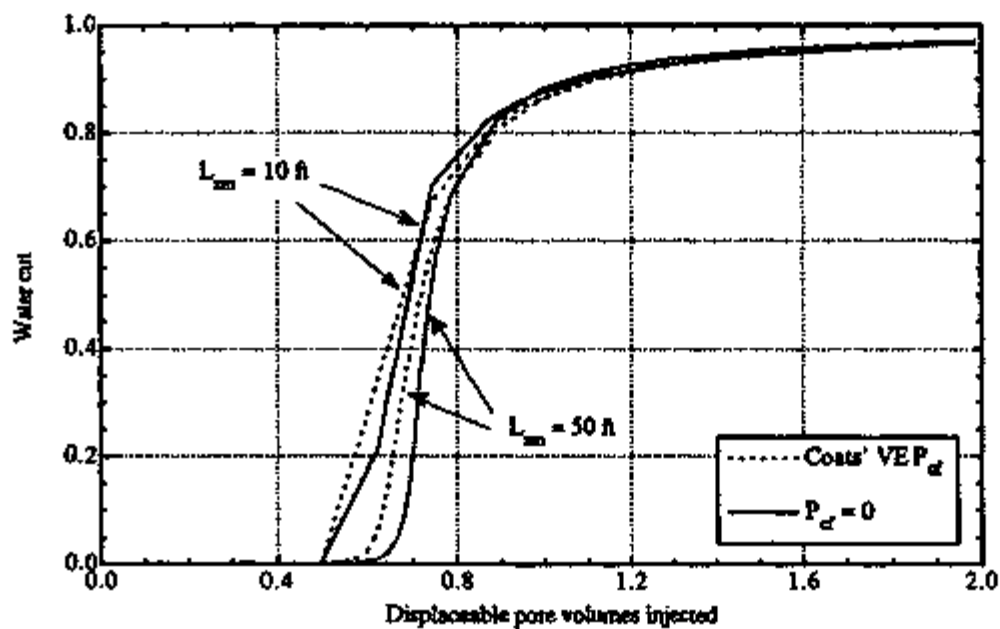
Fig. 4.31b Effects of Coats' (1989) pseudo-capillary pressure on water cut of ideal fractured reservoir.

171
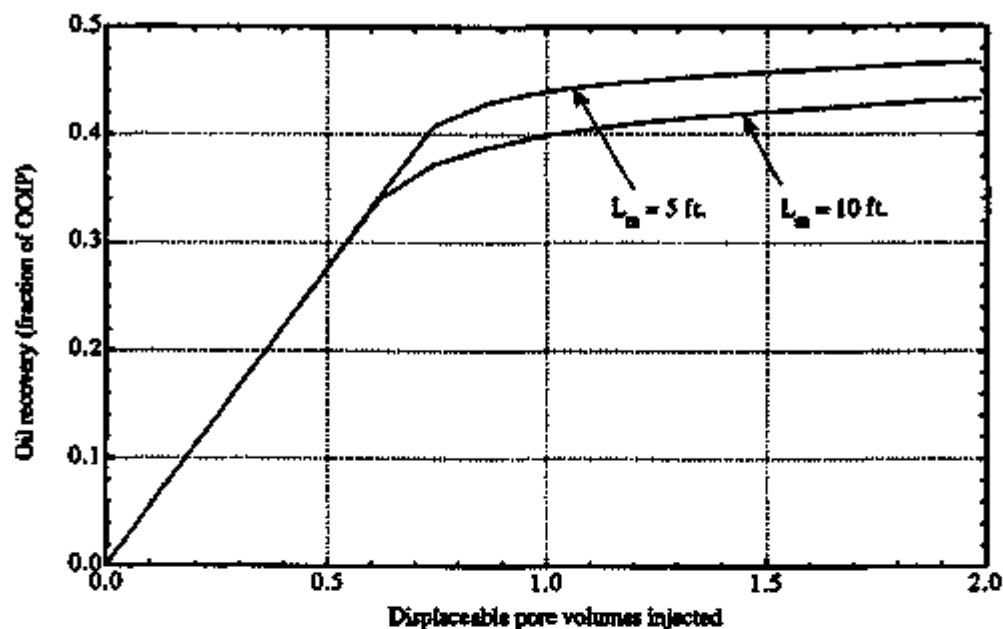
Fig. 4.32a Effect of matrix block size on oil recovery of ideal fractured reservoir.
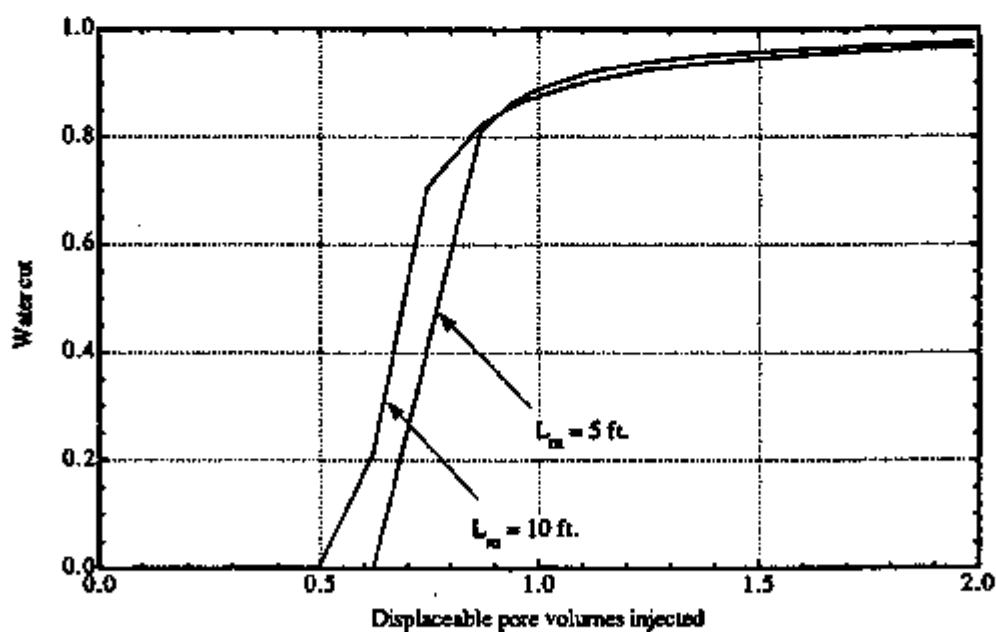
Fig. 4.32b Effect of matrix block size on water cut of ideal fractured reservoir.

172
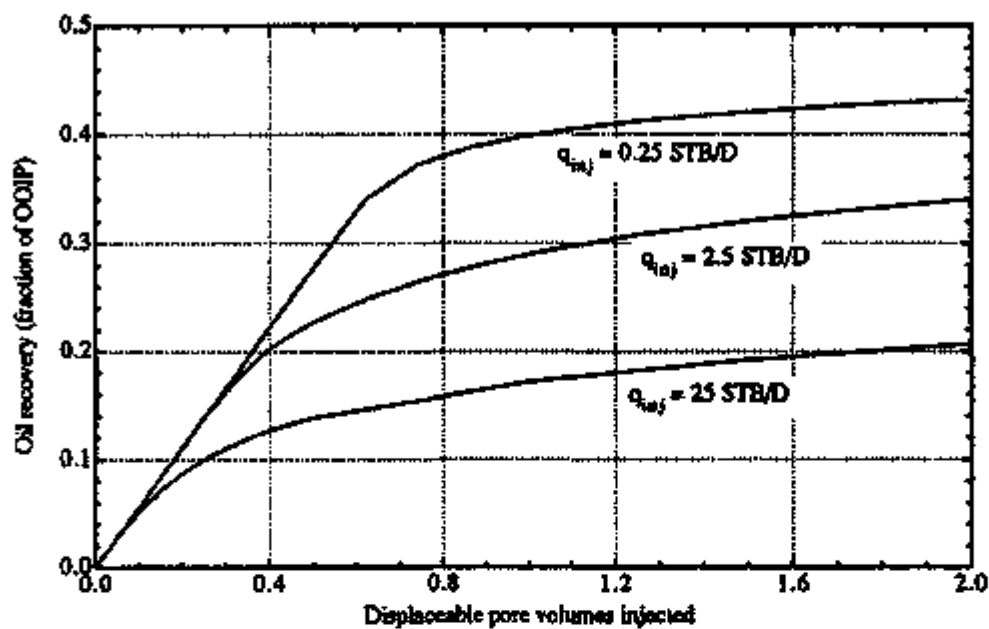
Fig. 4.33a Effect of water injection rate on oil recovery of ideal fractured reservoir.
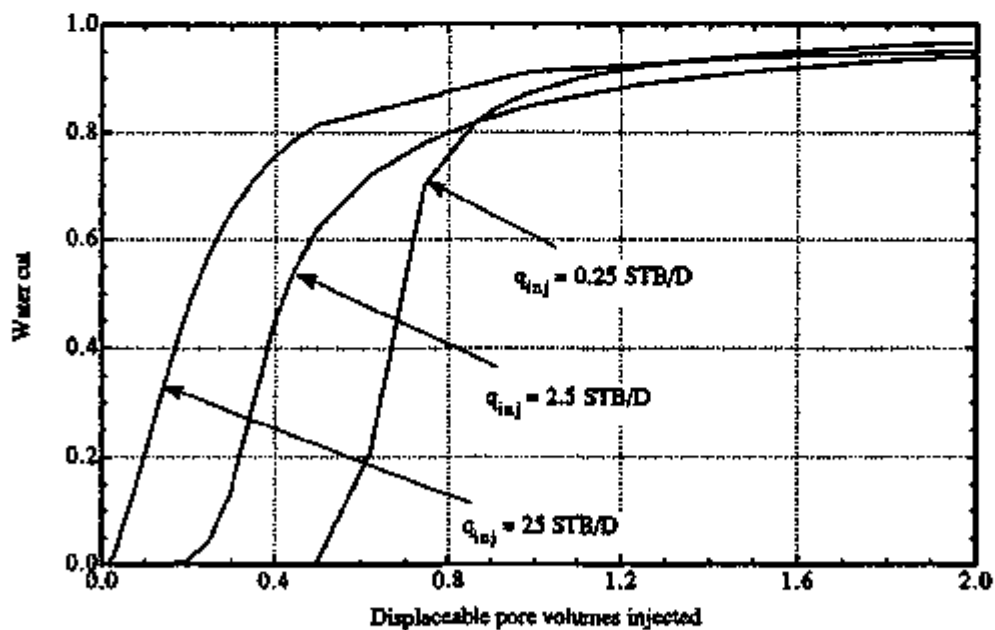
Fig. 4.33b Effect of water injection rate on water cut of ideal fractured reservoir.
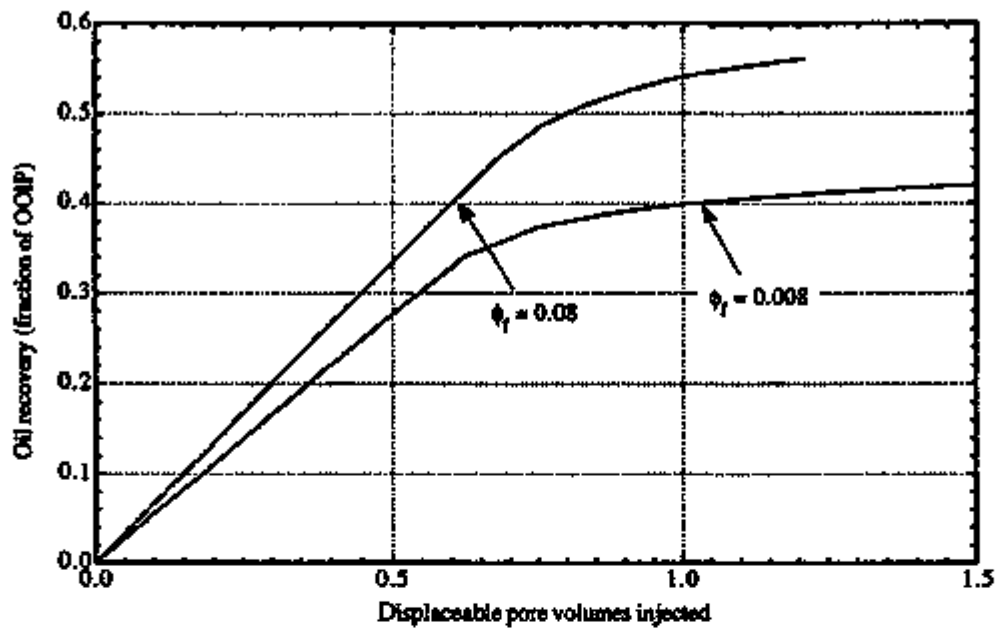
Fig. 4.34a Effect of equivalent fracture porosity on oil recovery of ideal fractured reservoir.
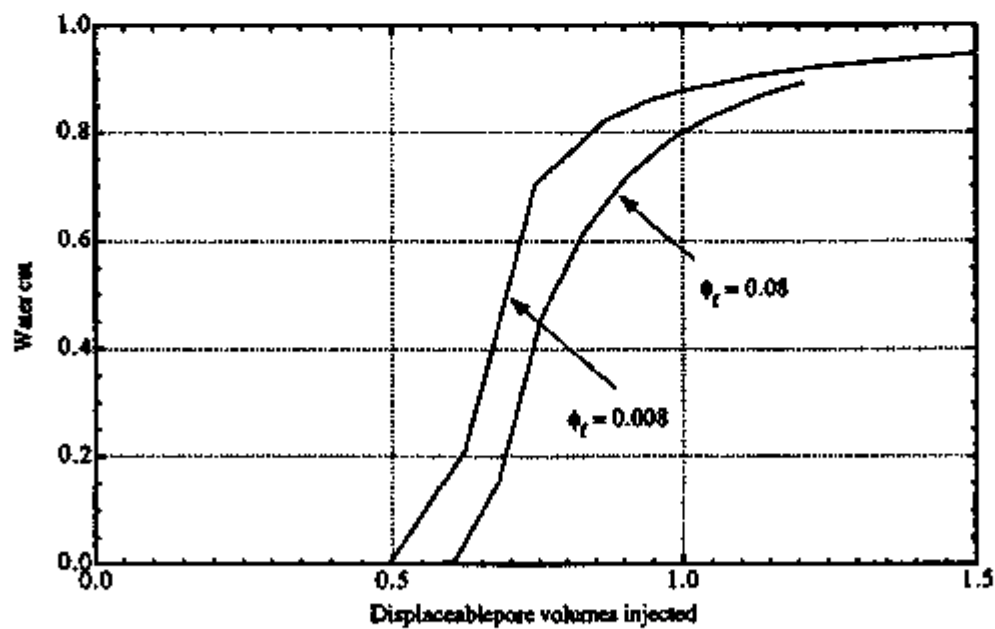
Fig. 4.34b Effect of equivalent fracture porosity on water cut of ideal fractured reservoir.

174
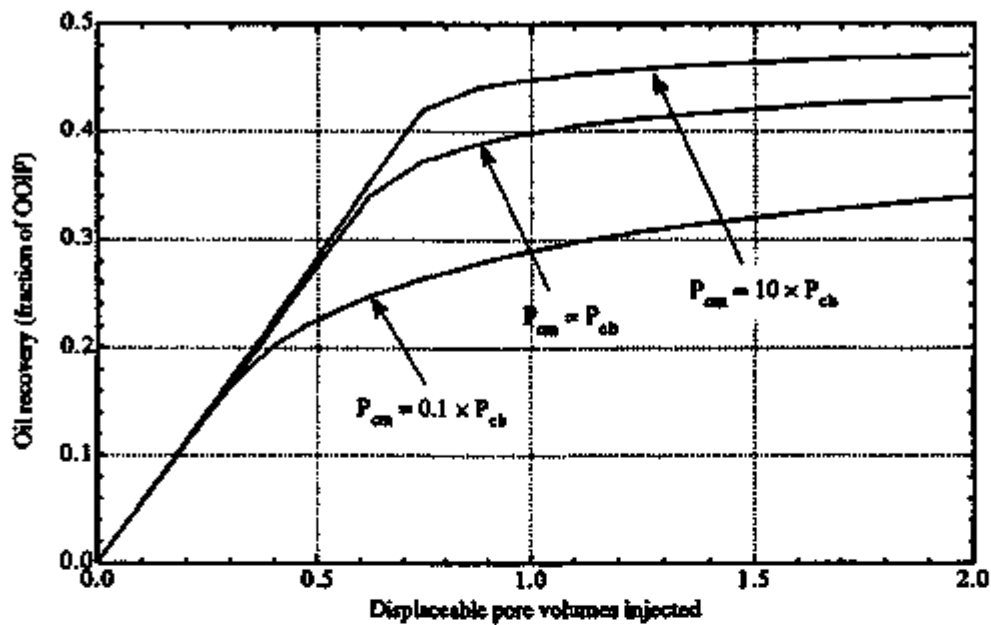
Fig. 4.35a Effect of matrix capillary pressure on oil recovery of ideal fractured reservoir.
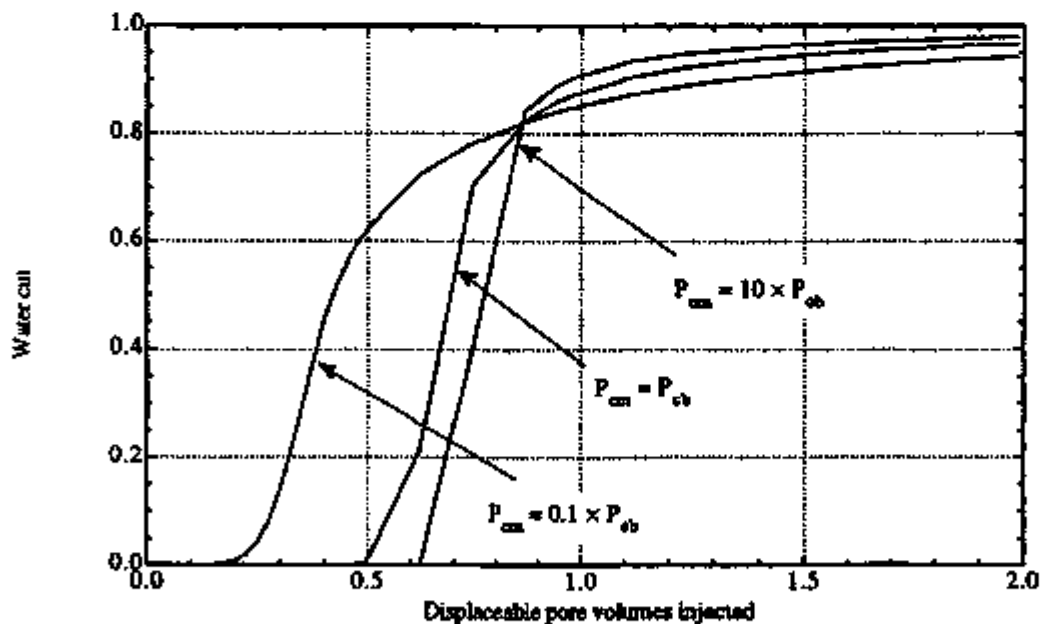
Fig. 4.35b Effect of matrix capillary pressure on water cut of ideal fractured reservoir.

175
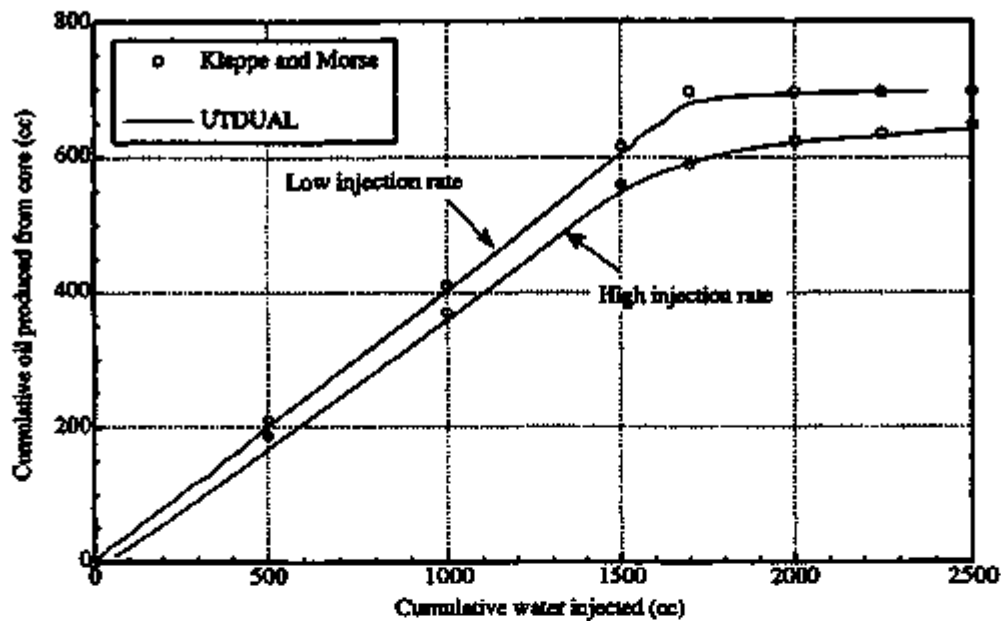
Fig. 4.36a Modeling of Kleppe and Morse's (1974) waterflooding experiment by
UTDUAL with IMPES option.
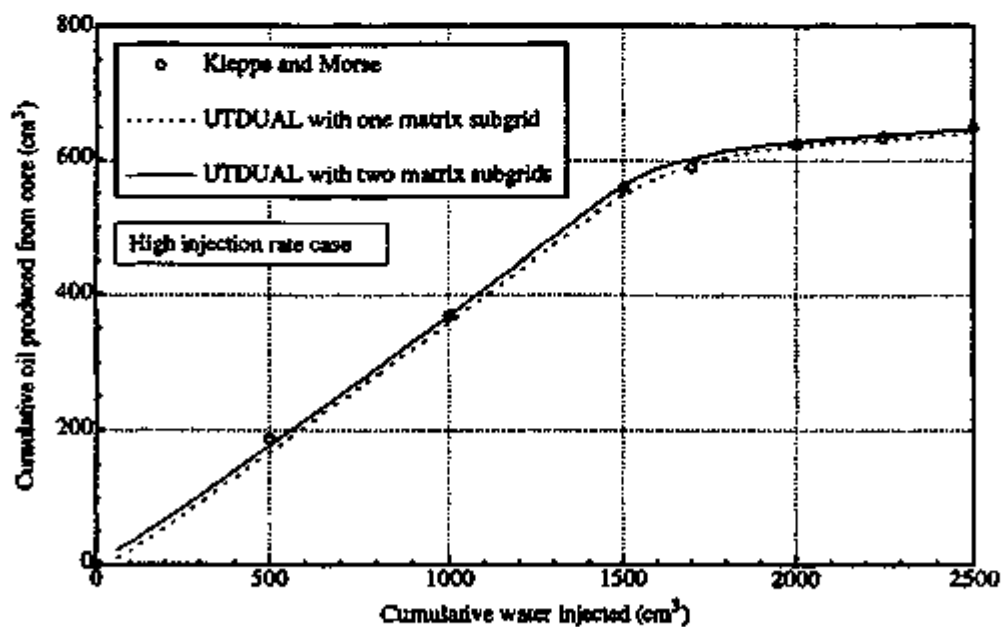
Fig. 4.36b Modeling of Kleppe and Morse's (1974) waterflooding experiment by
UTDUAL with IMPES option, showing effect of matrix subgriding.

176
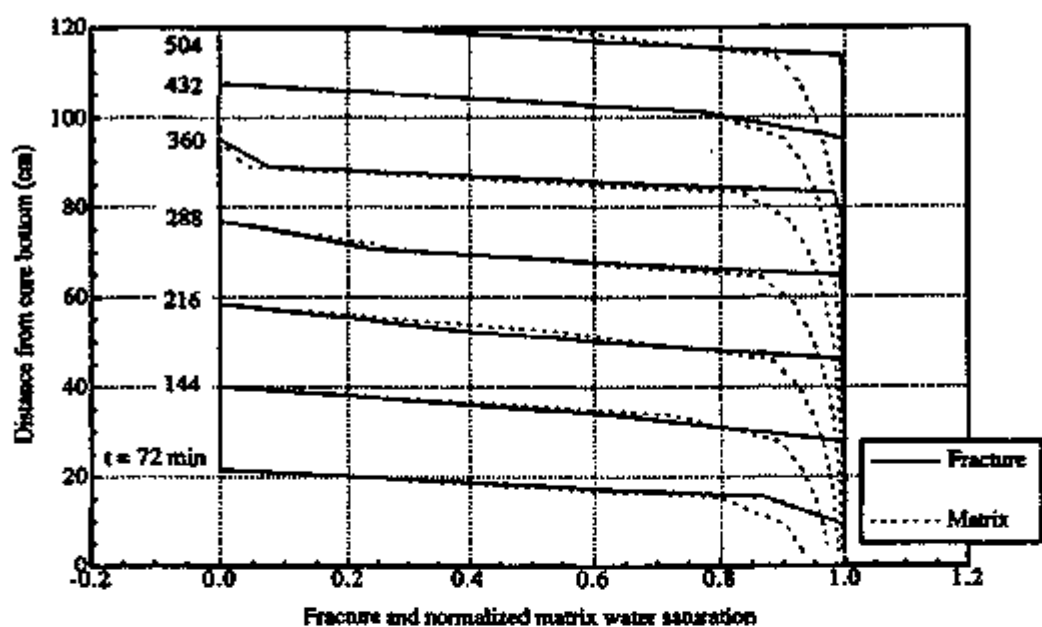
Fig. 4.36c Simulation-generated fracture and matrix saturation profiles for Kleppe and Morse's data (1974), low injection rate.
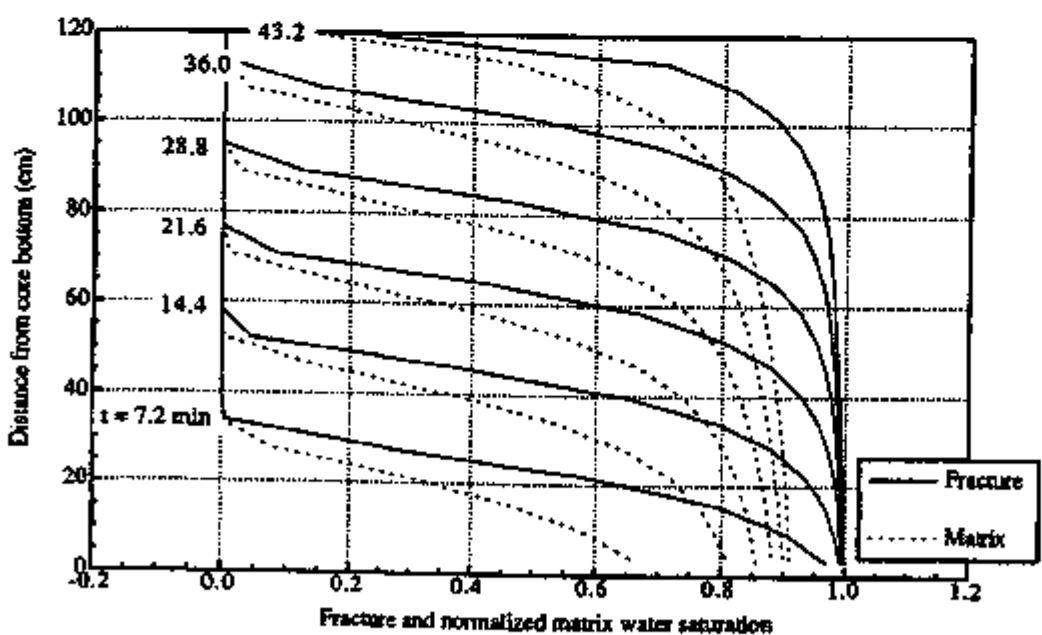
Fig. 4.36d Simulation-generated fracture and matrix saturation profiles for Kleppe and Morse's data (1974), high injection rate.

177
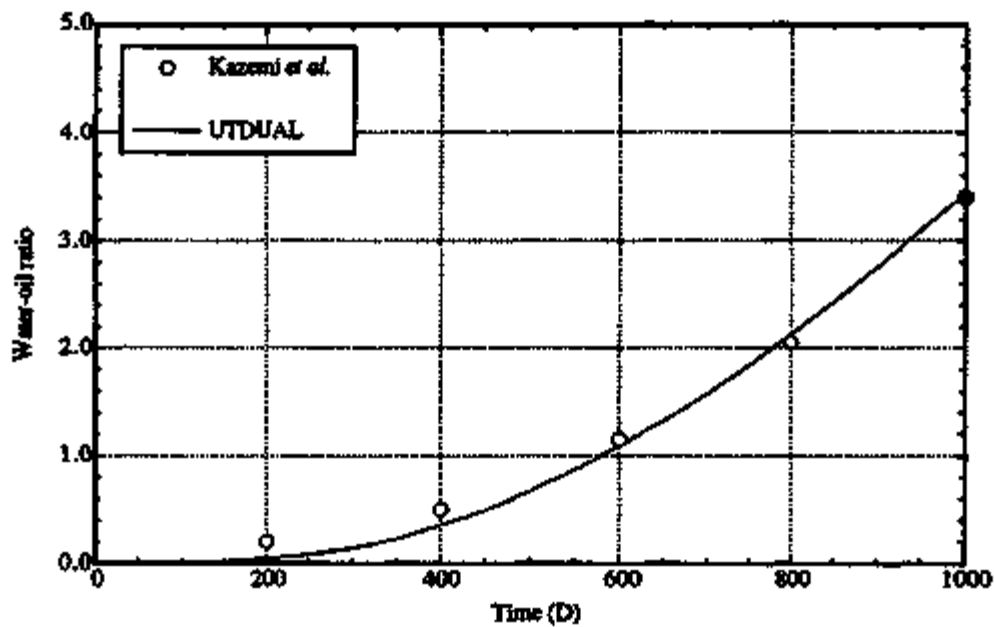
Fig. 4.37a Water-oil ratio comparison between UTDUAL simulation result without subgrid and Kazemi *et al.'s* (1976) results.
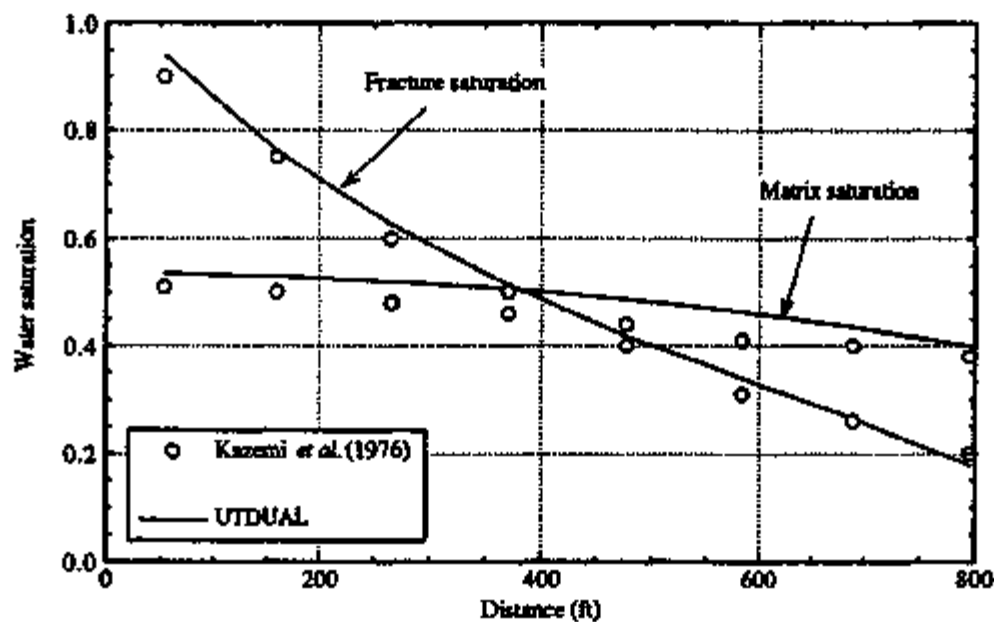
Fig. 4.37b Saturation profile at 499 days, comparison between UTDUAL simulation result without sub-grid and Kazemi *et al.'s* (1976) results.
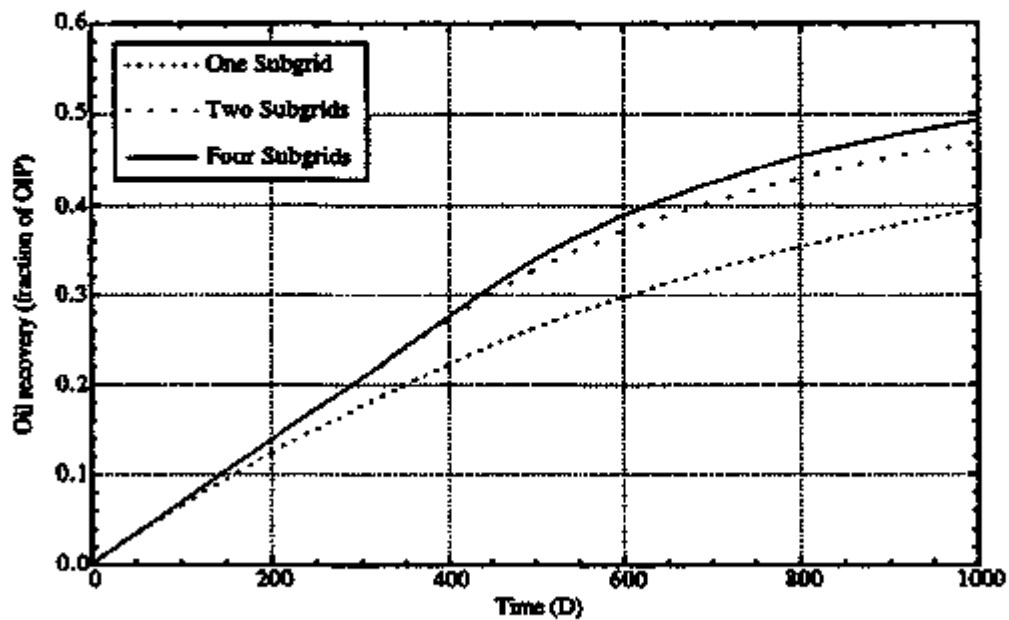
Fig. 4.37c Effect of matrix subgrid on oil recovery of Kazemi *et al.'s* (1976) five-spot.
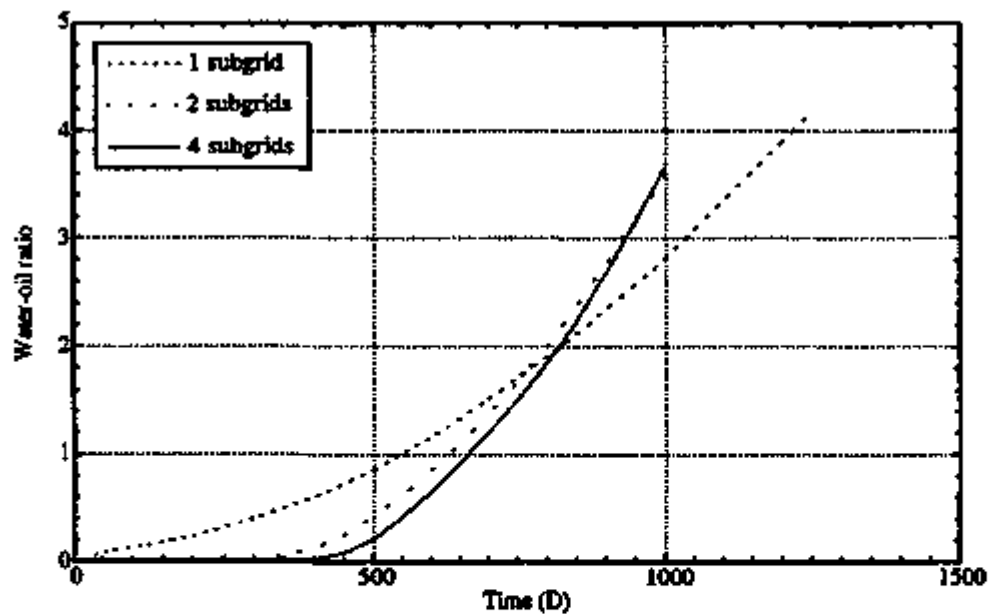
Fig. 4.37d Effect of matrix subgrid on water-oil ratio of Kazemi *et al.'s* (1976) five-spot.
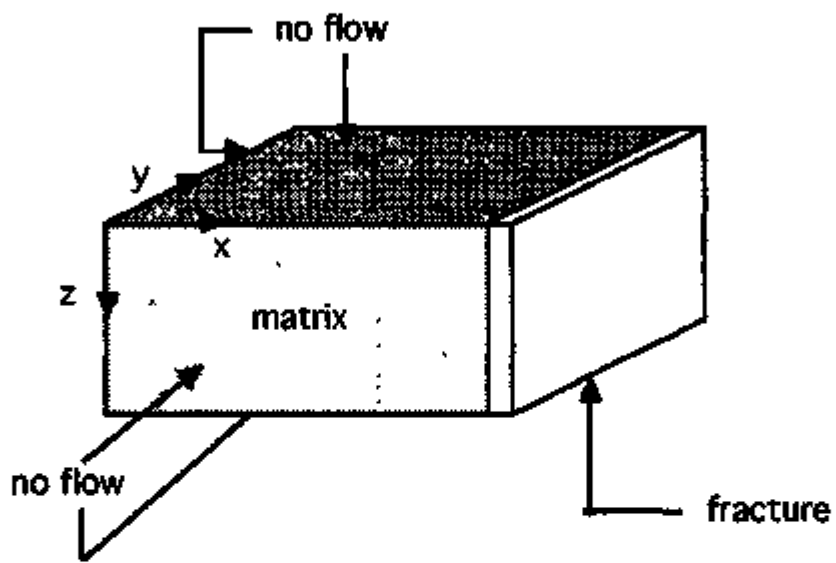
Fig. 4.38. Schematic of single matrix model.

Fig. 4.39. Water saturation distribution with different grid sizes at late time.
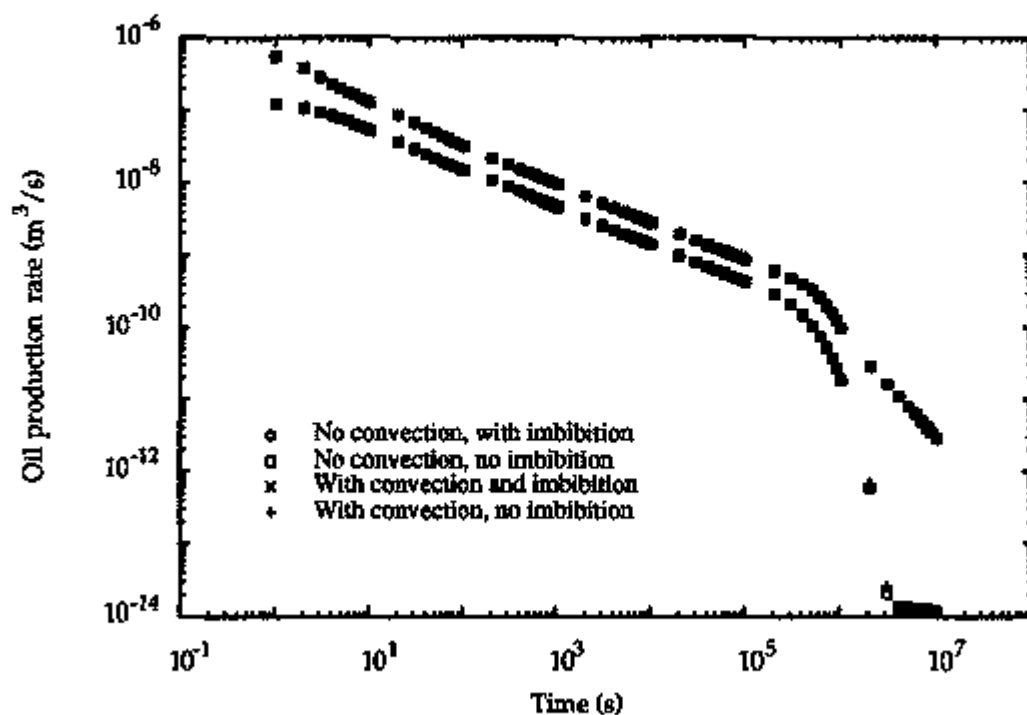
Fig. 4.40. Oil production with different transport mechanisms (expansion allowed).
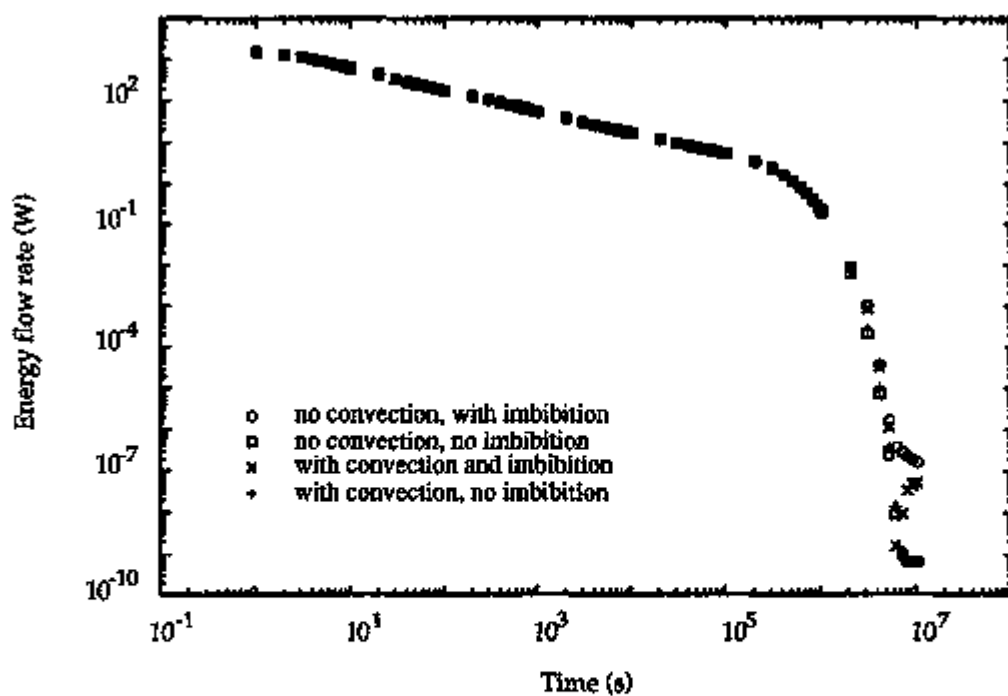
Fig. 4.41.   Energy transfer to matrix block with different transport mechanisms.

181
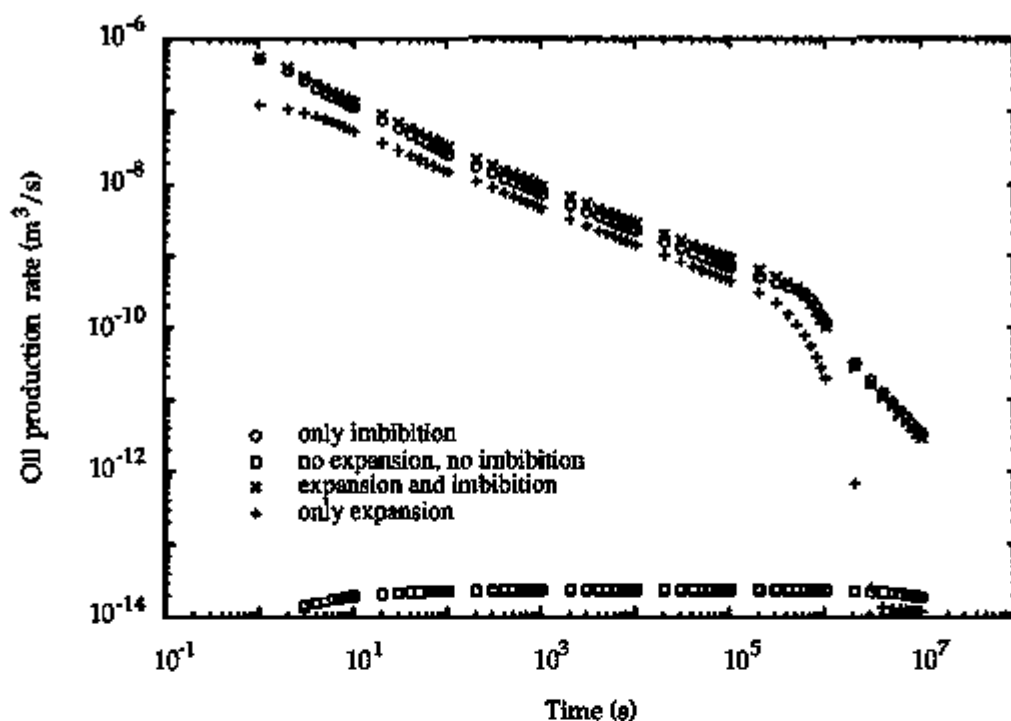
Fig. 4.42. Oil production rate from different recovery mechanisms.
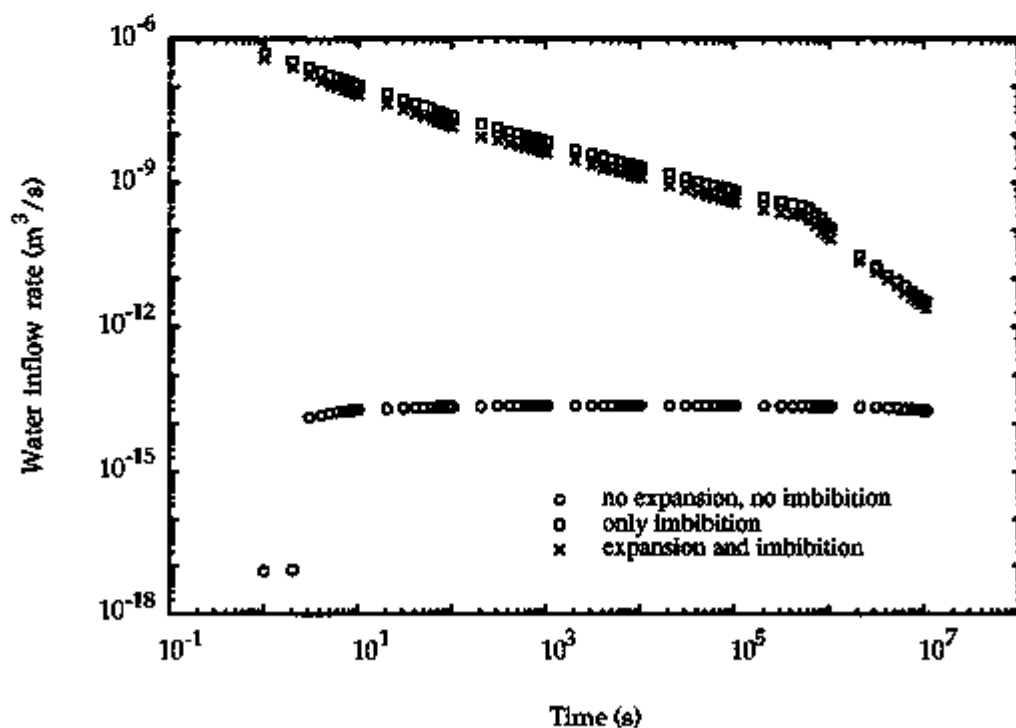
Fig. 4.43. Water inflow with various recovery mechanisms.
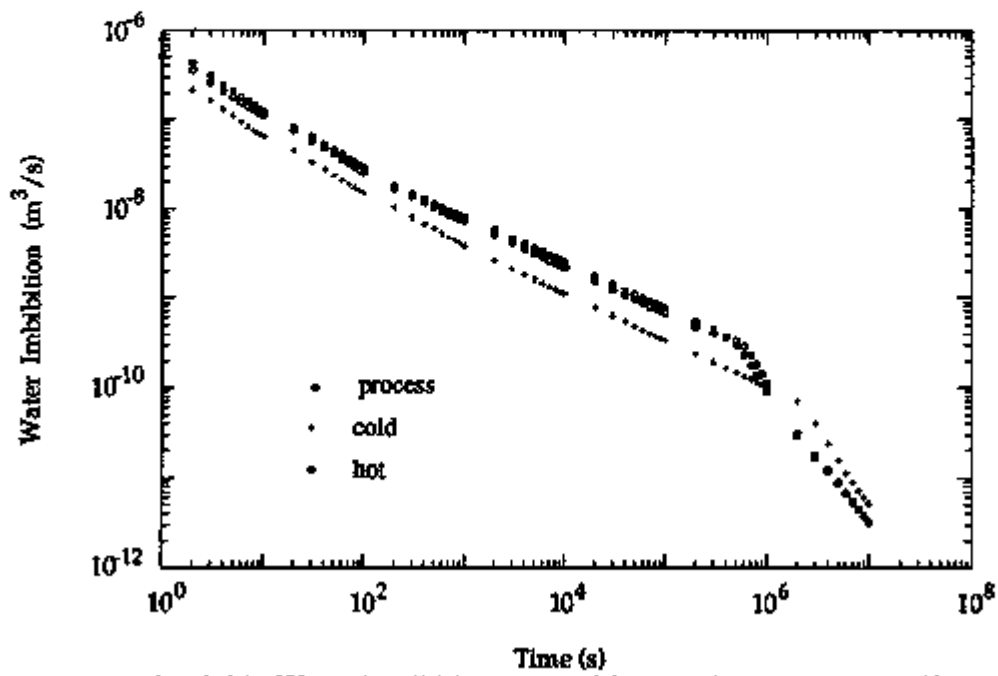
Fig. 4.44. Water imbibition rates with and without thermal effects.
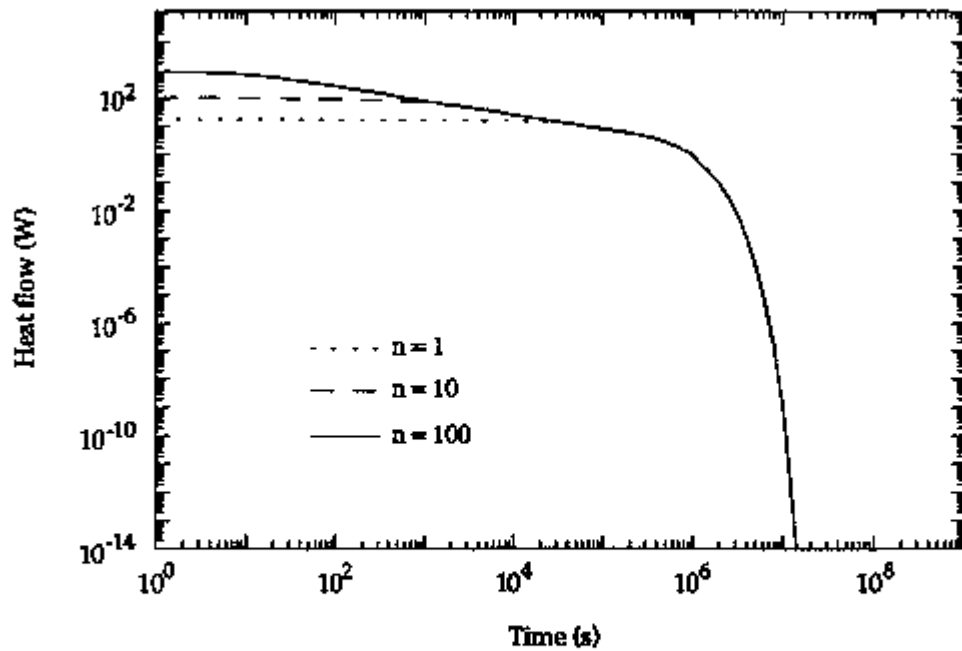
Fig. 4.45. Convergence of series solution in Eq. 4.111.
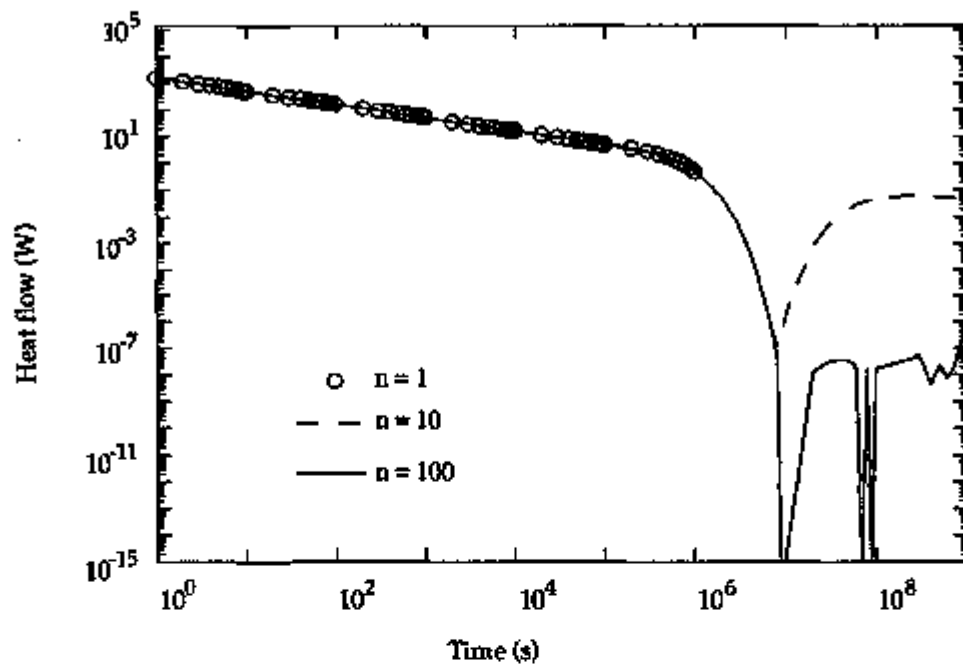
Fig. 4.46. Convergence of series solution in Eq. 4.112.
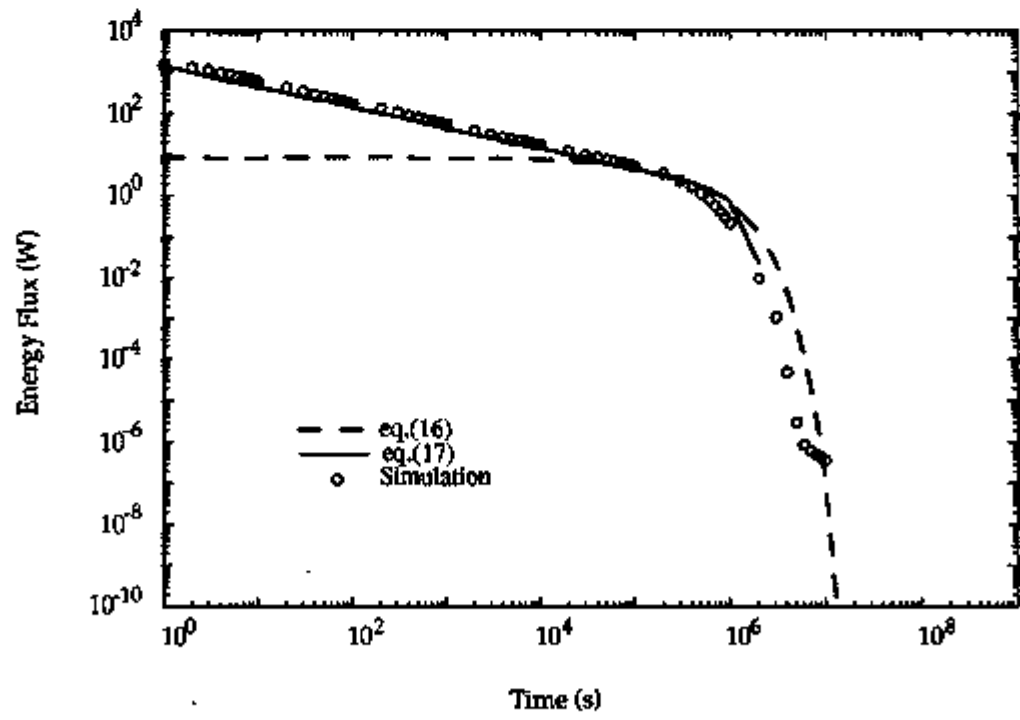
Fig. 4.47. Comparison of energy transfer rates between anlytical solution and simulation.
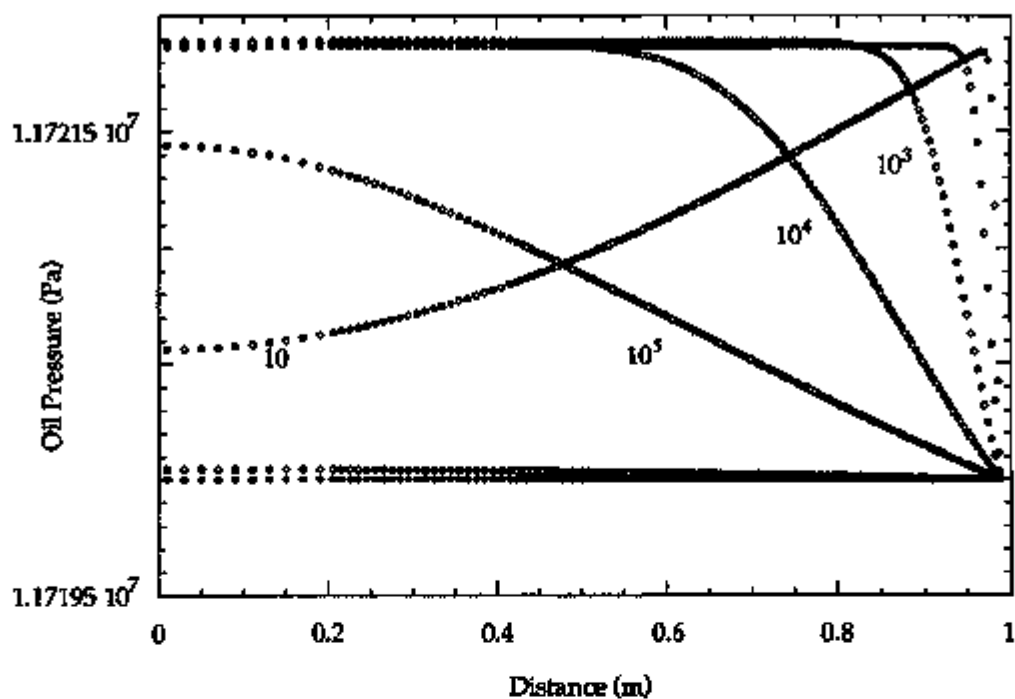
Fig. 4.48. Pressure distribution during expansion recovery at different heating times.
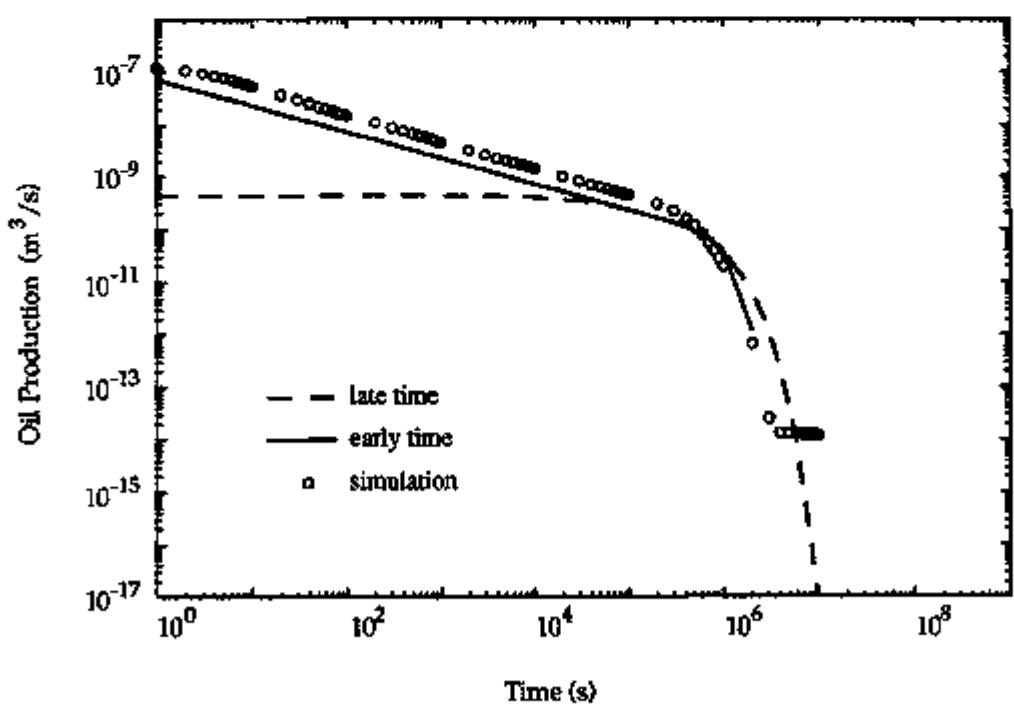
Fig. 4.49. Analytical vs. numerical solution for oil transfer by expansion.
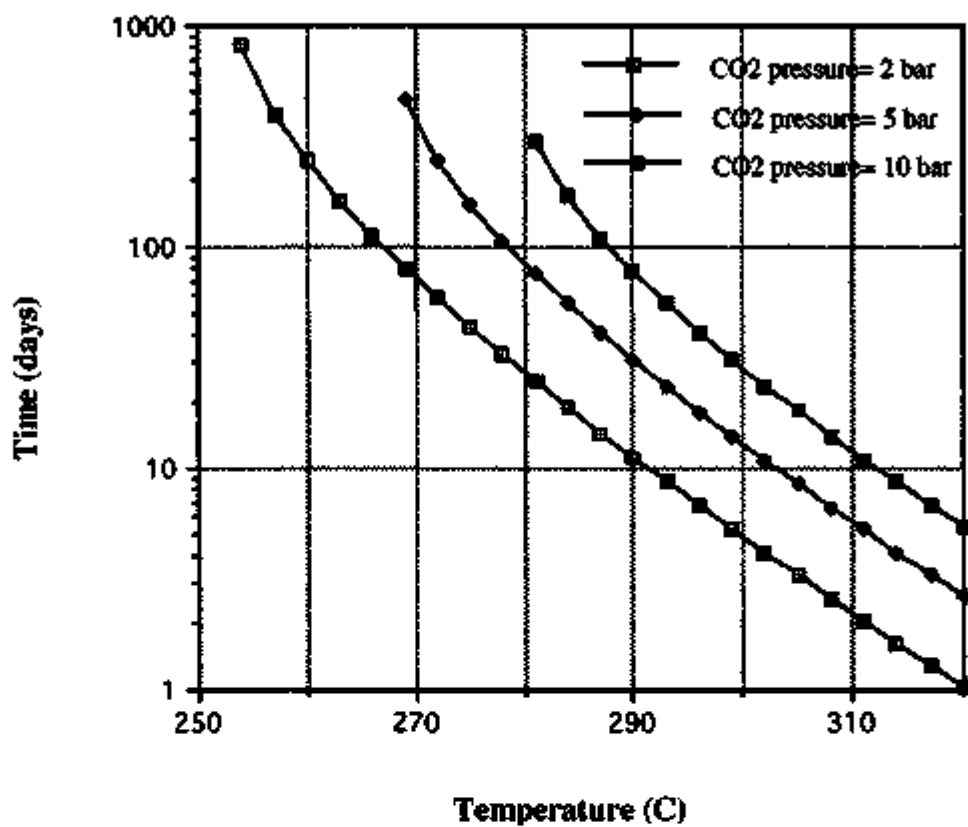
Fig. 4.50. Time required to generate critical gas saturation by chemical reaction.
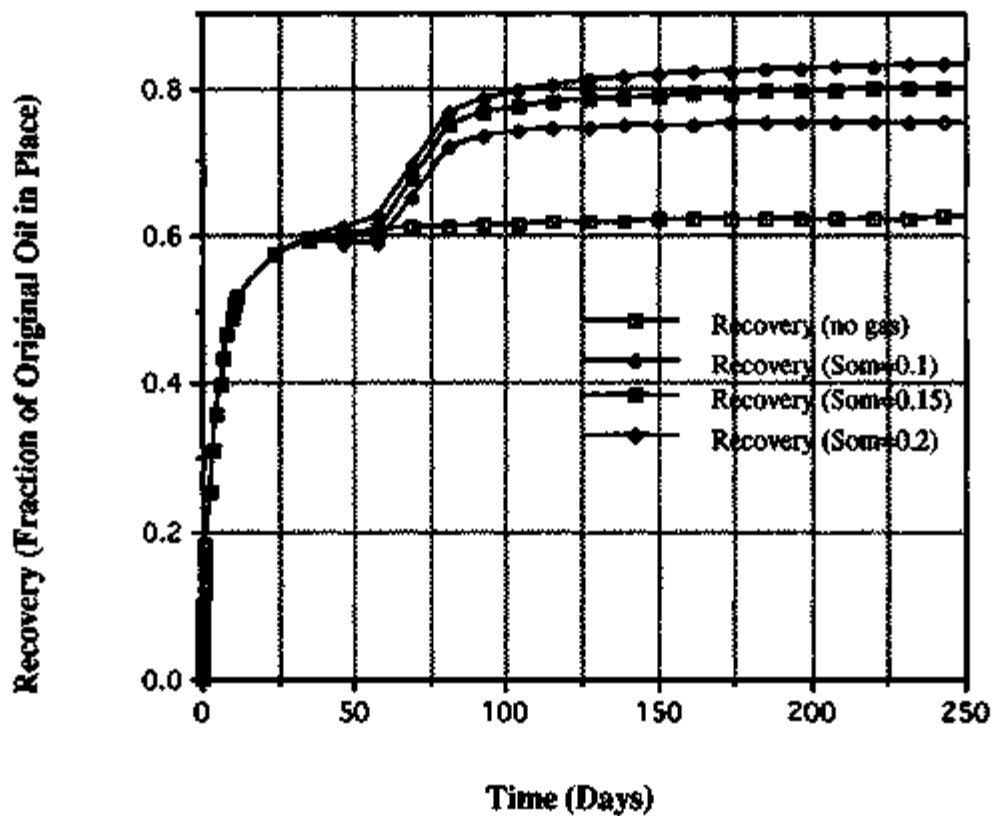
Fig. 4.51. Comparison of recovery for different residual oil saturations as a function of time. (T_f=290°C, P_{co2}= 5 bars).
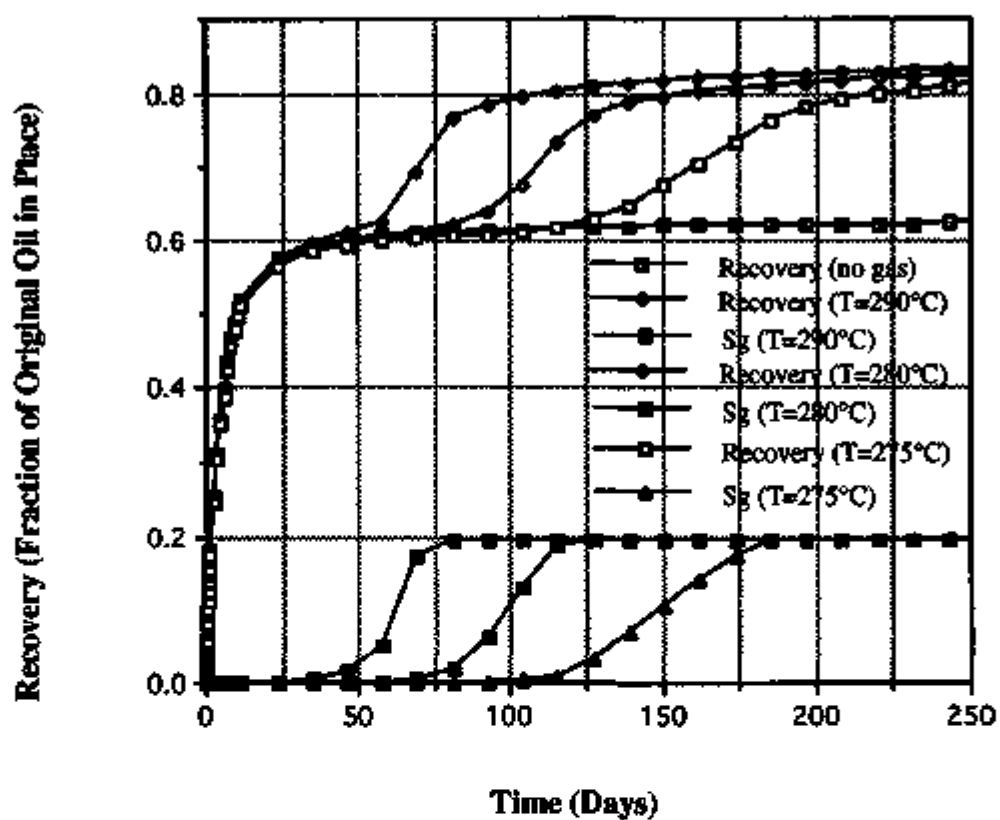
Fig. 4.52. Comparison of gas saturation and recovery for different temperatures as a function of time. (P_{co2}= 5 bars, S_{om}=0.2).
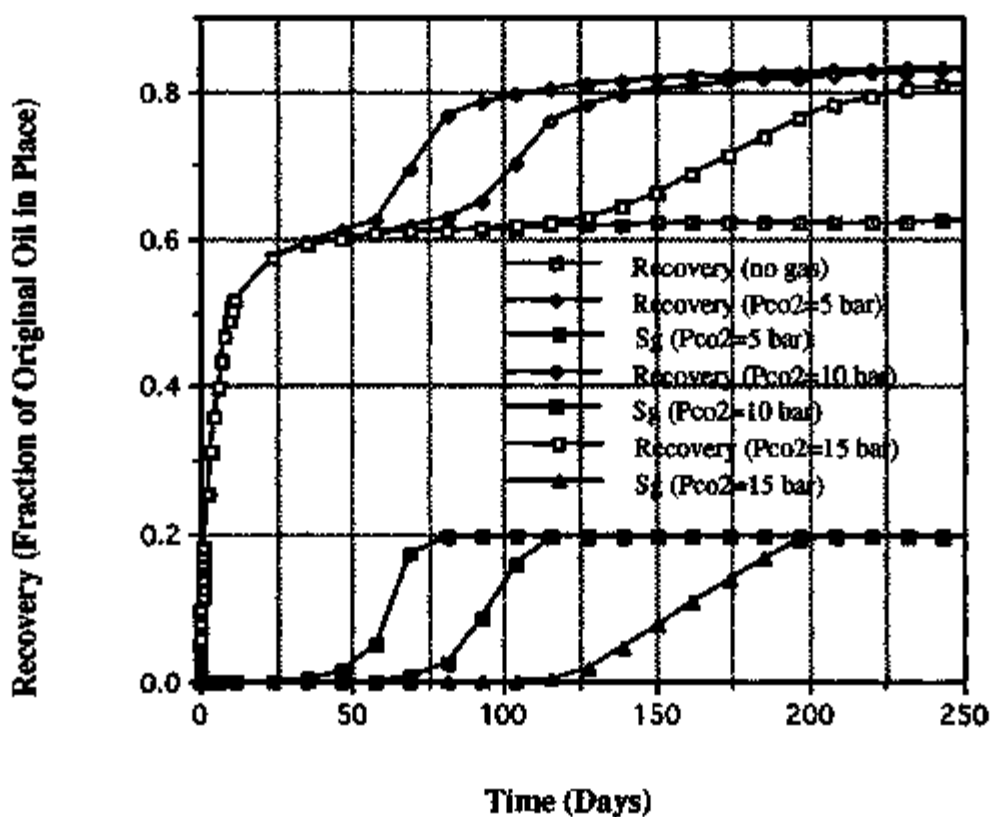
Fig. 4.53. Comparison of gas saturation and recovery at different pressures as a function of time. (T_f=290°C, S_{om}=0.2).
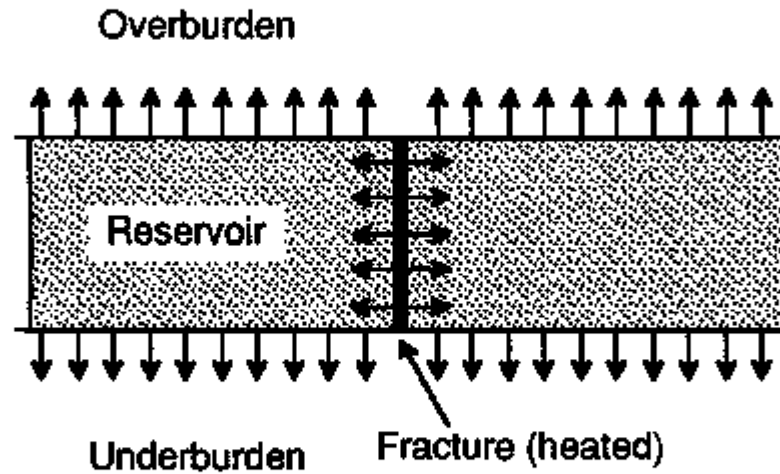
Fig. 4.54. Schematic of reservoir, overburden, and underburden being heated by a constant temperature fracture.
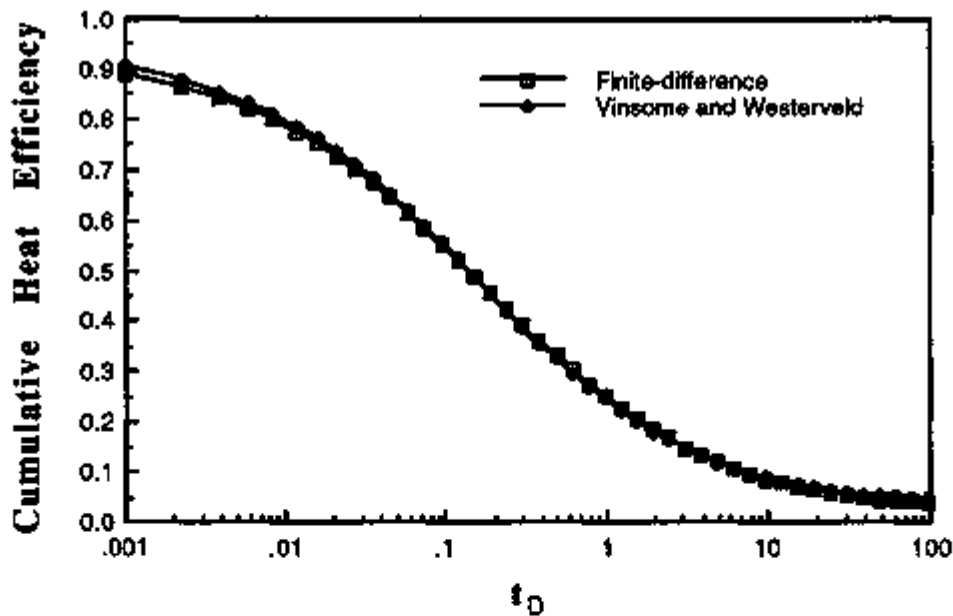
Fig. 4.55. Comparison of cumulative heat efficiency from a complete finite-difference heat conduction simulation vs. application of the Vinsome and Westerveld (1980) technique.
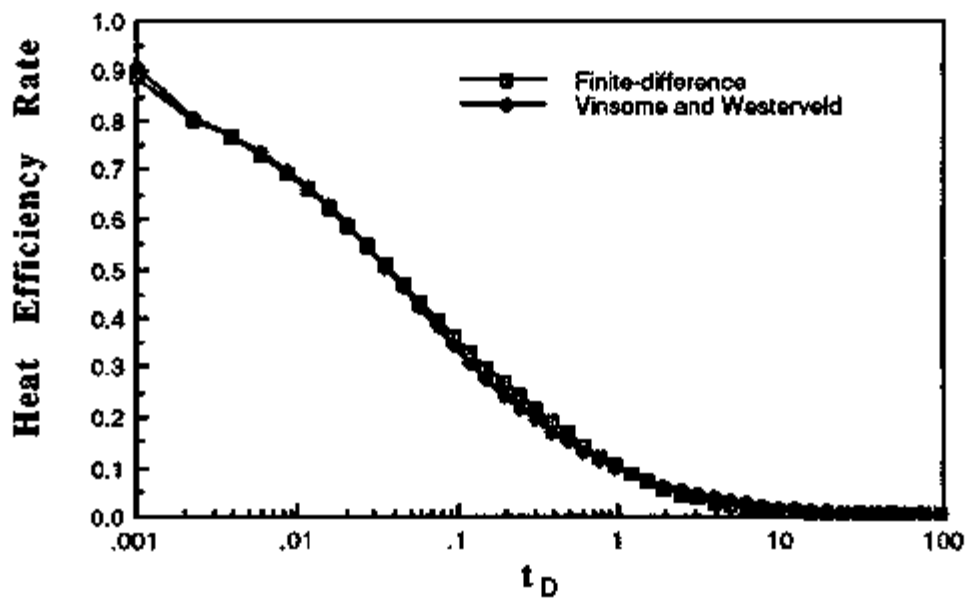
Fig. 4.56. Comparison of heat efficiency rate from a complete finite-difference heat conduction simulation vs. application of the Vinsome and Westerveld (1980) technique.
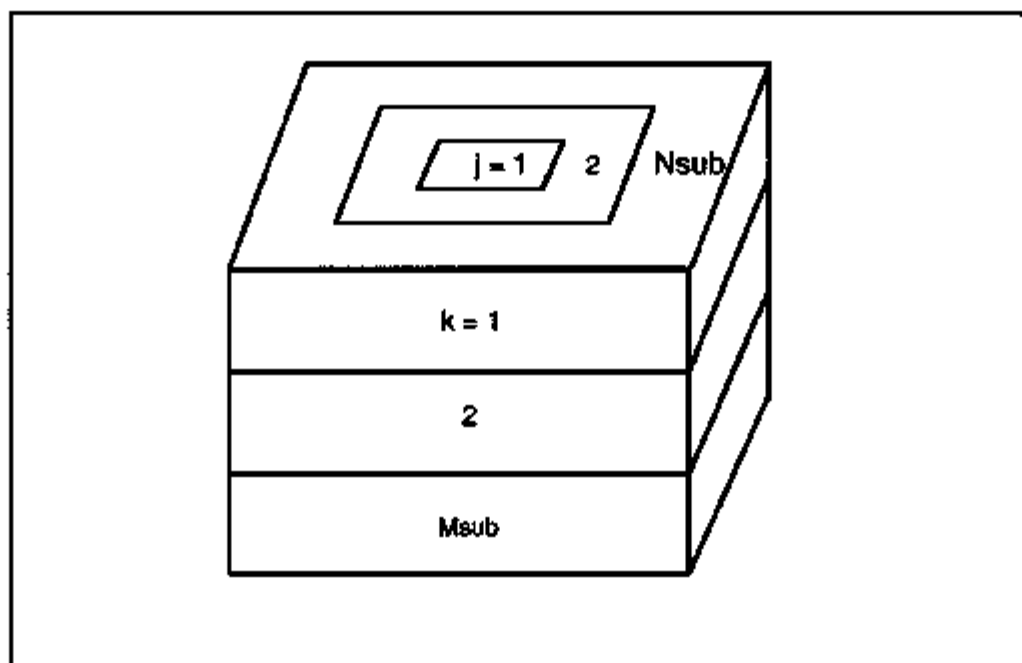
Fig. 4.57. Schematic of matrix block subgrids.
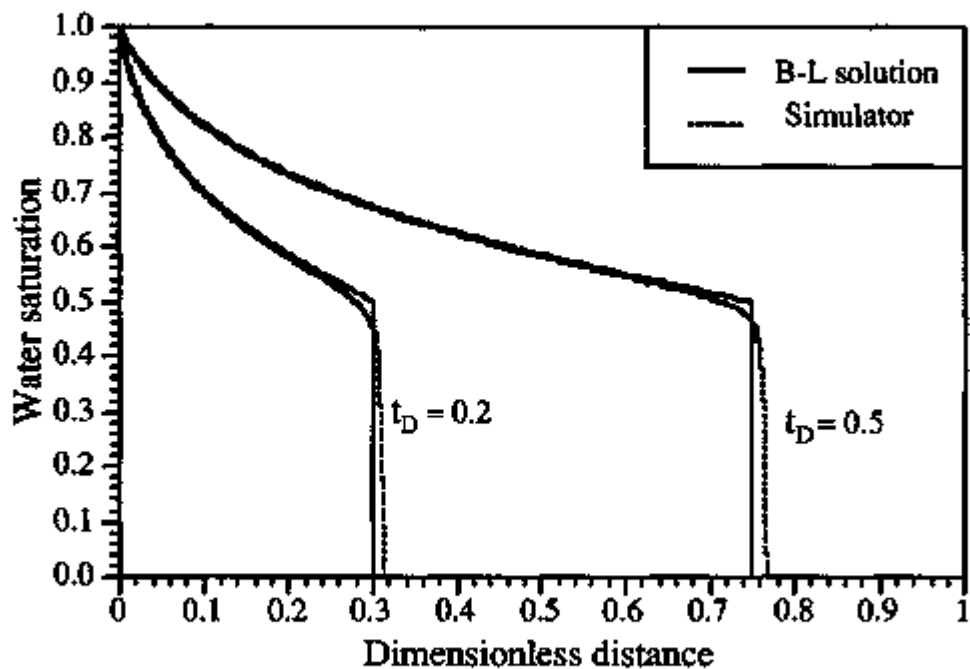
Fig. 4.58. Comparison of water saturation profiles from the Buckley-Leverett (B-L)
analytical solution compared to the model developed in this study.
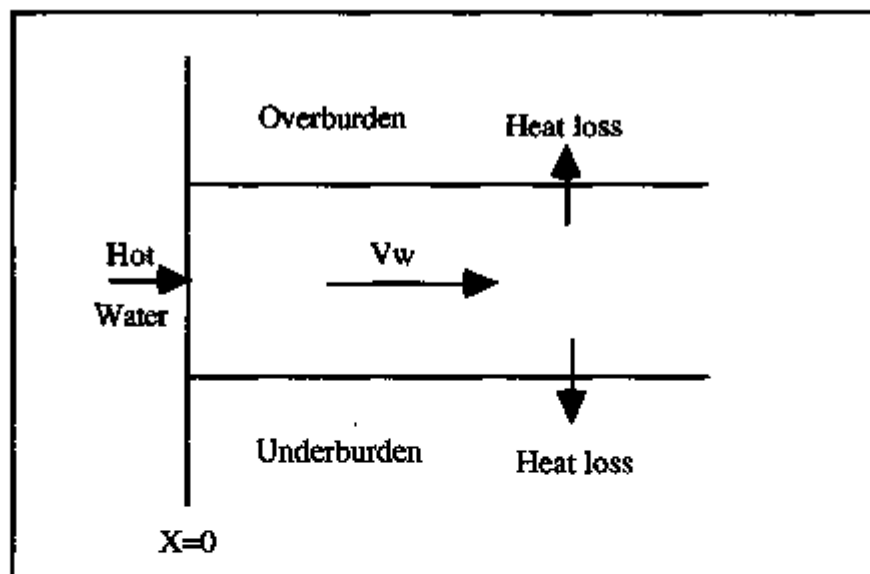
Fig. 4.59. Schematic of the Lauwerier (1955) hot water injection problem.
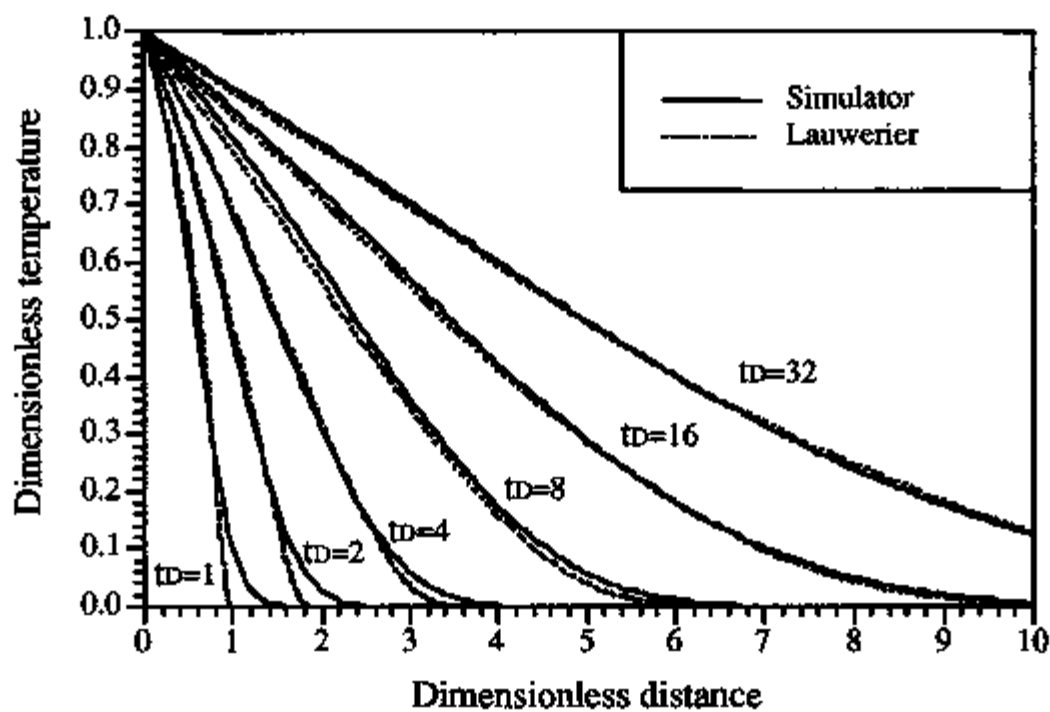
Fig. 4.60. Comparison of Lauwerier's (1955) solution with analytical simulation results.
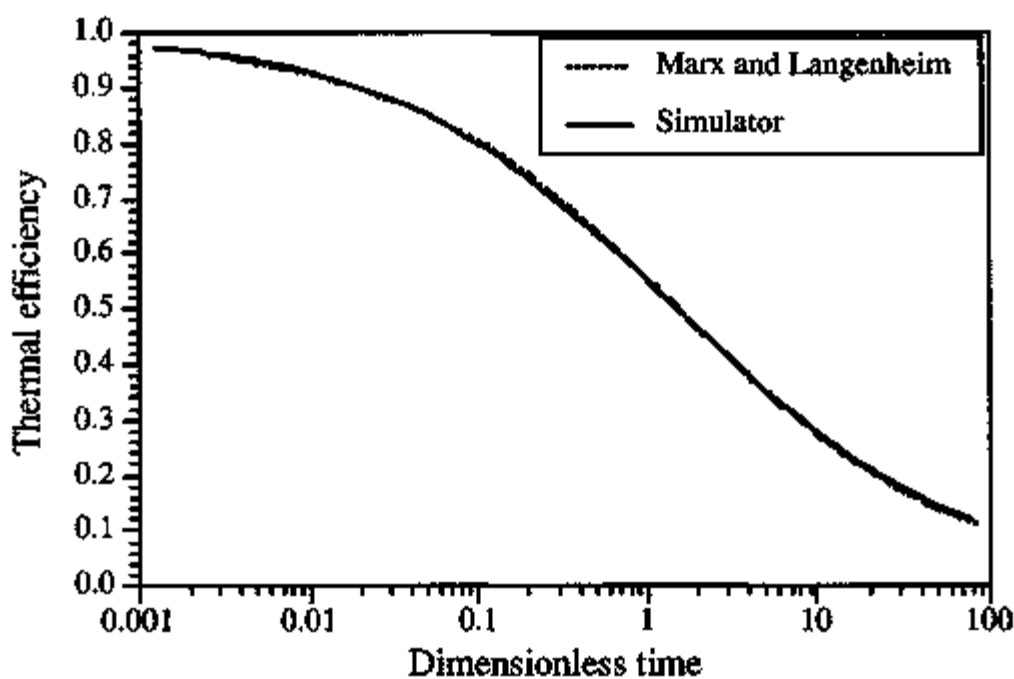
Fig. 4.61. Comparison of Marx and Langenheim (1959) solution with simulation.

193
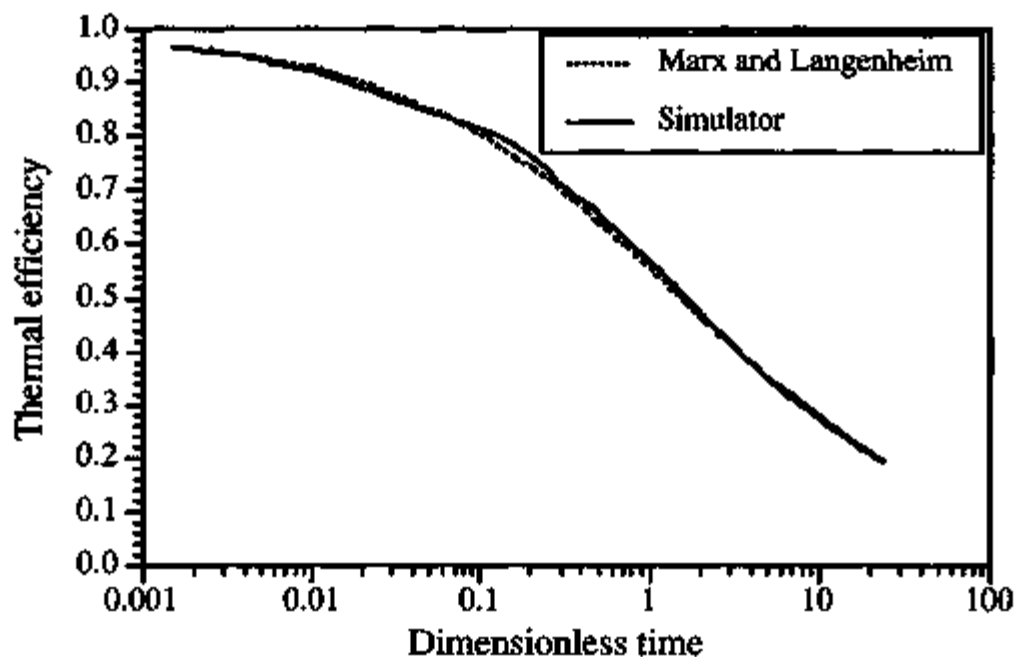
Fig. 4.62. Comparison of Marx and Langenheim (1959) solution with simulation, 2D case.
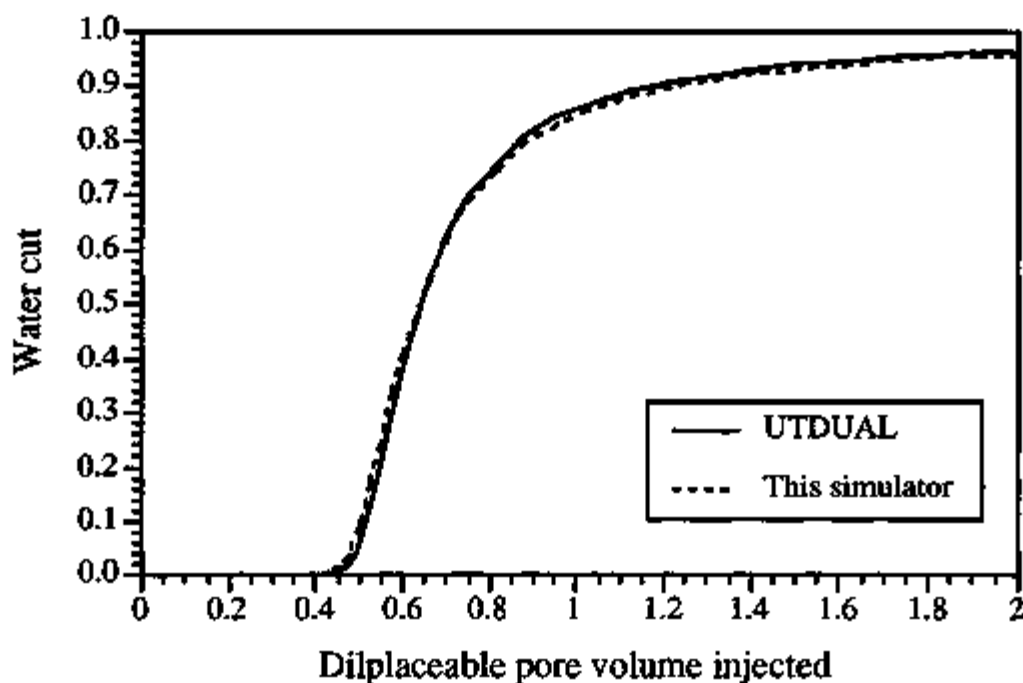
Fig. 4.63. Comparison with thermal dual porosity simulator against the isothermal dual porosity simulator UTDUAL for an ideal fractured reservoir.
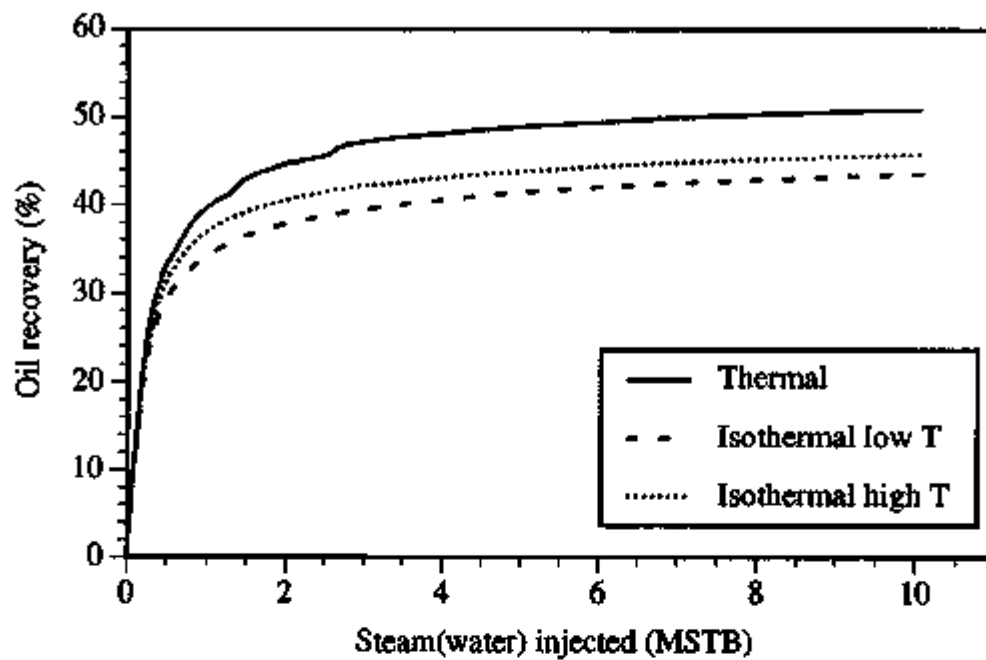
Fig. 4.64. Effect of thermal vs. isothermal Processes on oil recovery.
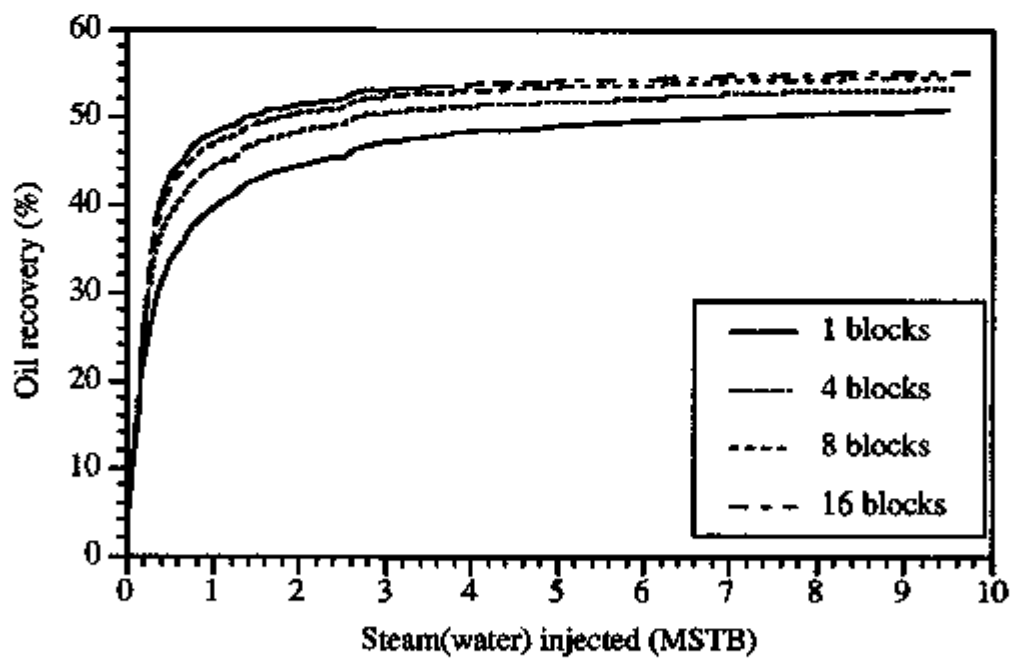
Fig. 4.65. Effect of different number of matrix grid blocks on oil recovery.

NOMENCLATURE

a	=	Shortest length of the rectangular prism matrix block
A_c	=	Area of cylinder face
A_L	=	Area of cylinder ends
A_L	=	Total surface area of the imbibition front inside matrix block
A_o	=	Total surface area of the matrix block through which imbibition occurs
A_x	=	Total surface area of the imbibition front inside matrix block at distance x
A_{x1}	=	Matrix block area perpendicular to the direction x_1 at distance x
A_{x2}	=	Matrix block area perpendicular to the direction x_2 at distance x
A_{x3}	=	Matrix block area perpendicular to the directions x_3 at distance x
b	=	Medium length of the rectangular prism matrix block
B_α	=	Formation volume factor of phase α
C	=	CO_2 concentration in water
c	=	Longest length of rectangular prism matrix block
$C_{p\alpha}$	=	Specific heat capacity at constant pressure of phase α
C_r	=	Pressure compressibility of oil
C_s	=	Specific heat capacity of rock
d	=	Fracture spacing
D_f	=	Diffusion coefficient of fluid
D_T	=	Thermal diffusion coefficient
E	=	Activation energy
e_s	=	Output voltage from the sensor
f	=	Generic function
f_q	=	Quartz content in the rock
f_j	=	Volume fraction of matrix subgrid j
f_{ow}	=	Ratio of CO_2 solubility in oil vs. water, dimensionless
f_w	=	Fractional flow
g_x	=	Conductance in X direction
g_y	=	Conductance in Y direction
h	=	Height of cylinder
h_α	=	Specific enthalpy of phase α
h_k	=	Thickness of k th layer of subgrid
h_s	=	Specific enthalpy of saturated vapor
h_w	=	Specific enthalpy of saturated water
i, j, k	=	Node identification
J	=	Jacobian matrix
K	=	Aspect ratio
k	=	Absolute permeability of the matrix block
k	=	Permeability
k_o	=	Kinetic pre-exponential coefficient
K_H	=	Henry's coefficient
k_h	=	Heat conductivity
k_r	=	Relative permeability
k_{rgas}	=	Relative permeability to gas
k_{rwater}	=	Relative permeability to water
$k_{r\alpha}$	=	Relative permeability of phase
k_s	=	Sensor constant
L	=	Length of the specimen
L	=	Limiting distance, half of the shortest distance across the matrix block

196

L'	=	Distance from the fracture face to the leading edge of the imbibition front
L_D	=	Dimensionless imbibition front distance
L_x or L_y	=	Half correlation lengths
L_x, L_y, L_z	=	Matrix block dimensions
m	=	Total CO_2 concentration
m_l	=	CO_2 concentration in liquid
$\bar{n}$	=	Unit normal vector
n_O	=	Oil relative permeability exponent
n_w	=	Water relative permeability exponent
P	=	Pressure
p	=	Probability of occurrence of conductors
P_α	=	Pressure of phase α
P_c	=	Capillary pressure
$P_{c,swi}$	=	Capillary pressure at the initial water saturation
P_{gas}	=	Pressure of the gas
PI	=	Productivity of well
P_{water}	=	Pressure of the water
q_α	=	Injection or production rate of phase α
q_{gas}	=	Total flow rate of gas in all directions
$q_{gas\,x_1}$	=	Flow rate of gas in x_1 direction
$q_{gas\,x_2}$	=	Flow rate of gas in x_2 direction
$q_{gas\,x_3}$	=	Flow rate of gas in x_3 direction
q_{gasC}	=	Gas flow rate from cylinder face
q_h	=	Source term in energy equations
q_{water}	=	Water flow rate from cylinder face
q_{gasL}	=	Gas flow rate from cylinder ends
q_{water}	=	Water flow rate from cylinder ends
Q_h	=	Energy injection or production rate
Q_l	=	Heat loss to the overburden and underburden
q_s	=	Heat flux through the sensor
q_{sw}	=	Steam condensation rate
Q_{water}	=	Cumulative water imbibed
q_{water}	=	Total flow rate of water in all directions
$q_{water\,x_1}$	=	Flow rate of water in x_1 direction
$q_{water\,x_2}$	=	Flow rate of water in x_2 direction
$q_{water\,x_3}$	=	Flow rate of water in x_3 direction
Q_∞	=	Cumulative water imbibed at the end of imbibition
R	=	Gas constant
R	=	Radius of cylinder
r	=	Radius
$R_b(p)$	=	RG transformation of p
r_{co2}	=	Rate of CO_2 production
S	=	Saturation, dimensionless
s	=	Laplace variable in dimensional space
s^*	=	Laplace variable in dimensionless space
S_α	=	Saturation of phase α
S_{water}	=	Water saturation
S_{wi}	=	Initial water saturation

T	=	Temperature
T_h	=	Hot (steam) temperature
T_i	=	Initial reservoir temperature
t	=	Time
t^*	=	Time to reach the center of the block
TH	=	Transmissibility in horizontal direction of matrix block
T^i	=	Initial temperature
TV	=	Transmissibility in vertical direction of matrix block
TX	=	Transmissibility in x-direction
TXC	=	Transmissibility of energy by conduction in x-direction
TXH	=	Transmissibility of energy in x-direction
TY	=	Transmissibility in y-direction
TYC	=	Transmissibility of energy by conduction in y-direction
TYH	=	Transmissibility of energy in y-direction
TZ	=	Transmissibility in z-direction
TZC	=	Transmissibility of energy by conduction in z-direction
TZH	=	Transmissibility of energy in z-direction
U_α	=	Internal energy of phase α
U_r	=	Internal energy of matrix
V	=	Volume of the grid block
WI	=	Injectivity of well
x, y, z	=	Cartesian coordinates
X	=	Position
x_1, x_2, x_3	=	Directions
z	=	Gas deviation factor, dimensionless

Greek Symbols

α	=	Phase α
α	=	Thermal diffusivity
B_α	=	Formation volume factor of phase α
β_r	=	Thermal expansion coeficient of rock
γ_α	=	Specific gravity of phase α
$\gamma^{(h)}$	=	Semivariogram
Δ	=	Change of a parameter
Δ_x	=	Node to node distance in X direction
ζ	=	Correlation length
δ_x	=	Block dimension in X direction
θ	=	Contact angle
θ or φ	=	Normalized temperature
λ	=	Thermal conductivity
λ_α	=	Mobility of phase α
λ_{eff}	=	Effective thermal conductivity
λ_f	=	Fluid thermal conductivity
λ_L	=	Lower bound on thermal conductivity
λ_s	=	Solid thermal conductivity

λ_t	$=$	Effective conductivity of formation
λ_U	$=$	Upper bound on thermal conductivity
μ_α	$\simeq$	Dynamic viscosity of phase α
μ_α	$\simeq$	Viscosity of phase α
μ_{gas}	$=$	Viscosity of the gas
μ_s	$\simeq$	Viscosity of saturated vapor
μ_w	$=$	Viscosity of saturated water
μ_{water}	$=$	Viscosity of the water
ρ	$=$	Density
ρ_α	$=$	Density of phase α
ρ_α	$=$	Density of phase α
ρ_r	$\simeq$	Density of matrix
ρ_s	$\simeq$	Density of saturated vapor
ρ_w	$=$	Density of saturated water
ρ_{sc}	$=$	Density at standard conditions
σ	$=$	Electrical conductivity
σ	$=$	Interfacial tension
τ	$=$	Time
$\tau_{\alpha mf}$	$\simeq$	Matrix-fracture transfer rate of phase α
τ_{hmf}	$=$	Matrix-fracture transfer rate of energy
υ	$=$	Kinematic viscosity
ω	$=$	Upstream weighting factor
∂	$=$	Differential operator
Φ	$=$	Formation resistivity factor
ϕ	$=$	Porosity
∇	$=$	Hamilton operator

Subscripts

α	$=$	Phase
cow	$=$	Capillary pressure for oil and water two phase
$eq1$	$\simeq$	Value at chemical equilibrium
$eq2$	$\simeq$	Value at thermodynamic equilibrium
f	$=$	Fracture
g	$=$	Gas
i	$=$	Initial
m	$\simeq$	Matrix
o	$=$	Oil
om	$=$	Residual oil in three-phase system
org	$=$	Residual oil in oil-gas system
orw	$=$	Residual oil in oil-water system
r	$=$	Relative, rock
rg	$=$	Relative permeability of gas

rgo	=	Relative permeability of gas at residual oil saturation
rog	=	Relative permeability of oil in oil-gas system
rogo	=	Relative permeability of oil in oil-gas system at residual gas saturation and zero water saturation
row	=	Relative permeability of oil in oil-water system
rowo	=	Relative permeability of oil in oil-water system at residual water saturation and zero gas saturation
rw	=	Relative permeability of water
rwo	=	Relative permeability of water at residual oil saturation
s	=	Steam
w	=	Water
wc	=	Connate water
wi	=	Irreducible water
x, y, z	=	x, y and z directions

Superscript

*	=	Normalized value

REFERENCES

"2400B System Guide," John Fluke Mfg. Co., Inc. (1984).

Aharony, A., E.L. Hinrichsen, A. Hansen, J. Feder, T. Jossang and H.H. Hardy: "Effective Renormalization Group Algorithm for Transport in Oil Reservoirs," *Phys. Rev. A* (1991) **177** 260-66.

Ahmed, E., A. Tawansi, and M.A. Soliman: "Grey Scaling, A New Approximation for Random Resistor Networks," (1991) *Physics Letters A*, **141** 5,6 301.

American Institute of Physics Handbook, second edition, Table 4g-11, McGraw-Hill, Inc., New York, NY (1963) 4-96.

Anand, J., W.H. Somerton, and E. Gomma: "Predicting Thermal Conductivities of Formation from Other Known Properties," *Soc. Pet. Eng. J.* (October 1973) 267.

Arovas, D., R.N. Bhatt, and B. Shapiro: "Anisotropic Bond Percolation in Two Dimensions," *Phys. Rev. B* (1983) **28**, No. 3, 1433-37.

Barber, M.N. and B.W. Ninham: *Random and Restricted Walks Theory and Applications* Gordon and Breach Science Publishers, New York (1970).

Barenblatt, G.E., I.P. Zheltor, and I.N. Kockina: "Basic Concepts in the Theory of Homogeneous Liquids in Fissured Rocks," *J. Appl. Math. Mech.* (USSR) (1960) **24**, No. 5, 1286-1303.

Barenblatt,G.E., I.P. Zheltov and I.N. Kochina: "Basic Concepts in the Theory of Homogeneous Liquids in Fissured Rocks," *J. Appl. Math.* (USSR) **24**, No.5 (1960) 1286-1303.

Baxley, A.L., N.C. Nahas, and T.R. Couper: *Proceedings of the Seventh Conference on Thermal Conductivity*, NBS Special Publ. No. 302 (Sept. 1968) 685-694.

Beckner, B., A. Firoozabadi, and K. Aziz: "Transverse Imbibition in a Double Porosity Simulator," paper SPE 17414 presented at the 1988 SPE California Regional Meeting, Long Beach, Mar. 23-25.

Beckner, B.L., H.M. Chan, A.E. McDonald, S.O. Wooten and T.A. Jones: "Simulating Naturally Fractured Reservoirs Using a Subdomain Method," paper SPE 21241 presented at the 1991 SPE Symposium on Reservoir Simulation, Anaheim, CA., Feb.

Ben-Mizrahi, A. and D.J. Bergman: "Non-Universal Critical Behavior of Random Resistor Networks with a Singular Distribution of Conductances," *J. Phys. C: Solid State Phys.* (1981) **14**, 909-22.

Beran, M.: "Use of the Variational Approach to Determine Bounds for the Effective Permittivity in Random Media," *Nuovo Cimento* (1965) **38**, 771-82.

Bernasconi, J.: "Real Space Renormalization of Bond-Disordered Conductance Lattices," *Phy. Rev. B* (Sept. 1978) **18**, No. 5, 2185-91.

Berryman, J.G.: "Measurement of Spatial Correlation Functions Using Image Processing Techniques," *J. Appl. Phys.* (1985) **57**, No. 7, 2374-84.

Bickley, W.G.: *Bessel Functions and Formulae*, University Press, Cambridge (1953).

Birch, F. and H. Clark: "The Thermal Conductivity of Rocks and Its Dependence on Temperature and Composition," *Am. J. Science* (1940) **238**, No. 8 and 9, 529-58 and 613-35.

Blackwell, J.H.: "Radial-Axial Heat Flow in Regions Bounded Internally by Circular Cylinders," *Canadian J. Phys.* (1953) **31**, 472-9.

Blackwell, J.H.: "The Axial-Flow Error in Thermal Conductivity Probe," *Canadian J. Phys.* (1956) **34**, 412-7.

Bridgman, P.W.: "Thermal Conductivity and Compressibility of Several Rocks Under High Pressure," *Amer. Jour. Sci.* (1924) **7**, 31.

Broadbent, S.R. and J.M. Hammersley: "Percolation Processes- I. Crystals and Mazes, II. The connective Constant," *Proc. Cambridge Phil. Soc.* (1957) **53**, 629-45.

Brown, W.F.: "Solid Mixture Permitivities," *J. Chem. Phys.* (1955) **23**, 1514-17.

Bruggemann, D.A.G.: "Berechnung Verschiedener Physikalischer Konstanten von Heterogenen Substanzen," *Annalen der Physik* (1935) **24**, 636-79.

Burger, J., P. Sourieau, and M. Combarnous: *Thermal Methods of Oil Recovery*, Gulf Publishing, Houston (1985).

Butler, R.M.: *Thermal Recovery of Oil and Bitumen*, Prentice Hall, London (1991).

Carslaw, H.S. and J.C. Jaeger: *Conduction of Heat in Solids*, Clarendon Press, Oxford (1959) 10-11.

Cathles, L.M., M. Schoell, and R. Simon: "CO_2 Generation During Steamflooding: A Geologically Based Kinetic Theory That Includes Carbon Isotope Effects and Application to High-Temperature Steamfloods," paper SPE 16267 presented at the 1987 SPE International Symposium on Oilfield Chemistry, San Antonio, TX, Feb. 4-6.

Cervenan, M. R., F.E. Vermeulen, and F.S. Chute: "Thermal Conductivity and Specific Heat of Oil Sand Samples," *Can. J. Earth Sci.* (1981) **18**, 926.

Chase, C.A. and O.M. O'Dell: "Application of Variational Principals to Cap and Base Rock Heat Losses," *Soc. Pet. Eng. J.* (Aug. 1973) 200-209.

Chaves, C.M., P.M. Oliveira, and L.A. de Queiroz: "Remarks on the Percolation Problem in Anisotropic Systems," *Prog. Theo. Phys.* (1979) **62**, No. 6, 1550-55.

Chen, J., V. Maroongoge, M.A. Miller, and K. Sepehrnoori: "Characterization of Fluid and Energy Transport in Naturally-Fractured Geological System," Enhanced Oil and Gas Recovery Research Program Annual Report, U. of Texas Center for Petroleum and Geosystem Engineering (1989).

Chen, J.: "New Approaches to Dual Porosity Modeling of Waterflooding in Naturally Fractured Reservoirs," PhD dissertation, U. of Texas at Austin (Aug. 1993).

Chen, W.H., M.L. Wasserman, and R.E. Fitzmorris: "A Thermal Simulator for Naturally Fractured Reservoirs", paper SPE 16008 presented at 1987 9th SPE Symposium on Reservoir Simulation, San Antonio, TX, Feb., 169-180.

Cheney, E.W. and D. Kinacid: *Numerical Mathematics and Computing*, Brooks/Cole Pub. Co., Monterey, CA(1980).

Cheng, S.C. and R.I. Vachon: "The Prediction of the Thermal Conductivity of Two and Three Phase Solid Heterogeneous Mixtures," *Intern. J. Heat Mass Transfer* (1969) **12**, 249-64.

Chien, S.: "Empirical Correlations of Saturated Steam Properties," *SPE Res. Eng.* (May 1992) 295-303.

Clark, K.A.: "Some Physical Properties of a Sample of Alberta Bituminous Sand," *Canadian J. Research* (June, 1944), **22**, Sec F, 174.

Clark, K.K.: "Reduction of Fracture Pressures of Rocks by Intensive Borehole Heating," MS thesis, U. of California, Berkeley (1964).

Closmann, P.J.: "An Aquifer Model for Fissured Reservoirs," *Soc. Pet. Eng. J.* (Oct. 1975) 385-398.

Coats, K.H. : "In-Situ Combustion Model," *Soc. Pet. Eng. J.* (Dec. 1980) 533-554.

Cohen, M.H. and M.P. Anderson: *The Chemistry and Physics of Porous Media*, M. Tomkiewicz and P.N. Sen (Ed.), Pennington, New Jearsey (1985) 1.

Coniglio, A., H.E. Stanley, and W. Klein: "Site-Bond Correlated-Percolation Problem: A Statistical Mechanical Model of Polymer Gelation," *Phys. Rev. Lett.* (1979) **42**, No. 8, 518-22.

Corson, P.B. "Correlation Functions for Predicting Properties of Heterogeneous Materials: II. Empirical Construction of Spatial Correlation Functions for Two-phase Solids," *J. App. Phys.* (1974) **45**, No. 7, 3165-70.

Coumou, K.G. and R.P. Tye: "A Laboratory Instrument for Rapid Determination of Thermal Conductivities in the Range 0.4-5 W/m-K," *High Temperatures - High Pressures* (1981) **13**, 695-99.

Crawford, G.D., A.R. Hagedorn and A.E. Pierce: "Analysis of Pressure Buildup Tests in a Naturally Fractured Reservoir," *J. Pet. Tech.* (Nov. 1976) 1295-1300.

De Ponte, F. and P. Di Filippo: "Design Criteria for Guarded Hot Plate Apparatus," Heat Transmission Measurements in Thermal Insulations, ASTM STO 544, American Society for Testing and Materials (1974) 97-117.

de Gennes, P.G.: *Scaling Concepts in Polymer Physics* (1979) Cornell University Press, Ithaca, New York.

de Magalhaese, A.C.N., C. Tsallis, and G. Schwachheim: "Renormalisation Group Treatment of Bond Percolation in Anisotropic and In homogeneous Planar Lattices," *J. Phys. C: Solid State Phys.* (1981) **14**, 1393-1408.

de Swaan, A.: "A Three-Phase Model for Fractured Reservoirs Presenting Fluid Segregation," paper SPE 10510 presented at the 1982 Symposium on Reservoir Simulation, New Orleans, LA, Jan.

de Swaan, A.: "Theory of Waterflooding in Fractured Reservoirs," *Soc. Pet. Eng. J* (Apr. 1978) 117-122.

de Vries, D.A.: "Het Warmtegeleidings-Vermogen Van Ground," *Med. Landbouwhogeschool, Wageningren* (1952) **52**, 1-73.

Dean, R.H. and L.L. Lo: "Development of a Natural Fracture Simulator and Examples of Its Use," paper SPE 14110 presented at the 1986 International Meeting, Beijing, China, Mar.

"Definition of Heat Insulating Therms and Methods of Determining Thermal Conductivity," British Standard 874 (1965).

Deissler, R.G. and C.S. Eian: "Investigation of Effective Thermal Conductivities," NACA RM E52 C05 (1952).

Deutsch, C.V. and A.G. Journel: "The Application of Simulated Annealing to Stochastic Reservoir Modelling, paper SPE 23568 submitted for publication, Society of Petroeum Engineers, Richardson, TX (1991).

Devries, D.A.: *Bull. Intern. Inst. Refrig.*, Annexe 1952-1 (1952) **32**, 115.

Dogu, G., K. Murtezaoglu, and T. Dogu: "A Dynamic Method for the Effective Thermal Conductivity of Porous Solids," *AIChE J.* (1989) **35**, 4, 683-5.

Doyle, P.G. and J.R. Snell: *Random Walks and Electrical Networks*, The Mathematical Association of America (1984).

Dreher, K.D., D.E. Kenyon and F.O. Iwere: "Heat Flow During Steam Injection into a Fractured Carbonate Reservoir," paper SPE 14902 presented at 1986 SPE/DOE Symposium on Enhanced Oil Recovery, Tulsa, OK.

Ejiogu, G.C. and M. Fiori: "High-Pressure Saturated-Steam Correlations," *J. Pet. Tech.* (Dec. 1987) 1585-1590.

Essam, J,W.: *Phase Transition and Critical Phenomena*, C. Domb and M.S. Green (ed.) Academic Press, London (1972) 197-270.

Eucken, A.: "The Thermal Conductivity of Ceramic Refractory Materials," V.D.I. Forschungsh, Ausgabe B. Band 3 (Mar.-Ap., 1932).

Evans, R.D.: "A Proposed Model for Multiphase Flow Through Naturally Fractured Reservoirs," *Soc. Pet. Eng J* . (Oct., 1982) 669-680.

Fanchi, J.R., K.J. Harpole, and S.W. Bujnowski: "BOAST: A Three-Dimensional, Three-Phase Black Oil Applied Simulation Tool (Version 1.1)," Program User's Manual, Contract No. AC19-90BC10033, U.S. DOE (Sept. 1982).

Fassihi, M.R., K.O. Meyers, and K.R. Welsbrod: "Thermal Alteration of Viscous Crude Oils," *SPE Res. Eng.*, (Aug. 1990), 393-401.

Fidelle, T., Jr. and R.S. Kirk: "A study of Unidirectional Versus Tridirectional Heat Flux Models and Effect of Particle Size on Heat Conduction in Composite Solids," *AIChE J.* (1971) **17**, No. 6, 1427-34.

Fortuin, C.M. and P.W. Kasteleyn: "On the Random-Cluster Model I. Introduction and Relation to Other Models", *Physica* (1972) **57**, 536-564.

Frisch, H.L. and J.M. Hammersly: "Percolation Processes and related Topics," *J. Soc. Indust. Appl. Math.* (1963) **11**, 894.

Gilbo, C.F.: "Experiments with a Guarded Hot Plate Thermal Conductivity Set," Symposium on Thermal Insulating Materials, Am. Soc. Testing Mats. (1951) 45-55.

Gilman, J.R. and H. Kazemi: "Improved Calculations for Viscous and Gravity Displacement in Matrix Blocks in Dual-Porosity Simulators," paper SPE 16010 presented at the 1987 Symposium on Reservoir Simulation, San Antonio, TX, Feb.

Gilman, J.R. and H. Kazemi: "Improvements in Simulation of Naturally Fractured Reservoirs," *Soc. Pet. Eng. J.* (Aug. 1983) 695-707.

Gilman, J.R.: "An Efficient Finite-Difference Method for Simulating Phase Segregation in the Matrix Blocks in Double-Porosity Reservoirs," *SPE Res. Eng.* (July 1986) 403-413.

Gomez-Hernandez and R.M. Srivastava: "ISIM3D: an ANSI-C Three-dimensional Multiple Indicator Conditional Simulation Program,: *Computers & Geosciences* (1990) **16**, No. 4, 395-440.

Gomma, E. and W. Somerton: "Transient Method for Measuring Thermal Properties of Fluid-Saturated Porous Media," Proceedings XII Thermal Conductivity Conference, Birmingham, AL (Sept. 15, 1972) 284-94.

Gomma, E.E. and W.H. Somerton: "Thermal Behavior of Multifluid-Saturated Formations, Part 1: Effect of Wettability, Saturation and Grain Structure," paper SPE 4896-A presented at the 1974 Annual SPE California Regional Meeting, San Fransisco, CA, April 4-5.

Gomma, E.E.: "Thermal Behavior of Partially Liquid Saturated Porous Media," PhD dissertation, U. of California, Berkeley (1973).

Gonzalez, A.E. and P.J. Reynolds: "Universality of "Four-Cordinated Correlated Percolation and Random Percolation," *Phys. Lett.* (1980) **80** 5,6, 357-360.

Gorring, R.L. and S.W. Churchill: "Thermal Conductivity of Heterogeneous Materials," *Chem. Eng. Prog.* (1961) **57**, 7, 53-59.

Goss, R., J. Combs, and A. Timur: "Prediction of Thermal Conductivity in Rocks from Other Physical Parameters and from Standard Geophysical Well Logs," 16th. Annual Logging Symposium, SPWLA (June 4-7, 1975).

Gouker, M. and F. Family: "Evidence for Classical Critical Behavior in Long-Range Site Percolation," *Phys. Rev. B* (1983), **28**, No. 3, 1449-52.

Haar, L., J.S. Gallagher, and G.S. Kell: *Steam Tables*, National Bureau of Standards, Washington, D.C./National Research Council of Canada, Ottawa (1984).

Hageman, L.A. and D.M. Young: *Applied Iterative Method*, Academic Press, Inc. New York (1981).

Hamilton, R.L. and O.K Crosser: *Ind. Eng. Chem. Fundamentals* (1962) **1**, 3, 187.

Hanafi, A. and G.A. Karim: "The Thermal Conductivity of Oil Sands Using a Transient Method," *J. Energy Resources Technology* (1986) **108**, 315-20.

Hashin, Z. and S. Shtrikman: "A Variational Approach to the Theory of the Effective Magnetic Permeability of Multiphase materials," *J. Appl. Phys.* (1962) **33**, 1514-17.

Hashin, Z.: *Theory of Composite Materials*, Pergamon Press (1970).

Hayashitani, M., D.W. Bennion, J.K. Donnelly, and R.G. Moore: "Thermal Cracking Models for Athabasca Oil Sands Oil," paper SPE 7549 presented at the 1978 Annual Fall Technical Conference and Exhibition of the Society of Petroleum Engineers, Houston, TX, Oct. 1-3.

Hensen, J.P. and I.R. McDonald: *Theory of Simple Liquids* Academic Press, New York (1976).

Herin, P. and P. Thery: "Measurements on the Thermoelectric Properties of Thin Layers of Two Metals in Electrical Contacts. Application for Designing New Heat-Flow Sensors," *Meas. Sci. Technol.* (1992) 3, 495-500.

Horai, K.: "Thermal Conductivity of Rock Forming Minerals," *J. Geophy. Res.* (1971) **76**, No. 5, 1278-308.

Hoshen, J., R. Kopelman, and E.M. Monberg: *J. Stat. Phys..* (1978) **9**, 219.

Howell, J. R.:"STNA4 – A Simple Format Interactive Computer Program for Solving Problems in the Fields of Energy Systems Analysis and Heat Transfer," Univ. of Texas Center for Energy Studies, Austin, TX (1983).

Howell, J.R.: private communication (1992) U. of Texas at Austin.

Hughes, B.D. and S. Prager: "Random Process and Random Systems: an Introduction," *Lecture Notes in Mathematics, The Mathematics and Physics of Disordered Media*, A. Dold and B. Eckmann (eds.), Springer-Verlag, New York (1983) 1-108.

Ikeda, H.: "Percolation in Anisotropic Systems- Real-Space Renormalization Group," *Prog. Theor. Phys.* (1979) **61**, 3, 842-849.

Isaaks and R.M. Srivastava: Oxford University Press, New York (1989).

Jacob, M. and G.A. Hawkins: *Heat Transfer and Insulation*, John Wiley and Sons, Inc., New York (1942).

Jensen, T.B., M.P. Sharma, H.G. Harris, and D.L. Whitman: "Numerical Investigations of Steam and Hot-Water Flooding in Fractured Porous Media," paper SPE 24172 presented at the 1992 SPE/DOE Symposium on Enhanced Oil Recovery, Tulsa, OK, Apr.

Jerauld, G.R., J.C. Hatfield, L.E. Scriven, and H.T. Davis: "Percolation and Conduction on Voronoi and Triangular Networks: A Case Study in Topological Disorder," *J. Phys. C* (1984) 17, 1519-29.

Journel, A.G. and F.G. Alabert: "New Method For Reservoir Mapping," *J. Pet. Tech.* (1990) 212-18.

Journel, A.G.: "Constrained Interpolation and Soft Kriging, Proc. 19th APCOM Symp. Publ. Soc. Min. Eng., Littleton, Colorado (1986) 15-30.

Kac, M.: "Random Walk and Theory of Brownian Motion," *Selected Papers on Noise and Stochastic Processes*, Dover Publications, Inc., New York (1954) 295-317.

Kakac, S. and Y. Yener: *Heat Conduction*, 2nd ed., Hemisphere Publishing Corp., (1985).

Kampf, H. and G. Kersten: "Effects of Different Types of Void Volumes on the Radial Temperature Distribution of Fuel Pins," *Nucl. Appl. Technol.* (1970) 9, 288.

Karim, G.A. and A. Hafani: "The Thermal Conductivity of Oil Sands," *Can. J. Chem. Eng.* (Aug., 1981) 59, 461-64.

Kazemi, H., L.S. Merrill, Jr., K.L. Porterfield, and P.R. Zeman: "Numerical Simulation of Water-Oil Flow in Naturally Fractured Reservoirs," *Soc. Pet. Eng. J.* (Dec. 1976) 317-326.

Kazemi, H.: "Pressure Transient Analysis of Naturally Fractured Reservoirs with Uniform Fracture Distribution," *Soc. Pet. Eng. J.* (Dec. 1969) 451-462.

Khan, A. M., and I. Fatt: "A Thermoelectric Device for Measuring Thermal Conductivity of Rock," *Soc. Pet. Eng. J.* (June, 1965) 113.

King, P.: "The Use of Renormalization for Calculating Effective Permeability," *Transport in Porous Media* (1989) 4, 37-58.

Kirkpatrick, S.: "Classical Transport in Disordered Media: Scaling and Effective-Medium Theories," *Phys. Rev. Lett.* (1971) 27, 3, 1722-25.

Kirkpatrick, S.: "Models of Disorderd Materials," *Ill-Condensed Matter*, R. Balian, R. Maynard, and G. Toulouse (eds.), (1979) North-Holland Publishing Company, New York (Course 5).

Kirpatrick,S.: " Percolation and Conduction," *Rev. Mod. Phys* (Oct., 1973) 45, No. 4, 574-588.

Kleppe, J. and R.A. Morse: "Oil Production from Fractured Reservoirs by Water Displacement," paper SPE 5084 presented at the 1974 Annual Meeting, Houston Oct. 6-9.

Knight, R.; A. Chapman, and M. Knoll: "Numerical Modeling of Microscopic Fluid Distribution in Porous Media," *J. App. Phys.* (1990) **68**, 994-1001.

Kreith, F. and W.Z. Black: *Fundamentals of Heat Transfer*, Harper & Row Publishers, New York (1980).

Kreyszig, E.: *Advanced Engineering Mathematics*, 6th ed. John Wiley & Sons, New York (1988).

Kroner, E. and B. Schulz: "Thermophysical Properties of Composites," *High Temperature - High Pressure* (1984) **16**, 115-18.

Krupiczka, R.: "Analysis of Thermal Conductivity in Granular Materials," *Intern. Chem. Engr.* (1967) **7**, No. 1, 122-44.

Kunii, D. and J.M. Smith: "Heat Transfer Characteristics of Porous Rocks," *AIChE J.* (1960) **6**, 71.

Kunii, D. and J.M. Smith: "Thermal Conductivity of Porous Rocks Filled with Stagnant Fluid," *Soc. Pet. Eng. J.* (Mar., 1961) 37.

Kuzay, T.M.: "Effective Thermal Conductivity of Porous Solid-Gas Mixtures," ASME Paper 80-WA/HT-64, ASME Winter Annual Meeting, Chicago, Ill. (1980).

Larson, R.G. and H.T. Davis: "Conducting Backbone in Percolating Bethe Lattices," *J. Phys. C: Solid State Phys.* (1982) **15**, 2327-31.

Laubitz, M.J.: "Measurement of the Thermal Conductivity of Solids at High Temperatures by Using Steady-State Linear and Quasi-Linear Heat Flow," *Thermal Conductivity*, R.P. Tye (ed.), Academic Press, New York (1969) **1**, 111-185.

Lauwerier, H.A.: "The Transport of Heat in an Oil Layer Caused by the Injection of Hot Fluid," *Appl. Sci. Res. A* (1955) **5**, 145-150.

Lee, B.Y.Q. and T.B.S. Tan: "Application of a Multiple Porosity/Permeability Simulator in Fractured Reservoir Simulation," paper SPE 16009 presented at the 1987 Symposium on Reservoir Simulation, San Antonio, TX, Feb.

Lobb, C.J., D.J. Frank, and M. Tinkham: "Percolative Conduction in Anisotropic Media: A Renormalization-group Approach," *Phys. Rev. B* (1981) **23**, No. 5, 2262-68.

Luenberger, D.G.: *Introduction to Linear and Nonlinear Programming*, Addison-Wesley, Reading, Mass. (1973).

Luikov, A.C.: *Heat Flow Through Capillary Porous Bodies*, Pergamon Press, Oxford (1966).

Marx, J.W. and R.N. Langenheim: "Reservoir Heating by Hot Fluid Injection," *Pet. Trans. AIME* (1959) **216**, 312-315.

Maxwell, J.C.: *A Tretise on Electricity and Magnetism*, 3rd ed., V. I, Ch. 9, Art. 314, Dover, New York.

Messmer, J. H.: "The Effective Thermal Conductivity of Quartz Sands and Sandstones," SPE Reprint Series No. 7, *Thermal Recovery Processes*, Society of Petroleum Engineers, Richardson, TX (1985) 33-39.

Messmer, J.H.: "Thermal Conductivity of Porous Media IV Sandstones: The Effect of Temperature and Saturation," presented at the Fifth Thermal Conductivity Conference, Denver, Colorado, October 20-22, 1965.

Messmer, J.H.: "Thermal Conductivity of Porous Media: III. Packings of Particles," presented at the Fourth Thermal Conductivity Conference, San Fransisco, CA, Oct. 12-14, 1964.

Miller, M.A. and S. Mohanty: "Thermal and Thermo-Mechanical Effects in Thermal Oil Recovery", Category B Research, Eighth Annual Report, Enhanced Oil and Gas Recovery Research Program, Center for Petroleum and Geosystems Engineering, U. of Texas, Austin (March 1991).

Miller, M.A., M.M. Sharma, and S. Mohanty: "Thermal and Thermo-Mechanical Effects in Thermal Oil Recovery," Category B Research, Sixth Annual Report, Center for Enhanced Oil and Gas Recovery Research, U. of Texas, Austin (March 1989) 65-100.

Miller, M.A., M.M. Sharma, O. Trevisan, S. Mohanty, and M. Vega: "Thermal Enhanced Oil Recovery Part IV: Thermal Properties of Reservoir Rocks," Category B Research, Ninth Annual Report, Enhanced Oil and Gas Recovery Research Program, Center for Petroleum and Geosystems Engineering, U. of Texas, Austin (April 1992).

Milton, G.W.: "Bounds on the Electromagnetic, Elastic and Other Properties of Two-Component Composites, *Phys Rev. Lett.* (1981) **46**, 542-45.

Milton, G.W.: "Correlation of the Electromagnetic and Elastic Properties of Composites and Microgeometries Corresponding with Effective Medium Approaximation," *Physics and Chemistry of Porous Media*, Johnson, D.L. and P.L. Sen (eds.), AIP Conference Proceedings No. 107, New York (1984) 66-77.

Mirkovich, V.V., W.B. Durham, and H.C. Heard: "Measurement of Thermal Diffusivity of Rock at High Pressure," High Temperature and High Pressures, 8 ETPC Proceedings (1983) **15**, 255-4.

Mirkovich, V.V.: "Thermal Diffusivity Measurement of Amoco Iron by a Novel Method," *Rev. Sci. Instrum.* (1977) **48**, No. 5, 560-5.

Mohanty, S. and M.M. Sharma: "A Monte Carlo RSRG Method for the Percolation/Conduction Properties of Correlated Lattices," *Phys. Letters A* (1991) **154**, No. 9, 475-81.

Mohanty, S. and M.M. Sharma: "A Recursive Method for Estimating Single and Multiphase Permeabilities," paper SPE 20477 presented at the 1990 Soc. Pet. Eng. Annual Tech. Conf. and Exhibition, New Orleans, LA, Sept 22-24.

Nakanishi, H., P.J. Reynolds, and S. Redner: "Anisotropic Bond Percoaltion by Position-Space Renormalisation Group," *J. Phys. A: Math. Gen.* (1981) **14**, 855-71.

Nakanishi, H.: "Some Remarks on Diffusion on Fractals," *Material Science Forum* (1985) **4**, 129-44.

Napiorkwski, M. and P.C. Hemmer: "Combined Site and Bond Percolation with Nearest- and Next-Nearest-Neighbor Bonds," *Phys. Lett.* (1980) **75A**, No. 3, 153-55.

Nash-Williams, C. St J.A.: "Random Walk and Electric Currents in Networks," *Proceedings of the Cambridge Philosophical Society* (1959) **55**, 181-94.

Neumann, W.: "Thermal Conductivity Measurements on Granule-Based Composites," *High Temperatures–High Pressures* (1981) **13**, 687-694.

Niemeijer, T. and J.M.J. van Leeuwen: "Renormalization Theory for Ising Like Spin Systems," *Phase Transition and Critical Phenomena,* C. Domb and M.S. Green (eds.), Academic Press, New York (1974) **6**, 425-507.

Odeh, A.S.: "Unsteady-State Behavior of Naturally Fractured Reservoirs," *Soc. Pet. Eng. J* (Mar. 1965) 60-66.

Owens, W. W. and D.L. Archer: "Waterflood Pressure Pulsing for Fractured Reservoirs," *J. Pet. Tech.* (June 1966) 745-752.

Pascal, A.: "La Mesure de la Conduction Thermique des Materiaux du Batiment," *Inst. Technique du Batiment et des Travaux Publics,* No. 90 (June 1955) 583-598.

Polymer Corporation: private communication (1990).

Prats, M. and S.M. O'Brien: "The Thermal Conductivity and Diffusivity of Green River Oil Shales," *J. Pet. Tech.* (January 1975) 97-107.

Prats, M.: *Thermal Recovery,* Soc. Pet. Eng. of AIME, Richardson, TX (1984).

Pratt, A.W.: "Analysis of Error Due To Edge Heat Loss in Measuring Thermal Conductivity by the Hot Plate Method," *J. Sci. Instrum.* (1962) **39**, 63-68.

Press, W.H., B.P. Flannery, S.A. Teukolsky and W.T. Vetterling: *Numerical Recipes, The Art of Scientific Computing,* Cambridge University Press, New York (1982).

Pruess, K. and T.N. Narasimhan: "A Practical Method for Modeling Fluid and Heat Flow in Fractured Porous Media," paper SPE 10509 presented at the 1982 Symposium on Reservoir Simulation, New Orleans, LA, Jan.

Pruess, K. and T.N. Narasinham: "A Practical Method for Modeling Fluid and Heat Flow in Fractured Porous Media," *Soc. Pet. Eng. J.* (Feb. 1985) **25**, No. 1, 14-26.

Pruess, K. and Y. Wu: "A New Semianalytical Method for Numerical Simulation of Fluid and Heat Flow in Fractured Reservoirs," paper SPE 18426 presented at the 1989 Symposium on Reservoir Simulation, Houston, TX, Feb.

Redner, S. and P.J. Reynolds: "Position-Space Renormalisation Group for Isolated Polymer Chains," *J. Phys. A: Math. Gen.* (1981) **14**, 2679-703.

Reimann, G. and H.M. Weber: *Die Partiellen Differential-Gleichunger der Mathematischen Physic*, Band 1, (1919) F. Vieweg and Sohn, Braunschweig, 474.

Reis, J. C. and M.A. Miller: "Oil Recovery from Naturally Fractured Reservoirs Using Steam Injection," Annual report, Contract No. DE-AC22-90BC14661, U.S. DOE (Oct. 1991).

Reis, J.C.: "An Analysis of Oil Expulsion Mechanisms From Matrix Blocks During Steam Injection in Naturally Fractured Reservoirs," *In Situ* (1992), **16** (1), 43-73.

Reynolds, P.J., H.E. Stanley, and W. Klein: "Large-Cell Monte Carlo Renormalization Group for Percolation," *Physical Review B* (Feb., 1980) **21**, No. 3, 1223-45.

Reynolds, P.J., H.E. Stanley, and W. Klein: "Percolation by Position-Space Renormalisation Group with Large cells," *J. Phys. A: Math. Gen.* (1978) **11**, 8, L199-L207.

Reynolds, P.J., W. Klein, and H.E. Stanley: "A Real Space Renormalization Group for Site and Bond Percolation," *J. Phys. C: Solid State Phys.* (1977) **10**, L167-72.

Rossen, R.H.: "Simulation of Naturally Fractured Reservoirs with Semi-Implicit Source Terms," *Soc. Pet. Eng. J.* (June 1977) 201-210.

Roy, R.F., A.E. Beck, and Y.S. Touloukian: "Thermophysical Properties of Rocks," *Physical Properties of Rocks and Minerals*, Y.S. Touloukian, W.R. Judd, and R.F. Roy (eds.) Hemisphere Publishing Corporation, New York (1988) 409.

Russel, H.W.: "Principles of Heat Flow in Porous Insulators," *J. Am. Ceram. Soc.* (1935) **18**, 1.

Sahimi, M., B.D. Hughes, L.E. Scriven, and H.T. Davis: "On the Improvement of the Effective-medium Approximation to the Percolation Conduction Problem," *J.Phys. C: Solid State Phys.* (1984) **17**, 1941-48.

Sahuquet, B.C. and J.J. Ferrier: "Steam-Drive Pilot in a Fractured Carbonate Reservoir: Lacq Superieur Field," *J. Pet. Tech.* (April 1982) **34**, No. 4, 873-880.

Saidi, A.M.: "Simulation of Naturally Fractured Reservoirs," paper SPE 12270 presented at the 1983 Symposium on Reservoir Simulation held in San Francisco, CA, Nov.

Sass, J.H., A.H. Lachenbruch, and R.J. Munroe: "Thermal Conductivity of Rocks from Measurements on Fragments and its Application to Heat-flow Determination, *J. of Geophysical Research* (1971) **76**, 3391-3401.

Schumann, T.E.W. and V. Voss: "Heat Flow Through Granulated Materials," *Fuel in Science and Practice* (1934) **13**, 249-56.

Schwartz, L.M. and J. Banavar: "Transport Properties of Disordered Continuum Systems," *Phys. Rev. B* (1989) **39**, No. 16, 11965-70.

Schwartz, L.M.: "Modelling Transports in Granular Porous Media," paper presented at SPWLA 31st Annual Logging Symposium, June 24-27, 1990.

Scott, J.P. and A.C. Seto: "Thermal Property Measurements on Oil Sands," *J. Can. Pet. Tech.* (Nov.-Dec. 1986) 70-77.

Seki, N., K.C. Cheng and S. Fukusako: "Measurement of Thermal Conductivity of Alberta Oil Sands," *Thermal Conductivity 17*, Plenum Press, NY (1982) 635.

Selim, M., I. Fatt, and W. Somerton: "Temperature Rise in a Semi-Infinite Medium Heated by a Disc Source," Kononkl Akademie von Wetensch., Amsterdam, Indag. Math. No. 5.

Shah, N. and J.M. Ottino: "Effective Transport Properties of Disordered, Multiphase Composites: Application of Real Space Renormalization Group Theory," *Chemical Engineering Science* (1986) 41, No. 2, 283-96.

Shallcross, D.C. and D.G Wood: "The Accurate Measurement of Heat Flux Using a Film Heat Flux Sensor With Application to Axisymetric Bodies," *Heat Transfer 1986: Proceedings of the Eighth International Heat Transfer Conference*, San Fransisco, CA.

Somers, E.V. and J.A. Cyphers: "Analysis of Errors in Measuring Thermal Conductivity of Insulating Materials," *Rev. of Sci. Instru.* (Aug., 1951) 22, No. 8, 583-86.

Somerton, W. and M. Mossahebi: "Ring Heat-Source Probe for Rapid Determination of Thermal Conductivity," *Rev. of Sci. Instr.* (1967) 38, No. 10, 1368-71.

Somerton, W. H. "Some Thermal Characteristics of Porous Rocks," *J. Pet. Tech.* (1958) 61.

Somerton, W.H. and G.D. Boozer: "A Method for Measuring Thermal Diffusivities of Rocks at Elevated Temperatures," *AIChE J.* (1961) 7, No. 1, 87-90.

Somerton, W.H. and G.D. Boozer: "Thermal Characteristics of Porous Rocks at Elevated Temperatures," *Trans.*, AIME (1960) 219, 418-422.

Somerton, W.H.: "Deformation Moduli of Water-bearing Formations at Elevated Temperatures," University of California Report (Jan., 1974).

Somerton, W.H.: "Some Thermal Characteristics of Porous Rocks," *J. Pet. Tech.* (May, 1958) 61-64; Technical Note 2008.

Somerton, W.H.: *Thermal Properties and Temperature-Related Behavior of Rock/Fluid Systems*, Elsevier, New York (1992).

Sommerton, W.H., J.A. Keese, and S.L. Chu: "Thermal Behavior of Unconsolidated Oil Sands", *Soc. Pet. Eng. J.* (Oct. 1974) 14, No. 5, 513-521.

Sonier, F. and R. Eymard: "A New Simulator for Naturally Fratured Reservoirs," paper SPE 16006 presented at the 1987 Symposium on Reservoir Simulation, San Antonio, TX, Feb.

Sonier, F., P. Souillard and F.T. Blaskovich: "Numerical Simulation of Naturally Fractured Reservoirs," paper SPE 15627 presented at the 1986 Annual Technical Conference and Exhibition, New Orleans, LA, Oct.

"Standard Test Method for Steady-State Thermal Transmission Properties by Means of the Guarded Hot Plate," ANSI/ ASTM C 177-76, 20-53.

"Standard Test Method for Steady-State Thermal Transmission Properties by Means of the Heat Flow Meter," ANSI/ASTM c 518 - 76, Phildelphia (1978) 222-253.

Standing, M.B.: *Volumetric and Phase Behavior of Oil Field Hydrocarbon Systems*, Society of Petroleum Engineers, Richardson, TX (1977).

Stell, G.: "Models of Disordered Media: Some New Results, Including Some New Connections Between Composite-Media, Fluid State, and Random-Flight Theories," *Lecture notes in Mathematics, The Mathematics and Physics of Disordered Media*, A. Dold and B. Eckmann (eds.), Springer-Verlag, New York (1983) 260-82.

Stinchcombe, R.B. and B.P. Watson: "Renormalization Group for Percolation Conductivity," *J. Phys. C: Solid State Phys.* (1976) 9, 3221-47.

Straley, J.P.: "Critical Exponents for the Conductivity of Random Resistor Lattices," *Phys. Rev. B* (1977) 15, No. 12, 5733-37.

Straley, J.P.: "Scaling Predictions for Physical Properties," *Percolation Structures & Process*, G. Deutscher, R. Zallen, J., Adler (eds.) (1983) 5, 353-65.

Sugawara, A. and Y. Yoshizawa: "An Experimental Investigation on the Thermal Conductivity of Consolidated Porous Materials," *J. Appl. Phys.* (1962) 33, No. 9, 3135.

Sykes, M.F. and J. Essam: "Some Exact Critical Percolation Probabilities for Bond and Site Problems in Two Dimensions," *Phys. Rev. Lett.* (1963) 10, 3-4.

Taylor, F.E. and H. Groot: "Thermophysical Properties of Geometrical Materials," Thermal Conductivity 17, J.G. Hust (Ed.), Plenum Press, New York (1982) 611-18.

"Thermal Conductivity V.1 & V. 2," R.P. Tye (ed.) Academic Press (1969).

Thomas, L.K., T.N. Dixon, and R.G. Pierson: "Fractured Reservoir Simulation," *Soc. Pet. Eng. J.* (Feb. 1983) 42-54.

Thompson, A.H., A.J. Katz, and C.E. Krohn: "The Microgeometry and Transport Properties of Sedimentary Rock," *Adv. Phys.* (1987) 36, No. 5, 625-94.

Tissot, B.P., R. Pelet, and P. Ungerer: "Thermal History of Sedimentary Basins, Maturation Indices, and Kinetics of Oil and Gas Generation," *The American Association of Petroleum Geologists Bulletin* (Dec. 1987), 17, No. 12, 1445-1466.

Torquato, S. and G. Stell: "Bounds on the Effective Thermal Conductivity of a Dispersion of Fully Penetrable Spheres," *Lett. Appl. Eng. Sci.* (1985) 23, 375-84.

Torquato, S.: "Electrical Conductivity of Two-phase Disordered Composite Media," *J. App. Phys.* (1985) 58, 3790-97.

Torquato, S.: "Thermal Conductivity of Disordered Heterogeneous Media from the Microstructure," *Rev. Chem. Eng.* (1987) 4, Nos. 3&4, 151-204.

Tortike, W.S. and S.M. Farouq Ali: "Saturated-Steam Property Functional Correlations for Fully Implicit Thermal Reservoir Simulation," *SPE Res. Eng.* (Nov.1989) 471-474.

Tsao, G.T.: "Thermal Conductivity of Two Phase Materials," *Ind. Eng. Chem.* (1961) **53**, No.5, 395.

Turban, L.: "Anisotropic Critical Line from Anisotropic Scaling," *J. Phys. C. Solid State Physics* (1983) **12**, 4245-50.

Verma, L.S., A.K. Shrotriya, R. Singh, and D.R. Chaudhary: Ind. *J. Pure Appl. Phys.* (1991) **29**, 220.

Vinsome, P.K.W. and J. Westerveld: "A Simple Method for Predicting Cap and Base Rock Heat Losses in Thermal Reservoir Simulators," *J. Can Pet. Tech.* (Jul.-Sep. 1980) 87-90.

Warren, J.E. and J.H. Messmer: "Thermal Conductivities of Two-Phase materials," *Ind. Eng. Chem. Fundamentals* (1962) **1**, No. 3, 222-3.

Warren, J.E. and P.J. Root: "The Behaviour of Naturally Fractured Reservoirs", *Soc. Pet. Eng. J.* (Sept. 1963) **3**, No. 3, 245-255.

Weinstein, H.G.: "Extended Semi-Analytic Method for Increasing and Decreasing Boundary Temperature," *Soc. Pet. Eng. J.* (Apr. 1974) 152-164.

Weinstein, H.G.: "Semi-Analytic Method for Thermal Coupling of Reservoir and Overburden," *Soc. Pet. Eng. J.* (Oct. 1972) 439-447.

Wilhelm, R.H., W.L. Johnson, R. Wynkoop, and D.W. Collier: "Reaction Rate, Heat Transfer, annd Temperature Distribution in Fixed-Bed Catalytic Convereters, *Chem. Eng. Prog.* (1948) **44**, No. 2, 105-16.

Wilson, K.G. and J. Kogut: "The Renormalization Group and the ε Expansion," *Phys. Rep.* (1974) **12C**, 75-200.

Wolff, M.: "Geologically Based Fractured Reservoir Simulator", PhD dissertation, U. of Texas, Austin (1987).

Woodside, W. and J.H. Messmer: "Thermal Conductivity of Porous Media I. Unconsolidated Sands," *J. Appl. Phys.* (1961) **32**, No. 9, 1688.

Woodside, W. and A.G. Wilson: "Unbalance Error in Guarded Hot Plate Measurements," *Symposium on Thermal Conductivity Measurements and Application of Thermal Insulations*, ASTM Special Technical Publication No. 217, Philadelphia (1957) 32-48.

Woodside, W. and J.H. Messmer: "Thermal Conductivity of Porous Media. II. Consolidated Rocks," *J. Appl. Phys.* (September, 1961) **32**, No. 9, 1699-706.

Woodside, W.: "Analysis of Errors Due to Edge Heat Loss in Guarded Hot Plates," *Symposium on Thermal Conductivity Measurements and Application of Thermal*

Insulations, ASTM Special Technical Publication No. 217, Philadelphia (1957) 49-64.

Woodside, W.: "Calculation of the Thermal Condutivity of Porous Media," *Canadian J. Phys.* (1958) **36**, 815-23.

Wu, Y.S. and K. Pruess: "A Multiple-Porosity Method for Simulation of Naturally Fractured Petroleum Reservoirs," paper SPE 15129 presented at the 1986 California Regional Meeting, Oakland, CA, Apr.

Wyllie, M.R.J. and P.F. Southwick: "An Experimental Investigation of S.P. and Resistivity Phenomena in Dirty Sand," *J. Pet. Tech.* (1954) 3750.

Xia, W. and M.F. Thorpe: "Percolation Properties of Random Ellipses," *Phys. Rev. A* (1988) **38**, No. 5, 2650-56.

Yamamoto, R.H., J.B. Padgett, W.T. Ford, and A. Boubeguira: "Compositional Reservoir Simulator for Fissured Systems-The Single Block Model," *Soc. Pet. Eng. J.* (June 1971) 113-128.

Yang, Y.S.: "Heat Transfer Through a Randomly Packed Bed of Spheres by the Monte Carlo Method," PhD Dissertation, U. of Texas at Austin, Austin, TX (1981).

Young, A.P. and R.B. Stinchcombe: "A Renormalization Group Theory for Percolation Problems," *J. Phys. C: Solid State Phys.* (1975) **8**, L535-40.

Zierfuss, H., and G. van der Vliet: "Laboratory Measurements on Heat Conductivity of Sedimentary Rocks," *American Assoc. of Petroleum Geologists, Bull. No. 10* (Oct., 1956) **40**, 2475-88.

APPENDIX A. NEW FUNCTIONAL CORRELATIONS FOR SATURATED STEAM PROPERTIES

A new set of continuous correlation functions of saturated steam properties (density, enthalpy and viscosity) has been developed. The new correlations cover the saturation envelope from 20°C to 360°C and are highly accurate and continuous over a wide temperature range. In terms of simplicity, accuracy, and continuity, these functions offer advantages in certain applications over those previously published.

NEW FUNCTIONAL CORRELATIONS

The most commonly used methods for determining saturated steam properties in computer applications are to use table look-up, or a series of equational approximations to fit the data. In this study we have developed a set of simple continuous correlation functions for saturated steam properties, which have certain advantages over those previously published in terms of combined simplicity and accuracy. These functions cover a temperature range from 20°C to 360°C, the temperature range of interest in most thermal recovery operations.

Recent work on steam properties presented some new polynomial equations for steam properties. Ejiogu and Fiori (1987) presented polynomial interpolations that cover the high temperature range from 241°C to 353°C. Tortike and Farouq Ali (1989) developed a set of steam properties as polynomials throughout most of the temperature range of saturated steam from 0°C to 353°C. Chien (1992) presented empirical correlations which are highly accurate but are mostly discontinuous and require a large number of coefficients. These studies provide a baseline for comparison with our new correlations.

Theoretically , any data can be fit by a polynomial no matter how complicated. However, as the degree of a polynomial increases, the fitting curve may include many changes in derivative. For most applications it is desirable to choose a degree of fit as low as possible in order to reduce oscillations, while still retaining desired accuracy. Using different correlations to fit data in different ranges is another way to obtain more accurate results. But this may cause discontinuities in the derivatives that could lead to, among other things, convergence problems in simulation. The best correlations are accurate enough to cover the required range, continuous in its derivative, and simple to use.

The data used in this study were tabulated data from the National Bureau of Standards/National Research Council of Canada (1984). For saturated water and steam, the correlations were developed using polynomial and nonlinear regression. Regression coefficients and residuals were used to judge the accuracy and suitability of each correlation. All correlations are presented in SI units. Temperature was chosen as the independent variable. This makes the correlations simple and easy to use in thermal reservoir simulation. Relative residuals were calculated between the correlations and the steam table data, expressed as percentages of actual values. The maximum and mean absolute values of the residuals are also reported.

Saturated water density

$$\rho_w = 398.942 + 8.288558\sqrt{5335.9562 - T^{1.45}} \tag{A.1}$$

Saturated vapor density

$$\rho_s = EXP\left[-5.6294 + 0.14564T^{0.8} - 2.1242 \times 10^{-4}T^{1.6} \right.$$
$$\left. -7.4288 \times 10^{-6}T^{2.4} + 4.7323 \times 10^{-8}T^{3.2}\right] \tag{A.2}$$

Saturated water enthalpy

$$h_w = 2751 - 212.23333\sqrt{170.86 - T^{0.85}} \tag{A.3}$$

Saturated vapor enthalpy

$$h_s = 178.758 + 5.14455T + 119.8224\sqrt{374.09 - T} \tag{A.4}$$

Saturated water viscosity

$$\mu_w = EXP\left[0.484045 - 3.1115 \times 10^{-2}T^{0.95} + 1.3192 \times 10^{-4}T^{1.9} \right.$$
$$\left. -2.2934 \times 10^{-7}T^{2.85}\right] \tag{A.5}$$

Saturated vapor viscosity

$$\mu_s = 0.0085 + EXP\left[-7.0661 + 2.1106 \times 10^{-2}T \right.$$
$$\left. -7.2058 \times 10^{-5}T^2 + 1.0111 \times 10^{-7}T^3\right] \tag{A.6}$$

Comparisons of the new correlations to recent studies are listed in Tables A.1 through A.7 and Figs. A.1 through A.7. As can be seen, the new correlations generally have both greater accuracy and fewer coefficients than the equations of Tortike and Farouq Ali (1989). The equations of Chien (1992) are highly accurate, but have a large number of equations and coefficients.

For water density and vapor enthalpy, the new correlations have a maximum residual smaller than 0.25%. The highest residual among the new correlations is for vapor density, which reaches nearly 3% at 360°C. All the others have maximum residuals less than 2%. Absolute residuals between 100°C and 300°C are even smaller.

Comparisons of water and vapor viscosities are made only between the new correlations and those of Chien (1992). The residuals calculated using the correlations of Tortike & Farouq Ali (1989) are larger than they reported, which leads us to believe that the published equations may be incorrect.

Table A.1. Comparison of saturated water density equations and residuals.

	Continuous	Number of Equations	Number of Coefficients	Temperature Range (C)	Max. Absolute Residual %	Mean Absolute Residual %
This work	yes	1	3	20-360	0.20	0.07
Chien (1992)	no	2	12	100-370	0.12	0.03
Tortike and Farouq Ali (1989)	yes	1	6	0-367	A.87	0.22

Table A.2. Comparison of saturated vapor density equations and residuals.

	Continuous	Number of Equations	Number of Coefficients	Temperature Range (C)	Max. Absolute Residual %	Mean Absolute Residual %
This work	yes	1	5	20-360	2.98	0.56
Chien (1992)	no	2	15	100-369	0.11	0.03
Tortike and Farouq Ali (1989)	yes	1	6	0-372	7.71	A.29

Table A.3. Comparison of saturated water enthalpy equations and residuals.

	Continuous	Number of Equations	Number of Coefficients	Temperature Range (C)	Max. Absolute Residual %	Mean Absolute Residual %
This work	yes	1	4	20-360	A.67	0.71
Chien (1992)	yes	1	12	20-369	0.07	0.03
Tortike and Farouq Ali (1989)	yes	1	7	0-372	2.93	0.52

Table A.4. Comparison of saturated vapor enthalpy equations and residuals.

	Continuous	Number of Equations	Number of Coefficients	Temperature Range (C)	Max. Absolute Residual %	Mean Absolute Residual %
This work	yes	1	3	20-360	0.25	0.085
Chien (1992)	yes	1	12	20-369	0.10	0.044
Tortike and Farouq Ali (1989)	yes	1	7	0-367	0.50	0.08

Table A.5. Comparison of saturated water viscosity equations and residuals.

	Continuous	Number of Equations	Number of Coefficients	Temperature Range (C)	Max. Absolute Residual %	Mean Absolute Residual %
This work	yes	1	4	20-360	1.56	0.78
Chien (1992)	no	2	12	50-370	0.22	0.06
Tortike and Farouq Ali (1989)	yes	1	6	0-372	7.6(2.87)	1.98(1.07)

Table A.6. Comparison of saturated vapor viscosity equations and residuals.

	Continuous	Number of Equations	Number of Coefficients	TemperatureRange (C)	Max. Absolute Residual %	Mean Absolute Residual %
This work	yes	1	5	20-360	A.34	0.45
Chien (1992)	no	2	14	70-370	0.17	0.10
Tortike andFarouq Ali (1989)	yes	1	6	0-372	18.2(6.41)	3.87(1.59)

Note: The data in parentheses were reported by Tortike and Farouq Ali (1989).

Table A.7. Comparison of heat of vaporization.

	Continuous	Number of Equations	Number of Coefficients	Temperature Range (C)	Max. Absolute Residual %	Mean Absolute Residual %
This work	yes	1*	6	20-360	0.56	0.216
Chien (1992)	yes	1*	23	20-369	0.24	0.062
Tortike and Farouq Ali (1989)	yes	1	6	0-372	0.323	0.104

*The heat of vaporization is calculated using the water and vapor enthalpy correlations.
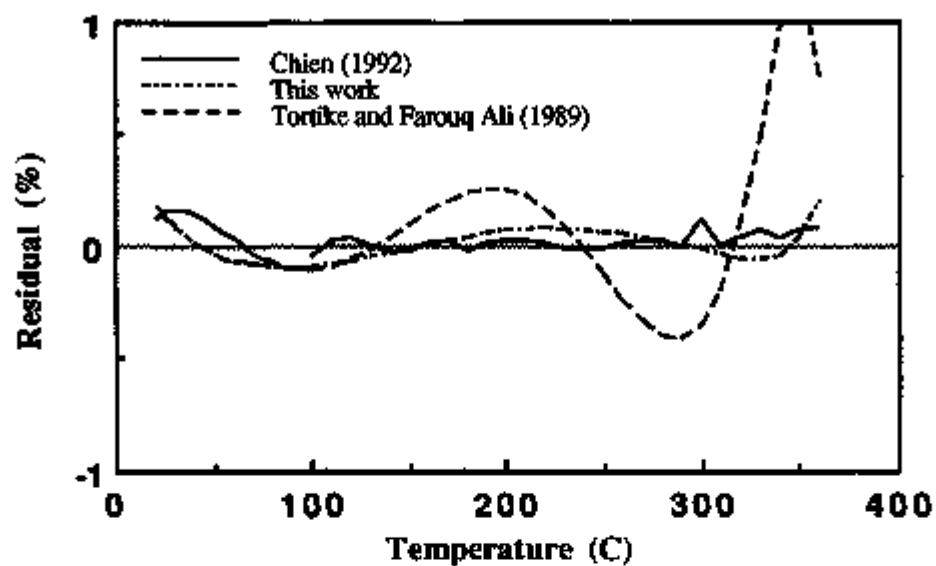
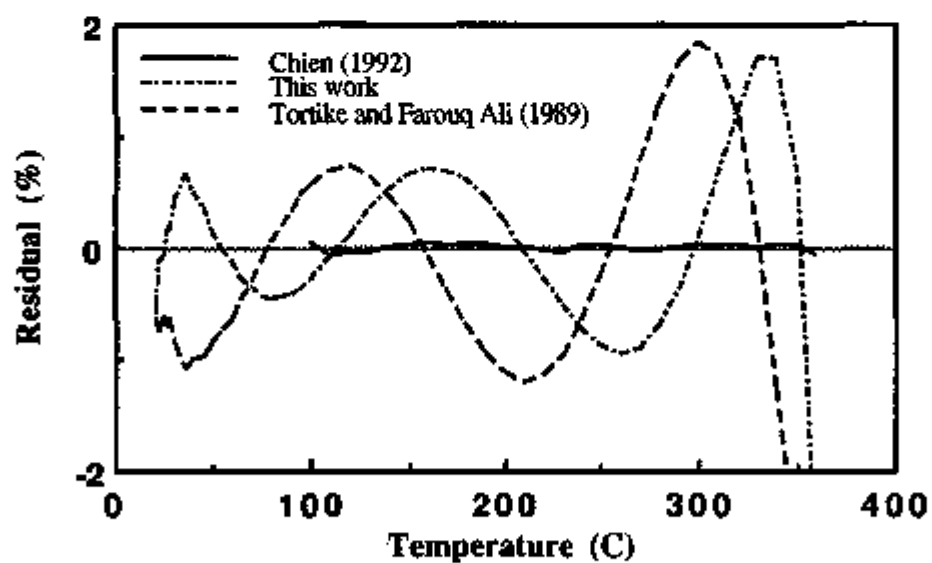Fig. A.1. Water density residual vs. temperature
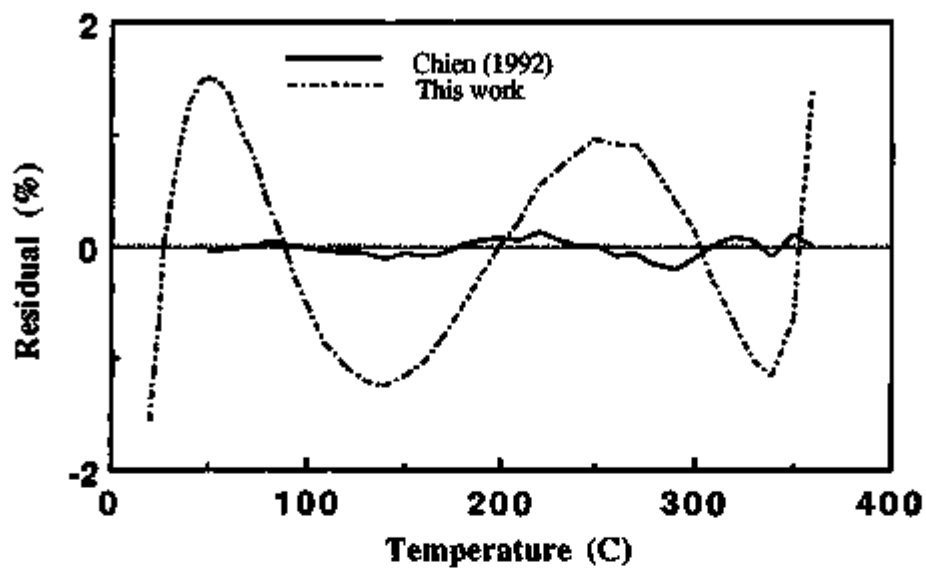

Fig. A.2. Vapor density residual vs. temperature
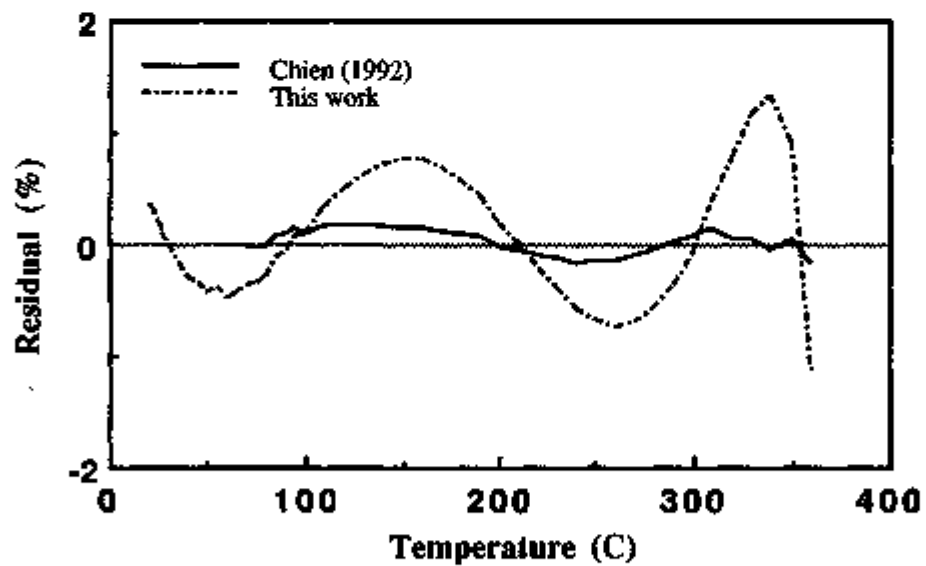
Fig. A.3. Water viscosity residual vs. temperature

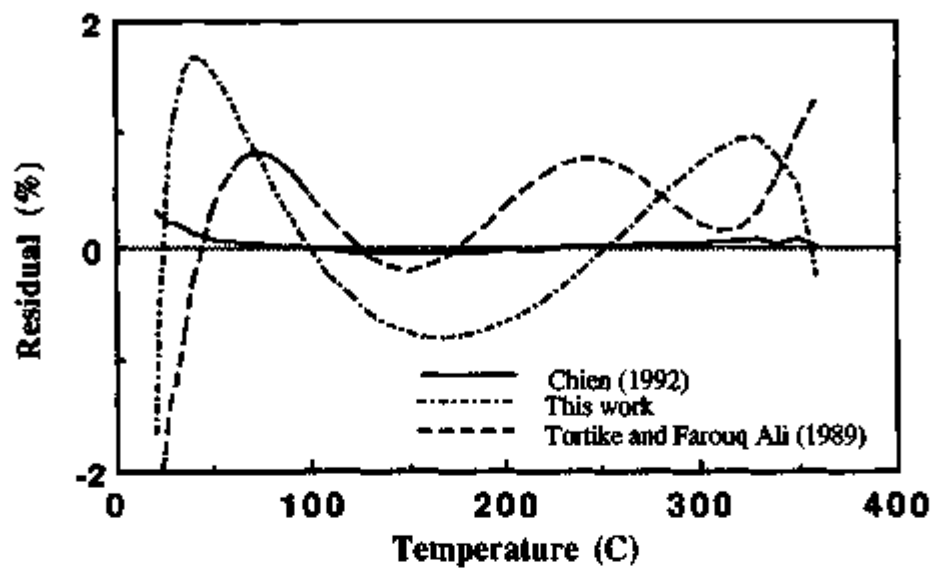Fig. A.4. Vapor viscosity residual vs. temperature

221

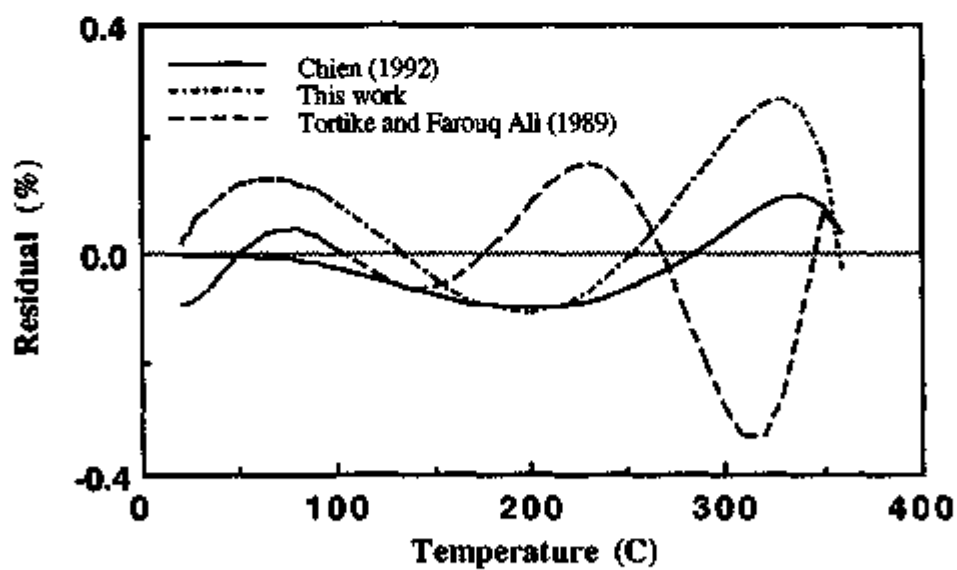Fig. A.5. Water enthalpy residual vs. temperature
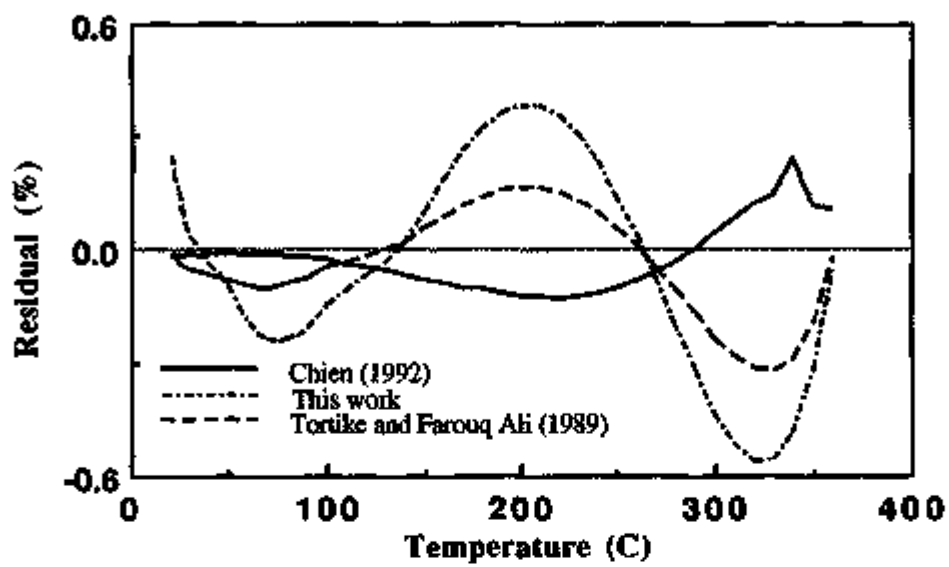

Fig. A.6. Vapor enthalpy residual vs. temperature

Fig. A.7. Heat of vaporization residual vs. temperature